

LIDAR AND INFRARED RADIOMETER STUDIES
OF
STRATOCUMULUS CLOUDS

A thesis submitted

By

Matthew Charles Pickett



For the degree of

DOCTOR OF PHILOSOPHY

Optical Technology Research Laboratory

School of Communications and Informatics

Victoria University

February 1999



FTS THESIS
551.576 PIC
30001005559200
Pickett, Matthew Charles
Lidar and infrared
radiometer studies of
stratocumulus clouds

Declaration

I, **Matthew Charles Pickett**, declare that the thesis titled,

“Lidar and Infrared Radiometer Studies of Stratocumulus Clouds”

is my own work and has not been submitted previously, in whole or in part, in respect of any other academic award.



M. C. Pickett,

Dated the 22nd day of February, 1999.

Acknowledgments

I owe my sincere thanks to:

Principal acting supervisor Dr. Stuart Young of the CSIRO Division of Atmospheric Research (Australia), and co-supervisor Dr. Martin Platt formerly of the Division now with the Colorado State University (USA), for their expert guidance;

Prof. David Booth of the Optical Technology Laboratory, Department of Applied Physics, Victoria University of Technology (Australia), for making this project possible;

Reinout Boers for assisting me with questions on the cloud microphysics and dynamics and for providing the microwave radiometer data, Paul Krummel for doing a great job providing me with the airborne data and the weather and satellite images, (satellite image processing - Mary Edwards), all of CSIRO;

Denis O'Brien for introducing me to the DISORT radiative transfer program, and again Denis, Bob Cechet and Reinout Boers (all of CSIRO) for their comments on the thesis;

Graeme Patterson, Richard Austin, and Stephen Marsden of the CSIRO's lidar group for providing assistance with reducing some of the lidar and infrared radiometer data, and Dan Gogaosa (ex-VUT) for some assistance with C-programming;

The engineers and technicians of the CSIRO electronics and mechanical workshops for working on the lidars and radiometers;

And the Bureau of Meteorology staff at the Cape Grim Baseline Air Pollution Station, Tasmania, for their assistance during SOCEX.

I owe special thanks to my parents Keith and Coralie Pickett for their enduring support and encouragement.

Finally, thanks to Sue for seeing me out.

Summary

This thesis comprises a study of marine stratocumulus clouds measured by ground-based Lidar and Infrared RADiometry (or LIRAD). The clouds were measured in northwestern Tasmania in the winter of 1993 and summer of 1995 during the Southern Ocean Cloud EXperiment (SOCEX). The study done for this thesis represents the first application of the LIRAD method to low boundary layer clouds. This application was possible due to the wide variation in the optical depths of the clouds; approximately 20% (summer study) and 40% (winter study) of the clouds had visible optical depths less than unity. The LIRAD results included the height of cloud base, the effective visible extinction-to-backscatter ratio (ηS) and effective visible extinction-to-infrared absorption ratio ($\eta\alpha$) both modified by the multiple scatter factor (η), infrared optical depth (τ_i) and emittance (ϵ_i), and effective visible optical depth ($\eta\tau_v$).

Comparisons of the LIRAD results with Mie properties of the cloud droplets and aerosols obtained from *in situ* measurements were an important part of the LIRAD study. First, *in situ* measurements of the aerosols were used for the validation and calibration of the lidar measurements. Excellent agreement was found between the aerosol backscatter determined from *in situ* measurements and the lidar measurements, but only after the swelling of the aerosols in the humid boundary layer was taken into account. From this combined lidar and *in situ* study of the aerosols it was found that the larger (swollen) aerosols, with radii of greater than 1 μm , made the largest contribution to the visible aerosol backscatter. Second, multiple scattering in lidar returns is normally an obstacle to the analysis of lidar returns which is overcome by theoretical work. However in this study the multiple scatter factors (η) were determined experimentally by a comparison of the LIRAD-retrieved microphysical quantities ηS and $\eta\alpha$ with S and α determined from the *in situ* measurements. The results for η were, for the moderately thin clouds ($0.12 < \tau_v < 0.88$), $\eta = 0.6 \pm 0.2$, and for the thicker clouds with $\tau_v \approx 1.3$, $\eta = 0.77 \pm 0.05$. To the author's knowledge this is the first time measurements of η have been made by comparing *in situ* measurements of clouds with LIRAD results.

Simultaneous microwave radiometer measurements were also utilised in the analysis of the LIRAD data. Water vapour paths retrieved by microwave radiometer were used to assist with the retrieval of continuous downward infrared radiances of the cloud-free atmosphere over Cape Grim. Also, retrieved cloud liquid water paths were used to obtain some order of magnitude values of the thicker boundary layer clouds.

The work done for this thesis indicates that the LIRAD method can be applied to boundary layer clouds, and further LIRAD studies of boundary layer clouds should provide valuable new information on the optical properties of these clouds. Also, the results of the thesis indicate that the following areas of study require further investigation: (1) Optically thin clouds ($\tau_v < 1$ or $\epsilon < 0.3$) and large aerosols ($r > 1 \mu\text{m}$) in the marine boundary layer and their effects on the optical properties of the atmosphere. 2) The utility of calculations of η from LIRAD and aircraft measurements, as obtained in this study, for improving theoretical studies of the multiple scattering in lidar returns.

1. Introduction

1.1 Clouds and Climate	1-1
1.2 Boundary Layer Clouds and Marine Aerosols	1-3
1.3 Lidar Studies of Boundary Layer Clouds	1-5
1.4 Infrared (10-12 μm) Radiometry of Clouds and the LIRAD Method	1-7
1.5 Outline of the Thesis	1-9

2. Cloud Optical Properties by Lidar and the LIRAD Method

2.1 Introduction	2-1
2.2 Analysis of Lidar Returns	2-1
2.2.1 <i>The Lidar Equation</i>	2-1
2.2.1.1 Returned Optical Power	2-1
2.2.1.2 Measured Signal	2-3
2.2.1.3 Multiple Scattering in Lidar Returns from Clouds	2-4
2.2.1.4 Range-Corrected and System-Independent Lidar Equation	2-5
2.2.2 <i>Lidar Equation Solutions for Extinction and Backscatter</i>	2-7
2.2.2.1 Introduction	2-7
2.2.2.2 The Iterative Technique	2-9
2.2.2.3 The Slope Technique	2-10
2.2.2.4 The Analytic Solution (Logarithmic Variable)	2-10
2.2.2.5 The Analytic Solution (Linear Variable)	2-11
2.2.3 <i>Integrated Attenuated Backscatter</i>	2-13
2.2.4 <i>Calculated Visible Optical Depths</i>	2-16
2.3 The Lidar and Infrared Radiometer (LIRAD) Method	2-17
2.3.1 <i>Introduction</i>	2-17
2.3.2 <i>Measured Infrared (10-12 μm) Radiances</i>	2-18
2.3.3 <i>Calculated Infrared Properties of Cloud-Free Air</i>	2-19
2.3.4 <i>The LIRAD Equation</i>	2-20
2.3.5 <i>The LIRAD Analysis Technique</i>	2-23
2.3.6 <i>Errors</i>	2-24
2.3.6.1 Errors due to Multiple Scattering in Lidar Returns from Clouds	2-24
2.3.6.2 Errors in the Cloud Infrared Radiances	2-25

3. Experiment

3.1 Introduction	3-1
3.1.1 <i>The Southern Ocean Cloud Experiment (SOCEX)</i>	3-1
3.1.2 <i>The Cape Grim Baseline Air Pollution Station (CGBAPS)</i>	3-1
3.2 Equipment	3-2
3.2.1 <i>Ground-Based Lidars</i>	3-2
3.2.2 <i>Lidar Data Acquisition Program for SOCEX2</i>	3-3
3.2.3 <i>Ground-Based Infrared Radiometers</i>	3-3
3.2.4 <i>Ground-Based Microwave Radiometer</i>	3-5
3.2.5 <i>Airborne Aerosol Probe (ASASP)</i>	3-5
3.2.6 <i>Airborne Water Droplet Probes (FSSP and 2D-C)</i>	3-6
3.3 LIRAD Measurements During SOCEX	3-6
3.4 Case Studies Selected for Analysis	3-8
3.4.1 <i>16 July 1993 (SOCEX1)</i>	3-8
3.4.1.1 Introduction	3-8
3.4.1.2 Weather Condition, Clouds, and Measurements (16 July 1993)	3-9

3.4.2	8 February 1995 (SOCEX2)	3-14
3.4.2.1	Introduction	3-14
3.4.2.2	Weather Condition, Clouds, and Measurements	3-14

4. Analysis Methods

4.1	Introduction	4-1
4.2	Cloud Heights Measured by Lidar	4-1
4.2.1	<i>Introduction</i>	4-1
4.2.2	<i>Measurement of Cloud Heights</i>	4-2
4.2.3	<i>Vertical Distribution of Cloud Base Height</i>	4-3
4.3	LIRAD Measurements of 16 July 1993 (SOCEX1)	4-5
4.3.1	<i>Introduction</i>	4-5
4.3.2	<i>In Situ Properties of the Stratocumulus Clouds</i>	4-6
4.3.2.1	Introduction	4-6
4.3.2.2	Visible Properties of Small Cloud Droplet Mode (FSSP)	4-7
4.3.2.3	Visible Properties of the Large Droplet Mode (2D-C)	4-8
4.3.2.4	Infrared Properties of the Small Droplet Mode (FSSP)	4-10
4.3.2.5	Infrared Properties of the Large Droplet Mode (2D-C)	4-10
4.3.3	<i>Lidar Calibration</i>	4-12
4.3.3.1	Introduction	4-12
4.3.3.2	In Situ Measurements of the Maritime Aerosols	4-12
4.3.3.3	Measured Aerosol Size Distributions	4-15
4.3.3.4	Composition and Refractive Indices of the Measured Aerosols	4-16
4.3.3.5	Effect of Humidity	4-17
4.3.3.6	Optical Properties of the Marine Boundary Layer Aerosols	4-18
4.3.3.7	Optical Properties of the Free Troposphere Aerosols	4-20
4.3.3.8	Method for Lidar Calibration Using a Reference Molecular Atmosphere	4-20
4.3.3.9	Lidar Calibration Constant Obtained During Cloud-Free Periods	4-22
4.3.4	<i>Combined Lidar and Infrared Radiometer Data</i>	4-27
4.3.4.1	Introduction	4-27
4.3.4.2	Measured Total Infrared Radiances	4-27
4.3.4.3	Integrated Attenuated Cloud Backscatter	4-28
4.3.4.4	Measured Clear Sky Radiances	4-32
4.3.4.5	Comparison of Water Vapour Path with Clear Sky Radiance	4-37
4.3.4.6	Calculated Infrared Properties of Water Vapour	4-41
4.3.4.7	Estimate of Infrared Scattering using the DISORT Program	4-46
4.3.4.8	Application of the LIRAD Method to Low Water Droplet Clouds	4-49
4.4	LIRAD Measurements of 8 February 1995 (SOCEX2)	4-51
4.4.1	<i>Introduction</i>	4-51
4.4.2	<i>Comparisons Between the Mie Properties of Stratocumulus Clouds for the Nd:YAG Laser Wavelengths 1064 nm and 532 nm</i>	4-51
4.4.3	<i>Calibration of the Minilidar</i>	4-52
4.4.4	<i>Clear Sky Radiances and Infrared Transmittances</i>	4-54

5. Results

5.1	Introduction	5-1
5.2	Lidar Observations of Cloud Heights During SOCEX	5-2
5.3	Properties of Clouds Observed on 16 July 1993 (SOCEX1)	5-6
5.3.1	<i>Introduction</i>	5-6
5.3.2	<i>Lidar Observations of Cloud Heights on 16 July 1993 (In Detail)</i>	5-8
5.3.3	<i>Microphysical and Optical Properties of Stratocumulus Clouds by the In Situ Scattering Probes (FSSP and 2D-C) On 16 July 1993 (Flight 8)</i>	5-10
5.3.3.1	Introduction	5-10
5.3.3.2	Droplet Size Distributions	5-11

5.3.3.3	Droplet Concentrations	5-20
5.3.3.4	Cloud Droplet Effective Radius	5-22
5.3.3.5	Liquid Water Content	5-27
5.3.3.6	Liquid Water Path	5-31
5.3.3.7	Visible Extinction	5-34
5.3.3.8	Visible Backscatter	5-36
5.3.3.9	Visible Extinction-to-Backscatter Ratio	5-39
5.3.3.10	Infrared Absorption	5-41
5.3.3.11	Ratio of Visible Extinction to Infrared Absorption	5-44
5.3.3.12	Visible Optical Depths	5-46
5.3.3.13	Infrared Absorption Optical Depths	5-48
5.3.4	<i>LIRAD Study of Stratocumulus Clouds Observed On 16 July 1993 (SOCEX1)</i>	5-50
5.3.4.1	Introduction	5-50
5.3.4.2	Infrared Properties of the Clouds by LIRAD	5-52
5.3.4.3	Extinction-to-Backscatter Ratio Modified by the Multiple Scatter Factor	5-56
5.3.4.4	Visible Optical Depths Modified by the Multiple Scatter Factor	5-58
5.3.4.5	The Multiple Scatter Factor and Distributions of the Visible Optical Depths	5-60
5.3.5	<i>Microwave Radiometer Results</i>	5-63
5.3.5.1	Introduction	5-63
5.3.5.2	Limitations of the Measurements	5-63
5.3.5.3	Liquid Water Paths by Microwave Radiometer	5-64
5.3.5.4	LIRAD and In Situ Measurements by FSSP and 2D-C (16 July 1993)	5-65
5.3.5.5	Visible Optical Depths from Liquid Water Paths (16 July 1993)	5-66
5.3.5.6	Visible Optical Depths by Microwave Radiometer (16 July 1993)	5-67
5.3.5.7	Infrared Optical Depths from Liquid Water Paths (10 July 1993)	5-68
5.4	Properties of Clouds Observed on 8 February 1995 (SOCEX2)	5-72
5.4.1	<i>LIRAD Study of Stratocumulus Clouds (8 February 1995)</i>	5-72
5.4.1.1	Introduction	5-72
5.4.1.2	Infrared Properties of the Clouds by LIRAD	5-77
5.4.1.3	Estimate of the Multiple Scatter Factor	5-82
5.4.2	<i>Visible Optical Depths by Microwave Radiometer (8 February 1995)</i>	5-84
5.5	Discussion of Results	5-86
5.5.1	<i>Introduction</i>	5-86
5.5.2	<i>Lidar Measured Cloud Heights (SOCEX)</i>	5-87
5.5.3	<i>Properties of Clouds Observed on 16/7/93 (SOCEX1)</i>	5-88
5.5.3.1	Aircraft <i>In Situ</i> Measurements	5-88
5.5.3.2	LIRAD Study of Stratocumulus Clouds Observed on 16/7/93	5-89
5.5.3.3	Optical Depths of Stratocumulus Clouds by Microwave Radiometer (16/7/93)	5-90
5.5.4	<i>Properties of Clouds Observed on 8/2/95 (SOCEX2)</i>	5-90
5.5.4.1	LIRAD Study of Stratocumulus Clouds Observed on 8/2/95	5-90
5.5.4.2	Optical Depths of Stratocumulus Clouds by Microwave Radiometer (8/2/95)	5-91
5.5.5	<i>Cloud Optical Depths</i>	5-91
5.5.6	<i>Lidar Multiple Scattering Factor</i>	5-94
6.	Conclusions	
	<i>Introduction</i>	6-1
6.1	Lidar Measured Heights of Boundary Layer Clouds	6-1
6.2	Lidar and Infrared Radiometer (LIRAD) Studies of Boundary Layer Clouds	6-2
6.3	Optically Thin Boundary Layer Clouds	6-3
6.4	Multiple Scattering in Lidar Returns from Stratocumulus Clouds	6-3
6.5	Cloud Optical Depths by Lidar, In Situ Measurements and Microwave Radiometer	6-4
6.6	Optical Properties of Moist Boundary Layer Aerosols	6-5
6.7	Recommendations for Future Work	6-5

Appendix A1. Radiative Quantities and List of Symbols	A-1 to A-3
Appendix A2. Optical Properties of Air Molecules, Spherical Aerosols and Cloud Droplets	
A2.1 Introduction	A-4
A2.2 Microphysical Properties and Measures of Cloud Water	A-4
A2.3 Radiative Quantities	A-5
A2.4 Basic Radiative Transfer Theory	A-7
A2.4.1 <i>Extinction</i>	A-7
A2.4.2 <i>Extinction by Scattering</i>	A-9
A2.4.3 <i>Thermal Emission</i>	A-10
A2.4.4 <i>The Equation of Radiative Transfer</i>	A-10
A2.4.5 <i>Calculation of Beam Emittance from an Absorption Profile</i>	A-12
A2.5 Absorption of Electromagnetic Radiation by Air Molecules	A-12
A2.5.1 <i>Introduction</i>	A-12
A2.5.2 <i>Absorption of Visible and Infrared (10 - 12 μm) Radiation by Air Molecules</i>	A-13
A2.6 Rayleigh Scattering by Air Molecules	A-14
A2.6.1 <i>Introduction</i>	A-14
A2.6.2 <i>The Rayleigh Scattering Coefficients</i>	A-14
A2.6.3 <i>Calculation of Attenuated Molecular Backscatter for Lidar Calibration</i>	A-15
A2.7 Optical Properties of Spherical Aerosols and Cloud Droplets	A-17
A2.7.1 <i>Introduction</i>	A-17
A2.7.2 <i>The Mie Theory of Scattering of Electromagnetic Radiation by Spheres</i>	A-18
A2.7.3 <i>Mie Properties of Polydispersions</i>	A-19
A2.7.4 <i>Mie Properties for Scattering of Visible (532 nm) Light by Stratocumulus Cloud Droplets</i>	A-20
A2.7.5 <i>Infrared (10 - 12 μm) Scattering in Water Droplet Clouds and Emittance</i>	A-22
A2.7.6 <i>Cloud Infrared Optical Properties and Liquid Water Properties</i>	A-26
Appendix A3. Derivations of Solutions to the Lidar Equation	
A3.1 The Lidar Equation and Basic Quantities	A-28
A3.2 Solution for a Homogeneous Atmosphere (The Slope Technique)	A-28
A3.3 Solution for an Inhomogeneous Atmosphere (Logarithmic Variable)	A-29
A3.4 Solutions for Inhomogeneous Atmospheres (Linear Variable)	A-30
Appendix A4. Lidar Data Acquisition Program	A-37
Appendix A5. List of Publications and Reports by the Author	A-39
References	[9 pages]

1. Introduction

1.1 Clouds and Climate

Solar radiation incident on the lower more dense part of the atmosphere, the troposphere, is scattered and absorbed by air molecules, small suspended solid and liquid particles (aerosols), cloud water droplets and ice crystals. The atmosphere scatters some of the incident radiation back towards space, and the radiation absorbed by the atmosphere increases its temperature. The solar radiation transmitted through the atmosphere is both reflected and absorbed by the earth's ocean and land surfaces. The warm earth and atmosphere both emit thermal radiation into space and back towards the earth. These solar and terrestrial radiative fluxes determine the state of the earth's climate and the earth's surface temperature. Averaged over a year, say, the net solar plus thermal radiative fluxes are zero. So, for example, an increase in the absorption of solar radiation by the atmosphere causes the earth-atmosphere system to heat until the absorbed radiation is balanced by the thermal radiation emitted back to space.

Without the atmosphere the mean temperature of the earth's surface would be about -18°C . With the addition of the earth's current molecular atmosphere, without aerosols or clouds, the temperature of the earth's surface would be increased to about $+30^{\circ}\text{C}$ (Platt, 1989). This warming is the so-called greenhouse effect, and is caused by the absorption of terrestrial infrared radiation by trace gases in the atmosphere, mainly CO_2 and H_2O , and the re-emission of some of this energy back towards the earth.

Clouds cause two effects: a cooling of climate by the reflection of solar radiation to space, and the absorption and re-emission of terrestrial radiation by clouds has a net warming effect. For certain cloud types, the degree to which the warming effect offsets the cooling effect depends on the cloud heights (*i.e.* differences in temperature from the earth's surface), and their optical depths (*i.e.* solar albedos): {see, for example, Platt (1981b)}. The net effect of clouds on climate is calculated at present as a cooling. Clouds are thus considered an important controlling element in determining the state of the earth's climate (Platt *et al.*, 1994).

The water droplets and ice crystals of clouds are strong scatterers of visible radiation and reflect a large portion of the incident solar radiation back to space. The molecular greenhouse effect is thus weakened by the presence of clouds such that the mean surface temperature is about +12°C (Platt, 1989). Low clouds have the largest cooling effect on climate through solar reflection because they have higher albedos. The potential for changes in the properties of low clouds to impact the earth's climate may be great: Randall *et al.* (1984) estimated that a small increase in the coverage of low clouds would cool the average temperature of the earth's surface by enough to offset global warming caused by a doubling of CO₂ in the atmosphere. Slingo (1990) calculated that the warming due to a doubled concentration of CO₂ could be balanced by a 15-20% increase in the amount of low clouds.

Blackbodies at terrestrial temperatures, say at 0°C, emit strongly between the wavelengths 8 μm and 14 μm, with the peak radiances occurring between the wavelengths 10 μm and 11 μm. In the atmosphere, a window of low molecular absorption exists for wavelengths 8 - 14μm, providing a means of escape for terrestrial radiation to space. Water droplets and ice crystals are strong absorbers of infrared radiation, including the terrestrial radiation that would normally escape through the 8 - 14 μm window. So clouds form a better trap of terrestrial radiation than air molecules alone. Clouds absorb upwelling terrestrial thermal radiation, re-emit it back towards the earth, and reduce the emission to space. Thus, they cause an additional Greenhouse warming. High clouds emit thermal radiation to space at temperatures tens of degrees Celsius below freezing, however clouds in the lowest few kilometres of the atmosphere emit thermal radiation from their tops at temperatures nearer to those of the earth's surface. The smaller upward infrared fluxes from the tops of high clouds means they are greater warmers of climate.

At present, our knowledge of radiative transfer in clouds and the variation in the distribution and microphysics of clouds is incomplete. A great deal of work is being done to more accurately determine the way in which clouds affect the radiative balance (see, for example, Schiffer and Rossow, 1983; Randall *et al.*, 1996), so that they may be more accurately modelled in global circulation models (see, for example, Cess *et al.*, 1989). This thesis gives a further contribution to these studies.

1.2 Boundary Layer Clouds and Marine Aerosols

There is a connection between increased concentrations of pollutants in the atmosphere and the optical properties of clouds that may have an impact on climate. Some early satellite observations showed ship tracks in clouds, where smoke from ship stacks injected into clouds increased their reflectivity (Conover, 1966). Many studies of ship tracks in clouds have been made since (see, for example, Ackerman *et al.*, 1995). The visibility of ship tracks from space can be explained by the increased amounts of aerosols in the atmosphere providing more Cloud Condensation Nuclei (CCN) cloud droplets form. With the assumption that the amount of water vapour in the atmosphere remains the same, increases in CCN cause an increased number of (smaller) droplets in clouds. This leads to an increase in cloud albedo so that more solar radiation is reflected to space (Twomey, 1977).

Cloud optical properties also vary in clouds that form in air free of anthropogenic aerosols. (Throughout this thesis the terms 'marine' and 'maritime' shall be used to describe air free of anthropogenic or terrestrial pollutants). The shortwave reflective and longwave absorption properties of these marine boundary layer clouds depend on both the concentrations and size distributions of the water droplets, characteristics which in turn are dependent on the properties of the aerosols from which the droplets formed. The reflective properties of these clouds are also susceptible to changes in the size and concentration of CCN (see, for example, Twomey *et al.*, 1984). Some stratocumulus cloud field experiments have been conducted in conditions mainly uncontaminated by aerosols (Boers *et al.*, 1996). As an example, the Southern Ocean Cloud EXperiment (SOCEX) (in which the measurements reported in this thesis were made) was held with the aims of increasing knowledge of the optical properties of marine stratocumulus clouds, and increasing understanding of the modification of the cloud optical properties by aerosols (Boers *et al.*, 1996). The former aim was achieved by locating the SOCEX off the northwestern coast of Tasmania in southerly airstreams of Southern Ocean origin. The latter aim was achieved by conducting the experiment in summer and winter periods because seasonal differences in the aerosol properties were expected. Some studies of marine aerosols that led to the concept and planning of SOCEX are discussed below.

In marine environments aerosols are produced by the emission of gases and droplets from the sea surface. Biggs (1980), Gras and Ayers (1983) and Gras (1991) measured aerosols in marine air and found sea salt particles with radii typically between 0.1 μm and 1 μm , and smaller but more

numerous ammonium sulfate particles with radii typically between 0.01 μm and 0.1 μm . Dimethylsulfide (DMS) gas is produced by phytoplankton and is a precursor to the non-sea-salt sulphate aerosols. Charlson *et al.* (1987) suggested this DMS pathway may be the primary source of marine CCN, and, following several years of measurements of CCN at Cape Grim, Ayers and Gras (1991) provided strong evidence supporting this hypothesis. Charlson *et al.* (1987) noted that the DMS emissions were greatest from the warmest, most saline, and most intensely illuminated regions of the oceans. It follows that in an oceanic region the DMS concentrations may peak in the summer. At the Cape Grim Baseline Air Pollution Station (CGBAPS), situated on the northwestern coast of Tasmania, this has been found to be so with seasonal variations in the concentrations of the marine CCN (Ayers and Gras; 1991) and DMS (Ayers *et al.*; 1995) peaking in the summer months.

Now, Boers *et al.* (1994) found that variations in the CCN concentrations correlated reasonably well with cloud optical depths derived from satellite measurements of clouds near Cape Grim. Therefore, it may be expected that the limits of the variations in optical properties of these maritime clouds could be observed during the seasonal maxima and minima of the CCN concentrations. To coincide with these maxima and minima in the CCN concentrations SOCEX held an observational winter phase, from 5 July 1993 to 25 July 1993 (SOCEX1), and a summer phase from 15 January 1995 to 9 February 1995 (SOCEX2); {Boers *et al.* (1996); Boers *et al.* (1998)}. These authors did indeed find a variation in aerosol numbers, cloud optical depth and albedo, between winter and summer seasons, with a maximum in summer as predicted.

At CGBAPS during SOCEX, ground-based Lidar and Infrared RADIometer (LIRAD) measurements of stratocumulus clouds were made as an adjunct to the airborne experiment, and the study of these LIRAD measurements was the major work undertaken for this thesis. The LIRAD method will be discussed further in the following sections. It is emphasised that the airborne *in situ* measurements of the aerosols and cloud droplets were made independently of the LIRAD measurements and were not required by the LIRAD method. Primarily, the *in situ* aircraft measurements were used to improve the calibration of the lidar, and make comparisons of the *in situ* measurements of the cloud droplets with the LIRAD measurements; comparisons that yielded information on the multiple scattering in clouds, as will be seen later.

1.3 Lidar Studies of Boundary Layer Clouds

Lidars have been used extensively in studies of the optical properties of high clouds, from the early studies of lidar returns from cirrus clouds made by Davis (1969) and Platt (1973), through to the more recent and complex studies in which lidar measurements are combined with results from satellites and radiometers (see, for example, Minnis *et al.*, 1990). The first and most obvious disadvantage in using lidars to study water droplet clouds is that most low clouds rapidly attenuate laser beams due to strong scattering. Penetration of the laser pulses is limited to only a few hundred metres. However as shown by the results of this thesis a significant proportion of low clouds are optically thin, (this is supported by the finding of Pal *et al.*, 1995), so lidar studies of low clouds are worthwhile.

Before the 1980s there were few lidar studies for the retrieval of the optical properties of low clouds. One of the exceptions to this was the study of the depolarisation in lidar returns by Pal and Carswell (1973). The depolarisation in lidar (backscattered) returns from clouds containing only water droplets is due to multiple scattering, unless the droplets are deformed from a spherical shape. Depolarisation in lidar returns from high clouds is induced mainly by scattering in non-spherical ice crystals. From the earlier studies of multiple scattering in lidar returns (Eloranta, 1972; Kunkel and Weinman, 1976; Platt, 1981), to the more recent studies (Bissonnette *et al.*, 1995; Nicolas *et al.*, 1997), multiple scattering has remained a significant problem in the analysis of lidar returns from both low and high clouds. This problem of strong attenuation by low water droplet clouds causes difficulties in retrieving lidar backscatter and extinction coefficients from low clouds. For these reasons reports in the literature of lidar studies of low clouds for the retrieval of extinction and optical depth were rare, although Klett's (1981) lucid study of the stable solution for lidar returns from highly attenuating clouds was of considerable assistance.

Klett (1981) showed that height profiles of the effective (because they still contained multiple scattering effects) visible extinction of optically thick clouds could be retrieved from lidar signal profiles. This study spawned a number of similar studies to retrieve the visible extinction from lidar measurements of low stratiform clouds (Lindberg *et al.*, 1984; Carnuth and Reiter, 1986; Kolev *et al.*, 1989), as well as many studies investigating the behaviour and uncertainties of the analytic solutions (see, for example, Sasano and Nakane, 1984; Bissonnette, 1986; Qiu Jinhuan, 1988; Kovalev, 1995). Meanwhile, in the 1980s and onwards other lidar observations of liquid water clouds continued.

Sassen and Petrilla (1986) made further measurements of the depolarisation in lidar returns from water clouds, (see the review of depolarisation lidar by Sassen, 1991). Spinhirne *et al.* (1989) made airborne lidar observations of the tops of marine stratocumulus. Young (1995) determined the transmittance of a thin stratocumulus cloud by comparing the signals returned from above and below a cloud. None of the above studies considered, or were able to measure, the effects of multiple scattering. The present study is the first to obtain a measurement of multiple scattering in boundary layer clouds.

From these lidar studies of low clouds, and of high clouds (see, for example, Platt *et al.*, 1998), including those which employ technologies other than the detection of elastic-backscattering from clouds, (see, for example, Grund and Eloranta, 1990; Ansmann *et al.*, 1992), it is clear that lidar has become an indispensable tool for studies of clouds. Measures (1984) provides a broad overview of the capabilities of lidar in atmospheric research. To obtain results from lidars in quantities useful for climatological studies of atmospheric radiation many results are required, and the Experimental Cloud Lidar Pilot Study (ECLIPS) program attempted to show if this was feasible (Platt *et al.*, 1994). The ECLIPS programs used lidar techniques to gather information on the vertical and temporal extent of cloud extinction, optical depth and lidar depolarisation ratio. The ECLIPS program raised the importance of very thin ('subvisual') clouds in their interactions with the radiative fluxes in the atmosphere (Pal *et al.*, 1995). However from reports such as those of Platt *et al.* (1994) and Pal *et al.* (1995) it seems that much work remains to be done before the ECLIPS program, or others like it, will lead to the retrieval of cloud optical properties from long-term or large-scale observations. Studies of lidar returns from clouds have been limited to a few case studies and the reasons for this are discussed below.

There are two major factors that complicate the analysis of lidar returns. The lidar measured backscatter is not solely proportional to the backscattering properties of the atmospheric particles. Attenuation and multiple scattering need also to be considered. Theoretically, without further measurements of the scattering properties of the particles under investigation, the effect of attenuation cannot be separated from the backscatter, and the multiple scattering of visible light in clouds cannot be easily separated from the single scattering properties. However it is these single scattering properties, especially those of aerosols and clouds, that lead to the calculation of optical properties

such as optical depth, single scattering albedo, and asymmetry parameter; properties important for determining the transfer of radiation through clouds on a global scale.

The majority of the effort in the analysis of lidar measurements of clouds for the retrieval of their optical properties is therefore geared towards:

- (1) Calculations of extinction near the cloud boundaries of optically deep clouds (see, for example, Klett, 1981; Pal *et al.*, 1995),
- (2) Determining the effects of attenuation in the profiles by assuming homogeneous microphysical properties for each lidar measurement and combining the results with independent measurements, (Fernald *et al.*, 1972; Platt, 1979; Platt *et al.*, 1980; Minnis *et al.*, 1990; Platt *et al.*, 1998), and
- (3) Estimates of the effects of multiple scattering on the lidar profiles using either measurements (Bissonnette and Hutt, 1990; Sassen *et al.*, 1992) or using theoretical and modelled predictions (Kunkel and Weinman, 1976; Platt, 1981; Zege *et al.*, 1995; Nicolas *et al.*, 1997).

Several thousands of lidar returns were studied in the course of this thesis. The LIRAD algorithm, an iterative technique described by Platt (1979), was used to invert the lidar signal profiles for backscatter. By using the LIRAD algorithm, some of the instability problems associated with forward analytical techniques were avoided. A disadvantage of the LIRAD algorithm used here was that calibrated lidar signal profiles were required as inputs.

1.4 Infrared (10-12 μm) Radiometry of Clouds and the LIRAD Method

There is strong thermal absorption and emission by H_2O and CO_2 over much of the region of the infrared spectrum. Emission from clouds can only be detected at the ground by infrared radiometers in the relatively clear 8 - 14 μm window (Allen, 1970; Platt, 1971; Platt *et al.*, 1993). In this region of the spectrum the primary absorption (and emission) from a cloud-free atmosphere is due to water vapour, with some absorption by the far edge of an O_3 band, a weak CO_2 band and aerosols (Platt *et al.*, 1984).

Infrared radiometers have been used for measurements of the downwelling thermal radiances by clouds (Allen, 1970; Platt, 1971), as well as alongside lidars in the Lidar and Infrared RADiometer (LIRAD) method for the measurement of clouds (Platt, 1979). These infrared measurements of high clouds are sometimes difficult to distinguish from those of clear air (Platt *et al.*, 1998), particularly in

tropical atmospheres. However, the infrared signal from low water droplet clouds is much stronger than the clear air emission (Platt and Gambling, 1971a; Platt, 1972). Infrared radiometers have been used for aircraft *in situ* studies of stratocumulus clouds in attempts to determine the relationship between their radiative properties and the liquid water they contain, and to determine at what depths into these clouds they become radiatively black (Platt, 1972; Paltridge, 1974; Platt, 1976; Stephens *et al.*, 1978; Slingo *et al.*, 1982).

Although the single scattering albedo of clouds in the (10 - 12 μm) wavelength region of the spectrum is near to 0.5, the majority of the measured infrared radiances from clouds can be determined by considering absorption only. This is due to the strong forward scattering of the infrared radiation in clouds (Paltridge and Platt, 1976). There is a small additional amount in the measured radiances which can be explained by scattering effects. Theoretical studies are normally used to determine this additional radiance in order to retrieve cloud radiances due to absorption only (Platt and Stephens, 1980), from which the optical and microphysical properties of the clouds are more readily determined. The infrared reflectance of thick clouds is approximately 5%, (see, for example, Yamamoto *et al.*, 1970; O'Brien *et al.*, 1997), and so the maximum beam emittances of water droplet clouds is approximately 0.95.

Early simultaneous lidar and infrared radiometer measurements near the edges of cumulus clouds were made by Platt and Gambling (1971a), and of cirrus and altocumulus clouds by Platt and Gambling (1971b). The LIRAD analysis technique was developed after Platt (1973) found a good correlation between the lidar-measured integrated backscatter and the infrared absorption optical depth. The LIRAD method combines infrared (10 - 12 μm) radiometer and lidar measurements of clouds to determine cloud microphysical and optical properties (Platt, 1973; Platt, 1979). Until the LIRAD study for this thesis, the LIRAD method has only been applied to high and mid-level clouds (Platt and Dilley, 1979; Platt and Dilley, 1981; Platt *et al.*, 1984; Platt *et al.*, 1986; Platt *et al.*, 1997).

The reasons for the application of the LIRAD method to the study of low clouds are summarised here. The importance of clouds in determining state of the earth's climate was discussed in 1.1. This included references to studies that highlighted the sensitivity of climate to the properties of low clouds. Further, the modification of low cloud optical properties by anthropogenic aerosols was discussed in 1.2. The few lidar reports of measurements of low clouds and the reasons for this

were given in 1.3. The application of the LIRAD technique for studying the properties of clouds was discussed in this section (1.4). These discussions lead to the reasons for applying the LIRAD method to the present study of low clouds as: 1) To investigate the visible and infrared properties (and the implied climatic impacts) of marine stratocumulus clouds using a new application of a tried technique. 2) To overcome some of the deficiencies in applying lidar alone to low clouds.

1.5 Outline of the Thesis

The aims of this thesis were to determine:

- The distribution of heights of boundary layer clouds in two seasons.
- The utility of the LIRAD method in its application to boundary layer clouds.
- The blackness or optical depths of the boundary layer clouds.
- The effects of multiple scattering on the lidar returns from these clouds.
- The utility of combining microwave radiometer measurements with lidar and infrared radiometer measurements for retrieving cloud liquid water and for extending optical depth retrievals to higher values.

Several major achievements arose from this multifarious study of boundary layer clouds. The unique set of atmospheric measurements by remote sensing and *in situ* techniques, using measurements of radiation spread over a broad range of the electromagnetic spectrum, provided good results linking the optical, infrared absorptive and liquid water properties of the clouds.

The first and primary achievement of this study was that the LIRAD method was successfully applied to low clouds for the first time, revealing that many of the measured stratocumulus clouds had low infrared emittances (*i.e.*, were optically thin). As well as the success of the new application of the LIRAD technique, the low emittance of stratocumulus was an unusual and interesting finding as often in theoretical studies of radiation in the atmosphere, low water droplet clouds are assumed to be radiatively black.

The second major achievement was that the lidar was accurately calibrated by a careful consideration of the properties of moist boundary layer aerosols. As well as providing valuable information on the optical properties of atmospheric aerosols, this calibration improved the quality of the analysis of the cloud data by the LIRAD method.

The third major achievement of the thesis was that comparisons of *in situ* measurements of the clouds with the measurements by the lidar and infrared radiometer allowed a retrieval of the lidar multiple scattering factor (η). The determination of η is a traditional problem of lidar, and the retrieval of η made here represents a rare if not unique result.

Perhaps the last of the noteworthy achievements of this work was that the lidar measurements of the heights of the boundary layer clouds, revealed a seasonal difference in the heights that was not inconsistent with those expected from meteorological variables. Further measurements are required to determine whether lidar can be used, not only to detect seasonal differences in the heights of boundary layer clouds, but also to detect seasonal differences in their optical properties.

The structure of the thesis is outlined as follows. Chapter 2 reviews the analysis techniques for studying lidar returns from clouds, and includes a discussion on the analysis of LIRAD measurements. The original work for this thesis begins in Chapter 3, in which the LIRAD measurements of the stratocumulus clouds observed during both phases of SOCEX are described. The analysis methods used for the two case studies of 16 July 1993 (SOCEX1) and 8 February 1995 (SOCEX2) are described in detail in Chapter 4. On these two days, the *in situ* measurements of some cloud microphysical properties obtained from an instrumented Fokker F-27 aircraft were investigated in detail (Boers *et al.*, 1996; Boers *et al.*, 1998). Krummel (1998) also used the same *in situ* data for a study of the dynamical structure of the clouds (Krummel, 1998).

The results of the study of the combined lidar and infrared radiometer measurements are presented in Chapter 5. Cloud heights measured by lidar over both parts of SOCEX are presented in section 5.2. The LIRAD results, some *in situ* results and microwave radiometer results for the winter case study (SOCEX1) are presented in section 5.3, and LIRAD and microwave radiometer results for the summer case study (SOCEX2) in section 5.4. Cloud optical depths obtained from microwave radiometer measurements of the clouds are also given in sections 5.3 and 5.4. The conclusions are presented in Chapter 6.

2. Cloud Optical Properties by Lidar and the LIRAD Method

2.1 Introduction

The theory of analysis of lidar returns from the atmosphere for the retrieval of optical properties is now a large field of research. The theory is well developed, but the application of the theory to experimental data is complicated, especially for lidar returns from clouds. For lidar measurements of clouds the signal-to-noise ratio is adequate and does not pose a problem for analysis, but, because of large optical depths, very large uncertainties can easily occur in retrievals of the optical properties of clouds, for example, via solutions to the lidar equation. In describing the theory of lidar relevant to this thesis, this chapter is also a review of the literature on the subject of the analysis of lidar returns, with an emphasis on the application of the analysis methods to real measurements.

2.2 Analysis of Lidar Returns

2.2.1 *The Lidar Equation*

2.2.1.1 Returned Optical Power

The laser transmitter and telescope receiver in a lidar are most commonly positioned either with the same axis (monostatic), or the laser and telescope are placed side-by-side with optical axes apart (biaxial). A ground-based lidar so arranged and pointing vertically transmits a visible laser pulse into the atmosphere and photons from the pulse are elastically scattered into all directions by air molecules, aerosols, and sometimes cloud droplets and ice crystals. Some of this scattered light arrives back at the receiving telescope of the lidar. The intensity and time-of-flight of this backscattered light from a single pulse is measured and recorded as a profile of the returned signal versus range. The instantaneous optical power received at the aperture of the lidar telescope is

$$\phi(z) = \phi_o \frac{c\Delta t}{2} \frac{A(z)}{z^2} \beta(z) T^2(0, z); \quad (2.1a)$$

(e.g. Collis and Russell, 1976; Measures, 1984). The constant ϕ_o is the average power of the transmitted laser pulse, $A(z)$ is the effective area of the telescope objective lens or mirror, c is the

speed of light and Δt the pulse duration. Thus, $c\Delta t$ is the pulse length. The inverse range-squared term (z^{-2}) is due to the spherical geometry of scattering. β is the volume backscatter coefficient ($\text{m}^{-1}\text{sr}^{-1}$), and $T^2(0,z)$ is the two-way transmittance along the path from the lidar to the atmospheric target at height z . The range resolution of the lidar is determined by either half the laser pulse length or the digitiser sample interval, whichever is larger.

The transmittance $T(0,z)$ is a function of the optical depth (τ):

$$T(0, z) = \exp(-\tau(0, z)), \quad (2.1b)$$

and τ is a function of the volume extinction coefficient (σ):

$$\tau(0, z) = \int_0^z \sigma(z') dz'. \quad (2.1c)$$

In practice, ϕ_0 and Δt are not measured but rather the energy of the transmitted pulse (E), so that a more practical lidar equation is,

$$\phi(z) = E \frac{c}{2} \frac{A(z)}{z^2} \beta(z) T^2(0, z). \quad (2.1d)$$

An example of a returned lidar signal is shown in Figure (2.1). The lidar was positioned at an elevation of 90 m ASL. Just below the height of 200 m ASL the first backscatter by aerosols and air molecules is detected (*i.e.* the 'near field' return). The peak in the signal near 300 m results from the product of the atmospheric backscatter signal, and the overlap function, which increases from zero at about 180 m, reaching unity at about 350 m. The profile contains a stratocumulus cloud signal, with cloud base and apparent cloud top at approximately 1000 m ASL and 1180 m ASL respectively.

Lidar Return from a Stratocumulus Cloud

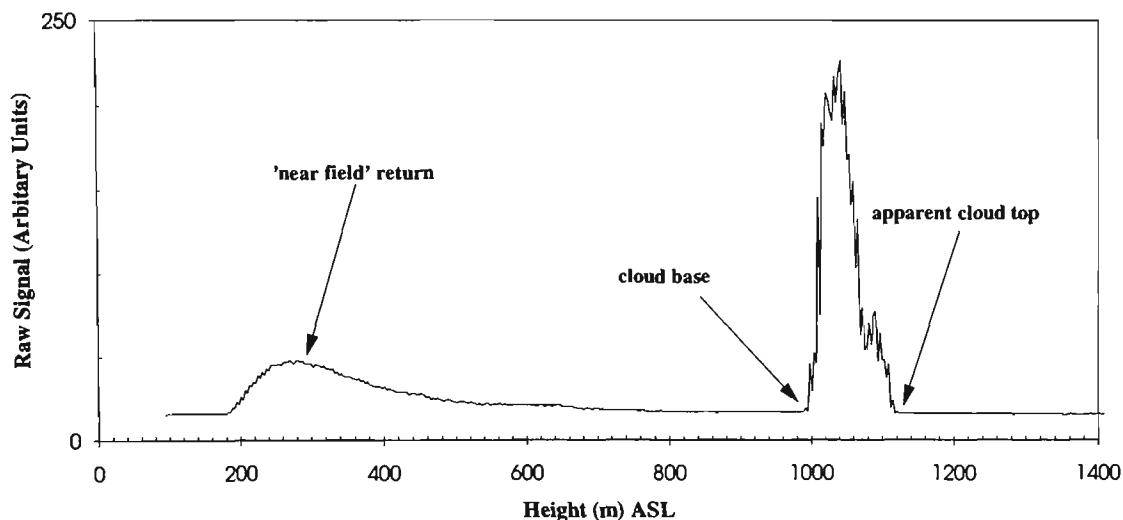


Figure 2.1 Example of a lidar return from a stratocumulus cloud in a marine atmosphere. The level of the signal at each point along the profile is proportional to the optical power returned from the heights shown. Backscattering by air molecules and aerosols close to the lidar is easily discernible between the heights of 200 m and 400 m. The greater backscatter by water droplets in a stratocumulus cloud appears in the profile near the height of 1000 m.

2.2.1.2 Measured Signal

The lidar signal voltage $V(z)$ is proportional to the received power $\phi(z)$. Where a lidar is equipped with a photomultiplier tube the measured signal at the anode is (e.g. Young, 1980);

$$V(z) = R_L \eta_o Q_A \phi(z) + V_o, \quad (2.2)$$

where R_L is the anode resistance (Ω), η_o is the optical efficiency of the receiver, Q_A is the conversion factor of the photomultiplier tube (A/W), and V_o is an offset voltage. Young (1980) defined the system constant as

$$C' = R_L \eta_o Q_A. \quad (2.3)$$

It is useful to form another system constant by incorporating the remaining instrument parameters from equation (2.1d);

$$C = C'E \frac{c}{2} A_o . \quad (2.4)$$

This form of the system constant is appropriate for ranges beyond the overlap range of the lidar, and A_o is the effective area of the telescope for far ranges where the laser pulse is fully inside the telescope field of view. The instrumentation parameters of a specific lidar may be combined to give

$$V(z) = Cz^{-2} \beta(z) T^2(0, z) + V_o . \quad (2.5)$$

2.2.1.3 Multiple Scattering in Lidar Returns from Clouds

So far the expression for transmittance in the lidar equation has been described by Lambert's Law (or Bouguet's Law) of extinction, and does not account for photons scattered again once they have been scattered out of the incident beam. However, in a laser beam propagating through the atmosphere, some of the scattered photons may be scattered again and reappear in both the incident and backward directions, causing an increase in the returned signal over that caused by single scattering (*e.g.* Platt, 1973). Lidar observations of the depolarised returned signal (*e.g.* Pal and Carswell, 1976; Sassen *et al.*, 1992), and lidar observations in which the field of view of the receiving telescope is adjustable (*e.g.* Allen and Platt, 1977; Bissonnette and Hutt, 1990), indicate that the light backscattered from clouds contains a significant portion which has been multiply-scattered. Thus any lidar retrieval of the optical depths of clouds, for example, will be affected significantly by multiple scattering.

Plass and Kattawar (1971) and Kunkel and Weinman (1976) calculated multiple-scattered components in lidar returns from water clouds by the Monte Carlo technique. Platt (1981) improved the efficiency of these computations and introduced a multiple scatter factor correction (η) to the optical depth in the lidar equation, so that the transmittance term of the lidar equation becomes,

$$T(0, z) = \exp(-\eta(z)\tau(0, z)) . \quad (2.6a)$$

However, to make the retrieval tractable Platt (1973) assumed η was constant throughout the depth of the cloud:

$$T(0, z) = \exp(-\eta\tau(0, z)) . \quad (2.6b)$$

This approach is the one most often used in the reduction of large volumes of experimental data (*e.g.* Platt *et al.*, 1998). In this LIRAD study and others, η was determined from Monte Carlo modelling studies of multiple scattering (*e.g.* Platt, 1981). Apart from Monte Carlo studies, there have been analytic approaches to the problem of multiple scattering in lidar returns (*e.g.* Eloranta and Shipley, 1982; Zege *et al.*, 1995; Katsev *et al.*, 1997), and our knowledge of the multiple scattering in lidar returns is advancing rapidly (*e.g.* Bissonnette *et al.*, 1995; Nicholas *et al.*, 1997).

In some Monte Carlo studies of multiple scattering in lidar returns from clouds, Platt (1981) found that η increases with optical depth. Using these results in a later study of cirrus clouds, Platt *et al.* (1987) parameterised η as a simple function of optical depth and found that the constant value of η deduced in the normal way was too high. However the treatment of a variable η in that study did not improve results for the retrieved microphysical and optical properties, because other uncertainties in the experimental results were larger. A significant problem in determining the amount of multiple scattering in experimental lidar returns is lack of accurate knowledge of the species and size distributions of the scatterers along the laser beam (*e.g.* Nicolas *et al.*, 1997). If the properties of the scatterers were known precisely their effects on the retrieved optical depth could be calculated.

The method of using constant η is an efficient way of retrieving the optical properties of clouds from large datasets, and it is possible that previous results using this method could be improved by later improved knowledge of multiple scattering.

Monte Carlo studies of multiple scattering of laser beams in water droplet clouds indicate that η is relatively constant with depth into these clouds. For example, the Monte Carlo study of the multiple scattering in Deirmendjian's (1969) type *C1* cloud by Platt (1981) showed η increases from about 0.5 near cloud base to a maximum of about 0.7 for an optical depth of 1. This finding agreed with the results of the study of multiple scattering in lidar returns by Kunkel and Weinman (1976). Thus the assumption of constant η for water droplet clouds does not seem unreasonable.

2.2.1.4 Range-Corrected and System-Independent Lidar Equation (χ)

The lidar equations presented in this section are specific to the problem of lidar calibration for this thesis described later in (section 4.3.3). The methods for inversion of these lidar equations follows in section 2.2.2, and the lidar equation also provides the starting point for the LIRAD analysis method

(section 2.3). In order to simplify the presentation of these analysis methods, the new variable (χ) is introduced: *i.e.*, the system-independent attenuated backscatter, assigned the symbol χ and defined as,

$$\chi(z) \equiv \frac{(V(z) - V_o)z^2}{C}. \quad (2.7)$$

Obviously equation (2.7) could be written in terms of the received optical power instead of the signal voltage; in that case the system constant (C) would simply take on a different value and units. Note that χ contains the lidar system constant as opposed to the range-corrected received optical power variable (X) (*e.g.* Fernald, 1984), or the range-corrected signal voltage (*e.g.* Young, 1995). The equation (2.7) leads to the range-corrected and system-independent lidar equation;

$$\chi(z) = \beta(z)T^2(0, z). \quad (2.8)$$

The following example describes lidar observations of the stratocumulus cloud-capped boundary layer during SOCEX (*e.g.* Young, 1995; Pickett *et al.*, 1996). The lidar profiles from these observations show that the aerosol and cloud signals can be divided into separate height regions. The boundary layer aerosols exist from the surface up to cloud base. A thinner layer of cloud droplets caps the boundary layer aerosols. A second class of aerosols lies above the cloud tops, in the free troposphere. The backscatter and transmittance terms in equation (2.8) may be expanded to account for these three separate species of scattering particles so that the part of the lidar profile below the cloud layer is described by

$$\chi(z) = (\beta_m(z) + \beta_{a_1}(z))T_m^2(0, z)T_{a_1}^2(0, z), \quad (2.9)$$

where the subscripts 'm' and 'a₁' stand for molecules and boundary layer aerosols respectively. The part of the profile inside the cloud is described by

$$\chi(z) = (\beta_m(z) + \beta_c(z))T_m^2(0, z)T_{a_1}^2(0, z_b)T_c^2(z_b, z), \quad (2.10)$$

where the subscript 'c' stands for cloud particles. The aerosol transmittance term is stopped at cloud base (z_b): to simplify the analysis all the particles inside the cloud are arbitrarily assumed to be either

water droplets or ice crystals. If the cloud fully attenuates the lidar pulse, the signal will disappear into the background noise before cloud top, a height termed the ‘apparent cloud top’. The cloud may be optically thin so that some backscatter by air and aerosols above the cloud layer is detected by the lidar. Then, above cloud top the profile is described by

$$\chi(z) = (\beta_m(z) + \beta_{a_2}(z)) T_m^{-2}(0, z) T_{a_1}^{-2}(0, z_b) T_c^{-2}(z_b, z_t) T_{a_2}^{-2}(z_t, z), \quad (2.11)$$

where the subscript ‘a₂’ stands for the second class of aerosols that exist above the clouds, and z_t is cloud top.

2.2.2 Lidar Equation Solutions for Extinction and Backscatter

2.2.2.1 Introduction

The lidar equation contains two unknowns, the volume backscatter (β), and extinction (σ), coefficients. To solve the lidar equation for either of these parameters, a common step is to assume a functional dependence of β on σ . Most often the extinction-to-backscatter ratio (S) is assumed to be constant with range (*e.g.* Hitschfeld and Bordan, 1954; Elterman, 1966; Barrett and Ben-Dov, 1967). {The symbol S chosen here follows the choice of Fernald *et al.* (1972) and Fernald (1984)}.

The value of S depends on the phase function of the ensemble of particles under investigation, and the reciprocal of S is equal to the phase function of the scatterers at 180° divided by 4π , ($P_\pi/4\pi$), {see Deirmendjian (1969), pp. 72-75}. The assumption of constant S throughout a single lidar return from a cloud means that the composition and size distribution of the scatterers is assumed constant throughout. That is, the variations in the signal amplitudes of range-corrected lidar profiles that are not due to attenuation or multiple scattering are assumed due to changes in particle concentrations only.

Given S the lidar equation may be solved by an iterative technique (*e.g.* Elterman, 1966; Gambling and Bartusek, 1972 a,b; Platt, 1973; Platt, 1979). Given constant S the lidar equation may be solved analytically (*e.g.* Barrett and Ben-Dov, 1967; Viezee *et al.*, 1969; Davis, 1969). These early presentations of the analytic solution to the lidar equation were based on the radar study by Hitschfeld and Bordan (1954).

The lidar and solar radiometer study of aerosols by Fernald *et al.* (1972) used a simplified form of the solution of Barrett and Ben-Dov (1967), and presented the analytic solution for a two component atmosphere (air molecules and aerosols). Barrett and Ben-Dov (1967) and Fernald *et al.* (1972) used a variable proportional to χ in their lidar equation (see previous section, 2.2.1.4). There is an advantage of using χ or a variable proportional to it, rather than a variable proportional to the logarithm of χ as many authors have done (*e.g.* Vezee *et al.*, 1969; Klett, 1981). The advantage is that where small signal-to-noise ratios cause the profiles to sometimes be negative, profiles of χ may still be analysed, whereas profiles described by a variable proportional to the logarithm of χ cannot (Young, 1995).

The thorough and clearly presented work of Klett (1981) demonstrated the stability of the so-called 'backward' or 'inward' solutions to the lidar equation, and it spawned a large number of error analyses of the various solutions (*e.g.* Sasano and Nakane, 1984; Bissonette, 1986; Qiu Jinhuan 1988; Kovalev, 1995). General conclusions that may be drawn from these error analyses and others is that the accuracy of the solutions for β rely on accurate estimates of S and the solution boundary values, which can be normally only supplied by independent measurements. The accuracy of the stable solutions for σ depends on the atmosphere being optically thick, (*e.g.* cumulus clouds), and suitable estimates of the boundary values for each profile. Clearly, considerable analysis effort is required for these solutions.

The assumption of constant S along a single lidar profile has been used for the retrieval of the optical properties of aerosols and cloud particles for some time, because of the obvious difficulty in obtaining independent and simultaneous measurements of S along the profile. However for this thesis, variations in S with height in the stratocumulus clouds were studied using *in situ* measurements. To some extent lidar measurements of height profiles of S for clouds have recently become practical. The combined Raman and elastic-backscatter lidar study by Ansmann *et al.* (1992) shows variations in S with height for cloud particles as well as aerosols. Thus the validity of the assumption of constant S with height should be tested for elastic-backscatter lidar measurements of aerosols and clouds, and particularly for ice clouds. This is because S changes significantly with ice crystal shape, as shown by the many LIRAD observations of cirrus clouds (*e.g.* Platt *et al.*, 1998).

There are some cases where the assumption of constant S is not required; the so-called 'slope technique' (e.g. Vizee *et al.*, 1969), and the stable forms of the analytic solutions for extinction (Klett, 1981). However the application of these solutions is limited because to be accurate they depend on certain atmospheric conditions; see Fernald (1984), for example. The various methods for solving the lidar equation are described in the following sections.

2.2.2.2 The Iterative Technique

The iterative technique was used by Elterman (1966) for the analysis of searchlight measurements of the atmosphere, and applied to analysis of lidar returns by Gambling and Bartusek (1972a,b), and Platt (1973). The iterative technique is presented here following the method of Platt (1973) and Platt (1979) for some details. A profile of χ is divided into a number of small layers of thickness Δz metres, and initially the backscatter profile is described by,

$$\beta_n = \frac{\chi_n}{\exp(-2\eta S \sum_{i=1}^{i=n} \beta_n \Delta z)}. \quad (2.12)$$

Now, it is required to calculate a profile of β given a value for ηS . The multiple scatter factor (η) (see Platt, 1981) is included here because practically it is the product ηS that must be estimated, not the single scattering quantity S . The method for forward calculation proceeds as follows. Starting at cloud base, initially the extinction of the first small layer is assumed to be equal to $S\beta_1/2$ so that β can then be calculated for that layer:

$$\beta_1^{(1)} = \frac{\chi_1}{\exp(-2\eta S(\chi_1 / 2)\Delta z)}. \quad (2.13)$$

The subscript '1' stands for the first layer in the profile and the superscript '1' stands for the first calculation in the iteration. After this first step the calculation of β underestimates the true value, but it provides a means of calculating the first estimate of the transmittance of the layer. This transmittance is used to calculate the second estimate of β for the layer;

$$\beta_1^{(2)} = \frac{\chi_1}{\exp(-2\eta S(\beta_1^{(1)} / 2)\Delta z)}, \quad (2.14)$$

and so on, until the calculated β converges. Convergence at each layer is determined by monitoring the successively calculated values of β , and this will occur if the estimate of ηS is accurate to within a specified amount, and depends on the optical depth, as shown by Platt (1979).

For each layer the backscatter coefficient is calculated, taking into account the previously calculated transmittances, until a profile of the backscatter coefficient over the entire cloud is achieved. The solution can be organised to run in the forward direction as shown here or the backward direction (*e.g.* Gambling and Bartusek 1972 a,b), which is more stable for cases of high optical thicknesses, although a far-field value of β or σ is required.

2.2.2.3 The Slope Technique

The slope technique (*e.g.* Viezee *et al.*, 1969) requires no estimate of the extinction-to-backscatter ratio S :

$$\sigma = -\frac{1}{2\eta} \frac{d\zeta(z)}{dz}, \quad (\text{A3.8})$$

where,

$$\zeta(z) \equiv \ln(\chi(z)). \quad (\text{A3.5})$$

The derivation of this equation is presented in Appendix A3. Provided the cloud backscatter coefficient is constant with range, and η can be estimated with reasonable certainty, the extinction of a homogeneous atmosphere may be calculated from the slope of the curve of ζ against range - hence the term 'slope technique'. Caution is required when using this technique because small heterogeneities in a lidar profile can introduce large errors in extinction calculated by this method (*e.g.* Klett, 1981).

2.2.2.4 The Analytic Solution (Logarithmic Variable)

As mentioned in the introduction (2.2.2.1) there are two unknowns in the lidar equation, the volume backscatter (β) and extinction (σ) coefficients. In order to invert the equation a linear or power law relationship must be assumed between the two coefficients (*e.g.* Barrett and Ben-Dov, 1967; Davis, 1969; Viezee *et al.*, 1969). The solution for extinction is,

$$\sigma(z) = \frac{\exp((\zeta(z) - \zeta_o)/g)}{\sigma_o^{-1} - \frac{2\eta}{g} \int_{z_n}^z \exp((\zeta(z') - \zeta_o)/g) dz'} \quad (\text{A3.11})$$

The derivations for this solution (A3.11) and the equation to follow (A3.12) are presented in Appendix A3. The boundary value of extinction (σ_o) for (A3.11) is situated at the calibration range z_n in the cloud, and the subscript 'n' stands for 'near' to the lidar. This equation is known as the forward or outward solution of the lidar equation, and its instability for larger optical depths is due to its mathematical structure (*e.g.* Hitschfeld and Bordan, 1954; Klett, 1981). The instability arises as follows. For optically thick atmospheres the denominator becomes the difference between two similarly-sized numbers, thus the solution can be highly inaccurate. For example if the error in the boundary value (σ_o^{-1}) is positive the solution may become negative. The more stable backward or inward solution often referred to in the literature as the 'Klett solution' is formed by reversing the direction of integration,

$$\sigma(z) = \frac{\exp((\zeta(z) - \zeta_d)/g)}{\sigma_d^{-1} + \frac{2\eta}{g} \int_z^{z_d} \exp((\zeta(z') - \zeta_d)/g) dz'} \quad (\text{A3.12})$$

Here z_d refers to a more distant calibration range. The stability of this solution arises out of the addition of two (positive) numbers in the denominator, as opposed to the subtraction in the denominator of equation (A3.11). The solution (A3.12) converges well in optically thick atmospheres even with reasonably large errors in the boundary value σ_d . However although the forward solution is unstable it can be just as accurate as the backward solution over a given range if the boundary parameters are precise and the solution properly constrained. Since the work of Klett (1981) many authors have investigated the behaviour and accuracy of these solutions (*e.g.* Sasano and Nakane, 1984; Bissonette, 1986; Qiu Jinhuan 1988; Kovalev, 1995).

2.2.2.5 The Analytic Solution (Linear Variable)

The solution to the lidar equation derived by Barrett and Ben-Dov (1967) used a linear variable proportional to χ and this solution was simplified and extended to account for a two component atmosphere by Fernald *et al.* (1972). It is common for regions of lidar profiles with low signal-to-

noise ratios to lead to negative values of χ , and as mentioned by Young (1995) this leads to analysis problems if the logarithmic variable is used. So the form of the analytic solution that uses the linear variable (*e.g.* Fernald *et al.*, 1972; Fernald, 1984) is preferable to the form that uses the logarithmic variable (*e.g.* Klett, 1981).

The derivations of the linear variable (χ) solutions are given in Appendix A3 and some of those results are reproduced here for convenience. First, the forward solution for a single-component atmosphere is,

$$\beta(z) = \frac{\chi(z)}{\frac{\chi(z_n)}{\beta(z_n)} - 2S \int_{z_n}^z \chi(z') dz'}, \quad (\text{A3.22})$$

where z_n stands for the near-point calibration range z_n . The solution for extinction is,

$$\sigma(z) = \frac{\chi(z)}{\frac{\chi(z_n)}{\sigma(z_n)} - 2 \int_{z_n}^z \chi(z') dz'}. \quad (\text{A3.23})$$

Note the absence of the extinction-to-backscatter ratio in the integral term of (A3.23), about which more will be said later. The backward solution for the backscatter coefficient is obtained by integrating from a more distant calibration height z_d down to a height z ,

$$\beta(z) = \frac{\chi(z)}{\frac{\chi(z_d)}{\beta(z_d)} + 2S \int_z^{z_d} \chi(z') dz'}, \quad (\text{A3.24})$$

and the corresponding backward solution for the extinction coefficient is,

$$\sigma(z) = \frac{\chi(z)}{\frac{\chi(z_d)}{\sigma(z_d)} + 2 \int_z^{z_d} \chi(z') dz'}. \quad (\text{A3.25})$$

The behaviour of the solutions is governed largely by errors in the terms of the denominators, and the discussion on the stability of the analytic solutions in section 2.2.2.4 also applies to these equations.

Fernald (1984) presented a summary of the solutions to the lidar equation for two classes of scatterers {see equations (A3.40) to (A3.44) in Appendix A3 of this thesis}. The applicability of these solutions depends on the laser wavelength, optical depth of the atmosphere, multiple scattering, and errors introduced by digitisation and sampling of profiles of χ (Fernald, 1984).

In optically thin atmospheres the visible optical properties of molecules and aerosols are often about the same order of magnitude. For example in the clean marine boundary layer at the wavelength 532 nm β_a and β_m are both about $10^{-6} \text{ m}^{-1}\text{sr}^{-1}$. In this case there is an advantage in using the solutions for β_a , *i.e.* equations (A3.41) and (A3.44). This is because the attenuation correction is very small so any error in the estimate of S_a affects the accuracy of the calculated β_a only weakly. Also, these solutions require only an accurate estimate of the boundary values for β_a , whereas the boundary values of the extinction solutions also require accurate estimates of S_a .

For the analysis of lidar returns from optically thick atmospheres the solutions (A3.41), (A3.42), (A3.44) and (A3.45) in turn reduce to the one component solutions (A3.22), (A3.23), (A3.24) and (A3.25). In this case the backward solutions (A3.44) and (A3.45) are stable and the forward solutions (A3.41) and (A3.42) are unstable.

In conclusion, for the analysis of lidar returns from optically thick clouds where the cloud backscatter coefficient $\beta_c \gg \beta_m$ and $\sigma_c \gg \sigma_m$, only the backward solution for the extinction coefficient can provide useful results. For thin atmospheres where $\beta_a \approx \beta_m$ and $\sigma_a \approx \sigma_m$, profiles of β_a may be determined with good accuracy by the solutions for β_a ; *i.e.* equations (A3.41) and (A3.44).

2.2.3 Integrated Attenuated Backscatter (χ')

The integrated attenuated backscatter from clouds is the lidar-measured cloud parameter that is combined with radiometer-measured infrared radiances in the LIRAD method (*e.g.* Platt *et al.*, 1998). The variable γ' was first introduced by Platt (1973). A new variable for the integrated attenuated backscatter (χ') is presented here that follows on more smoothly from the lidar equations that use the volume backscatter coefficient β as they have been presented in this thesis and in the majority of lidar studies.

In the following it is assumed the molecular and aerosol terms are known or are insignificant and have been eliminated from the lidar return from a cloud:

$$\chi(z) = \beta(z)T^2(z_b, z). \quad (2.15)$$

Integrating the profile of χ from height of cloud base (z_b) to height of apparent cloud top (z_t), the integrated attenuated backscatter (χ') may be defined by,

$$\chi' = \int_{z_b}^{z_t} \chi(z) dz. \quad (2.16a)$$

Note that Platt (1973) used,

$$\gamma' = \int_{z_b}^{z_t} B(z)T^2(z_b, z) dz, \quad (2.16b)$$

to define integrated attenuated backscatter. In the latter equation B is the isotropic backscatter coefficient, and has the same units as the extinction coefficient. At this point some clarification is required with respect to the definitions (2.16) and on the use of symbols. The isotropic backscatter coefficient is less commonly used in lidar studies, although used commonly in radar studies. The series of LIRAD studies of cirrus clouds is an exception (*i.e.* Platt (1973) through to Platt *et al.*, (1998)). Therefore, it is worthwhile presenting both χ' as well as the original γ' , with the notion that in future LIRAD results may be reported in terms of either χ' or γ' . Also, the extinction-to-backscatter ratio is variously named and defined and there is no convention on the use of symbols. As previously mentioned S has been adopted for this thesis following the choice of Fernald *et al.* (1972) and Fernald (1984). In all previous LIRAD studies the isotropic backscatter-to-extinction ratio k is used. The two constants S and k are related by

$$S \equiv \frac{\sigma}{\beta} \equiv \frac{4\pi\sigma}{B} \equiv \frac{4\pi}{k}. \quad (2.17)$$

As usual σ is the volume extinction coefficient. The extinction-to-backscatter ratio S has units (sr), whilst k is dimensionless. While on the subject of symbols, in future lidar studies a further simplification may be to drop any references to k , S , or any other 'lidar ratio' and instead return to using Deirmendjian's (1969) definition of the phase function in the backwards direction (P_{π}).

Now, χ' may be expressed in terms of the cloud optical depth as follows. Expanding equation (2.16a):

$$\chi' = \int_{z_b}^{z_t} \beta(z) \exp\left(-2\eta \int_{z_b}^z \sigma(z') dz'\right) dz. \quad (2.18)$$

The term η is again assumed to be constant. It is noted that with the change of variable (Platt, 1973),

$$d[T^2(z_b, z)] = -2\eta\sigma(z)T^2(z_b, z)dz. \quad (2.19)$$

and making use of S , equation (2.18) may be expressed as,

$$\chi' = \frac{1}{S} \int_{z_b}^{z_t} \sigma(z) \exp(-2\eta\tau_v(z_b, z)) dz. \quad (2.20)$$

So the resulting expression for χ' is

$$\chi' = \frac{1}{2\eta S} (1 - \exp(-2\eta\tau_v)), \quad (2.21a)$$

where τ_v is the cloud optical depth; the subscript 'v' on τ_v distinguishes the visible optical depth from the infrared absorption optical depth τ_a . Platt's (1973) integrated attenuated backscatter (γ') is greater than equation (2.21a) by a factor of 4π thus;

$$\gamma' = \frac{k}{2\eta} (1 - \exp(-2\eta\tau_v)). \quad (2.21b)$$

By inspection of equations (2.21),

$$\text{as } \tau \rightarrow \infty, \quad \chi' \rightarrow \frac{1}{2\eta S} \quad \text{and} \quad \gamma' \rightarrow \frac{k}{2\eta}. \quad (2.22)$$

Thus ηS may be retrieved from measurements of χ' (or γ') from optically thick clouds (Platt, 1979). The value of ηS so obtained may then be used as input for the analysis of profiles from thinner clouds. The clouds need not be very thick for the retrieval of ηS ; with cloud optical depths of less than the

relatively low (multiple scatter modified) optical depth of $\eta\tau = 1.50$, χ' is less than the asymptote $(2\eta S)^{-1}$ by only 5%. For clouds thicker than this the accuracy of the retrieval of ηS depends more heavily on the signal digitiser resolution, and the signal-to-noise ratio.

There are very few, if any, reports of measurements of χ' from water droplet clouds. Deirmendjian's (1969) modelled water cloud *C1* has a value for S of about 20, and η for this model was found to be about 0.65 in the Monte Carlo study by Platt (1981). Thus for a lidar return from a thick cumulus cloud with a droplet size distribution similar to *C1*; $\chi' \approx 0.0385$, and $\gamma' \approx 0.483$. For high clouds of ice crystals (cirrus), values of γ' tend to be lower, ranging from about 0.15 to 0.45 (*e.g.* Platt *et al.*, 1998); these values of γ' correspond to χ' of 0.012 to 0.036. Physically, χ' for high cirrus clouds are expected to exist over a larger range than those for water droplet clouds, because of the different shapes of ice crystals that exist in cirrus clouds, which in turn would lead to greater variability in S .

2.2.4 Calculated Visible Optical Depths

With ηS and χ' and reliable estimates of the uncertainties obtained, the visible optical depths modified by the multiple scatter factor ($\eta\tau_v$) may be calculated directly from χ' by re-arranging the expression for χ' , equation (2.21a),

$$\eta\tau_v = \frac{1}{2} \ln \left(\frac{1}{1 - 2\eta S \chi'} \right). \quad (2.23)$$

Errors in this retrieval can be estimated as follows. By the theory of the propagation of random errors the variance of $\eta\tau_v$ is,

$$s[\eta\tau_v]^2 = \left(\frac{\partial u}{\partial(\eta S)} \right)^2 s[\eta S]^2 + \left(\frac{\partial u}{\partial(\chi')} \right)^2 s[\chi']^2, \quad (2.24)$$

where

$$u = \frac{1}{2} \ln \left(\frac{1}{1 - 2\eta S \chi'} \right), \quad (2.25)$$

so,

$$s[\eta\tau_v]^2 = \left(\frac{\chi'}{1 - 2\eta S\chi'} \right)^2 s[\eta S]^2 + \left(\frac{\eta S}{1 - 2\eta S\chi'} \right)^2 s[\chi']^2. \quad (2.26)$$

2.3 The Lidar and Infrared Radiometer (LIRAD) Method

2.3.1 Introduction

Simultaneous observations of clouds by visible elastic-backscatter lidar and infrared radiometer are combined in the LIRAD method for the purpose of the retrieval of their optical and microphysical properties (Platt, 1973; Platt, 1979; Platt and Dilley, 1979; Platt and Dilley, 1981; Platt *et al.*, 1984; Platt *et al.*, 1987; Platt *et al.*, 1998). In the analysis of LIRAD data, calibrated lidar profiles are combined with corresponding measured infrared radiances, and the cloud properties are calculated with the assumption of constant cloud particle composition, shape, and size distribution throughout the depth of each cloud profile. The lidar is normally calibrated by fitting points on measured cloud-free lidar returns to a modelled molecular profile. The analysis also requires cloud temperatures to calculate blackbody radiances, and the temperatures are obtained by combining cloud heights sounded by lidar, and, a height profile of temperature obtained by radiosonde or by aircraft data.

The LIRAD analysis technique requires for its input sufficient cloud measurements to cover a range of infrared absorption optical depths (τ_i), from very small values of τ_i up to about $\tau_i = 1.2$ ($\epsilon_i \approx 0.7$), as will be seen later. This represents a range of small optical depths, and, in general, high clouds are optically thin because of their lower water content and larger particle size (*e.g.* Platt, 1979). This is partly why the LIRAD method has been applied exclusively to measurements of high and mid-level clouds to date (*e.g.*, see Platt *et al.*, 1998). The work for this thesis successfully employed the LIRAD method for the first time on measurements of boundary layer clouds, and the reason for this was that some of the (non-precipitating) stratocumulus clouds observed during the SOCEX experiments were optically thin (*e.g.* Young, 1995).

2.3.2 Measured Infrared (10-12 μm) Radiances

Infrared radiometers used with lidars in the LIRAD technique typically measure radiation in the 10 - 12 μm wavelength band of the spectrum. In this region of the spectrum there is low absorption by water vapour (see section 2.5.2), and, importantly for measurements of boundary layer clouds, this portion of the spectrum covers the maximum radiance emitted by a blackbody at a temperature of 0°C. The radiometers are operated with fields of view similar to those of the lidars (*e.g.* 10 mrad) and use spectral filters and detectors suitable for the measurement of rapid fluctuations in the downwelling radiances by the clouds (see section 4.2.3). The spectral filters typically have widths of 1 μm and measured radiances are typically recorded at a rate of 1 Hz (Platt *et al.*, 1993).

Platt *et al.* (1998) defined the downwelling effective cloud radiance (L_c) at cloud base by,

$$L_c = L_i + L_s + L_r, \quad (2.27)$$

where L_i is the cloud emission due to the absorptive properties of the cloud particles. (Note that the subscript 'i' is used here rather than the subscript 'a' normally used to describe infrared absorption in LIRAD studies - in this thesis the subscript 'a' has been used for the lidar parameters to stand for 'aerosol'). There are two infrared scattering terms in equation (2.27): the internal scattering L_s represents the contribution to the measured radiances due to scattering of infrared radiation in the clouds, and L_r is the radiance emitted by the earth's surface and reflected back down by the cloud. The scattering components L_s and L_r have been calculated for cirrus clouds by Platt (1973), Platt (1979), Platt and Dilley (1979), and Platt and Stephens (1980).

The total measured downward radiance L_g at the earth's surface is described by,

$$L_g = L_{air}^{(b)} + T_{air}^{(b)} L_c + T_i L_{air}^{(a)}, \quad (2.28)$$

where $L_{air}^{(b)}$ is the clear air radiance below the cloud, and $T_{air}^{(b)}$ is the infrared transmittance of the clear air between the ground and cloud base z_b . The clear air radiance incident on cloud top, $L_{air}^{(a)}$, is modified by the cloud (infrared absorption) transmittance T_i . In studies of cirrus clouds $L_{air}^{(a)}$ is negligible so the last term is dropped from equation (2.28) (*e.g.* Platt and Stephens, 1980; Platt *et al.*, 1998). The calculation of the clear air transmittance $T_{air}^{(b)}$ is described in the next section.

The internal scattering term L_s is the difference between the radiance scattered into the downward beam in a cloud, ($L_s^{(i)}$), and the radiance scattered out of the beam ($L_s^{(o)}$):

$$L_s = L_s^{(i)} - L_s^{(o)}. \quad (2.29)$$

In the 10 - 12 μm wavelength region of the region of the spectrum the single scattering albedo of water droplet clouds is about 0.5 (*e.g.* Deirmendjian, 1969). With a high probability of scattering it may be expected that a significant proportion of the thermal radiation from thick water clouds scatters out of downward beams, significantly reducing maximum beam emittances (or flux emittances) to below unity. However thick water clouds are known to be nearly black (*e.g.* Platt, 1972). The reason for thick water clouds behaving almost like blackbodies in this region of the spectrum is due to forward scattering: although a significant portion of the radiation is scattered out of a downward beam, a similar quantity of radiation is scattered into it. That is, the two terms $L_s^{(i)}$ and $L_s^{(o)}$ in equation (2.29) are quantities of similar size, so to determine their net effect both quantities must be determined accurately. The calculation of these scattering quantities is not a trivial matter. However, for the analysis of LIRAD data no such separation is required anyway, it is only required that the sum of these quantities be known. This is because only the cloud absorption component of the measured radiance is required to calculate an infrared (absorption) optical depth. For this thesis the radiative transfer program 'DISORT' was used to determine the net increase over the cloud absorption radiances due to both these scattering effects, (see section 4.3.3.7), without any need or attempt to calculate each of the components $L_s^{(i)}$ and $L_s^{(o)}$.

2.3.3 Calculated Infrared Properties of Cloud-Free Air

The primary infrared input to the main algorithm of the LIRAD analysis method is the cloud radiance L_c . The infrared transmittance $T_{air}^{(b)}$ and clear air radiance $L_{air}^{(b)}$ must be calculated to determine the cloud radiances L_c from the total measured radiance {see equation (2.28)}. In the previous LIRAD studies of cirrus clouds $T_{air}^{(b)}$ has been determined by combining theoretical studies with measurements of $L_{air}^{(b)}$.

The clear air radiance and transmittance may be determined from the absorptive properties of molecules and aerosols in the 10 - 12 μm band, and the methods for calculating these properties are

investigated in detail by Platt *et al.* (1984). The majority of the molecular emission is by water vapour, and there is also some emission by aerosols, ozone and CO₂. The infrared absorption by water vapour in the atmosphere depends on temperature, air pressure and humidity. Height profiles of these aerological data combined with estimates of the water vapour dimer absorption coefficients and line parameters (see Platt *et al.*, 1984) are used to determine the clear sky radiance and infrared transmittance (*e.g.* see Platt *et al.*, 1998). In previous LIRAD studies of tropical atmospheres a database of the calculated clear sky transmittance versus the clear sky radiance is built up over the course of an experiment from a number of radiosonde soundings, and the two are found to be well correlated. This can only be done in the tropics where temperature is reasonably constant. The calculated infrared transmittance is then parameterised as a function of the clear sky radiance.

The clear sky radiance is measured by infrared radiometer when the sky is clear of clouds. When clouds are present, water vapour paths measured by microwave radiometer can improve the calculation of a continuous value for L_{air} . The transmittance and radiance of the clear air below the cirrus can be calculated from independently measured profiles of the water vapour mixing ratio, and air temperature and pressure. Thus the measured L_{air} may be compared with a calculated value.

2.3.4 The LIRAD Equation

Lidar profiles of χ and the infrared parameters are linked as follows. It is recalled that the integrated attenuated backscatter, χ' , (or γ'), may be expressed in terms of the visible optical depth thus {equations (2.21) are repeated here for convenience};

$$\chi' = \frac{1}{2\eta S} (1 - \exp(-2\eta\tau_v)). \quad [2.21a]$$

$$\gamma' = \frac{k}{2\eta} (1 - \exp(-2\eta\tau_v)). \quad [2.21b]$$

The quantitative link between the visible and infrared properties is the visible extinction-to-infrared absorption ratio (α), assumed to be constant with range,

$$\alpha = \frac{\sigma_v}{\sigma_i}. \quad (2.30)$$

The LIRAD studies by Platt (1973) through to Platt *et al.* (1998) express γ' as a function of infrared optical depth,

$$\gamma' = \frac{k}{2\eta} (1 - \exp(-2\eta\alpha\tau_i)), \quad (2.31)$$

and the infrared absorption emittance (ε_i) is defined by,

$$\varepsilon_i = 1 - \exp(-\tau_i), \quad (2.32)$$

{see also equation (2.40)}, so γ' is related to the infrared emittance by

$$\gamma' = \frac{k}{2\eta} \left\{ 1 - \exp\left(-2\eta\alpha \ln \frac{1}{(1 - \varepsilon_i)}\right) \right\}. \quad (2.33)$$

This equation, and for the earlier studies, (2.31), formed the basis of the analysis for the series of LIRAD studies of clouds by Platt (1973) through to Platt *et al.* (1998).

Writing (2.21a) in terms of $\eta\varepsilon_i$,

$$\chi' = \frac{1}{2\eta S} (1 - \exp(-2\eta\alpha\tau_i)). \quad (2.34)$$

By inspection of this equation as,

$$\tau_i \rightarrow \infty, \chi' \rightarrow \frac{1}{2\eta S}.$$

In terms of the infrared emittance equation (2.34) is,

$$\chi' = \frac{1}{2\eta S} \left\{ 1 - \exp\left(-2\eta\alpha \ln \frac{1}{(1 - \varepsilon_i)}\right) \right\}. \quad (2.35)$$

The form of the curve given by (2.35) is shown in Figure (2.2) using some microphysical properties of stratocumulus and cirrus clouds obtained from LIRAD measurements.

Note that equation (2.23) is obtained by re-arrangement of (2.34),

$$\eta\tau_v = \frac{1}{2} \ln \left(\frac{1}{1 - 2\eta S \chi'} \right), \quad \text{\{equation (2.23)\}}$$

where,

$$\eta\tau_v = \eta\alpha\tau_i. \quad (2.36)$$

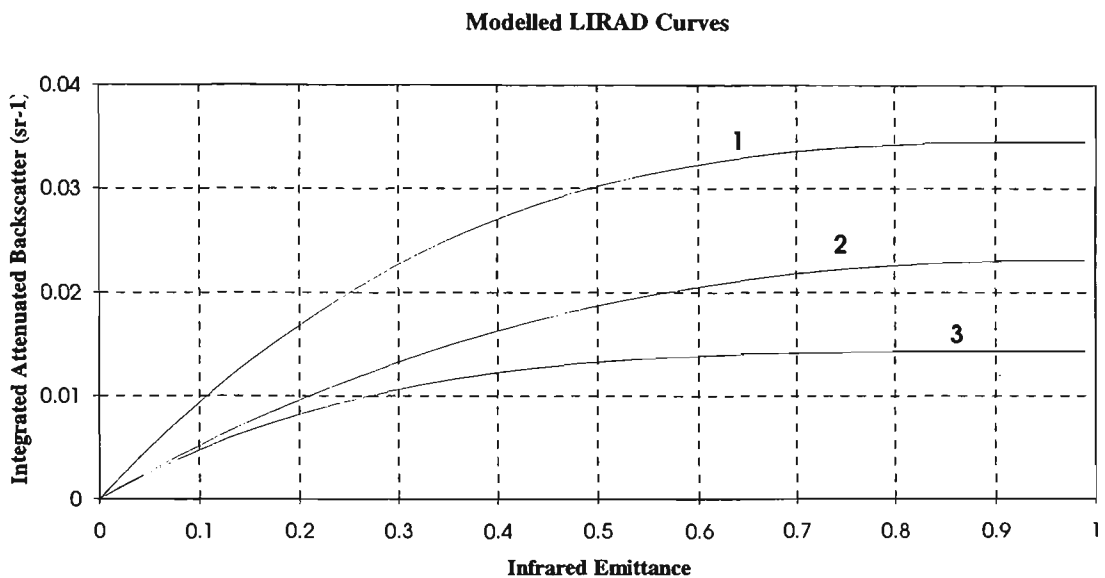


Figure 2.2. LIRAD results for marine stratocumulus clouds containing only water droplets; $\eta S = 14.5$ sr and $\eta\alpha = 1.5$ (1, top curve). Cirrus clouds at a temperature of -35°C to -25°C ; $\eta S = 22$ and $\eta\alpha = 1.2$ (2, middle curve). Cirrus clouds at a temperature of -65°C to -55°C ; $\eta S = 35$ and $\eta\alpha = 1.9$ (3, bottom curve). Example (1) was obtained from the results of this thesis, examples (2) and (3) are from Platt *et al.* (1998).

2.3.5 The LIRAD Analysis Technique

The analysis of LIRAD data can proceed as follows. First, values of χ' are obtained by integrating the calibrated lidar profiles of χ with respect to height (z). An initial estimate of ηS is obtained from the lidar measurements of the thickest clouds, those that fully attenuate the lidar pulse, or from previous observations (Platt *et al.*, 1998). Fully attenuating clouds may be identified by inspection of the region in the lidar profiles above the apparent cloud tops for the presence of a (small) molecular scatter signal. Where the identification of this small signal is not practical, the values of χ' can be compared with the simultaneously measured infrared radiances - the values of χ' and these radiances both reach a maximum for about the same depth of cloud. Otherwise, if there are no measurements of thick clouds, ηS must be estimated from theoretical studies of the Mie scattering and multiple scattering properties of the clouds, given some independent measurements of the cloud particle microphysics.

Using the value of ηS (or $k/2\eta$) thus obtained, the profiles of χ are inverted for the volume backscatter coefficient. The implementation of the LIRAD method for this thesis was based on the same computer code as used by Platt *et al.* (1998), and in both these studies each calibrated lidar profile was inverted for the isotropic backscatter coefficient (B) via the linear iterative technique. If the solutions for B were found to be unstable the estimate of $k/2\eta$ was increased by small increments until the solution converged (Platt, 1979). The stability of the inversions were monitored by comparing changes in the calculated backscatter coefficients for corresponding small changes in $k/2\eta$.

After the lidar profiles were inverted for the backscatter coefficient, a profile of infrared absorption was calculated via the assumption of the ratio between the visible extinction and the infrared absorption being constant, as well as the assumption of a constant multiple scatter factor (η). In some previous implementations of the LIRAD method (*e.g.* Platt *et al.*, 1984; Platt *et al.*, 1987), to make the computations more efficient, the terms in brackets of,

$$\sigma_i(z) = \left(\frac{\eta}{k}\right) \left(\frac{1}{\eta\alpha}\right) B(z), \quad (2.37a)$$

were combined to define the new constant,

$$\xi = \frac{\sigma_i(z)}{B(z)} = \frac{1}{k\alpha}. \quad (2.37b)$$

The first estimates of ξ were obtained by calculations from the Mie theory. In the LIRAD method the cloud radiance is calculated by,

$$L_i = \int_{z_b}^{z_t} \sigma_i(z) L_B(z) \exp\left(-\int_{z_b}^z \sigma_i(z') dz'\right) dz. \quad (2.38)$$

This theoretical cloud radiance, with the height profile of σ_i determined from the inverted lidar profile, is compared with the cloud radiance measured by the radiometer. If they do not match to within a desired accuracy the constant defined by (2.37b) is adjusted. The infrared absorption profile $\sigma_i(z)$ followed by the theoretical L_i are recalculated until a match of desired accuracy is achieved between the calculated and measured radiances. The whole procedure is repeated for each measured cloud.

However, regarding the main iteration process in the LIRAD algorithm, if ηS is known with a certainty better than that obtained from studies of the stability of inversions of lidar profiles with poor signal-to-noise ratios, then there should be no adjustment to ηS {or k , in (2.37b)}. In the case where lidar signal-to-noise ratios are poor, the LIRAD technique should only adjust the value of $\eta\alpha$. Otherwise, the incorrect (underestimated) values of ηS obtained from the inversions of the noisy lidar profiles will lead to spurious profiles of infrared absorption.

The primary results of the LIRAD analysis process for each measured cloud are: the microphysical quantities $(2\eta S)^{-1}$ (or $k/2\eta$) and $\eta\alpha$, and the visible and infrared optical depths, ($\eta\tau_v$ and τ_i respectively). The emittances are then calculated by equation (2.32).

2.3.6 Errors

2.3.6.1 Errors due to Multiple Scattering in Lidar Returns from Clouds

The LIRAD retrieved visible optical depths (τ_v) are modified by the multiple scatter factor (η). In previous LIRAD studies of cirrus clouds, to determine S and α from the LIRAD results η was predicted from Monte Carlo calculations of the multiple scattering in the clouds (Plass and Kattawar, 1971; Kunkel and Weinman, 1976; Platt, 1981). For the LIRAD studies of stratocumulus clouds for this thesis, the effective η was determined by comparing the LIRAD results with *in situ* (single

scattering) measurements of the clouds. This could be done because the variations in S and α with corresponding variations in the droplet size distributions of the water droplet clouds were slight. Further theoretical and experimental studies are required to predict the variations in η with depth into water droplet clouds. To do this the recently developed MULTIPLE SCATTERING Lidar Experiment (MUSCLE) algorithms, (e.g. Bissonnette *et al.*, 1995), could be modified to model particular lidar systems and clouds more accurately.

2.3.6.2 Errors in the Cloud Infrared Radiances

Errors in the measured infrared radiances lead to errors in the cloud optical properties retrieved by the LIRAD method. These are considered in the following: re-arrangement of equation (2.28) gives the cloud radiance,

$$L_c = \frac{L_g - L_{air}^{(b)} - T_i L_{air}^{(a)}}{T_{air}^{(b)}}, \quad (2.39)$$

and by the theory of errors,

$$|\Delta L_c| = \frac{\Delta L_g + \Delta L_{air}^{(b)} + \Delta T_i L_{air}^{(a)} + \Delta L_{air}^{(a)} T_i + \Delta T_{air}^{(b)} L_c}{T_{air}^{(b)}}. \quad (2.40)$$

For thick low clouds $T_i \rightarrow 0$ and $L_{air}^{(a)} \rightarrow 0$, so equation (2.40) may be approximated by,

$$|\Delta L_c| \approx \frac{\Delta L_g + \Delta L_{air}^{(b)} + \Delta T_{air}^{(b)} L_c}{T_{air}^{(b)}}. \quad (2.41)$$

This equation is similar to equation (A12) of Platt *et al.* (1998) in which it was assumed all the radiances due to cloud-free air were emitted from below the clouds. That is, using a total clear sky radiance (L_{air}) and total transmittance of the cloud-free air (T_{air}),

$$|\Delta L_c| = \frac{\Delta L_g + \Delta L_{air} + \Delta T_{air} L_c}{T_{air}}. \quad (2.42)$$

The error in the cloud absorption radiance (L_i) is,

$$|\Delta L_i| = \Delta L_c + \Delta L_s, \quad (2.43)$$

where the reflection component (L_r) and scattering component (L_s) of equation (2.27) have been combined into a single scattering component (L_s) {see also equation (A11) of Platt *et al.*, (1998)}. The infrared scattering quantities L_s and ΔL_s can be determined from theoretical studies, as was done in the high clouds study by Platt and Stephens (1980). For the measurements of the stratocumulus clouds studied for this thesis, the discrete-ordinate radiative transfer method (Stamnes *et al.*, 1993) was used to determine L_s . Further theoretical studies of infrared scattering in stratocumulus clouds are required to improve techniques for determining L_s for LIRAD measurements. Such studies should include accurate modelling of the cloud microphysics and optical properties as well as variations in cloud structure with height.

3. Experiment

3.1 Introduction

3.1.1 The Southern Ocean Cloud Experiment (SOCEX)

The Southern Ocean Cloud Experiment (SOCEX) was planned with the primary research goal of improving our understanding of the optical properties of marine stratocumulus clouds, and the modification of their properties by aerosols (see section 1.2). Instruments for measuring aerological properties and aerosol and cloud microphysics were mounted aboard a Fokker F-27 aircraft and flown during both phases of SOCEX. The F-27 flew on days when there was a good coverage of stratocumulus clouds over the sea to the west of Tasmania, as determined from satellite images, and when the air was free of anthropogenic aerosols (*i.e.* 'baseline' weather conditions, see next section). The airborne instruments made *in situ* measurements of the atmosphere in the boundary layer and just above it, up to heights of about 2500 m, over large regions of the sea to the west of Tasmania. The airborne measurement campaign for the winter phase of SOCEX, (SOCEX1) is described by Boers *et al.* (1996), and the summer phase of the experiment (SOCEX2) is described by Boers *et al.* (1998).

As well as increasing our understanding of the properties of stratocumulus clouds, SOCEX provided an opportunity for the validation of lidar and radiometer measurements for planned long term lidar cloud measurements to be made at CGBAPS (*e.g.*, see Pickett *et al.*, 1996a). LIRAD studies of low clouds are rare, and the LIRAD measurements of boundary layer clouds obtained during SOCEX1 represented the first attempt at determining the optical properties of boundary layer clouds by the LIRAD method (Platt, 1979; Platt *et al.*, 1998). Some of these measurements, as well as a sample of LIRAD measurements of stratocumulus clouds obtained during SOCEX2 were studied in this thesis.

3.1.2 The Cape Grim Baseline Air Pollution Station (CGBAPS)

The LIRAD measurements of the stratocumulus clouds for both phases of SOCEX were made at the Cape Grim Baseline Air Pollution Station (CGBAPS). The atmospheric measurement and research activities carried out at CGBAPS form part of an international effort to increase our knowledge of the background (unpolluted) atmosphere. The activities of CGBAPS represent Australia's primary contribution to the Background Air Pollution Monitoring Network, a part of the Global Atmospheric Watch of the World Meteorological Organization (*e.g.* Francey *et al.*, 1996).

Measurements of meteorological parameters such as air temperature, pressure, humidity and wind direction have been measured on a daily basis at CGBAPS since the mid-1970s. Annual reports of these measurements, as well as those of radiation, gases, and precipitation appear in the Commonwealth of Australia publication, 'Baseline', (e.g. see Francey *et al.*, 1996).

At the CGBAPS maritime air is identified as 'baseline' (*i.e.* clean) when the wind direction is between 190° and 280° and the Condensation Nuclei (CN) concentration is less than 600 cm⁻³ (Francey *et al.*, 1996). Air from these directions has normally followed long trajectories over the Southern Ocean and is free of anthropogenic aerosols.

3.2 Equipment

3.2.1 Ground-Based Lidars

The CSIRO Multiwavelength Scanning Lidar ('maxilidar') was operated by S. Young and P. Manson during SOCEX1 at CGBAPS (Young *et al.*, 1996). Details of the maxilidar measurements are shown in Table 3.1, {reproduced from Pickett *et al.* (1996a)}. To achieve the increased dynamic range required for an analysis of the data described by Young (1995), and for the analysis of the lidar data required for this thesis, each lidar profile was recorded simultaneously but at different sensitivities on both channels of the digital oscilloscope. Profiles were measured once every minute except when the F-27 aircraft was in the area, and then a ten second firing interval was used. A lower-powered, single-wavelength, non-scanning lidar known as the 'minilidar' was operated during SOCEX2 at CGBAPS (Pickett *et al.*, 1996a, Pickett *et al.*, 1996b). Details of the measurements by this lidar are also shown in Table 3.1.

The overlap ranges shown in Table 3.1 refer to the ranges closest to the lidars at which the whole cross-sections of the laser beams are within the fields of view of the lidar receivers. The FOV of the maxilidar was relatively large to provide an overlap range suitable for the analysis of low clouds. The design of the minilidar was rudimentary and the large FOV was the result of the simple placement of the large-area photodiode detector at the prime focus of the large-diameter receiver- a result of the desire for simplicity and sensitivity. These large FOVs meant that multiple scattering was a significant part of the returned signals.

Table 3.1. Specifications of lidars used for this study.

		<i>Maxilidar (SOCEX1)</i>	<i>Minilidar (SOCEX2)</i>
<i>Transmitter</i>			
Nd:YAG laser		Quanta Ray GCR 11-3	Kigre MK-480
energy per pulse	mJ	150	20
wavelength	nm	532	1064
maximum firing rate	s ⁻¹	10	0.5
angular divergence	mrad	0.5	2.6
<i>Receiver</i>			
detector		EMI 9816B PMT	EG&G YAG-444
field of view	mrad	5.0	11.5
receiving area	m ²	0.096	0.13
conversion efficiency	A/W	1976 @ 1500 V	0.42
<i>Lidar overlap range</i>	m	236 m (5.0 mrad) 114 m (10 mrad)	107 m (11.5 mrad)
<i>Digitiser</i>			
range resolution	m	3	7.5
maximum amplifier sensitivity	mV	40 mV full scale	200 mV full scale

3.2.2 Lidar Data Acquisition Program for SOCEX2

A data acquisition program was written for the minilidar by this author that enabled the instrument to be used close to its full capacity for the SOCEX2 experiment. The program was written in the computer language 'C' and used subroutines obtained from a commercially produced software-oscilloscope package named the 'Compuscope220'. The short period of time available to develop the program, only a few weeks prior to its use in the field, led to a simple but robust design. For ease of use and easy development and maintenance the main structure of the program was based on the logic required to run an heirarchical-menu system. The raw signals were displayed in real-time and the data were stored in an easily read (ASCII) format. Thus problems with the signals were easily identified prior to and during SOCEX. The laser shots caused interference with the settings on the Compuscope220 microprocessor chip, so the chip was reinitialised after every shot.

The simple and well-structured program design enabled easy maintenance of the computer code in the field, the successful acquisition of a large dataset (over 30,000 lidar returns), and allowed for a smooth transition from development through to its operation and finally to the analysis of the data. The design of the program is treated in more detail in Appendix A4.

3.2.3 Ground-Based Infrared Radiometers

The CSIRO Mark II Infrared Radiometer was operated alongside the maxilidar during SOCEX1, and before SOCEX1 the measurements by this instrument had been used in two previous LIRAD studies:

Platt *et al.* (1984), and Platt *et al.* (1987). The MarkII was basically similar in design and operation to the MarkI described by Platt (1971), but used a Newtonian optical system.

The field of view of the MarkII was 10 mrad, and a spectral filter restricted the measured wavelengths to between 10 - 12 μm {see Figure (3.1)}. The MarkII used a Golay cell detector (Platt, 1971). The incident radiance to the MarkII was chopped against the radiance from a grooved blackbody that filled half the aperture and was maintained at a warm temperature (*i.e.* close to $40^\circ \pm 0.1^\circ\text{C}$). The measured signal was proportional to the difference between the source radiance and the reference radiance, and recorded at a rate of 1 Hz. The radiometer was adjusted prior to measurements to give zero output for an input signal at 40°C .

The MarkII radiometer viewed the atmosphere in the vertical, and as a part of its calibration was swivelled downwards to view a reference blackbody radiance, *i.e.*, liquid nitrogen placed in a dewar situated directly underneath the instrument. An upward facing cone sat in the base of this dewar and the interior of the dewar and cone were painted matt black. (The calibration of the MarkII measurements is described in Chapter 4).

Table 3.2. Specifications of the infrared radiometers used during SOCEX.

Specifications	CSIRO MarkII	ARM MarkI
Receiving full aperture	10 mrad	3-30 mrad
Measured wavelengths	$10.84 \mu\text{m} \pm 1 \mu\text{m}$	$10.86 \mu\text{m} \pm 0.50 \mu\text{m}$
Detector	Unicam Golay cell	HgCdTe
Minimum detectable radiance	$134 \text{ mW m}^{-2} \text{ sr}^{-1} \text{ Hz}^{-1/2}$	$3.67 \text{ mW m}^{-2} \text{ sr}^{-1} \text{ Hz}^{-1/2}$

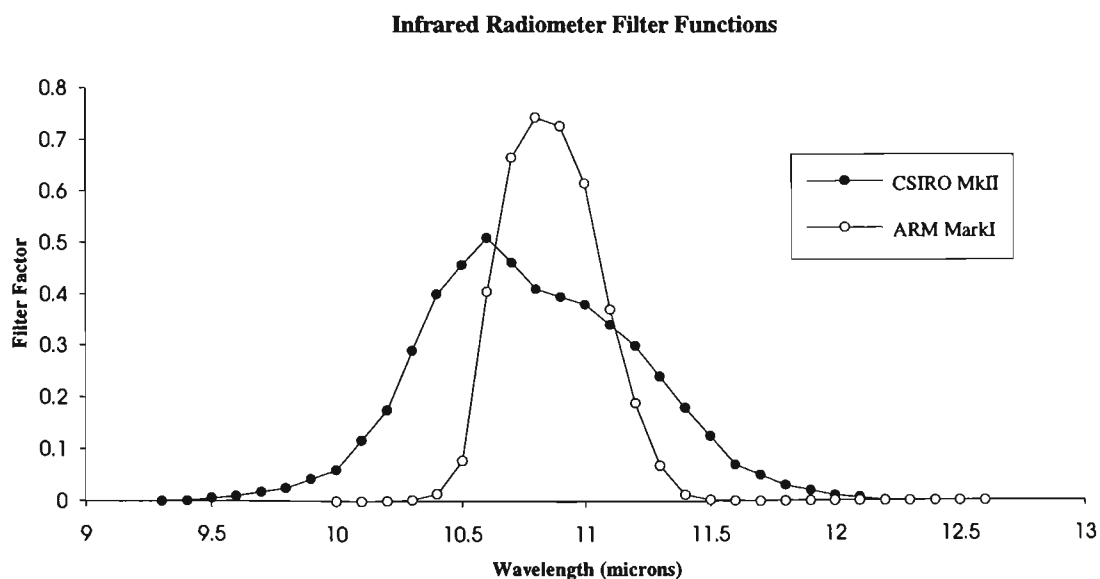


Figure 3.1. Spectral filter functions for the CSIRO MarkI infrared radiometer, (SOCEX1), and the ARM MarkI infrared radiometer (SOCEX2).

The Atmospheric Radiation Measurement Program (ARM) MarkI infrared radiometer was used for SOCEX2 LIRAD measurements. This radiometer used a liquid nitrogen-cooled HgCdTe detector, and was an improved instrument over the older CSIRO radiometers (Platt *et al.*, 1993). For viewing calibration sources placed underneath, downward swivelling of the radiometer optics of the ARM MarkI was mechanised. The ARM MarkI measured radiation with a centre wavelength 10.86 μm but with a slightly narrower spectral band than the CSIRO MarkII (Figure (3.1)). The field of view of the ARM MarkI was set to 10 mrad, similar to the field of view of the minilidar (11.5 mrad). The specifications of the ARM MarkI (SOCEX2) and the CSIRO MarkII (SOCEX1) infrared radiometers are shown in Table 3.2. In this table the minimum detectable radiances are those determined by Platt *et al.* (1998).

3.2.4 Ground-Based Microwave Radiometer

The CSIRO Dual-Frequency Microwave Radiometer measured thermal radiation in the microwave region of the electromagnetic spectrum, and some of this radiation was emitted by water vapour and liquid water (Hill and Long, 1995). This instrument is similar in design to that of Hogg *et al.* (1983). The microwave radiometer measured radiation emitted by water vapour at the frequency 20.6 GHz, and by liquid water at the frequency 31.65 GHz. Some of the physics and methods of microwave radiometry are described by Ulaby *et al.* (1981), Ulaby *et al.* (1986), and Janssen (1993).

The operation of the CSIRO MWR during SOCEX1 is described by Boers and Hill (1996), and retrievals of water vapour path (W_v) and liquid water path (W_L) for this instrument are described by Boers (1996). Observations by this radiometer at CGBAPS from 1994-1995 are reported by Boers and O'Brien (1996). The values of W_v and W_L were supplied by Boers to this author to assist with the analysis of the infrared radiometer measurements of water vapour during cloud-free periods. Also, values of the cloud optical depths obtained from W_L were compared with the LIRAD results.

3.2.5 Airborne Aerosol Probe (ASASP)

Measurements of the concentrations of the maritime aerosols in and above the boundary layer were required for assessing the accuracy of the calibration of the lidar for SOCEX1 (see Chapter 4). The Active Scattering Aerosol Spectrometer Probe (ASASP) aboard the F-27 measured particles of radii between 0.06 μm to 1.56 μm in 15 bins of varying sizes. It is assumed the ASASP measurements were of dry particles due to dehydration of the aerosols as they passed through the instrument (Strapp *et al.*,

1992). Garvey and Pinnick (1983) have noted that the ASASP will undersize haze droplets having the refractive index of water ($m = 1.33 - 0i$), and that particles with radii between $0.3 \mu\text{m}$ and $0.8 \mu\text{m}$ will be undersized by about a third. However in this study it is assumed that all the ASASP data represented particles dried before measurement. (For its calibration, the manufacturers of the ASASP used latex spheres with refractive index $m = 1.588 - 0i$). The optical properties of the aerosols determined from the ASASP measurements for this thesis are discussed in detail in sections 4.3.3.2 - 4.3.3.7.

3.2.6 Airborne Water Droplet Probes (FSSP and 2D-C)

Among the instruments mounted aboard the F-27 for the measurement of cloud droplet size distributions *in situ* were a Particle Measuring Systems (PMS) Forward Scattering Spectrometer Probe (FSSP-100), and a PMS Optical Array Two Dimensional Counter (2D-C).

The FSSP measured the size distributions of droplets with radii from $1 - 23.5 \mu\text{m}$ in 15 bins of step size $1.5 \mu\text{m}$. This instrument measured most of the droplets observed in the boundary layer clouds. As described by Boers *et al.* (1996) the FSSP observations were corrected for co-incidence and dead-time losses (see Baumgardner *et al.*, 1985), but the measurements were not corrected for any non-uniformity of the laser beam of the instrument. The FSSP cloud droplet size distribution measurements were made at a rate of 60 Hz and an average recorded every second, along with a value of the fraction of the 60 measurements of each second that were not null measurements ('fractional cloudiness'). Boers *et al.* (1996) performed calibrations of the FSSP within two weeks of the beginning and end of SOCEX1.

The 2D-C measured larger precipitating droplets ranging in size from $25 \mu\text{m}$ to $1000 \mu\text{m}$ in bins of width $12.5 \mu\text{m}$. There were no recorded measurements in the size range in between the FSSP and 2D-C size ranges, $23.5 \mu\text{m}$ to $25 \mu\text{m}$, however the effect of the absence of these measurements on the cloud liquid water and optical properties determined from the total measured DSDs is negligible.

3.3 LIRAD Measurements During SOCEX

At CGBAPS during each phase of SOCEX a ground-based lidar and infrared radiometer were situated side-by-side to measure clouds as they passed overhead at Cape Grim. During SOCEX1 the maxilidar and CSIRO MarkII radiometer were situated in a caravan (elev. $\approx 90 \text{ m ASL}$) next to the large

communications tower on the cliff at Cape Grim. The lidar and infrared radiometer were pointed vertically through hatches in the roof of the caravan. During SOCEX2 the minilidar and ARM MarkI radiometer were set up in the small room on the roof-deck of the CGBAPS building (elev. \approx 95 m ASL), and both instruments were pointed upwards through a single hatch. During SOCEX2 the lidar and radiometer were pointed at the same volume of cloud by adjusting the aim of the lidar to obtain a maximum correlation of the atmospheric signals from both instruments.

As a part of their calibration, about every hour the infrared radiometers were swivelled downwards to measure zero radiance reference blackbodies of liquid nitrogen. These calibration measurements were made over a period of a few minutes. At all other times the radiometers measured the downwelling infrared (10 - 12 μ m) radiances emitted thermally by the atmosphere. All these radiances were measured continuously and recorded at a rate of 1 Hz. At the same time as the infrared radiometer measurements were underway short 10 nS pulses of visible laser light were fired from the lidars. The lidars were fired at rates that depended on the cloud types and heights. Typically, the lidars measured stratocumulus clouds every 5-10 seconds.

Summaries of the LIRAD measurements for SOCEX1 are given in Table 3.3, and for SOCEX2 in Table 3.4. (In the tables the acronym IRR stands for InfraRed Radiometer).

Table 3.3. LIRAD measurements during SOCEX1.

Day	Date	<i>Maxilidar</i>				<i>CSIRO MarkII IRR</i>				Aircraft Flights	Clouds & Rain
		Hours:		Total	Shots	Hours:		Total			
		From	To						From	To	
1	8/07/93	13:02	17:31	4:29	116	-	-	-	No	-	
2	9/07/93	-	-	-	-	-	-	-	No	-	
3	10/07/93	10:53	17:44	6:51	1898	-	-	-	Yes	Sc, precip	
4	11/07/93	10:57	17:08	6:11	1970	11:59	17:47	5:48	Yes	Cu,Sc, precip	
5	12/07/93	15:43	16:40	0:57	86	-	-	-	No	-	
6	13/07/93	11:49	18:31	6:42	242	-	-	-	No	-	
7	14/07/93	11:01	18:21	7:20	130	-	-	-	No	As,Ci	
8	15/07/93	9:43	18:06	8:23	1018	13:15	17:20	4:05	Yes	Cu,Sc, precip	
9	16/07/93	9:06	18:21	9:15	2772	9:34	17:25	7:51	Yes	Sc, precip	
10	17/07/93	10:10	11:26	1:16	224	9:50	13:54	4:04	No	Cu,St,Sc	
11	18/07/93	11:57	18:01	6:04	864	10:40	11:44	1:04	Yes	Sc	
12	19/07/93	9:18	15:26	6:08	498	9:32	16:23	6:51	Yes	Cu,St, precip	
13	20/07/93	10:15	15:09	4:54	2100	10:21	17:12	6:51	Yes	Cu,Sc, precip	
14	21/07/93	-	-	-	-	-	-	-	No	Cu, precip	
15	22/07/93	9:04	14:34	5:30	1854	10:57	14:53	3:56	No	Cu,Sc,Ci	
16	23/07/93	9:04	17:21	8:17	1050	-	-	-	No	Cu,As,Ac	
17	24/07/93	9:13	10:34	1:21	142	9:32	11:36	2:04	No	St,As, precip	
Total: 14964 shots											

Table 3.4. Lidar measurements during SOCEX2.

<u>Day</u>	<u>Date</u>	<u>Minilidar</u>				<u>ARM MarkI IRR</u>			<u>Aircraft</u> <u>Flights</u>	<u>Cloud</u> <u>Types</u>
		<u>Hours:</u> <u>From</u>	<u>To</u>	<u>Total</u>	<u>Shots</u>	<u>Hours:</u> <u>From</u>	<u>To</u>	<u>Total</u>		
1	22/01/95	11:55	12:16	0:21	162	11:48	13:49	2:01	No	Cu
2	23/01/95	11:03	20:09	9:06	815	12:44	17:02	4:18	No	Sc,As(?)
3	24/01/95	7:22	13:20	5:58	283	12:30	13:17	0:47	No	Cu,Sc
4	25/01/95	9:34	16:33	6:59	1347	13:45	16:38	2:53	Yes	Cu,Sc
5	26/01/95	9:23	21:09	11:46	888	11:53	17:22	5:29	No	Cu,Sc,Ci
6	27/01/95	6:24	22:01	15:37	1656	9:35	14:36	5:01	No	Cu,As
7	28/01/95	15:20	15:21	0:01	13	-	-	-	No	Cu,St
8	29/01/95	9:51	17:29	7:38	997	16:37	17:40	1:03	No	Cu,Sc
9	30/01/95	6:19	19:44	13:25	2461	12:32	19:44	7:12	Yes	Cu,Sc
10	31/01/95	6:27	20:25	13:58	3315	7:25	16:27	9:02	No	Cu,Sc,Ci
11	1/02/95	6:29	15:47	9:18	1050	7:00	13:55	6:55	Yes	Cu
12	2/02/95	6:59	16:15	9:16	639	10:23	11:22	0:59	No	Cu,Sc?,As
13	3/02/95	6:53	17:28	10:35	725	15:25	17:48	2:23	No	Cu,Sc
14	4/02/95	-	-	-	-	-	-	-	No	Cu
15	5/02/95	6:52	18:21	11:29	803	14:22	16:45	2:23	No	Cu,Sc,As,Ci
16	6/02/95	6:21	18:54	12:33	3510	10:13	19:03	8:50	Yes	Cu,Sc
17	7/02/95	6:33	10:10	3:37	1308	7:12	11:04	3:52	No	Cu,Sc
18	8/02/95	6:34	22:45	16:11	6726	8:30	20:27	11:57	Yes	Cu,Sc,Ci
19	9/02/95	7:51	22:31	14:40	3963	8:11	22:24	14:13	Yes	Cu,Sc
Total: 30661 shots										

3.4 Case Studies Selected for Analysis

3.4.1 16 July 1993 (SOCEX1)

3.4.1.1 Introduction

On many of the days of SOCEX1 the lidar and IRR measurements of the low clouds were often disrupted because of rain. After about 1430 EST on 16 July 1993 there was an extensive period when it did not rain, and both the lidar and IRR successfully measured clean maritime stratocumulus clouds. There were two flights by the F-27 on this day, and the microwave radiometer also operated successfully. Therefore, because of the availability of substantial good quality data from all the remote sensing and *in situ* instruments the data obtained on the afternoon of this day were selected for detailed study.

3.4.1.2 Weather Condition, Clouds, and Measurements (16 July 1993)

On 16 July 1993 Cape Grim was under the influence of a high pressure system centred over southern Australia (Figure (3.2)). At Cape Grim the wind direction was westerly, and this combined with the low measured CCN concentrations meant that conditions at CGBAPS were declared baseline.

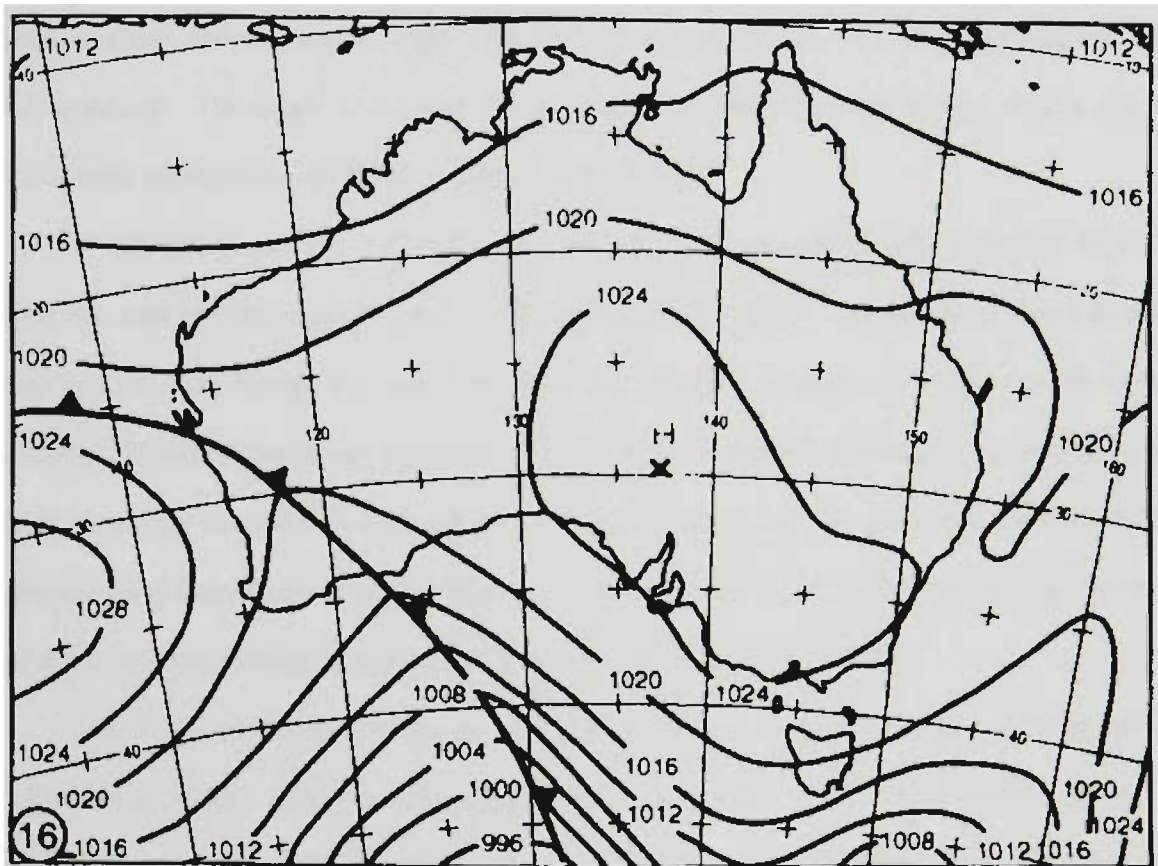


Figure 3.2. Surface air pressure systems over Australia on 16 July 1993 (Bureau of Meteorology, Melbourne). The position of Cape Grim is lat. 40° 40' 56" S, long. 144° 41' 18" East (northwestern tip of the island of Tasmania).

Between 0930 EST and 1030 EST on this day, broken and drizzling stratus and stratocumulus clouds were observed over Cape Grim by the LIRAD operators. Later, these clouds appeared to become thinner. Observations recorded in the fieldnotes include: (1135 EST) "thin (bluish) layer overhead", and (1200 EST) "sun can be seen clearly through very uniform layer of clouds and drizzle". At about 1430 EST the drizzle began to clear, and from this time the lidar and infrared radiometer were operated simultaneously and successfully, measuring thin stratocumulus clouds for several hours as they passed overhead. The data obtained on the afternoon of this day were the best quality LIRAD data obtained for all of SOCEX.

The stratocumulus clouds that crossed the Tasmanian coast near Cape Grim at 1600 EST were moving in a westerly direction. These clouds can be seen by inspection of the National Oceanic and Atmospheric Administration (NOAA) satellite image, NOAA-11 24777 {Figure (3.3)}. This Advanced Very High Resolution Radiometer (visible) image shows a band of clouds just crossing the Tasmanian coast, and, at about the same time the LIRAD instruments detected significantly thicker clouds overhead. The clouds to the east of Cape Grim look brighter in this image. This is due to different solar reflectances, not different altitudes of the clouds.

On the afternoon of 16 July 1993 when the LIRAD measurements were underway the F-27 aircraft was west of Cape Grim (Flight 8). During Flight 8 the clouds were measured during several ascents and descents through the clouds, and from 12 - 72 nautical miles to the west of Cape Grim. The vertical flight path and the ground track of the F-27 during Flight 8 is shown in Figure (3.4). The NOAA-11 satellite image of the clouds, the F-27 track of Flight 8, and the wind direction and LIRAD measurements at Cape Grim all indicate that the clouds measured *in situ* on Flight 08 were of the same band of thicker clouds observed passing overhead Cape Grim at about 1600 EST.

The F-27 instruments detected no ice in the clouds measured on Flight 8 (nor during Flight 7), (Boers *et al.*, 1996). Also, the temperature of the stratocumulus clouds, which were at a height of about 1000 m ASL, did not decrease below 0°C {Figure (3.5)}. Thus the LIRAD measurements of 16 July 1993 were assumed to be of water droplet clouds only. A height profile of the air pressure determined from aerological measurements made aboard the F-27 for Flight 8 is also shown, in Figure (3.6). The measured height profile of the water vapour mixing ratio is studied in detail in a later chapter - see section 4.3.4.

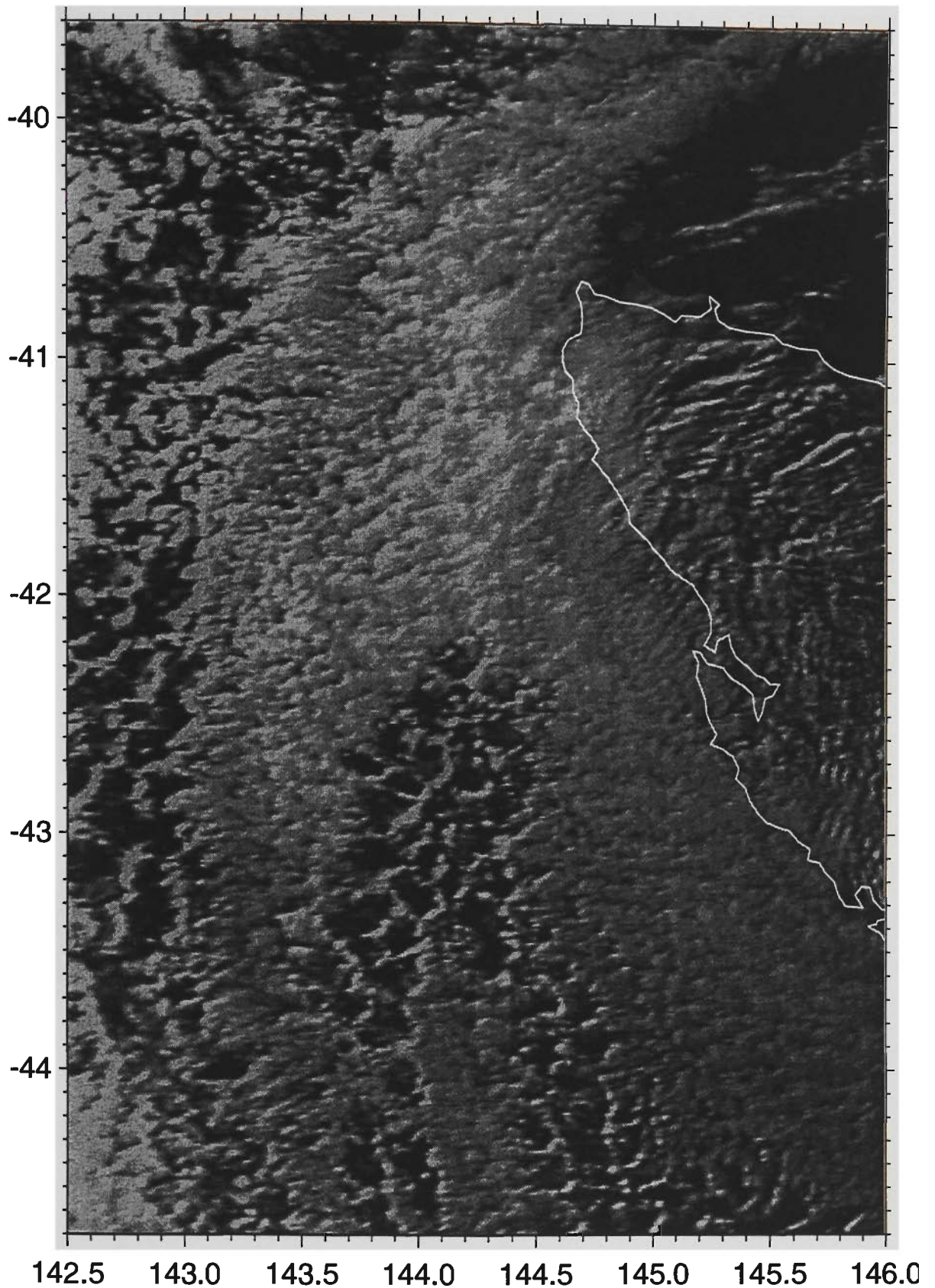


Figure 3.3. NOAA-11 satellite image (24777) of the clouds over the sea to the west of the island of Tasmania (1618 EST, 16 July 1993). Degrees of longitude are shown on the vertical scale, and degrees of latitude on the horizontal scale. Cape Grim is situated on the northwestern tip of of Tasmania. (Courtesy of M. Edwards and P. Krummel., CSIRO Division of Atmospheric Research).

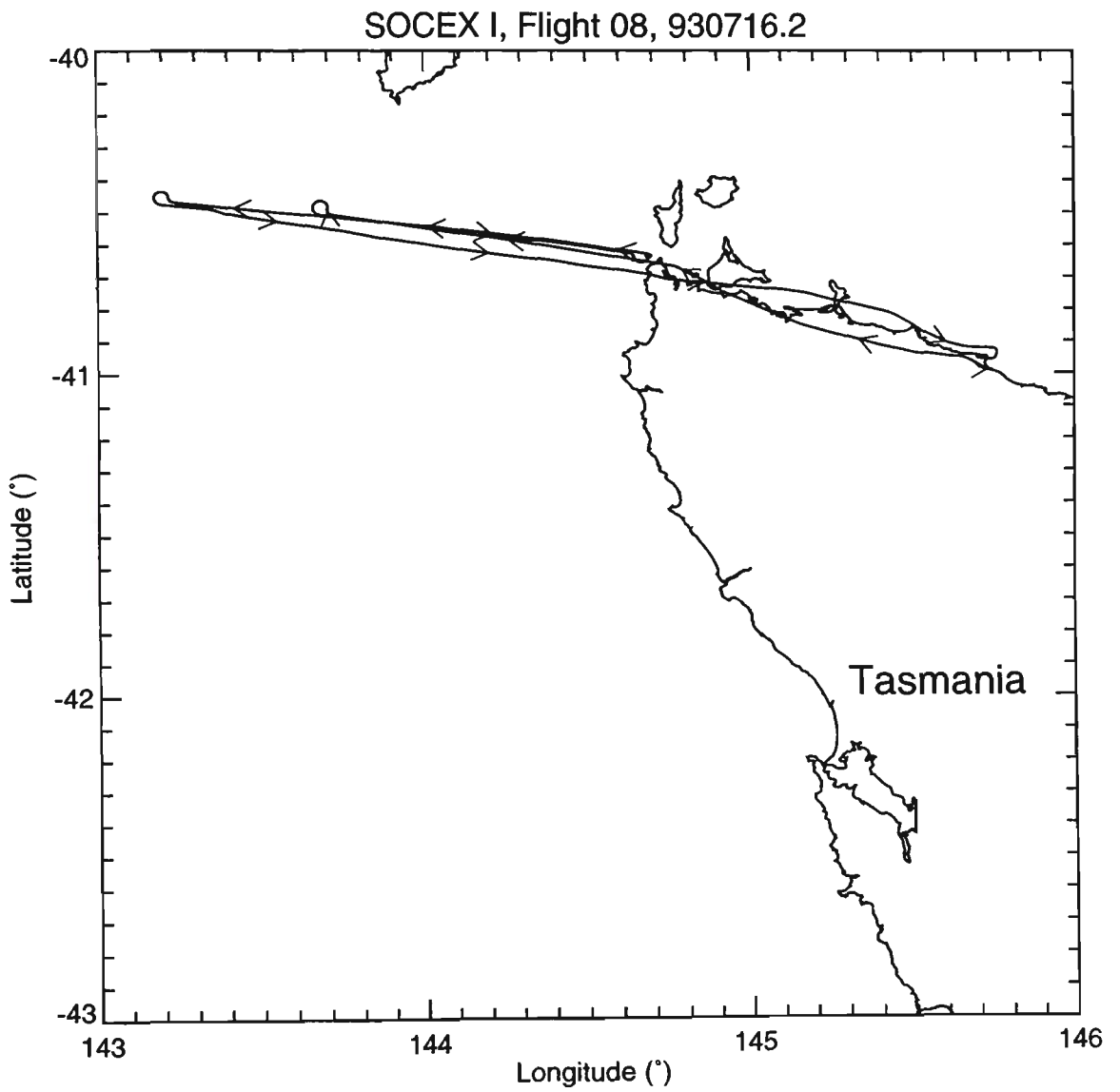
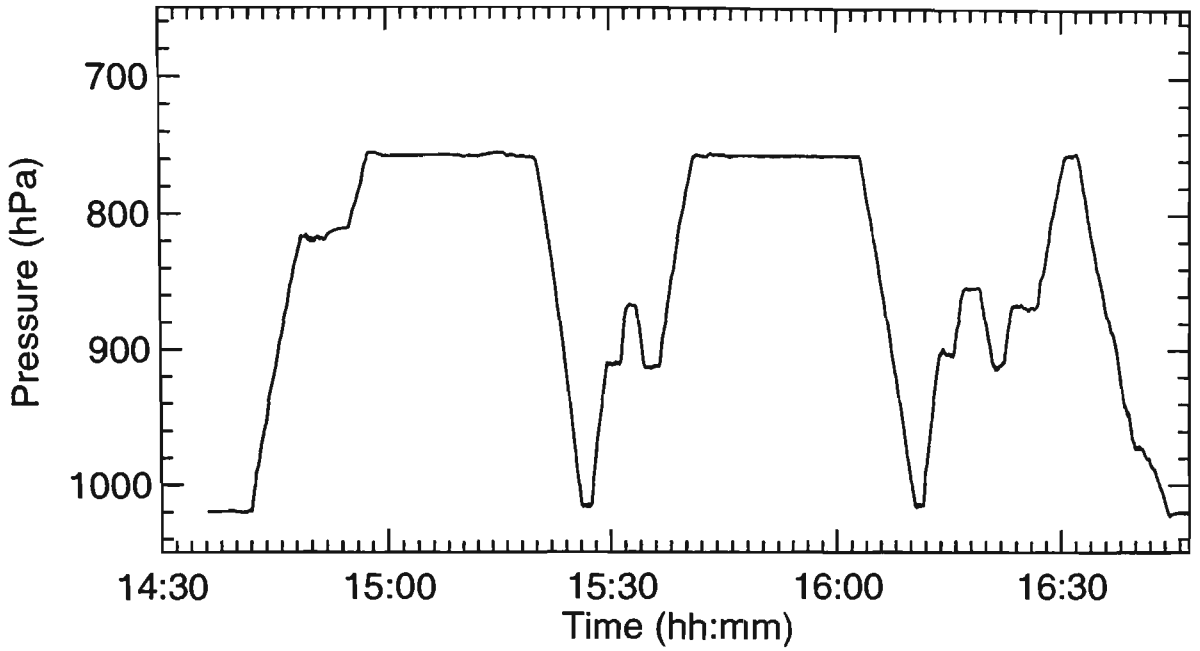


Figure 3.4. The vertical flight path (top) and the ground track (bottom) of the F-27 during Flight 8 on 16 July 1993. Courtesy of P. Krummel (CSIRO Division of Atmospheric Research).

Air Temperature: Flight 8, 16 July 1993

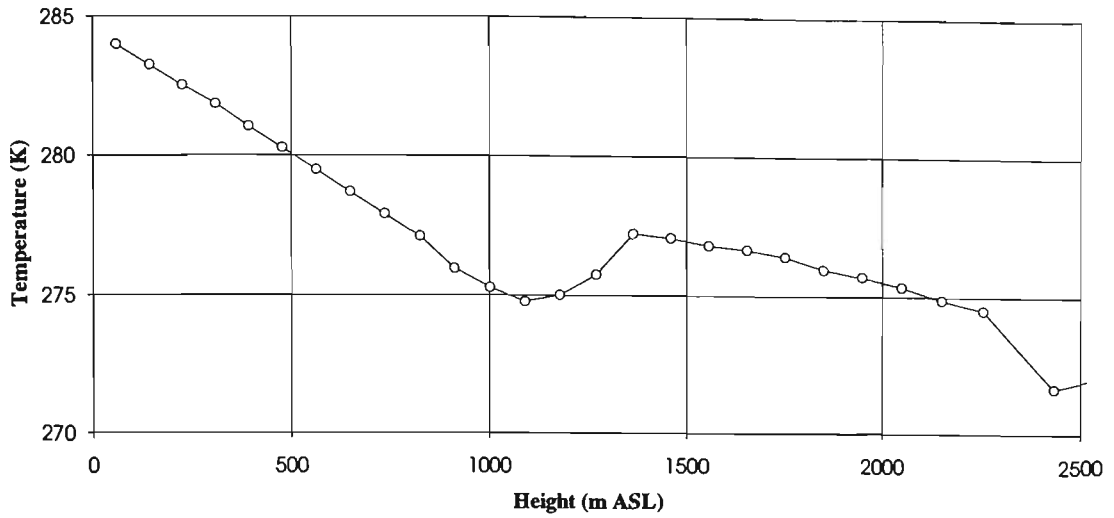


Figure 3.5. Air temperature determined from measurements made aboard the F-27 for Flight 8 on 16 July 1993. Data from R. Boers, P. Krummel, and J. Jensen (CSIRO Division of Atmospheric Research).

Air Pressure: Flight 8, 16 July 1993

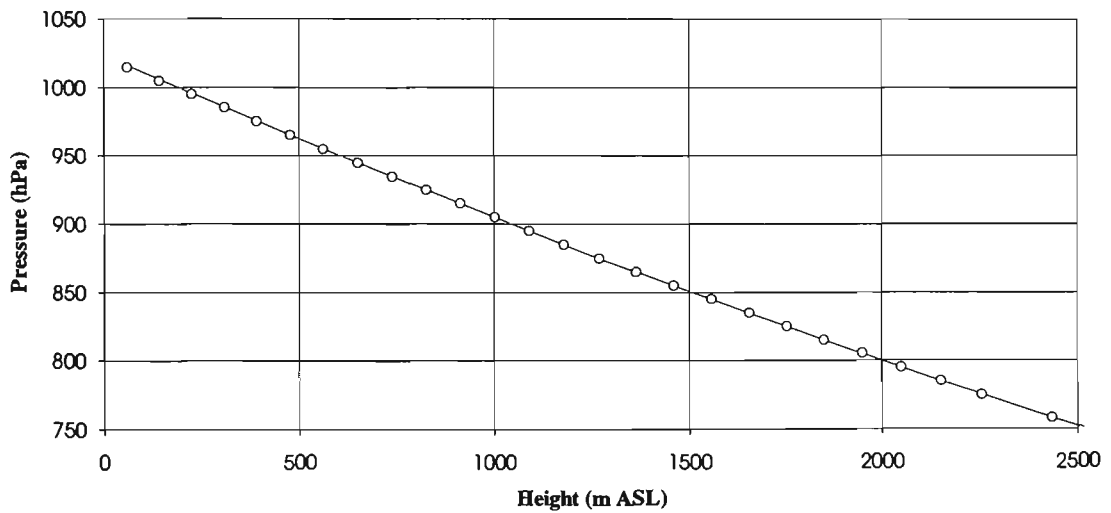


Figure 3.6. Air pressure determined from measurements made aboard the F-27 for Flight 8 on 16 July 1993. Data from R. Boers, P. Krummel, and J. Jensen (CSIRO Division of Atmospheric Research).

3.4.2 8 February 1995 (SOCEX2)

3.4.2.1 Introduction

To an observer at Cape Grim, it was obvious that the summer stratocumulus clouds (SOCEX2) were different from the winter clouds seen during SOCEX1. The summer clouds were several hundreds of metres higher, they did not precipitate as much as the winter clouds, and they existed as relatively small decks with well defined edges, as opposed to the nearly complete cloud coverage often seen during SOCEX1.

The LIRAD dataset of SOCEX2 was nearly twice as large as that of SOCEX1 because there was less rain to disrupt measurements, although the data obtained by the minilidar were of a poorer quality than those obtained by the maxilidar during SOCEX1. The infrared radiometer measurements of SOCEX2 were of a higher quality than those of SOCEX1. A quantity of measurements obtained on one day of SOCEX2 was selected for analysis. The data obtained on 8 February 1995 were chosen because of the baseline air conditions, the instruments aboard the F-27 were flown on this day, and a large number of LIRAD measurements of stratocumulus clouds of varying thicknesses were obtained over the course of the whole day.

3.4.2.2 Weather Condition, Clouds, and Measurements

On 8 February 1995 a high pressure system was centred over the Great Australian Bight, directing a southwesterly airflow over Tasmania {Figure (3.7)}. The satellite image NOAA-09 523625 was taken at 0917 EST and shows pancake-shaped masses of clouds organised in bands, with clear patches in between {Figure (3.8)}.

The vertical flight paths and flight tracks of the F-27 are shown in Figure (3.9) (Flight 9), and Figure (3.10) (Flight 10). There was no ice detected in the clouds by the F-27 instruments (Boers *et al.*, 1998), therefore the LIRAD measurements of the boundary layer clouds on 8 February 1995 were assumed to be of water droplet clouds only. The stratocumulus clouds existed at heights between 1500 m - 2000 m. The air temperatures determined by instruments aboard the F-27 show that the cloud temperatures did not drop below freezing level {Figure (3.11)}. The height profile of air pressure determined from the measurements aboard the F-27 is shown in Figure (3.12).

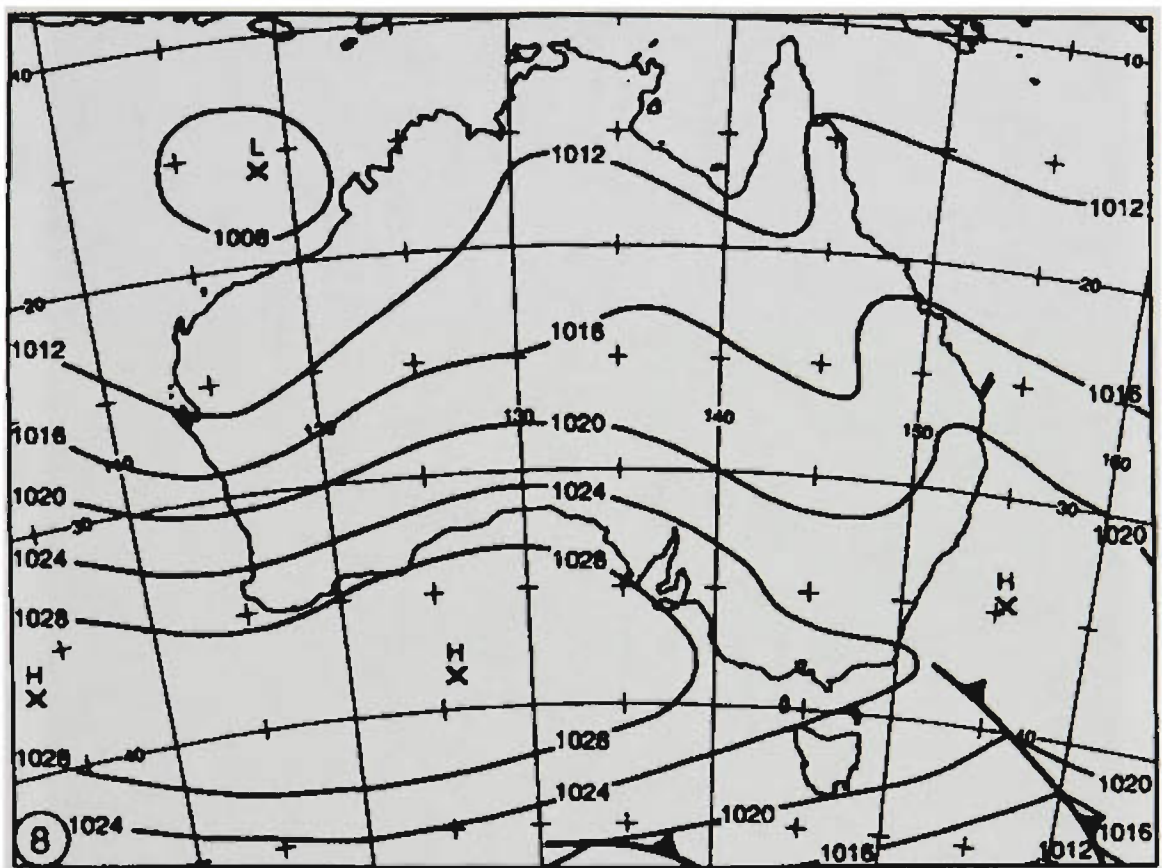


Figure 3.7. Surface air pressure systems over Australia on 8 February 1995 (Bureau of Meteorology, Melbourne). The position of Cape Grim is lat. $40^{\circ} 40' 56''$ S, long. $144^{\circ} 41' 18''$ East (northwestern tip of the island of Tasmania).

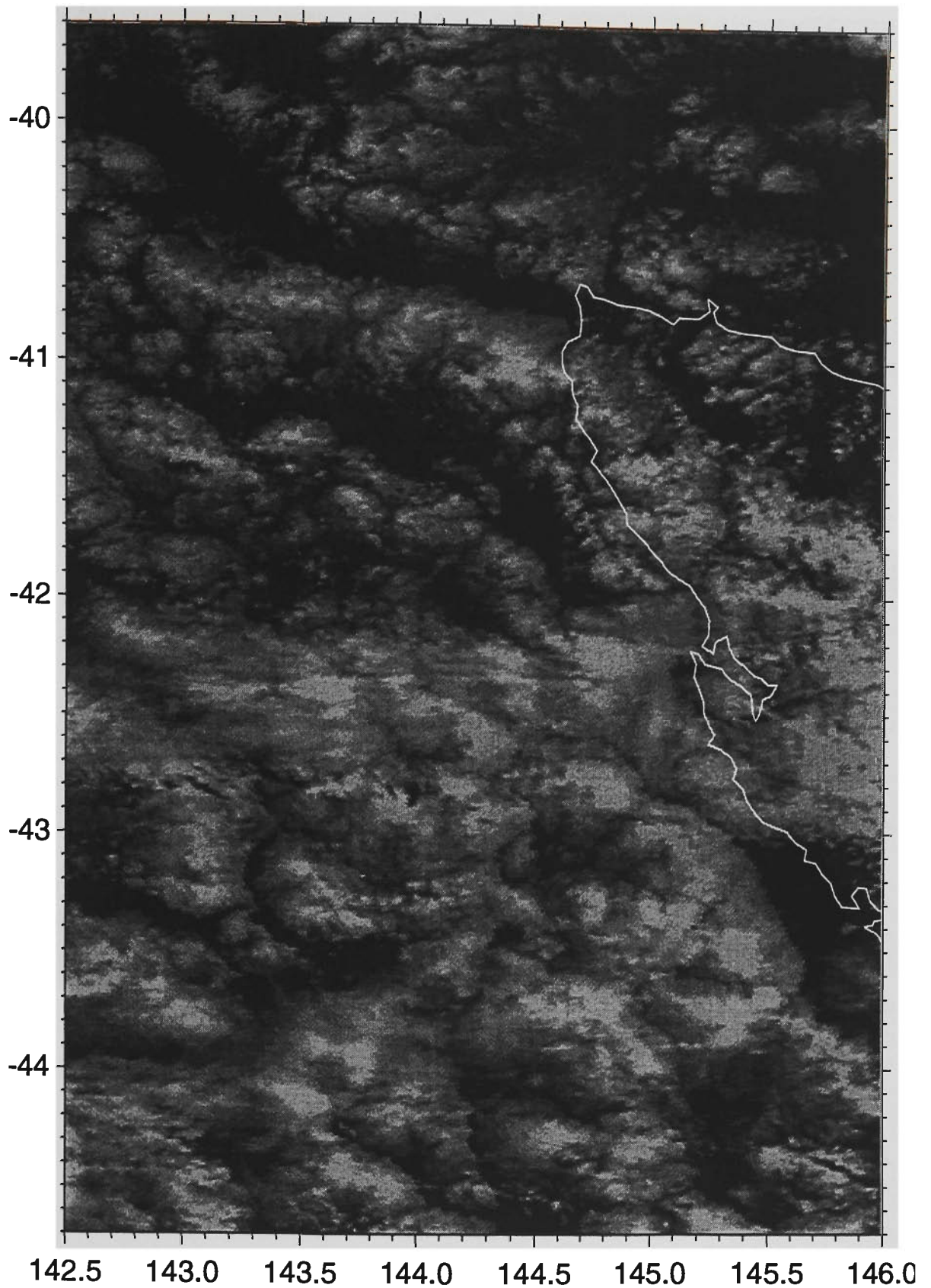


Figure 3.8. NOAA-09 satellite image (52365) of the clouds over the sea to the west of the island of Tasmania, and the coast of Tasmania (0917 EST, 8 February 1995). Degrees of longitude are shown on the vertical scale, and degrees of latitude on the horizontal scale. Cape Grim is situated on the northwestern tip of of Tasmania. (Courtesy of M. Edwards and P. Krummel., CSIRO Division of Atmospheric Research).

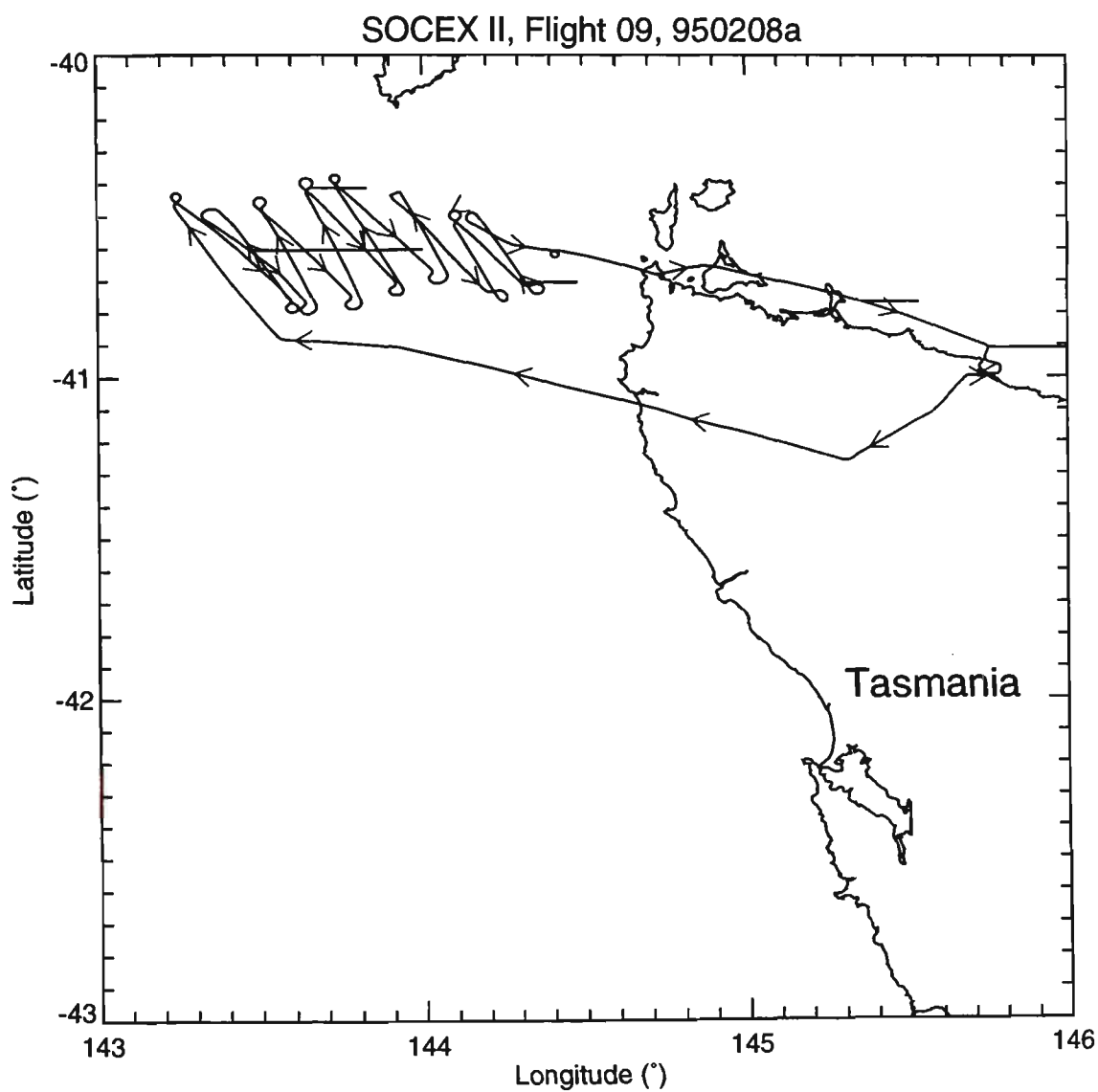
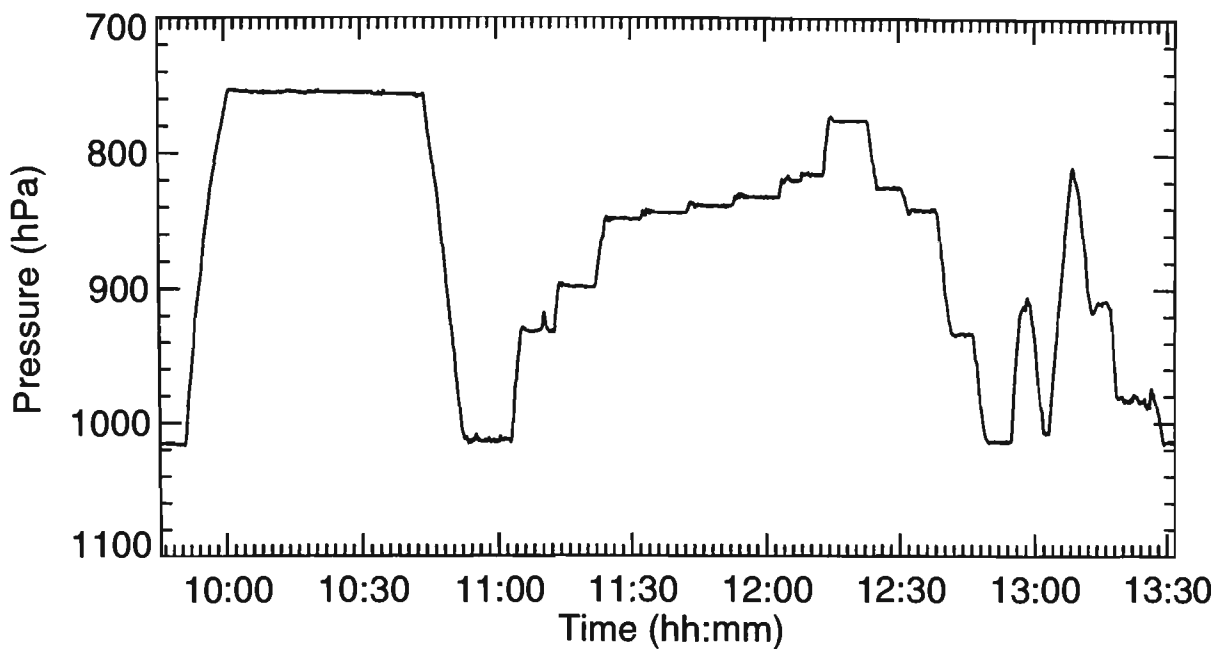


Figure 3.9. The vertical flight path (top) and the ground track (bottom) of the F-27 during Flight 9 on 8 February 1995. Courtesy of P. Krummel (CSIRO Division of Atmospheric Research). The horizontal dashes on the track indicate missing position data.

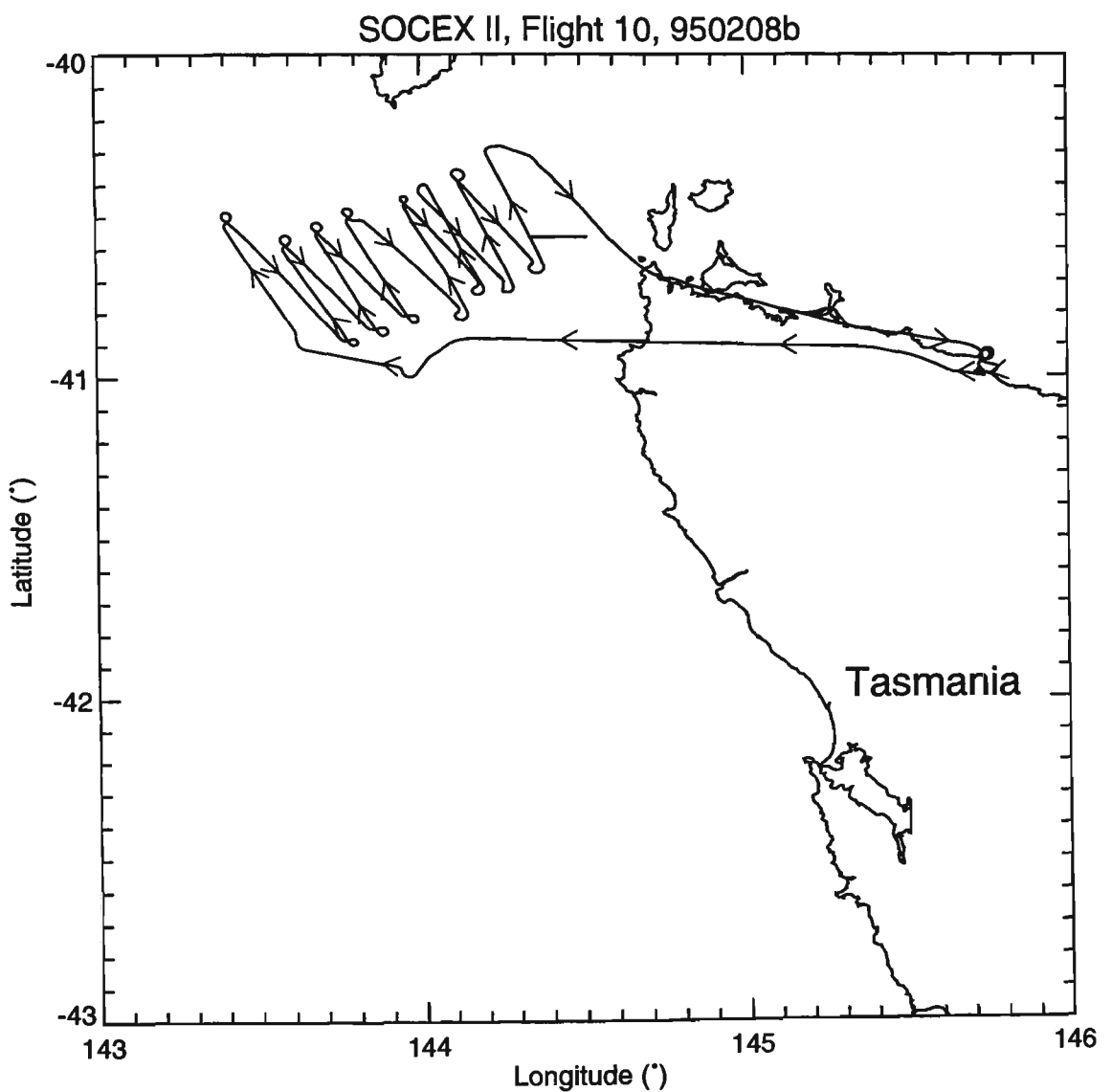
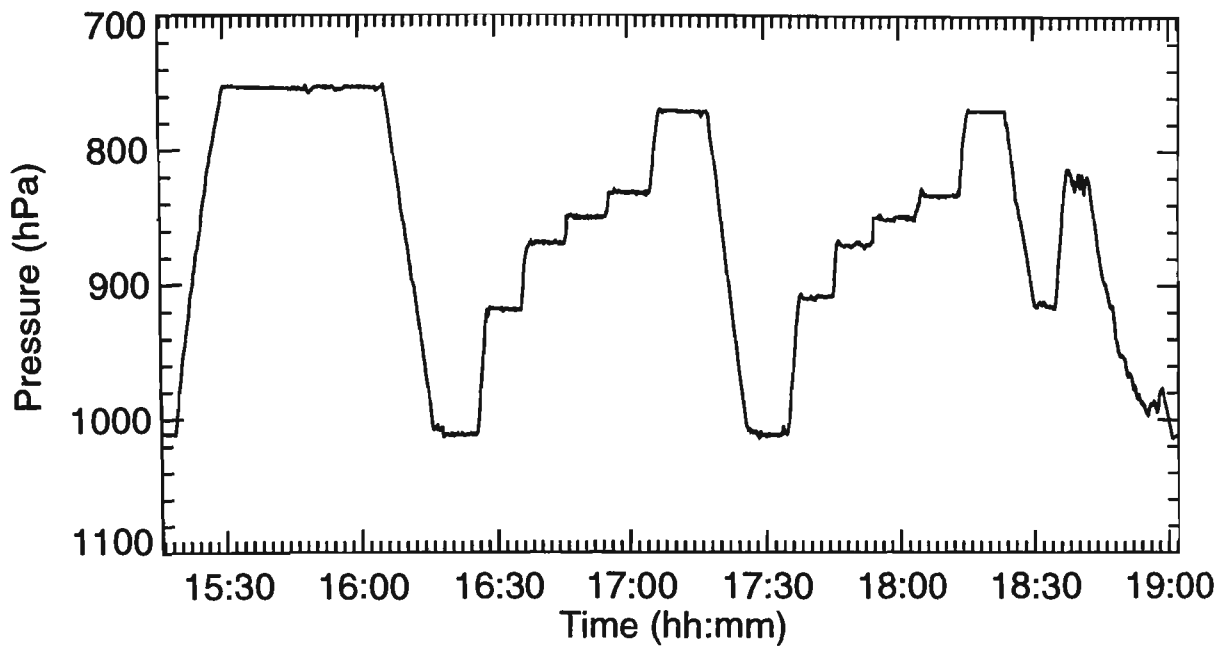


Figure 3.10. The vertical flight path (top) and the ground track (bottom) of the F-27 during Flight 10 on 8 February 1995. Courtesy of P. Krummel (CSIRO Division of Atmospheric Research). The horizontal dash marked on the track indicates missing position data.

Air Temperature: 8 February 1995, Flights 9 and 10

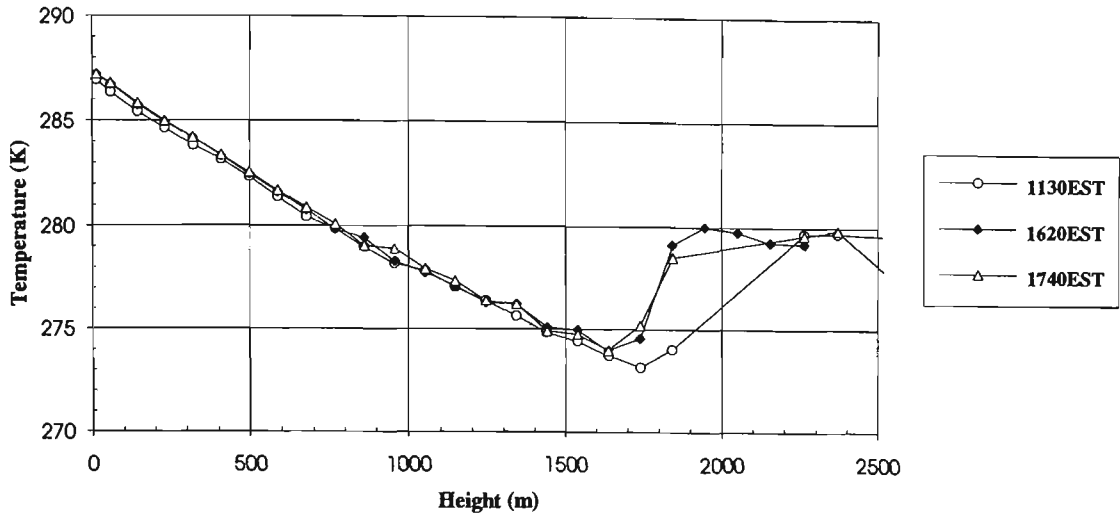


Figure 3.11. Height profiles of air temperature determined from measurements made aboard the F-27 for Flights 9 and 10 of 8 February 1995. Data from R. Boers, P. Krummel, and J. Jensen (CSIRO Division of Atmospheric Research).

Air Pressure: 8 February 1995, Flights 9 and 10

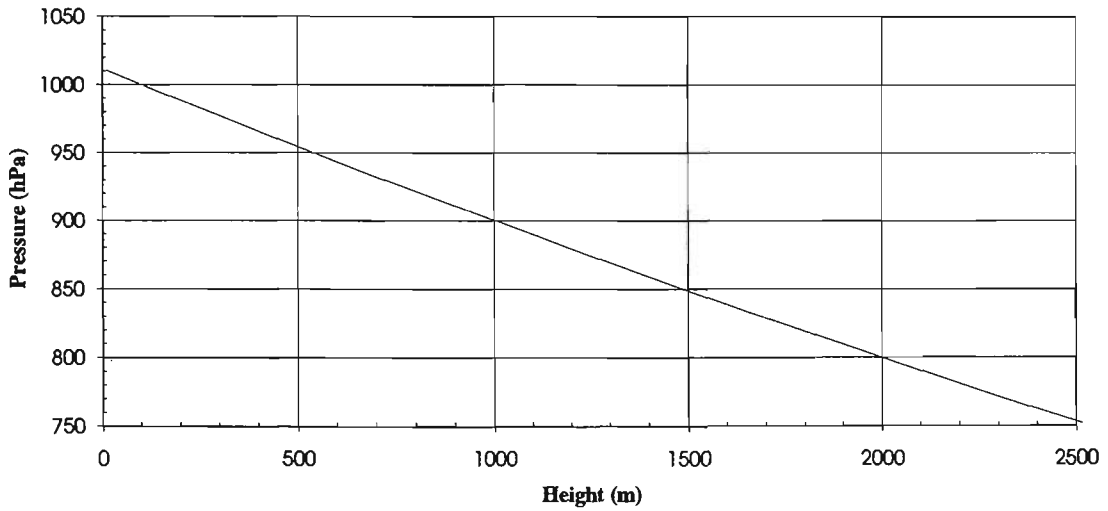


Figure 3.12. Height profile of air pressure determined from measurements made aboard the F-27 for Flights 9 and 10 of 8 February 1995. Data from R. Boers, P. Krummel, and J. Jensen (CSIRO Division of Atmospheric Research).

The lidar observations of the clouds over Cape Grim on 8 February 1995 showed cumulus clouds in the boundary layer that was capped by stratocumulus clouds, and this vertical structure matched the airborne observations of clouds made by the F-27 (Krummel, 1998). An inspection of the measured infrared radiances of the clouds measured over Cape Grim showed that the stratocumulus cloud decks were thinner at the edges and thicker towards the centres. This observation can be explained by Krummel's (1998) interpretation that the stratocumulus clouds were formed by cumulus clouds rising to the top of the boundary layer and then spreading out. This regime of cumulus clouds detraining into thin patches of stratocumulus clouds at the top of the boundary layer is similar to that observed during the Atlantic Stratocumulus Transition Experiment (Albrecht *et al.*, 1995).

Often the summer stratocumulus cloud decks were small: to sample as much of a single cloud deck as possible before it passed overhead, the lidar was fired at a rate limited only by the post-discharge recovery of the laser, that is, with a typical firing period of 3 to 5 seconds. The quality and amount of the lidar observations of stratocumulus clouds were considerably reduced by the strong returns from the lower cumulus clouds. (The lower cumulus clouds blocked the signal from the higher stratocumulus clouds). The greatest number of LIRAD measurements of maritime stratocumulus clouds during SOCEX2 were made on 8 February: there were a total of 6726 lidar measurements of clouds, although, by eliminating all the measurements of the cumulus clouds, only about 3500 measurements were used in the final analysis.

4. Analysis Methods

4.1 Introduction

This chapter describes the methods used to reduce and analyse the lidar and infrared radiometer measurements of stratocumulus clouds for the first application of the LIRAD analysis technique to these type of data. The chapter is divided into three sections. The first section (4.2) includes a description of the initial determination of the cloud heights measured by lidar, for both phases of SOCEX. These cloud heights were valuable in the selection of the two case studies for detailed analysis: i.e., for SOCEX1, the data obtained on the afternoon of 16 July 1993, and for SOCEX2, the data obtained on 8 February 1995. Plots of the cloud heights were a useful reference for identifying the heights and approximate depths of the clouds throughout the work for this thesis. Also, as mentioned previously, cloud height statistics are important for studies of atmospheric radiative fluxes (*e.g.* Platt *et al.*, 1994).

A description of the methods for analysis of cloud measurements obtained on 16 July 1993 are given in section 4.3. The LIRAD analysis technique was previously only applied to high clouds (*e.g.* cirrus), so the technique required some modifications for its application to the measurements of the stratocumulus clouds. These modifications are described in section 4.3.4. The analysis of these LIRAD data represented the bulk of the work for this thesis.

Section 4.4 is a description of the methods used to analyse the lower quality LIRAD dataset obtained on 8 February 1995 - the lower quality data was due to the poorer signal-to-noise ratio of the lidar used during SOCEX2 {see Figure (4.1)}, although the infrared data were better. Thus the methods for analysis of the LIRAD measurements obtained during SOCEX2 were not as complete, but they provided useful results.

4.2 Cloud Heights Measured by Lidar

4.2.1 Introduction

Cloud heights of both phases of the SOCEX experiment were retrieved from the lidar data. The cloud heights normally extracted from lidar returns of stratocumulus clouds are cloud base, and, because the

laser pulses are often fully attenuated by such clouds, the 'apparent cloud top', rather than true cloud top. In contrast, in the case of most cirrus clouds, the 'true' cloud top is measured.

4.2.2 Measurement of Cloud Heights

The maxilidar used during the SOCEX1 experiment was an instrument that recorded strong signals due to backscatter of the laser pulse by precipitation and clouds, and also strong near-air returns from aerosols and molecules. A cloud-free signal was easily discerned in the profiles through the entire depth of the boundary layer. The strong signals from precipitation often could not be easily distinguished from those of cloud particles, thus affecting measurement of cloud base. Also, in the SOCEX1 data, cloud base was sometimes difficult to define due to the gradually increasing aerosol backscatter with height, when swelling in size of the aerosols was caused by increased humidity with height in the boundary layer.

There was less interference by precipitation in the lidar profiles obtained during the SOCEX2, so, although the less powerful minilidar was used during this phase of the experiment, the retrieval of cloud heights was simpler and less ambiguous. In the SOCEX2 lidar data a cloud-free return near to the lidar was often discerned in the profiles, but only up to a height of little more than two hundred metres above the lidar. Above that height the molecular and aerosol backscatter signals disappeared into the noise.

For both lidars, typical signals from stratocumulus clouds are shown superimposed in Figure (4.1). These raw profiles are proportional to the measured signal, and it is clear from this plot that the signal-to-noise ratio is much worse for the minilidar. The reasons for this are: the energy of the laser pulse of the minilidar is less, the cloud signal is higher in the SOCEX2 case, (and so the signal is decreased due to the inverse-range-squared effect), and also the electrical noise in the detector was greater than in the maxilidar.

If not complicated by returns from precipitation, the retrieval of (low) cloud heights from a single lidar profile is normally a simple matter because of the good signal-to-noise ratio from clouds. Also, the visible backscatter by cloud droplets is normally about 2-3 orders of magnitude stronger than that of (boundary layer) aerosols. Thus, cloud heights may be retrieved from lidar profiles using an algorithm to detect significant and sustained rises and falls in $V(z)$, above the background signal from cloud-free signal (*i.e.* the 'clear air' signal), and noise (*e.g.* Platt *et al.*, 1994). However an attempt to use an algorithm that retrieved cloud heights in this way was found to be unsatisfactory for

Stratocumulus Cloud Signals

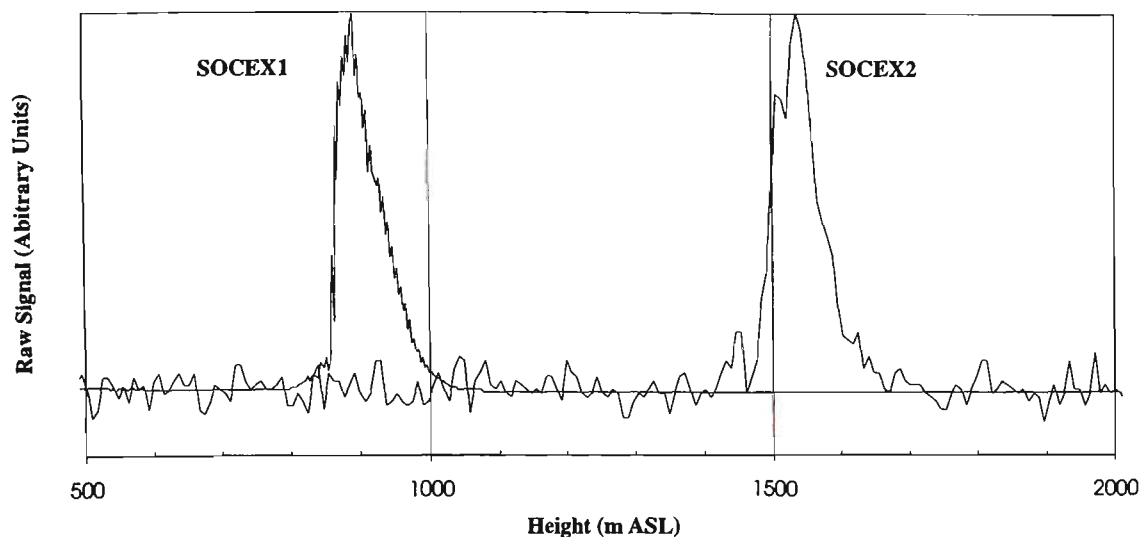


Figure 4.1. Parts of typical lidar profiles used for the retrieval of cloud heights, and obtained from the raw signals. The profiles were obtained with the 'maxilidar' (SOCEX1) and the 'minilidar' (SOCEX2). These profiles have been scaled so that the peaks of the cloud signals are approximately the same. The noisy signal is that of the minilidar.

the SOCEX dataset, due to the high variability of the shape of the cloud signals from one profile to the next. Lidar measurements of clouds just a few seconds apart, and apparently homogeneous to the eye, often showed high variability in the backscatter by cloud droplets and aerosols. There was a high variability in the cloud profile itself, variability near cloud base where aerosols are swelling into cloud droplets, and, for thin clouds, variability in the profile near cloud top.

The cloud-heights software was also found deficient for the automatic detection of the heights of multiple cloud layers, and precipitation always caused problems. The solution here was simply to select the cloud heights by eye using a graphics interface. (The results are presented in the first sections of Chapter 5). By this practice of determining cloud heights by eye, it was decided that the best way to select the heights was by viewing a number of profiles at once. (As opposed to the available cloud-height algorithm which operated on a single lidar profile). So, in future, a better cloud-detection algorithm may be to extract cloud heights using a pattern recognition method for the detection of cloud layers.

4.2.3 Vertical Distribution of Cloud Base Height

The dataset of derived cloud heights contains the following information: time of the lidar shot, cloud base, and apparent cloud top. The lidar sampling rate, (or shot rate), varied between each phase of

SOCEX, and even varied considerably over the course of one day. During SOCEX1 a typical shot rate was 1-2 per minute, increasing to about 1 shot per 10 seconds when the F-27 aircraft was in the vicinity of Cape Grim. During SOCEX2, the stratocumulus existed in smaller patches so that the sampling rate was usually high at around one shot per 3 - 5 seconds. Thus a cloud height distribution using simply the number of shots vs. cloud height would be biased towards those cloud heights sampled most often. In an effort to counter this the periods that clouds were overhead at particular heights were estimated using the lidar shot-times.

A cloud 'layer' was defined by a single lidar shot. The (constant) height of the base of the layer was determined from the lidar measurement, and the hypothetical layer existed up to a period of one minute - for 30 s on each side of the time of the lidar shot (a 'one minute window'). If previous or subsequent lidar shots existed inside these one minute windows, the layer was extended from the centre-time to half-way to the times of the adjacent lidar shots. Each layer made a contribution to the total cloud time for each height bin. By making the time-window too small the results would be biased to the cloud heights sampled more often, and by making the window too large, cloud layers would be placed where none existed. Again, a pattern-recognition algorithm would assist in determining the distribution of cloud heights.

A second problem of constructing a vertical distribution of the cloud heights was that sometimes the lidar detected multiple layers of cloud, whereas at other times upper layers were not detected due to attenuation by thick low clouds. For the results presented here, only the heights of the lowest cloud base in any one lidar profile were used to construct the vertical distribution of the clouds.

It should also be noted that during SOCEX1 lidar operations were not as frequent as during SOCEX2, due to intermittent precipitation. During both phases of SOCEX there were long periods when the lidars were not operational for various reasons. Thus although the vertical distributions of the clouds give an estimate of the time that cloud was observed at various heights, they do not estimate cloud time absolutely; hence fractional cloudiness cannot be determined from these results. The results show only the relative vertical distribution of the heights of lowest cloud base, which were measured mostly during daylight hours.

The lidar measurements of cloud heights described in this work were also part of a pilot study for the planned permanent deployment of the minilidar at CGBAPS.

4.3 LIRAD Measurements of 16 July 1993 (SOCEX1)

4.3.1 Introduction

This section describes the methods for analysis of the LIRAD measurements of stratocumulus clouds. To the knowledge of the author this was the first time boundary layer clouds were studied by LIRAD, and this was achieved by modifying the LIRAD analysis technique normally used for studies of high clouds (*e.g.* Platt *et al.*, 1998). The primary modifications were first, determining and accounting for the downwelling infrared radiances by the water vapour above the tops of the stratocumulus clouds, and second, accounting for the effect of infrared scattering in water droplet clouds on the measured downwelling radiances using the radiative transfer program 'DISORT' (Stamnes *et al.*, 1993).

An important part of the work described in this thesis was determining the *in situ* properties of the clouds (section 4.3.2 of this chapter) from measurements by an airborne FSSP and 2D-C (see Chapter 3). These measurements were described by Boers *et al.* (1996) and Boers *et al.* (1998). On 16 July 1993 these airborne measurements of similar stratocumulus clouds were observed over the sea and upwind of the LIRAD instruments. Some microphysical properties of the clouds were calculated showing only a small variation in the two important parameters used for comparisons with the LIRAD results - the lidar extinction-to-backscatter ratio (S) and the visible extinction-to-infrared absorption ratio (α). (This is different to the analysis of high clouds of ice crystals; the different ice crystal shapes lead to large variations in S).

The *in situ* measurements by the FSSP and aerosol probe, the ASASP, were important for calibration of the lidar. This is because the aerosol transmittance up to cloud base was required for the calibration, and the methods for determining the aerosol optical properties and calibration of the lidar are described in detail in section 4.3.3.

Having obtained good estimates of the cloud microphysical properties, and with (calibrated) lidar measurements of the height profiles of attenuated backscatter by the clouds, and with the cloud infrared radiances obtained from the total measured radiances (section 4.3.4), the LIRAD analysis technique was applied to the measurements of the stratocumulus clouds (also in section 4.3.4).

4.3.2 In Situ Properties of the Stratocumulus Clouds

4.3.2.1 Introduction

On the eighth experimental flight of SOCEX1 on 16 July 1993 the FSSP and 2D-C mounted aboard the F-27 aircraft measured continuously in cloud-free air and in stratocumulus clouds {see Boers *et al.* (1996), Boers *et al.* (1998); Krummel (1998) and section 3.2.6 of this thesis}. The droplet concentrations for each size-bin of the FSSP and 2D-C measurements were provided to the author - the cloud properties determined from these data and presented in this thesis were determined separately from those determined by the airborne team. The airborne team studied the properties of the clouds observed during all of SOCEX, {e.g. see Boers *et al.*, (1998)}, whereas for this thesis the *in situ* measurements obtained during Flight 8 only were studied, in considerable detail, to complement the LIRAD and microwave radiometer measurements obtained on the same day. The analysis of the supplied FSSP and 2D-C data is described in the following.

First, the FSSP measurements of the total droplet concentrations were used to identify eight separate vertical passes through stratocumulus clouds. The FSSP sampled the clouds at a rate of 60 Hz, and the droplet concentrations were recorded from averages determined over each one-second measurement. The fraction of the 60 measurements obtained in-cloud per second (F) was also recorded. When the F-27 flew in clouds it was common for droplets to be measured in every one of those 60 samples, (*i.e.* $F = 1$), and these data for which $F = 1$ were used to extract the cloud Droplet Size Distributions (DSDs).

The passes in flight 8 were named 'cloud 1' through to 'cloud 8'. Clouds 1 to 7 were observed over the Southern Ocean 12 - 72 nautical miles to the west of Cape Grim, and cloud 8 was observed over Bass Strait, just north of the coast near Smithton/Wynyard {the flight track is shown in Figure (3.4)}. Heights above sea level were determined by the SOCEX airborne team. For the DSD measurements in the boundary layer it was convenient to model a height profile in terms of the air pressure by,

$$z = H_o \ln \frac{P_o}{P(z)}. \quad (4.1)$$

The value for the sea surface pressure (P_o) was 1024 hPa, determined by extrapolation of the measured height profiles of air pressure by the F-27. A scale height (H_o) of 8100 m gave the best match between the measured pressure profile and the modelled pressure profile near the height of 1000 m, where the stratocumulus clouds were situated, and the errors in the heights of the measured DSDs calculated by equation (4.1) were only a few metres - an insignificant error.

The liquid water properties of the marine clouds 1-7 were determined separately from those of the single cloud observed over land, cloud 8 (see later, 5.3.3). It was clear from inspections of the plots of the DSDs, (see later, Chapter 5), that cloud 4 contained significantly more drizzle than the other clouds, 1-7, so some of the properties were calculated for the non-precipitating clouds only (1-3 and 5-7).

4.3.2.2 Visible Properties of Small Cloud Droplet Mode (FSSP)

The single scattering extinction of (monochromatic) light by a polydispersion of spherical water droplets was calculated by the numerical implementation of equation (A2.56):

$$\sigma_{ex} = \sum_{i=1}^{i=N_b} Q_{ex,i} N_i \pi r_i^2 \Delta r, \quad (4.2)$$

where i is the droplet size bin number and N_b is the total number of bins.

Values of the Mie extinction efficiency were calculated for spherical water droplets at the visible (Nd:YAG laser) lidar wavelength of 532 nm ($Q_{ex}^{(vis)}$), over the range of droplet sizes covered by the FSSP instrument (1 - 23.5 μm). Calculated Mie efficiencies covering a slightly larger range than this are shown in Figure (4.2). These extinction efficiencies were calculated for 1000 values of droplet radius between 0.025 μm and 25 μm , and the refractive index used for the calculations was $1.33372 - i1.50 \times 10^{-9}$ (Hale and Querry, 1973). Note that $Q_{ex}^{(vis)}$ is highly variable over 1.5 μm -wide intervals (the FSSP bin size). To account for this variability in the calculation of extinction for the measured DSDs, the droplets in each FSSP bin were distributed equally into radius increments of 0.0225 μm , and the Mie extinction efficiencies calculated for these increments. The resulting Mie efficiencies and droplet size distributions were used with equation (4.2) to determine the final volume extinction coefficients (σ_{ex}). The integration of (4.2) was carried out using the trapezoidal rule.

The volume backscatter coefficients (β) were obtained in a similar manner to σ_{ex} , except using equation (A2.55). The Mie backscatter efficiencies (and Q_β) up to a droplet radius of 20 μm are shown in Figure (A2.1).

4.3.2.3 Visible Properties of the Large Droplet Mode (2D-C)

Compared to the FSSP, the drizzle probe (2D-C) measured smaller concentrations of larger water droplets, spread over a larger size range (radii of 25 - 1000 μm). To determine the extinction of such a DSD using the Mie calculations would be slow, due to the large size parameters involved so that the Mie efficiencies were approximated. The oscillations in $Q_{ex}^{(vis)}$ are reasonably small for these large droplet radii and so may be modelled reasonably accurately {see Figure (4.3)}. The modelled extinction is due to Pinnick *et. al.* (1982), (equation (4) of that paper), and it was these modelled values of $Q_{ex}^{(vis)}$ and the corresponding mid-bin radius values that were used to calculate the extinction of the 2D-C measured DSDs:

$$Q_{ex}^{(vis)} = 2(1 + x^{-2/3}). \quad (4.3)$$

The backscatter efficiency of the larger particles is not so easily modelled. First, the values of $Q_\beta^{(vis)}$ were calculated by Mie theory for droplets 25 - 1000 μm in size, with a 0.975 μm interval. To model these backscatter efficiencies $Q_\beta^{(vis)}$ was averaged over the whole size range of the 2D-C probe, 25 - 1000 μm , with the result ≈ 1.02 . With $Q_{ex}^{(vis)} \approx 2.01$, the extinction-to-backscatter ratio for these drizzle droplets is ≈ 25 (sr). These gross estimates of the scattering of visible light by the larger drizzle droplets do not significantly affect the visible properties of the entire droplet spectra of the clouds, because of the small concentrations of drizzle droplets. (However, inspection of the DSDs measured during the SOCEX experiments indicated that drizzle does affect cloud visible extinction in an indirect way, by acting as a sink to the more numerous smaller-sized droplets with radii near 10 μm).

Mie Extinction Efficiency for Water Droplets (532 nm)

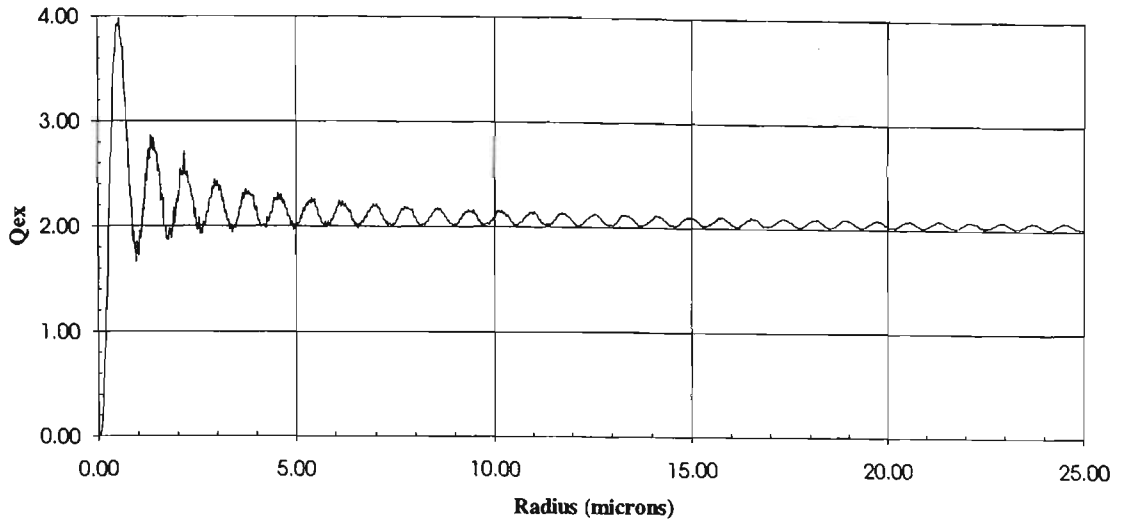


Figure 4.2. Mie extinction efficiency ($Q_{ex}^{(vis)}$) for water droplets, for the visible wavelength 532 nm. Nearly all the extinction is due to scattering; *i.e.* with a value for the complex part of the refractive index of water of 1.5×10^{-9} , $Q_{ab}^{(vis)}$ is of the order 10^{-6} .

Mie Extinction Efficiency for Water Droplets (532 nm)

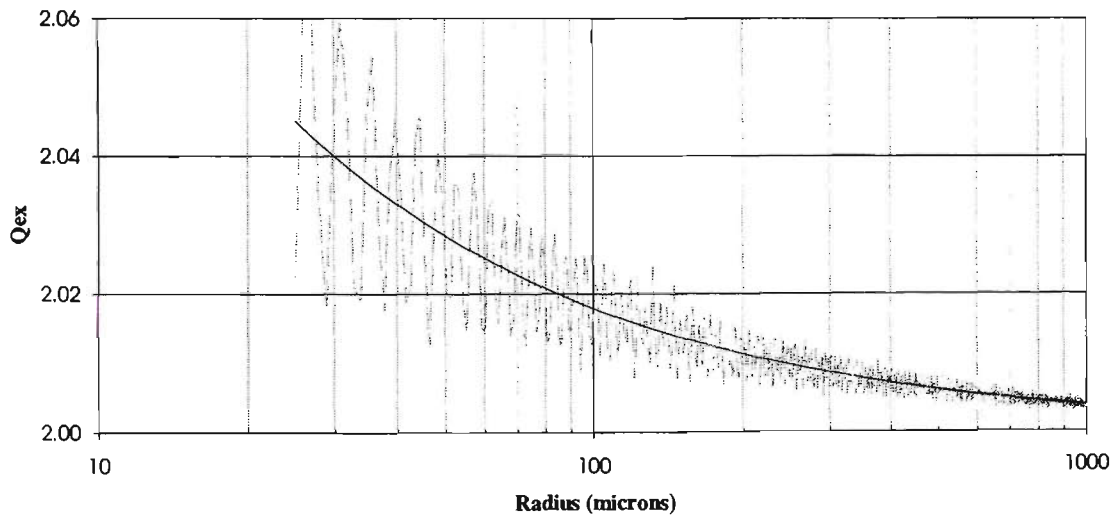


Figure 4.3. Mie extinction efficiency ($Q_{ex}^{(vis)}$) of water droplets, for the visible wavelength 532 nm. The oscillatory line is the result of Mie calculations, the solid line is a modelled $Q_{ex}^{(vis)}$ as described by equation (4.3) (see Pinnick *et al.*, 1982).

4.3.2.4 Infrared Properties of the Small Droplet Mode (FSSP)

The oscillations seen in the Mie extinction efficiencies for visible wavelengths are almost non-existent for infrared wavelengths in the 10 - 12 μm wavelength region of the spectrum {Figure (4.4)}, so that the calculation of the infrared extinction over all particle sizes need not be carried out to such a high resolution. However, to be consistent, values of the infrared Mie efficiencies over the measurement range of the FSSP were calculated in the same way as for the visible wavelength, using 1000 increments of droplet radius. The infrared measurements of stratocumulus clouds during SOCEX1 were made using the CSIRO/DAR MarkII radiometer at $10.84 \pm 1 \mu\text{m}$. At these wavelengths the refractive index of water is $\approx 1.63 - i0.087$ (Hale and Querry, 1973).

4.3.2.5 Infrared Properties of the Large Droplet Mode (2D-C)

The 2D-C drizzle probe measured droplets in the size range 25 μm to 1000 μm . The calculation of the Mie efficiencies for the droplets in this size range need not be carried out to a high resolution, because the values of Q vary only by a small amount with large variations in the droplet radius {Figure (4.5)}. Also, the larger size parameters of these larger droplets meant that the Mie computations were extremely slow. So, the Mie efficiencies were calculated only at the mid-bin radii of the 2D-C size bins for the calculation of the infrared properties of the DSDs measured by this instrument.

Mie Efficiencies for Water Droplets (Wavelength 10.84 microns)

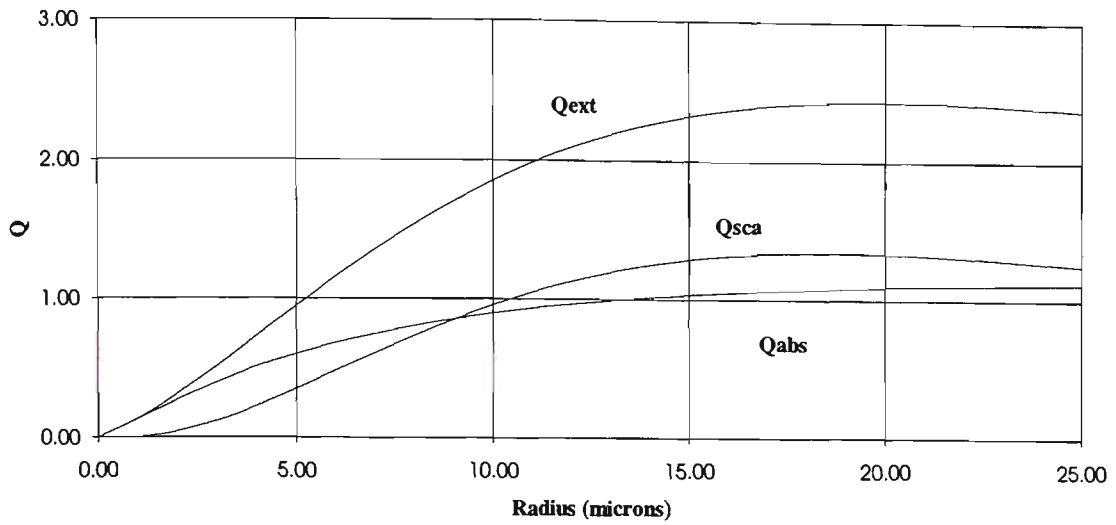


Figure 4.4. Mie extinction, scattering, and absorption efficiencies ($Q_{ex}^{(ir)}$, $Q_{sc}^{(ir)}$, and $Q_{ab}^{(ir)}$), of water droplets, for the infrared wavelength 10.84 μm . It can be seen that the infrared extinction by water droplets with radii near 10 μm , is due to nearly equal amounts of both scattering and absorption.

Mie Efficiencies for Water Droplets (Wavelength 10.84 microns)

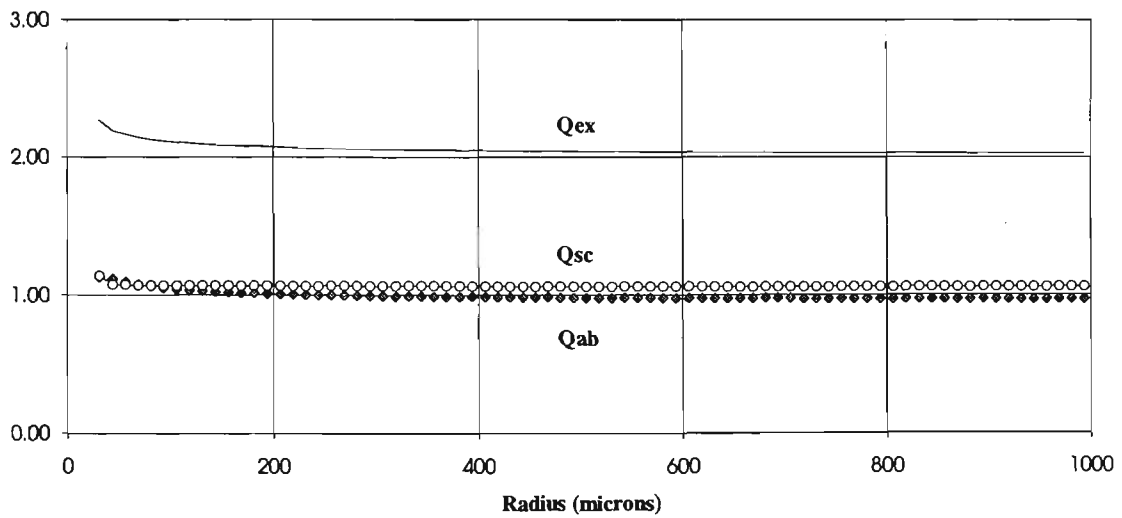


Figure 4.5. Mie extinction, scattering, and absorption efficiencies ($Q_{ex}^{(ir)}$, $Q_{sc}^{(ir)}$, and $Q_{ab}^{(ir)}$) of water droplets, for the infrared wavelength 10.84 μm . In this size range the droplet radii need not be known accurately to determine the (infrared) Mie properties with a high certainty.

4.3.3 Lidar Calibration

4.3.3.1 Introduction

Lidars are often calibrated using a part of the returned signal from the higher troposphere where the cleanest air is expected. At Cape Grim during SOCEX1 the gaps in the clouds were usually too small to allow a reconfiguration of the system to measure the high troposphere, in the time available. So the calibrations were performed on the clean and dry air observed in the 1-2000 m above the cloud tops.

The lidar measurements of 16 July 1993 were calibrated by performing linear regressions of aerosol-free regions of the cloud-free profiles to modelled molecular profiles (Young, 1995). Prior to the calibration the optical properties of the aerosols were determined from the *in situ* measurements by an ASASP (see Chapter 3), to identify a region of the atmosphere free of significant aerosol backscatter which could then be used for the calibration, and also the extinction-to-backscatter ratio of the boundary layer aerosols was required for the analysis of the lidar returns from clouds.

One of the most striking observations in lidar returns from 'clear' air is the tracing out of the depth of the boundary layer by aerosols trapped there (*e.g.*, see the recent study by Flamant *et al.*, 1997). Thus, apart from the aerosol optical properties required for the analysis of the lidar returns, by inspection of the measurements, the ASASP and FSSP measured aerosol concentrations provided a valuable opportunity to verify the form of the lidar height profiles of aerosol backscatter.

4.3.3.2 In Situ Measurements of the Maritime Aerosols

A Forward Scattering Spectrometer Probe (FSSP) and an Active Scattering Aerosol Spectrometer Probe (ASASP) were mounted aboard the F-27 to measure the size distributions of aerosols and cloud droplets during SOCEX1 (Chapter 3). On the afternoon of 16 July 1993 the F-27 tracked along east-west directions over the sea to the west of Cape Grim ('Flight 8'), and during this flight the ASASP probe measured the size distributions of marine aerosols from about 50 m above sea-level to a height of about 2400 metres. The ASASP measurements were not considered reliable in cloud so that where the FSSP measurements showed droplet concentrations greater than 1 cm^{-3} the data were ignored.

The ASASP measured particles of radii between 0.06 - 1.56 μm , in 15 size bins, and the FSSP measured particles with radii from 1 - 23.5 μm , also in 15 size bins. Apart from measurements of cloud droplets, the FSSP also detected larger aerosols beyond the maximum range of the ASASP.

The ASASP measurements were binned into 100 m intervals of height, and the average concentrations and the variabilities were calculated for each bin {Figure (4.6)}. There was a distinct difference in the aerosol concentrations between below 1100 m and above 1100 m; this is about the height of the top of the boundary layer as determined by inspection of the lidar measurements. (See also the height profiles of temperature and mixing ratio determined from measurements aboard the F-27; Chapter 3). Accordingly, the data were separated in the aerosol types: boundary layer aerosols (0-1100 m) and free troposphere aerosols (1100-2500 m). Statistics of the aerosol concentrations measured by the FSSP were calculated similarly {Figure (4.7)}.

It is assumed that the ASASP measurements were of dry particles, due to dehydration of the aerosols as they pass through the instrument (Strapp *et al.*, 1992). However the FSSP does not dry incident particles so that its measured size distributions are assumed faithful reproductions of the aerosols and water droplets as they exist in the atmosphere. Also, the FSSP measurements show an increase in total aerosol concentration up to a height of 900 m. This is consistent with increased numbers of particles moving into the FSSP size range due to swelling as they lift into the atmosphere; this hygroscopic particle growth was also observed in the FSSP observations of Strapp *et al.* (1992). An increase in particle concentration with height may also be discerned from the ASASP measurements in this study, but this increase is much less marked than that of the FSSP, and was ignored in the modelling work (see later).

The manufacturers of the ASASP use latex spheres (refractive index $m = 1.588 - 0i$) for its calibration, and because of this Garvey and Pinnick (1983) noted that the ASASP will undersize haze droplets having the refractive index of water ($m = 1.33 - 0i$). In particular, particles with radii between 0.3 and 0.8 μm will be undersized by $\approx 33\%$. However in this study it is assumed that all the ASASP data represent particles dried before measurement. The larger (dry) particles are mostly NaCl particles with refractive index approximately 1.5, a value closer to the refractive index of the latex spheres used in the calibration of the ASASP.

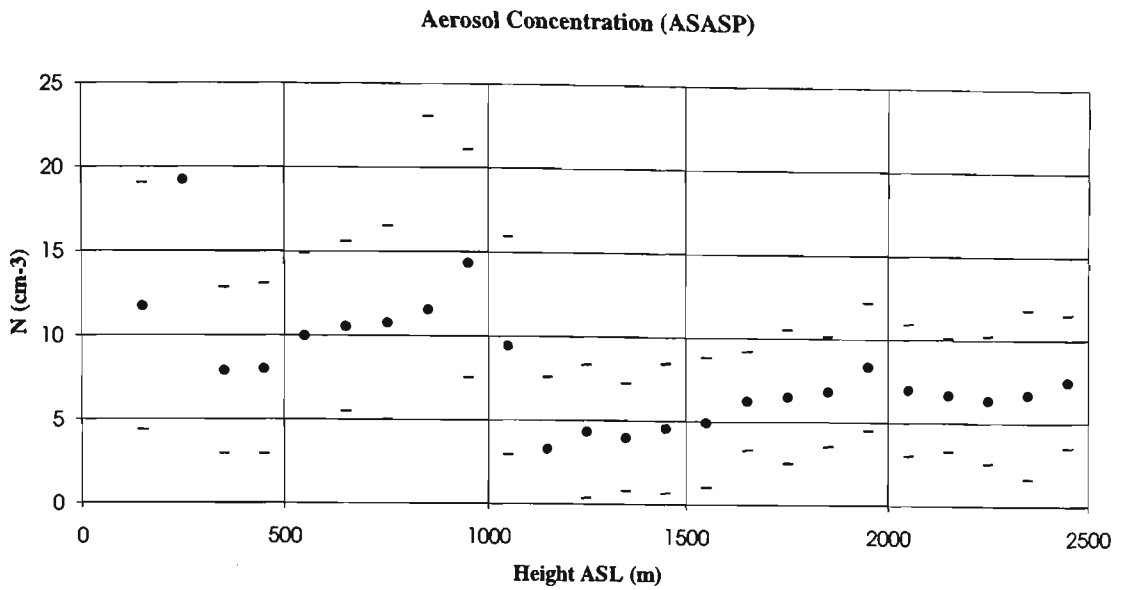


Figure 4.6. Aerosol concentrations ($N \text{ cm}^{-3}$) measured by ASASP and averaged over height intervals of 100 m, versus height m ASL. Measures of variability are indicated by \pm one standard deviation of the measurements (horizontal bars).

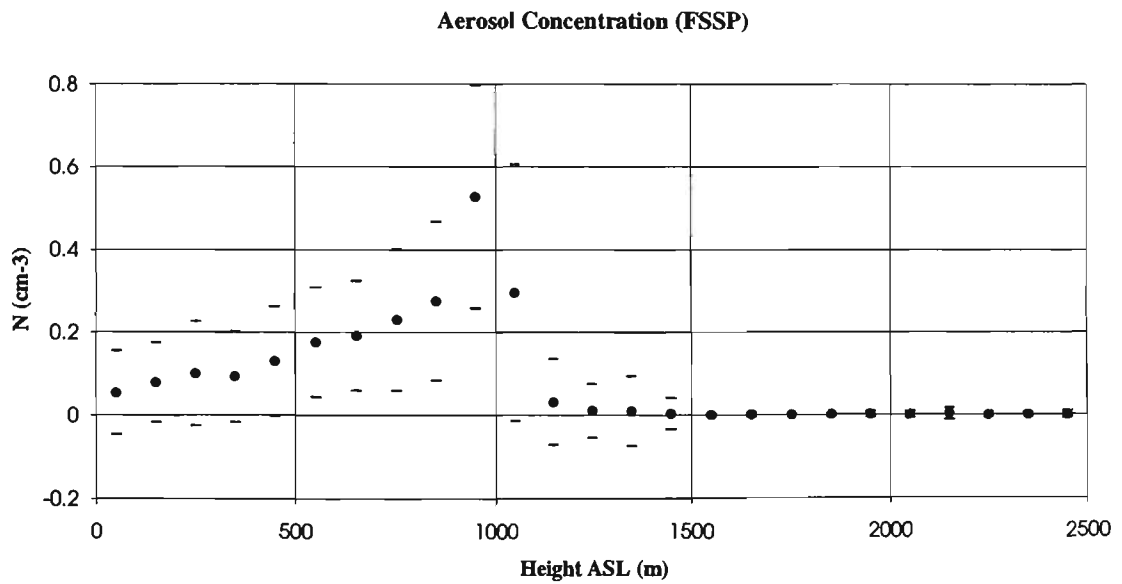


Figure 4.7. Aerosol concentrations ($N \text{ cm}^{-3}$) measured by FSSP and averaged over height intervals of 100 m, versus height ASL. Measures of variability are indicated by \pm one standard deviation (horizontal bars).

4.3.3.3 Measured Aerosol Size Distributions

The total particle concentrations measured by the ASASP and FSSP on flight 8 of 16 July 1993 were separated into three distinct particle size modes: (1) small particles with mode radius less than 0.1 μm , (the 'accumulation' mode), (2) particles with mode radius between 0.1 and 1 μm (the 'coarse' mode), and (3) particles with mode radius between 1 and 10 μm (the large particles). The accumulation and coarse particle modes corresponded reasonably well with those observed by Gras (1991). It will be seen later that the large particle mode, modelled using mainly the FSSP data, was the most significant aerosol type in determining the visible optical depth of the marine boundary layer aerosols for this study. Each particle size mode i was modelled by a lognormal distribution as follows (e.g. Gras *et al.*, 1991);

$$\frac{dN(a)}{d \ln a} = \frac{A_i}{\sqrt{2\pi \ln \sigma_i}} \exp \left\{ \frac{-[\ln(a / a_m)]^2}{2 \ln \sigma_i} \right\} \quad (4.4)$$

where A is the peak particle concentration, a_m is the median radius, and σ determines the spread of the mode. The parameters for each particle mode were obtained by the combination of a least squares technique and trial and error, until the linear correlation coefficients between the measurements and the models were better than 0.99. The correlation coefficients between the boundary layer aerosol measurements and model was 0.9968 for the 29 mid-radii points, and similarly the correlation coefficient between the free troposphere aerosol measurements and the model was 0.9910. The measurements and models for both the boundary layer and free troposphere aerosols are shown in Figure (4.8), and the model parameters for each particle size mode are shown in Tables 4.1 and 4.2 below.

Table 4.1. Model parameters for the size distribution of the boundary layer aerosols.

<i>Parameter</i>	<i>accumulation mode</i>	<i>coarse mode</i>	<i>large particle mode</i>
$A \text{ cm}^{-3}$	480	0.220	0.0904
$r_m \text{ } \mu\text{m}$	0.0201	0.297	2.00
$\sigma \text{ } \mu\text{m}$	1.44	1.22	2.08

Table 4.2. Model parameters for the size distribution of the free troposphere aerosols.

<i>Parameter</i>	<i>accumulation mode</i>	<i>coarse mode</i>	<i>large particle mode</i>
$A \text{ cm}^{-3}$	106	0.0419	0.00867
$r_m \text{ } \mu\text{m}$	0.0205	0.403	3.64
$\sigma \text{ } \mu\text{m}$	1.54	1.16	32.8

Aerosol Size Distributions

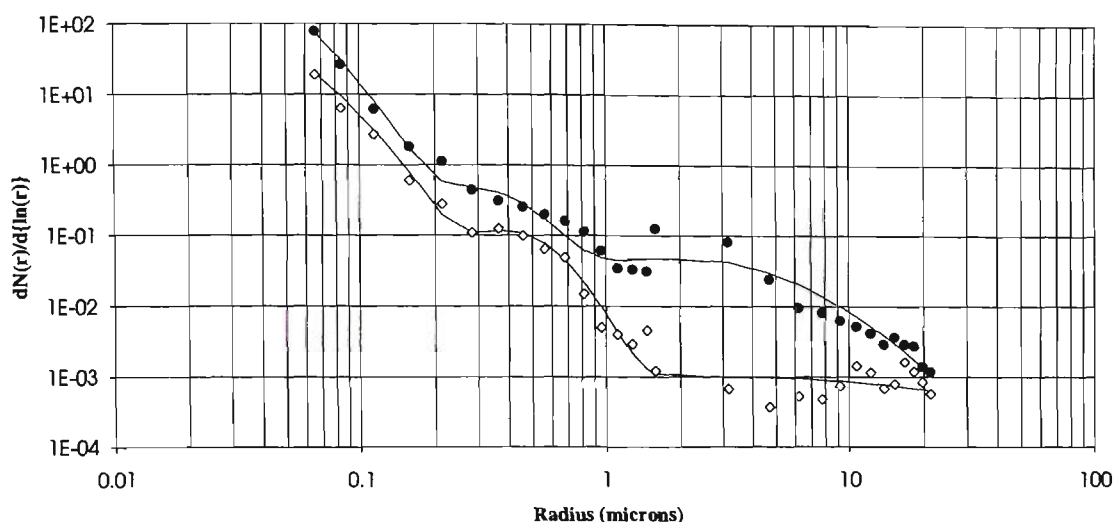


Figure 4.8. Measured aerosol size distributions in the boundary layer (filled circles), and in the free troposphere (open diamonds). The modelled size distributions for both the boundary layer and free troposphere measurements are shown by solid lines.

4.3.3.4 Composition and Refractive Indices of the Measured Aerosols

Studies of maritime aerosols, such as those by Bigg (1980), Gras and Ayers (1983), and Gras (1991), indicate that these measured (dry) particles are composed mainly of ammonium sulfates and sea salt. The sea salt is primarily NaCl. The sulfate particles are most commonly described as ammonium sulfate ($(\text{NH}_4)_2\text{SO}_4$), however little is known about their precise chemical composition. Cainey (1997) measured marine aerosols over a 30-month period at Cape Grim, and found that the ratio of ammonium ions to sulfate ions in the accumulation mode aerosols was about 1.25 in the summer, and lower than unity in the other seasons (0.80 - 0.95). Thus it appears that the accumulation mode aerosols observed near Cape Grim during the winter of 1993 are likely to be ammonium bisulfate (NH_4HSO_4) particles.

The real parts of the refractive indices (RIs) of the solid components of the marine aerosols are known reasonably well at some wavelengths (Table 4.3), but the complex parts of the RIs are not known precisely. The complex part of the RI for ammonium bisulfate was taken as 10^{-7} , because Toon *et al.* (1976) gave such a value for ammonium sulfate. The complex parts of the RIs of both NaCl and ammonium sulfate are upper limits based on extrapolation. (The real parts of the refractive indices of these particles tends to decrease slightly with an increase in wavelength). The RI for water was

determined from a linear interpolation between the values at 550 nm and 575 nm obtained from Hale and Querry (1973). The RIs for ammonium sulfate and sulfuric acid have not been used in the Mie calculations (see later), but have been added to Table for comparison.

Table 4.3. Refractive indices of some substances.

Substance:	Wavelength:	RI (real):	RI (complex):	Reference:
ammonium-bisulfate	589 nm	1.473	10^{-7}	CRC Handbook, (1982-1983)
ammonium-sulfate	535 nm	1.53	10^{-7}	Toon <i>et al.</i> (1976)
salt (NaCl)	500 nm	1.55	10^{-7}	Toon <i>et al.</i> (1976)
salt (NaCl)	580 nm	1.544	10^{-7}	Tang (1996)
water	532 nm	1.3337	1.50×10^{-9}	Hale and Querry, (1973)
25% sulfuric acid	556 nm	1.366	3×10^{-8}	Palmer and Williams (1975)
50% sulfuric acid	556 nm	1.397	2×10^{-8}	Palmer and Williams (1975)

4.3.3.5 Effect of Humidity

Changes in ambient humidity affect aerosol size and composition, in turn affecting the aerosol optical properties, so that it is important that the modelled aerosol properties reflect this. The height profile of relative humidity derived from airborne measurements shows an increase in the relative humidity from about 65% near the ground to over 90% near cloud base (see Chapter 3). Some marine aerosols form as droplets from bubbles bursting at the sea surface (*e.g.* Twomey, 1977), and the relative humidity would have to drop to below about 40% for these droplets to crystallise in the atmosphere, so it is assumed that in the boundary layer at least, the larger aerosols ($\approx 0.1 \mu\text{m} < a < 1 \mu\text{m}$) exist as liquid droplets only.

The particle growth factors (a/a_0) used to swell the modelled (dry) aerosol size distributions to values expected in the atmosphere are shown in Table 4.4. The growth factors for ammonium sulfate have not been used in the calculations but are added to the table for comparison with the growth factors of ammonium bisulfate.

Table 4.4. Effect of humidity on the particle growth factor (a/a_0).

Substance:	50%	60%	70%	80%	90%	95%	References:
ammonium bisulfate	1.24	1.30	1.41	1.55	1.84	2.35	Tang and Munkelwitz (1977)
ammonium sulfate	1.32	1.34	1.38	1.47	1.74	2.15	Tang (1996)
NaCl	1.67	1.73	1.83	2.00	2.40	2.92	Tang <i>et al.</i> (1977)

The refractive index for each particle mode was weighted according to the particle growth as follows (e.g. d’Almeida *et. al.*, 1991):

$$n = n_w + (n_o - n_w) \left(\frac{a_o}{a} \right)^3, \quad (4.5)$$

where n_w is the refractive index of water, and n_o is the refractive index of the dry particle. The results for the effect of humidity on the real parts of the refractive indices (Table 4.3) are shown below in Table 4.5.

Table 4.5. Effect of humidity on the real part of the refractive index.

Rel. Hum.	50%	60%	70%	80%	90%	95%
amm-bisulf	1.407	1.397	1.383	1.371	1.356	1.344
amm-sulf	1.419	1.415	1.408	1.395	1.371	1.353
NaCl	1.369	1.366	1.361	1.354	1.346	1.340

The complex refractive indices were calculated similarly and shown below in Table 4.6.

Table 4.6. Effect of humidity on the complex part of the refractive index.

Rel. Hum.	50%	60%	70%	80%	90%	95%
amm-bisulf	5E-08	5E-08	4E-08	3E-08	2E-08	9E-09
amm-sulf	5E-08	4E-08	4E-08	3E-08	2E-08	1E-08
NaCl	2E-08	2E-08	2E-08	1E-08	9E-09	5E-09

In preparation for the Mie calculations the aerosol size distribution models were created with the radius boundaries for each particle mode shown in Table 4.7. Each particle mode had 99 size bins.

Table 4.7. Ranges of radii sizes used to model aerosol size distributions.

Particle Mode	Radius Boundaries (µm)	Size increment (µm)
accumulation	0.06 - 0.6	≈ 0.005455
coarse	0.06 - 2	≈ 0.019596
large	0.20 - 20	0.2

The particle growth factors (see Table 4.4) were used to individually swell the accumulation and coarse particle modes but not the large particle mode, because the large particle mode was modelled primarily from the FSSP measurements which did not dry the particles before measurement.

4.3.3.6 Optical Properties of the Marine Boundary Layer Aerosols

The optical properties of the boundary layer aerosols were calculated with the modelled large particle mode treated in two ways: (1), the large particles as droplets of salt (NaCl) solution (‘Large1’), (2) the large particles as pure water droplets (‘Large2’). The results of the Mie calculations for the boundary

layer aerosols are shown in Table 4.8. In the table, for 5 humidities, are shown the optical properties of the individual modelled particle modes and the total aerosol optical properties. The properties 'Total1' were calculated from the accumulation mode, coarse mode, and 'Large1' mode, and 'Total2' was calculated similarly, except using the large particle mode 'Large2'. The calculated properties are the particle concentration (N), and the visible properties: the extinction coefficient (σ_{ex}), the absorption coefficient (σ_{ab}), the backscatter coefficient (β), and the extinction-to-backscatter ratio (S).

Note that in all cases the total aerosol optical properties are most heavily influenced by the properties of the large particle mode - even though the concentrations of these large aerosols measured by the FSSP are much less than the concentrations of the smaller aerosols measured by the ASASP. This is because the integrand in equation (4.2) peaks in this size range.

Table 4.8. Optical properties of the boundary layer aerosols.

Particle mode:	Accum. (amm.- bisulf.)	Coarse (NaCl)	Large1 (NaCl)	Large2 (pure water)	Total1 (Large1)	Total2 (Large2)
RH=60%						
N (cm^{-3})	27.99	0.49	0.10	0.10	28.59	28.59
σ_{ex} (m^{-1})	4.69E-07	1.67E-06	1.02E-05	1.02E-05	1.23E-05	1.23E-05
σ_{ab} (m^{-1})	2.35E-13	5.78E-13	3.97E-11	3.02E-12	4.05E-11	3.83E-12
β ($\text{m}^{-1}\text{sr}^{-1}$)	1.09E-08	5.05E-08	6.29E-07	5.40E-07	6.90E-07	6.02E-07
S (sr)	43.17	33.10	16.23	18.88	17.89	20.51
RH=70%						
N (cm^{-3})	27.99	0.49	0.10	0.10	28.59	28.59
σ_{ex} (m^{-1})	6.28E-07	1.84E-06	1.02E-05	1.02E-05	1.27E-05	1.27E-05
σ_{ab} (m^{-1})	2.45E-13	6.80E-13	3.80E-11	3.02E-12	3.89E-11	3.95E-12
β ($\text{m}^{-1}\text{sr}^{-1}$)	1.26E-08	5.96E-08	5.82E-07	5.40E-07	6.54E-07	6.13E-07
S (sr)	49.87	30.80	17.52	18.88	19.36	20.68
RH=80%						
N (cm^{-3})	27.99	0.49	0.10	0.10	28.59	28.59
σ_{ex} (m^{-1})	8.91E-07	2.14E-06	1.02E-05	1.02E-05	1.32E-05	1.32E-05
σ_{ab} (m^{-1})	2.50E-13	4.41E-13	1.85E-11	3.02E-12	1.92E-11	3.71E-12
β ($\text{m}^{-1}\text{sr}^{-1}$)	1.49E-08	7.77E-08	5.38E-07	5.40E-07	6.31E-07	6.33E-07
S (sr)	59.76	27.48	18.96	18.88	20.98	20.90
RH=90%						
N (cm^{-3})	27.99	0.49	0.10	0.10	28.59	28.59
σ_{ex} (m^{-1})	1.70E-06	2.92E-06	1.02E-05	1.02E-05	1.48E-05	1.48E-05
σ_{ab} (m^{-1})	2.91E-13	6.83E-13	1.67E-11	3.02E-12	1.77E-11	4.00E-12
β ($\text{m}^{-1}\text{sr}^{-1}$)	2.04E-08	1.32E-07	5.27E-07	5.40E-07	6.79E-07	6.93E-07
S (sr)	83.31	22.11	19.37	18.88	21.82	21.39
RH=95%						
N (cm^{-3})	27.99	0.49	0.10	0.10	28.59	28.59
σ_{ex} (m^{-1})	4.22E-06	4.13E-06	1.02E-05	1.02E-05	1.86E-05	1.86E-05
σ_{ab} (m^{-1})	2.89E-13	6.80E-13	1.15E-11	3.02E-12	1.25E-11	3.99E-12
β ($\text{m}^{-1}\text{sr}^{-1}$)	4.08E-08	2.17E-07	5.38E-07	5.40E-07	7.96E-07	7.98E-07
S (sr)	103.51	19.03	18.96	18.88	23.31	23.24

4.3.3.7 Optical Properties of the Free Troposphere Aerosols

The large particle mode in the free troposphere aerosol models was also treated in two ways: (1) the large particles were assumed dry salt (NaCl) particles (see the data labelled 'Dry' in Table 4.9), (2) the large particles were assumed salty water droplets, with the droplets formed at about the maximum measured relative humidity observed in the free troposphere between the heights 1500 - 3000 (m), 50% (see the data labelled 'RH=50%' in Table 4.9).

Table 4.9. Optical properties of the free troposphere aerosols.

Particle Mode:	Accumulation (amm.-bisulfate)	Coarse (NaCl)	Large (NaCl)	total
Dry				
N (cm ⁻³)	8.27E+00	1.09E-01	3.53E-03	8.39E+00
σ _{ex} (m ⁻¹)	9.12E-08	2.08E-07	1.02E-06	1.32E-06
σ _{ab} (m ⁻¹)	7.81E-14	3.04E-13	3.08E-11	3.12E-11
β (m ⁻¹ sr ⁻¹)	2.45E-09	2.70E-08	1.02E-07	1.31E-07
S (sr)	37.22	7.72	10.03	10.07
RH=50%				
N (cm ⁻³)	8.27E+00	1.09E-01	3.53E-03	8.39E+00
σ _{ex} (m ⁻¹)	1.77E-07	5.27E-07	1.02E-06	1.73E-06
σ _{ab} (m ⁻¹)	7.78E-14	2.30E-13	5.68E-12	5.99E-12
β (m ⁻¹ sr ⁻¹)	3.61E-09	2.22E-08	6.33E-08	8.90E-08
S (sr)	49.02	23.76	16.18	19.40

Here also, the total aerosol optical properties extinction, absorption, and backscatter, are most heavily influenced by the properties of the large moist aerosols.

4.3.3.8 Method for Lidar Calibration Using a Reference Molecular Atmosphere

The calibration procedure described here is exactly that of Young (1995) for an aerosol layer underlying a cloud, designed specifically for this dataset. First the retrieval of the system constant (C) is illustrated using a simple example. The equation for a lidar signal backscattered from a purely molecular atmosphere is,

$$V(z) = Cz^{-2} \beta_m(z) T_m^2(0, z) + V_o. \quad (4.6)$$

A linear regression performed between two heights, of equation (4.6) representing the measured signal against equation (A2.47) representing the modelled molecular profile, results in the retrieval of the system constant (C) and the signal offset (V_o). Primarily, this is what is done when calibrating a lidar return on a known atmosphere. The calibration of real signals is complicated by backscatter and

attenuation by atmospheric particles other than molecules and also by the region of incomplete overlap near to the lidar.

The lidar returns from the marine boundary layer of 16 July 1993 showed enhanced backscatter by moist aerosols, which were present there in greater concentrations than in the free troposphere. This was obvious also from the ASASP measurements of the aerosols (see section 4.3.2.2, and Figures 4.6 and 4.7). Thus the lidar signals could not be calibrated using the boundary layer part of the profile using the above method. The analysis of the ASASP data showed the backscatter by aerosols in the air in the first 2000 m above the boundary layer to be, at most, a tenth of the Rayleigh backscattering coefficient in the same region. Thus this region of air above the boundary layer was free of significant backscatter by aerosols and was used for the calibration. The influence on the lidar calibration of this small amount of aerosol backscatter in the free troposphere is investigated in detail later.

The lidar signal profile from cloud-free air in the boundary layer is,

$$V(z) = Cz^{-2}[\beta_m(z) + \beta_a(z)]T_m^2(0, z)T_a^2(0, z) + V_o, \quad (4.7)$$

where the subscript 'a' stands for aerosols. At the top of the boundary layer (z_{TBL}) and above equation (4.7) is written as,

$$V(z) = Cz^{-2}\beta_m(z)T_m^2(0, z)T_a^2(0, z_{TBL}) + V_o. \quad (4.8)$$

A linear regression of the measured profiles described by (4.8) to the calculated molecular profile, {equation (A2.47)}, over the range z_{TBL} to a range 1 or 2 km above the boundary layer, delivered the offsets V_o and the gradients

$$CT_a^2(0, z_{TBL}) \quad (4.9)$$

(Young, 1995).

The aerosol extinction profile was calculated from z_{TBL} down to the lowest range of complete lidar overlap (z_{OVL}) via an analytical solution to the lidar equation (Fernald; 1984). The boundary layer aerosol extinction-to-backscatter ratio (S_a) was assumed constant and determined from the

analysis of measurements of the aerosols (see section 4.3.2.6). The system constant attenuated by the aerosol transmittance between the lidar and the overlap height was then obtained,

$$CT_a^2(0, z_{OVL}). \quad (4.10)$$

To calibrate the lidar cloud signal profiles, the $T_a^2(0, z_{OVL})$ determined for the cloud-free profiles was assumed to be the same as that for the cloud signal profiles, and variations in this transmittance were assumed to be negligible. The quantity (4.10) was then used to initiate forward solutions for backscatter (Fernald, 1984) up to cloud base in the cloudy profiles to determine the attenuation of the cloud profiles by boundary layer aerosols.

4.3.3.9 Lidar Calibration Constant Obtained During Cloud-Free Periods

There was some pre-processing of the lidar profiles prior to the analysis of all the lidar returns. Each lidar return (or 'shot') was stored on a digital oscilloscope at two different sensitivities (Young, 1995). For example, the profile numbers 29 and 30 (see Table 4.10) are both profiles for a single lidar return (or 'shot') and were merged into a single profile. This increased the dynamic range of the lidar, resulting in the capture of both the full amplitude of the profile of attenuated cloud backscatter, as well as the best signal for the boundary layer aerosol backscatter and the small signal in the upper region (higher altitudes) of the profile. This process improves the lidar signal-to-noise ratio in the upper region of the profile by using more digitiser bits to record the data in these regions. The two profiles for each lidar return were then merged into a single profile.

The lidar returns of the afternoon of 16 July 1993 contain three periods where the returns are almost entirely clear of backscatter by clouds (Table 4.10), and these cloud-free profiles were used for the lidar calibration by the method described in the previous section. First, the five merged clear profiles 29-30, 31-32, 33-34, 35-36, and 37-38 were averaged to form a single averaged merged profile, 'clear profile #1'. Similarly, the other cloud-free profiles were merged and averaged to form the 'clear profiles #2 and #3'.

Table 4.10. Cloud-free periods used for lidar calibration.

Clear (averaged) profile #	Clear period	Profile numbers	Number of shots
1	14:45:02 - 14:50:03	29-37	5
2	15:33:25 - 15:44:00	453-503	26
3	16:08:23 - 16:09:23	679-691	7

The cloud-free profiles were calibrated (fitted to the clear air reference profile) in the region where scattering was a minimum with an assumed aerosol loading of zero. The height region chosen for this purpose was 1250-2000 (m) and contained 252 samples for all three profiles. (Recall that the three profiles are averages of many shots - see Table 4.10). The lower height boundary, 1250 m, was chosen to avoid aerosol backscatter near the top of the boundary layer. Inspection of the lidar returns and calculations using the *in situ* measurements showed there was some increased aerosol backscatter between 2000 - 3000 (m), so the upper bound of the calibration region, 2000 (m), was chosen well below the top height in the profiles of just over 3000 (m).

Then, to complete the lidar calibration the transmittance of the boundary layer aerosols was determined and this was done by assuming a constant S_a , and computing profiles of the backscatter coefficient using a backward solution for backscatter (Fernald, 1984). The boundary values at the height 1250 (m) used for the backscatter solutions are shown in Table 4.11 - the molecular transmittance indicated by subscript 'm' is also included in the values of this table.

Initially a boundary value of backscatter of zero was chosen for the clear profile #1, however the resulting calculated aerosol backscatter profile was negative (and not due to noise or uncertainties in the calculation) over a small region near the top of the boundary layer. Obviously the backscatter cannot be negative, indicating there was significant aerosol backscatter above the boundary layer in this case. It is conjectured that the drop in the level of aerosol backscatter near the top of the boundary layer was caused by entrainment of aerosol-free air subsiding from the free troposphere. The region of entrainment was defined as lying between the heights 980-1080 metres, and the solution boundary value adjusted until the calculated backscatter in the entrainment region became not significantly different from zero. The final solution for backscatter for this profile is shown in Figure (4.9).

Table 4.11. Lidar calibration parameters for the clear periods #1 - #3.

Clear (averaged) profile	Calibration region (m)	β_a ($m^{-1}sr^{-1}$)	Regression coefficient	$CT_{am}^2(0, z_{OVL})$	Rel. err., $CT_{am}^2(0, z_{OVL})$
1	1250-2000	1.40×10^{-7}	0.9931	0.1787	4.19%
2	1250-2000	0	0.9991	0.1786	1.54%
3	1250-2000	0	0.9973	0.1799	2.57%

Clear (averaged) profiles #1 and #3 were averaged with only a few data (5 and 7 shots respectively), so profile #2 (26 shots) was used to investigate the sensitivities of the retrieved system constants to the selection of backscatter boundary values, and also to selection of the aerosol extinction-to-backscatter ratios (S_a). The values and variations of S_a (Table 4.12) and the boundary values for the backscatter coefficients (Table 4.13) were selected following inspection of the optical properties calculated from the ASASP and FSSP measurements of the aerosols (section 4.3.3.6). These sensitivities were calculated by varying the various parameters over the ranges calculated in 4.3.3.6 and recalculating the solution profiles.

Table 4.12. Sensitivity of system constant with selection of boundary value (β_a).

β_a ($\text{m}^{-1}\text{sr}^{-1}$)	$\text{CT}_{\text{am}}^2(0, z_{\text{OVL}})$	$\Delta(\text{CT}^2)/(\text{CT}^2)$
-1×10^{-7}	0.1775	-0.624%
-5×10^{-7}	0.1780	-0.312%
-1×10^{-8}	0.1785	-0.063%
0	0.1786	-
$+1 \times 10^{-8}$	0.1787	+0.062%
$+5 \times 10^{-7}$	0.1792	+0.311%
$+1 \times 10^{-7}$	0.1797	+0.623%

Some of the boundary values in Table 4.12 are negative - this is due to the fact that the lidar profiles were sometimes negative in the calibration region due to noise.

Table 4.13. Sensitivity of system constant with selection of S_a .

S_a (BL)	$\text{CT}_{\text{am}}^2(0, z_{\text{OVL}})$	Rel. Error	S_a (FT)	$\text{CT}_{\text{am}}^2(0, z_{\text{OVL}})$	Rel. Error
18.5	0.178344	-0.1411%	29	0.178593	-0.00168%
19.5	0.178596	-	35	0.178596	-
20.5	0.178847	-0.1405%	41	0.178598	+0.00112%

It is evident that the errors due to inaccurate boundary values (β_a), or poor estimates of S_a either for the Boundary Layer (BL) or Free Troposphere (FT) aerosols were small; the combined relative errors are less than 1%. Taking a weighted mean and adding the relative errors the final result for the lidar system constant is,

$$\text{CT}_{\text{am}}^2(0, z_{\text{OVL}}) = 0.179 \pm 2.2\%.$$

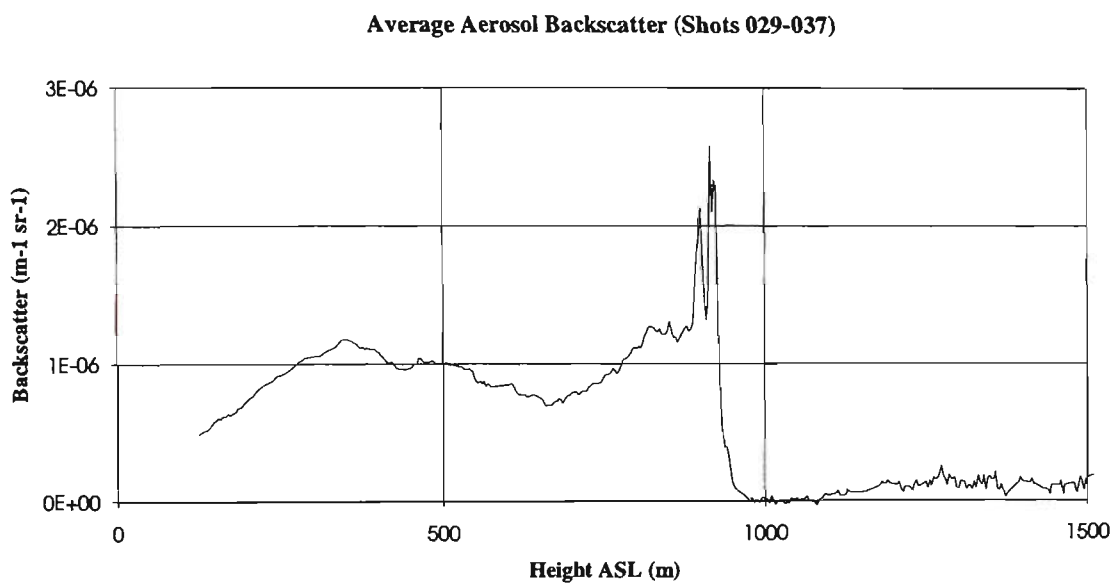


Figure 4.9. Aerosol backscatter ($\beta_a \text{ m}^{-1} \text{ sr}^{-1}$) calculated from an average of the 5 lidar shots 29 - 37, for the cloud-free period #1: *i.e.* 14:45:02 - 14:50:03. These shots were taken soon after a period of several hours of low cloud and rain at Cape Grim, and taken just prior to the stratocumulus cloud measurements studied for this thesis.

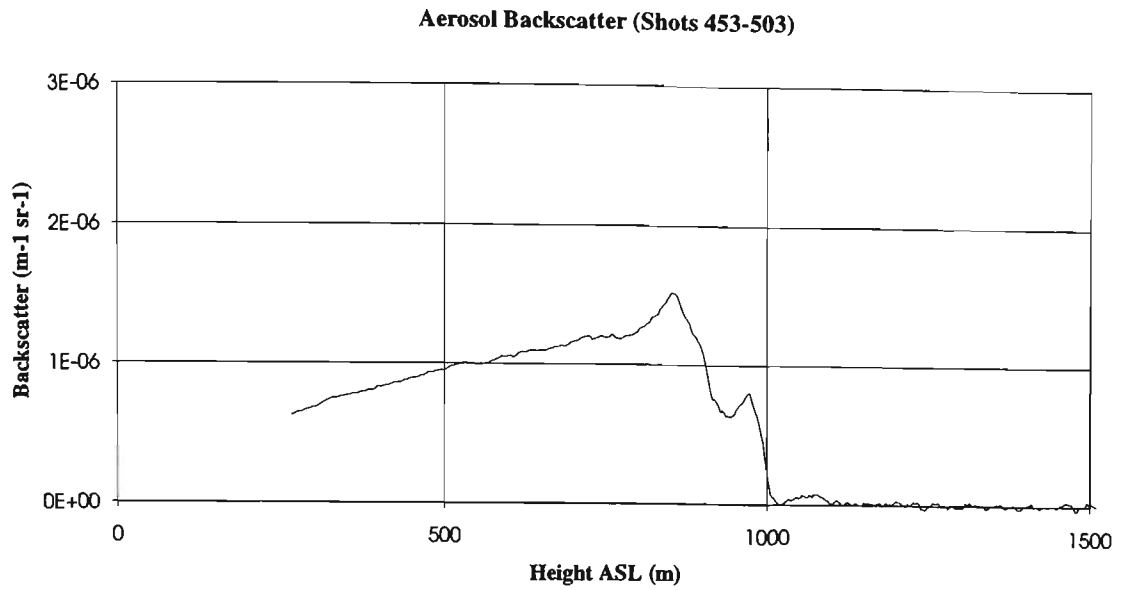


Figure 4.10. Aerosol backscatter ($\beta_a \text{ m}^{-1} \text{sr}^{-1}$) calculated from an average of the 26 lidar shots 453 - 503, for the cloud-free period #2: *i.e.* 15:33:25 - 15:44:00. These lidar returns from cloud-free air were the most important for calibration of the lidar.

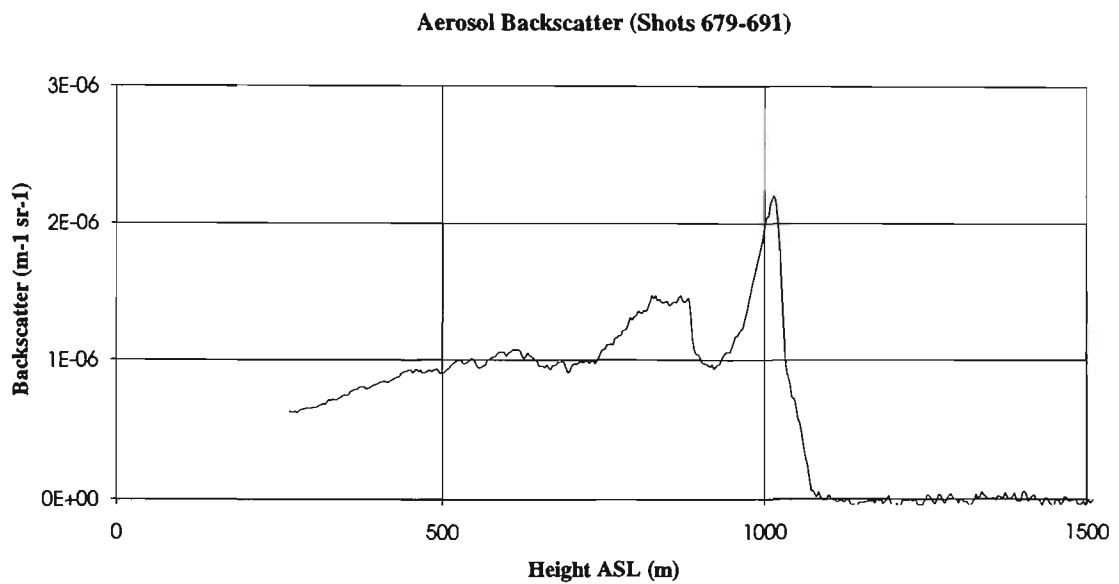


Figure 4.11. The aerosol backscatter ($\beta_a \text{ m}^{-1} \text{sr}^{-1}$) calculated from an average of the 7 lidar shots 679 - 691, for the cloud-free period #3 (16:08:23 - 16:09:23): these lidar returns from cloud-free air were studied for the lidar calibration.

4.3.4 Combined Lidar and Infrared Radiometer Data

4.3.4.1 Introduction

The methods for reduction and analysis of the data required for the LIRAD analysis technique are presented here in the same order in which they were performed, which progressed as follows: the total measured infrared downward radiances (L_T) were determined (section 4.3.4.2). The values of lidar measured χ' were determined from which an initial estimate of $(2\eta S)^{-1}$ was obtained (section 4.3.4.3). The Clear Sky Radiances (CSRs) measured by the infrared radiometer were determined (section 4.4.4.4). These measured CSRs were compared to Water Vapour Paths (WVPs) measured by a MicroWave Radiometer (MWR), in order to parameterise the cloudless radiance as a function of time (section 4.3.4.5). The CSRs and WVPs were calculated from the aerological profiles determined from the airborne (F-27) measurements. These calculated CSRs and WVPs were compared with the measured values, and a profile of the infrared transmittance of the clear sky was calculated using the results of this comparison (section 4.3.4.6). With the profiles of infrared radiance and transmittance of the clear sky so obtained, the cloud radiances were then separated from the total measured radiances, and the cloud radiances and profiles of χ were then combined in the LIRAD analysis technique (section 4.3.4.8).

4.3.4.2 Measured Total Infrared Radiances

The CSIRO MarkII infrared radiometer ("MarkII") and its operation during SOCEX1 is described in Chapter 3. The MarkII radiometer is the same instrument used in the studies of high clouds by Platt *et al.* (1984) and Platt *et al.* (1987). The analysis of the MarkII measurements is discussed in some depth by Platt *et al.* (1998), and is described here only briefly.

The incoming radiance to the MarkII is chopped with a reference radiance as in the original MarkI radiometer (Platt, 1971). By synchronous detection the measured DC signal (v_s) of the MarkII is proportional to the difference between the incoming radiance and the radiance of a reference blackbody, which is maintained at a temperature of near 40°C. Thus the signal v_s increases when the radiometer is viewing colder targets.

The measured radiance L_g was calculated by

$$L_g = L_o \frac{V_g}{V_{cal}} (L_o - L_{cal}), \quad (4.11)$$

where L_o is a 'null point' radiance obtained for $V_g = 0$, V_{cal} is the calibration voltage, and L_{cal} is the calibration radiance. The calibration radiance, or 'zero' radiance for this dataset, was obtained by swivelling the MarkII downwards to view a dewar filled with liquid nitrogen. A cone sat in the base of the dewar, and the cone and interior of the dewar were painted matt black to simulate a blackbody at liquid nitrogen temperatures.

The MarkII was swivelled to view the liquid nitrogen about every hour to counter long-term drifts in the calibration-signals. One file of data acquired on 16 July 1993 contained six calibration cycles and these were easily distinguished from the atmospheric signal. The radiances were calculated once all the liquid nitrogen and electrical-zero signals were identified and separated from the atmospheric signal. Any drift in the electronics was accounted for by assuming a linear drift between the hourly calibration-cycles, and L_{cal} was determined between these times by interpolation.

4.3.4.3 Integrated Attenuated Cloud Backscatter (χ')

To calculate the integrated attenuated backscatter of the clouds (χ') the raw cloud profiles had to be reduced to profiles of χ . To do this, first, the signal offsets were determined from the last 50 - 100 points of each raw profile. In this region of the profiles, about 2000 m above the heights of the cloud signals, the atmospheric signals were below the measurement limits of the digitiser. Once determined, the signal offsets were subtracted from each profile.

The backscatter by boundary layer aerosols and stratocumulus cloud droplets varies over about three orders of magnitude. In order to record the profiles by both these scattering species optimally, the dynamic range of the lidar was increased by recording profiles of different sensitivities for each shot (as per section 4.3.2.10). Once the signal-offsets of the lidar returns from the clouds were determined and subtracted from the profiles, each of these pairs of profiles were merged into a single profile by a simple scaling technique. These (merged) profiles were then range-corrected, and scaled by the system constant determined in section 4.3.2.10. (Based on the calibrations, the system constant was assumed unchanged over the course of the day).

These profiles of χ also contained attenuated backscatter by air molecules and aerosols. The expression for χ in the height region in the interior of a cloud is described by,

$$\chi(z) = [\beta_m(z) + \beta_c(z)] T_m^2(0, z) T_a^2(0, z_b) T_c^2(z_b, z). \quad (4.12)$$

So, prior to calculating χ' from these profiles it was first necessary to remove the aerosol and molecular terms from χ . The two-way aerosol transmittance up to cloud base was determined for each profile using a forward solution for backscatter (Fernald, 1984) (4.3.2.8), using the calibration constant for the boundary value (4.3.3.10), and the value of S_a determined from the analysis of the ASASP and FSSP measurements of the boundary layer aerosols (4.3.3.6).

$$\chi_{mc}(z) = [\beta_m(z) + \beta_c(z)] T_m^2(0, z) T_c^2(z_b, z). \quad (4.13)$$

Expansion of (4.13) shows the molecular terms cannot be completely separated from the cloud terms:

$$\chi_c(z) = \frac{\chi_{mc}(z)}{T_m^2(0, z)} - \beta_m(z) T_c^2(z_b, z). \quad (4.14)$$

To address this problem two approximations were used, one an underestimate of χ and the other an overestimate. The underestimate is (superscript '1'),

$$\chi_c^{(1)}(z) \approx \frac{\chi_{mc}(z)}{T_m^2(0, z)} - \beta_m(z), \quad (4.15)$$

and the overestimate (superscript '2'),

$$\chi_c^{(2)}(z) \approx \frac{\chi_{mc}(z)}{T_m^2(0, z)}. \quad (4.16)$$

Values for the integrated attenuated backscatter (χ') were then determined by both approximations by integrating over the cloud profiles of χ . Both approximations estimated χ' accurately (to within a few percent), because over most of the cloud profiles β_c is 2-3 orders of magnitude greater than β_m . The errors in χ' calculated by these approximations were estimated by comparing the χ' values calculated from both approximations to the mid-values. The approximations differed from the mid-values by an average of 1.9% for the thin clouds, (those with total infrared radiances of less than $2.5 \text{ Wm}^{-2}\text{sr}^{-1}$), and by an average 0.6% for the thicker clouds, (those with total infrared radiances greater than $2.5 \text{ Wm}^{-2}\text{sr}^{-1}$).

¹). The choice of the cut-off radiance of $2.5 \text{ (Wm}^{-2}\text{sr}^{-1}\text{)}$ was arbitrary, and made following an inspection of the measured radiances - see Figures 4.12 and 4.13. In conclusion, the uncertainty introduced in the calculation of χ' by taking the mid-values between equations (4.23) and (4.24) was small (a maximum uncertainty of $\approx 2\%$ for some of the data).

Having obtained values for χ' the next and obvious step was to identify the values of χ' for the thickest of the clouds, from which a value for $(2\eta S)^{-1}$ could be retrieved. We recall that as

$$\tau \rightarrow \infty, \chi' \rightarrow \frac{1}{2\eta S}. \quad \{\text{see equation (2.31)}\}$$

Again, the arbitrary cut-off measured total radiance of $2.5 \text{ Wm}^{-2}\text{sr}^{-1}$ was used to identify the thicker clouds. For radiances greater than this cut-off radiance the maximum χ' was

$$\chi'_{\max} = 0.0344 \pm 2.2\%, \quad (4.17)$$

where the uncertainty is \pm one standard deviation {see Figure (4.13)}. Note that this is an initial estimate of the maximum χ' only: a more accurate value is retrieved later. Adding the uncertainty due to the molecular terms, the final uncertainty is $\pm 4\%$. The boundaries of these final uncertainties are shown in Figure (4.13), which is an expanded part of the plot shown in Figure (4.12). A value of $0.0344 \pm 4\%$ for $(2\eta S)^{-1}$ leads to a value of ηS of $14.5 \pm 0.58 \text{ sr}$, values which agree well with the results of Young (1995): $\eta S = 13.6 \pm 1.36$, which was obtained for a single thin cloud profile from the same dataset.

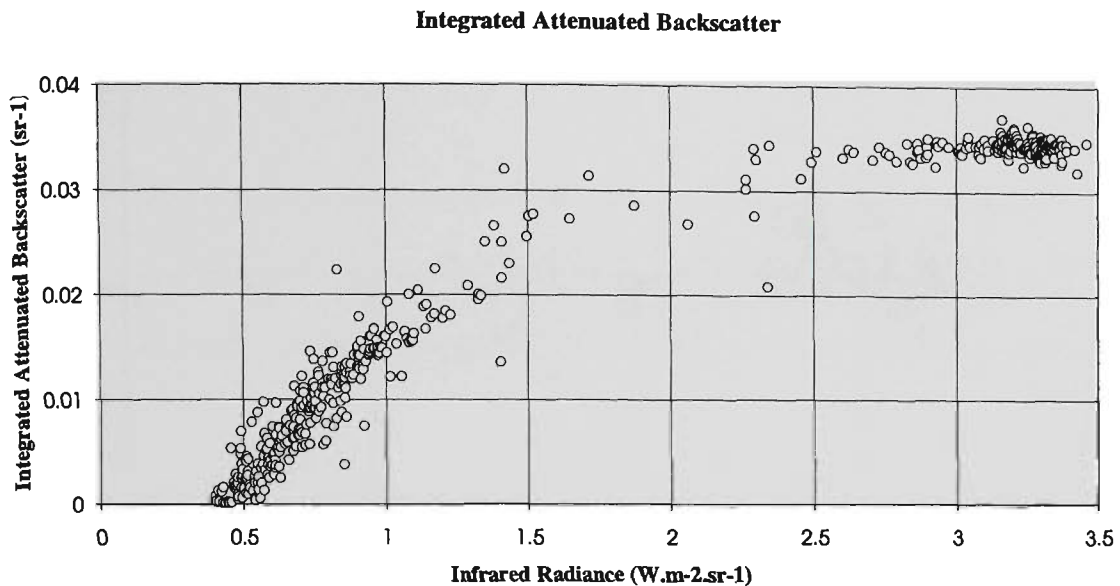


Figure 4.12. Integrated attenuated backscatter (χ' sr⁻¹) versus measured total infrared radiances. The values of χ' reach a maximum at ≈ 0.035 sr⁻¹ for radiances of greater than ≈ 2.5 W m⁻² sr⁻¹.

The value of ηS obtained from the thick clouds was then compared to Deirmendjian's (1969) theoretical result for the modelled cloud, type C1; $S = 19.9$ sr (see Deirmendjian, 1969; pp.184-185). (This result will be compared with S calculated from the DSDs measured *in situ* later). The difference between the measured extinction-to-backscatter ratio of 14.5 sr and the calculated value of 19.9 sr is due to multiple scattering in the lidar returns from the clouds. This gives a value of an effective multiple scatter factor (η) of 0.73. This measured value of η is close to that obtained by Platt (1981) in a Monte Carlo study of the multiple scattering in Deirmendjian's (1969) modelled C1 cloud. In Platt's (1981) study $\eta \approx 0.6 - 0.7$ for a 10 m field of view in the C1 cloud, and η was about constant at 0.7 for optical depths greater than approximately 1.

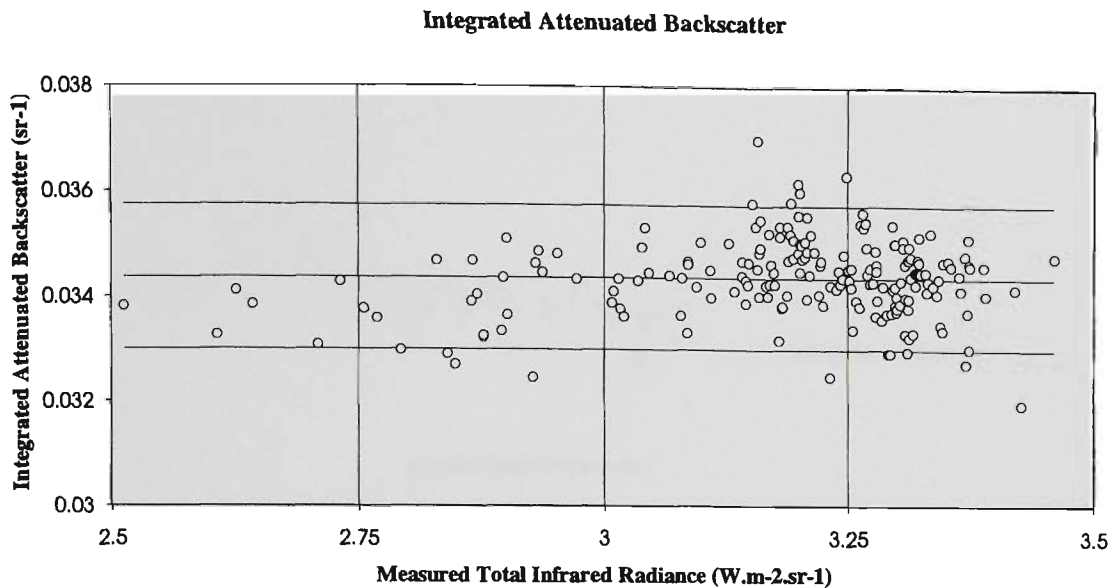


Figure 4.13. Integrated attenuated backscatter (χ') versus measured total infrared radiances for radiances greater than $2.5 \text{ W m}^{-2} \text{ sr}^{-1}$. Average value of χ' is 0.0344 sr^{-1} (middle horizontal line), the uncertainties shown are $\pm 4\%$ (outer lines). Note that this is only an initial estimate of the maximum χ' .

4.3.4.4 Measured Clear Sky Radiances

The clear sky radiances were needed to reduce the total measured infrared radiances to cloud radiances, which were required for the LIRAD analysis technique. On the afternoon of the 16 July 1993 there were three periods during the lidar and infrared radiometer (IRR) measurements when the sky was substantially clear of clouds. First, the clear periods were identified approximately using the lidar signals. Using the shot times of the cloud-free lidar profiles as a guide, averages and standard deviations of the IRR-measured cloud-free or Clear Sky Radiances (CSRs) were calculated. The IRR measurements were nearly continuous and provided a better picture of the duration of the clear period. Thus the durations of the clear periods initially determined by lidar were improved by using those periods where the measured radiances were less than these initial calculated average radiances, plus one standard deviation. To determine the final value of the CSR and its uncertainty the average and standard errors of the radiances were calculated for these new extended periods. The resulting CSRs are shown alongside the raw radiances in Figures 4.14 (clear period #1) to 4.16 (clear period #3). Variabilities shown in these plots are \pm one standard deviation. The results for average CSR and the uncertainties (standard errors) are summarised in Table 4.14.

Clear Sky Radiance (Period 1)

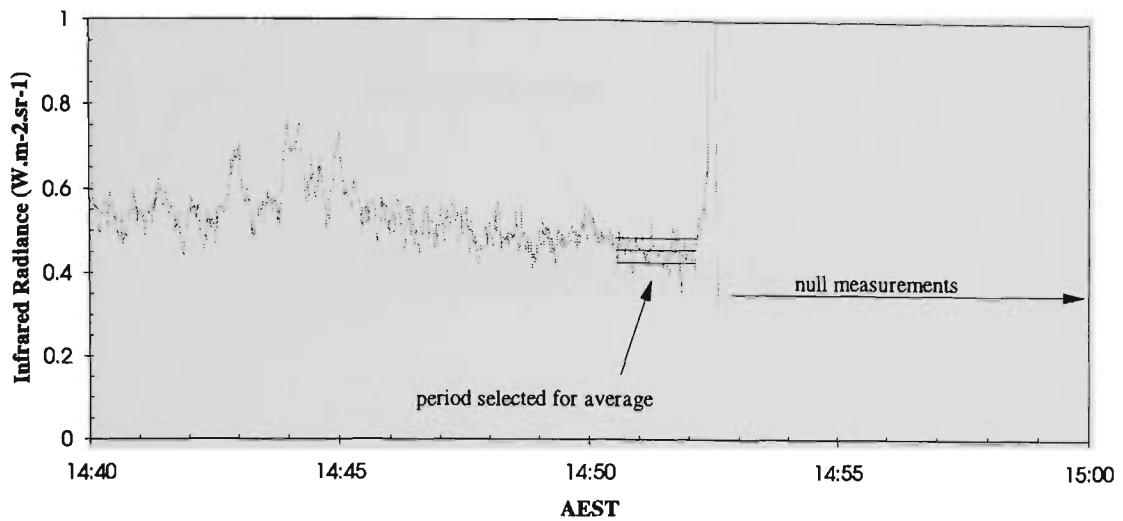


Figure 4.14. Clear sky radiance measured by infrared radiometer (MarkII); clear period 1 was from 14:50:33 - 14:52:09 AEST (1'36", 97 points). The average L_{sky} was determined to be $0.455 \pm 0.003 \text{ Wm}^{-2}\text{sr}^{-1}$. The variability is shown by one standard deviation (± 0.030) of the measurements.

Clear Sky Radiance (Period 2)

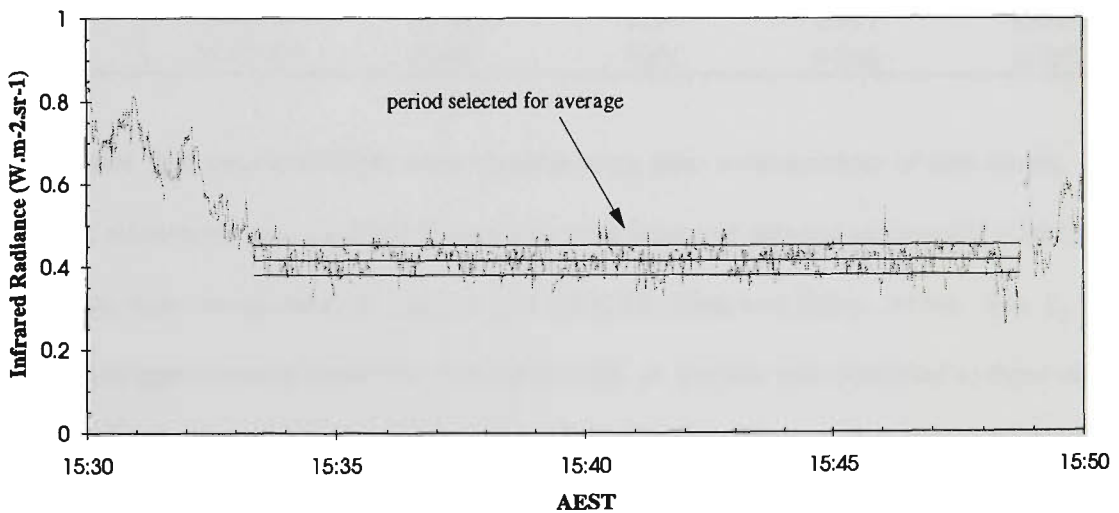


Figure 4.15. Clear sky radiance measured by infrared radiometer (MarkII); clear period 2 was from 15:33:23 - 15:48:45 AEST (15'22", 922 points). The average L_{sky} was determined to be $0.417 \pm 0.001 \text{ Wm}^{-2}\text{sr}^{-1}$. The variability is shown by one standard deviation (± 0.036) of the measurements.

Clear Sky Radiance (Period 3)

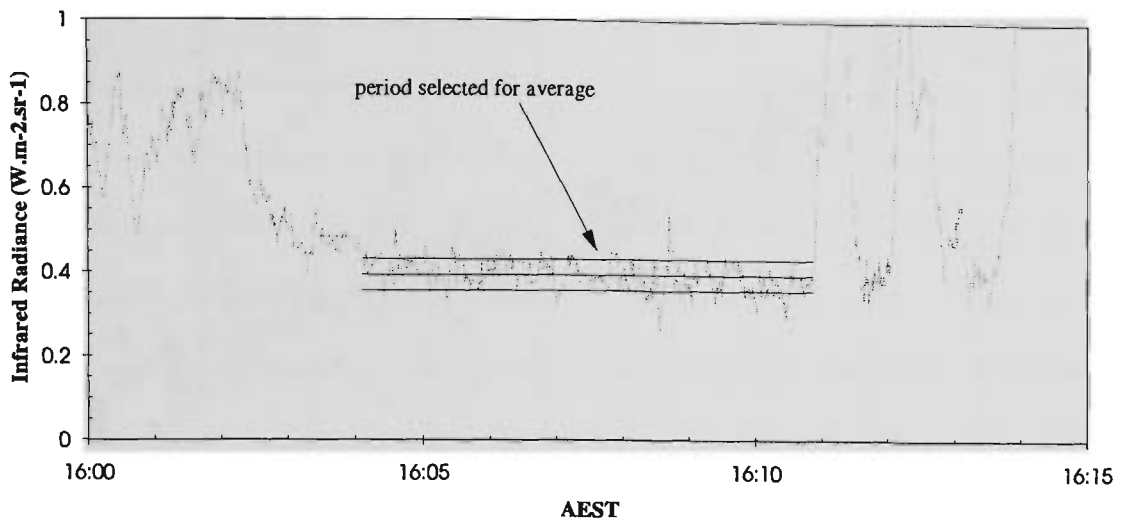


Figure 4.16. Clear sky radiance measured by the infrared radiometer; clear period 2 was from 16:04:06 - 16:10:52 AEST (6'46", 406 points). The average L_{sky} was determined to be $0.396 \pm 0.002 \text{ Wm}^{-2}\text{sr}^{-1}$. The variability is shown by one standard deviation of the measurements (± 0.038).

Table 4.14. Measured clear sky radiances for three periods clear of cloud.

Clear Period	Centre Time	Length of Period	Number of Points	CSR ($\text{Wm}^{-2}\text{sr}^{-1}$)	ΔCSR ($\text{Wm}^{-2}\text{sr}^{-1}$)
1	14:51:21	1'36"	97	0.455	0.003
2	15:41:04	15'22"	922	0.417	0.001
3	16:07:29	6'46"	406	0.396	0.002

These IRR-measured CSRs were checked using lidar measurements of thin clouds. To do this a linear relationship was assumed between the total measured infrared radiances (L_g) and χ' , then the χ' values were extrapolated to zero to give the CSR (Platt and Dilley, 1979). The L_g vs. χ' relationship is approximately linear for thin clouds only, so the data were restricted to those with less than $1 \text{ W m}^{-2} \text{ sr}^{-1}$. (It was determined later that, for the measurements of this day, a total measured infrared radiance of $1 \text{ W m}^{-2} \text{ sr}^{-1}$ corresponded to a cloud infrared emittance of just less than 0.2, and a cloud visible optical depth of about 0.4). The scatter plot of L_g vs. χ' for these thin clouds is shown in Figure (4.17), with the data separated into four distinct periods of measurements. Linear regressions were computed for these four periods delivering the extrapolated CSR (offset of regression), and its uncertainty (standard error of the offset). The results for the CSR from the lidar measurements of the thin clouds are shown in Table 4.15, and the results from Table 4.14 are also written in this table for comparison.

Clear Sky Radiances from Lidar Returns from Thin Clouds

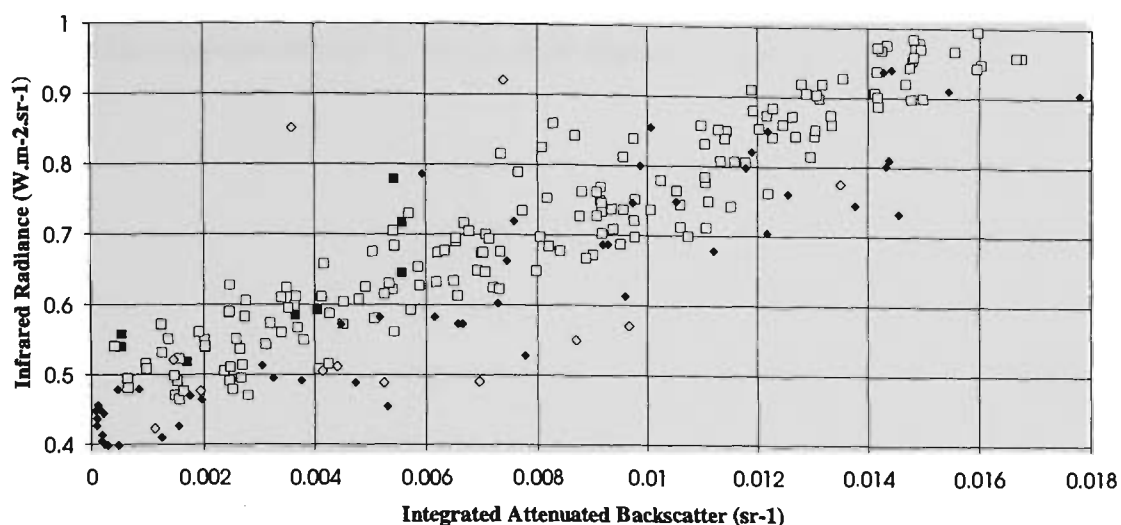


Figure 4.17. Measured total infrared radiance vs. χ' for some very thin clouds (τ_r less than about 0.2). Clear sky radiances were determined from linear regressions of these data.

Table 4.15. Clear sky radiances by infrared radiometer (IRR) and lidar.

Period	Centre Time	Length of Period	Number of Points	CSR (W.m ⁻² .sr ⁻¹)	Δ CSR (W.m ⁻² .sr ⁻¹)
cloud1 (lidar)	14:39:04	9'59"	8	0.501	0.038
clear1 (IRR)	14:51:21	1'36"	97	0.455	0.003
cloud2 (lidar)	15:16:17	32'08"	175	0.464	0.007
clear2 (IRR)	15:41:04	15'22"	922	0.417	0.001
cloud3 (lidar)	16:03:21	18'36"	54	0.416	0.013
clear3 (IRR)	16:07:29	6'46"	406	0.396	0.002
cloud4 (lidar)	16:31:24	2:49"	13	0.497	0.065

The lidar results for the CSRs compare reasonably well with those obtained by the IRR, however the CSRs obtained using the IRR measurements of the clear periods were adopted for the LIRAD analysis because they were more precise and more accurately placed in time. The CSRs were parameterised as a function of time by the line of best fit

$$CSR = -1.114t + 1.145, \quad (4.18)$$

{see Figure (4.18)}, with the CSR expressed in W.m⁻².sr⁻¹, and the time (t) expressed as a fraction of a day. By coincidence this line-fit is an extremely good fit and there were only three points, so it is not useful to quote the standard errors of the gradient and offset of the fit. The variabilities (\pm one

standard deviations) in the measured infrared radiances obtained over this period are plotted in Figure (4.18) instead. These variabilities provide a better indication of the uncertainty in the infrared radiances of the cloud-free air over the course of the afternoon of 16 July.

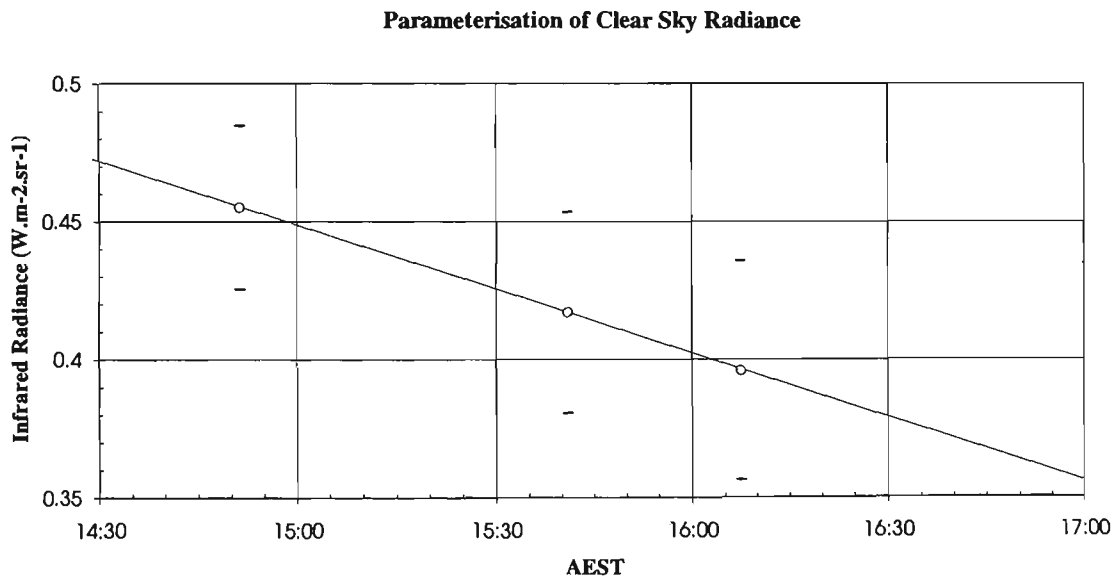


Figure 4.18. Clear sky radiances determined from the average IRR radiances during the 3 clear periods, versus time, and a line of best fit. The extremely good line-fit through the points is coincidental. Horizontal bars show the variabilities in the measured radiances determined from the cloud-free periods (± 1 standard deviation). The linear decrease with time of the clear sky radiance was verified by the microwave radiometer measurements of the water vapour path {see later, Figure (4.20)}.

4.3.4.5 Comparison of Water Vapour Path with Clear Sky Radiance

A MicroWave Radiometer (MWR) operates at CGBAPS on a routine basis for the retrieval of both Water Vapour Path (WVP) and Liquid Water Path (LWP) (see Chapter 3). The IRR-measured Clear Sky Radiances (CSRs) decreased during the afternoon of 16 July 1993, and, as the primary emitting gas contributing to the clear sky radiance is water vapour (*e.g.* Platt *et al.*, 1998), the WVPs could be used to check the (cloud-free) IRR measurements. Also, this comparison was done because there was a possibility that the WVPs could be used to provide a better parameterisation of a continuous value for the CSR than that described by equation (4.26) - and shown in Figure (4.18).

The MWR measured WVPs are shown alongside surface measurements of water vapour mixing ratio measured at Cape Grim in Figure (4.19). These measurements indicate that the WVP was decreasing over the course of the afternoon. It should be noted that one of these is a surface measurement and the other is a measurement of the water vapour column. It appears that the majority of the water vapour was in the boundary layer and that the boundary layer was well mixed.

The measured WVPs were compared to the IRR-measured CSRs for the three periods when the sky was clear of clouds. The average ratio of WVP to CSR for these periods was 0.602 (g.cm^{-2} per $\text{W.m}^{-2}.\text{sr}^{-1}$), and ranged from 0.591 - 0.619 (g.cm^{-2} per $\text{W.m}^{-2}.\text{sr}^{-1}$). The WVPs, IRR-measured CSRs, and the parameterisation of CSR given in the previous section are shown together in Figure (4.20). The WVPs were scaled by 0.6 for this plot. The plot shows that a linear parameterisation of CSR with WVP is reasonable. It was concluded that for this case there was nothing to be gained by including the WVPs in the parameterisation of the CSR.

Water Vapour Path ($\text{g}\cdot\text{cm}^{-2}$) and Surface Mixing Ratio ($\text{g}\cdot\text{kg}^{-1} \times 0.1$)

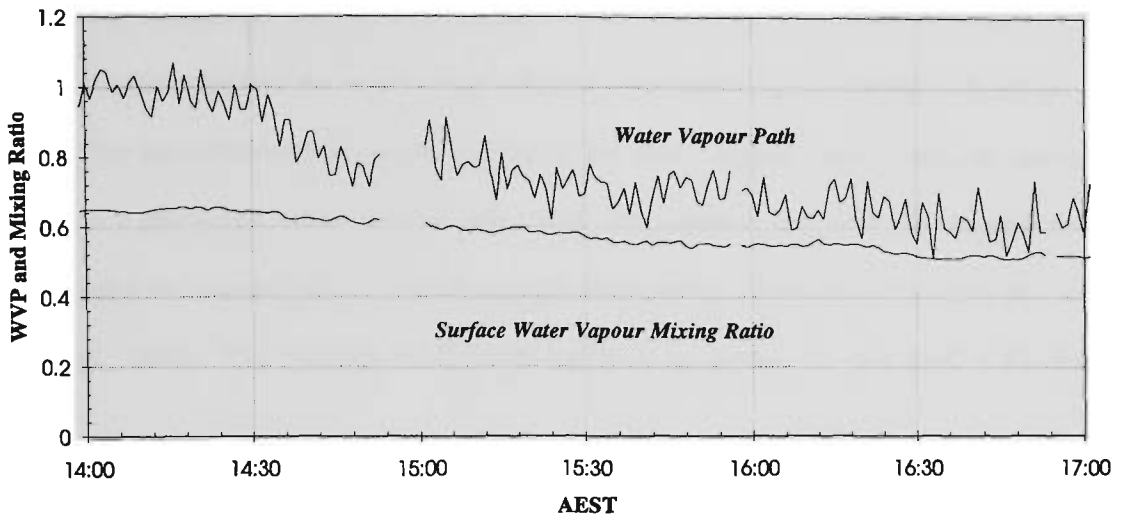


Figure 4.19. Microwave radiometer retrieved water vapour path ($\text{g}\cdot\text{cm}^{-2}$; upper lines), and water vapour mixing ratio ($\text{g}\cdot\text{kg}^{-1} \times 0.1$; lower lines) versus time.

Clear Sky Radiance

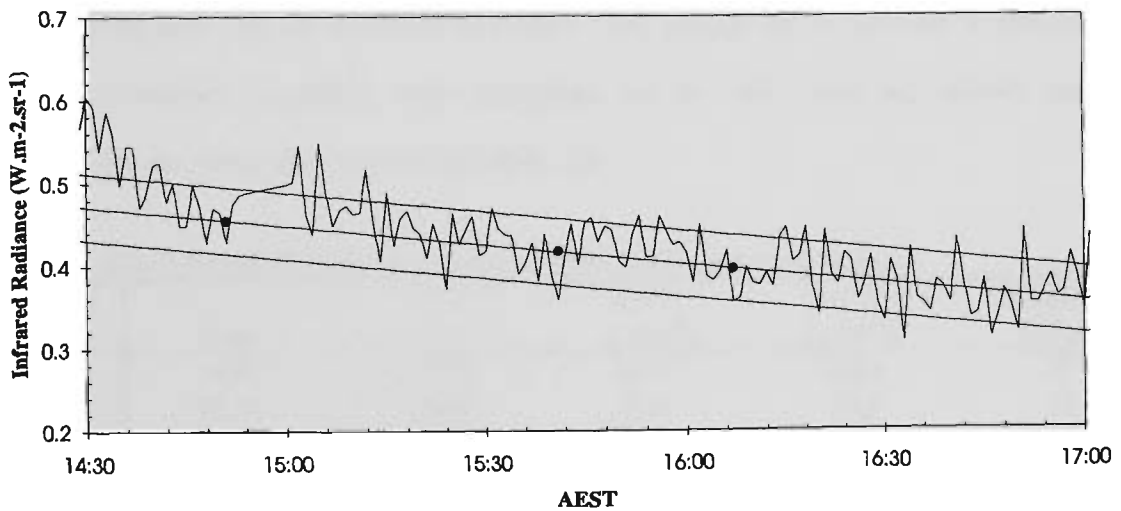


Figure 4.20. Clear sky radiances ($\text{W}\cdot\text{m}^{-2}\cdot\text{sr}^{-1}$). The three filled circles are the IRR measured CSRs during the three clear periods. The straight line (dark) is the CSR parameterised as a function of time, and the two outside lines (light) show the uncertainties in that parameterisation. The noisy line represents the MWR measured WVPs ($\text{g}\cdot\text{cm}^{-2}$) scaled by 0.6.

4.3.4.6 Calculated Infrared Properties of Water Vapour

In the LIRAD method the infrared transmittance of the cloud-free air beneath the clouds is used to determine the attenuation of the zenith cloud radiances measured by ground-based radiometers. To do this, from the aircraft-measured height profiles of the water vapour mixing ratio, air pressure and temperature a theoretical water vapour path, clear sky radiance, and infrared transmittance were calculated, and the infrared transmittances were parameterised as a function of the clear sky radiances (Platt *et al.*, 1985). The methods for determining these quantities are described in the following sections.

First, infrared clear sky radiances were calculated for typical water vapour continuum mass absorption coefficients (k); the results are shown in Table 4.16.

Table 4.16. Calculated clear sky infrared radiances from the aerological profiles.

k ($\text{cm}^2 \text{g}^{-1} \text{atm}^{-1}$)	CSR ($\text{W m}^{-2} \text{sr}^{-1}$)
7.0	0.47
7.5	0.48
8.0	0.49
8.5	0.51
9.0	0.52

The WVP calculated from the same aerological profiles was 1.26 g.cm^{-2} . These calculated properties were then compared with the measured properties. The average MWR-retrieved WVPs and their variabilities (standard deviations) were determined for the three clear sky periods described previously, and the results are shown in the Table 4.17.

Table 4.17. MWR measured water vapour paths for the three clear sky periods

Clear Sky Period	from:	to:	WVP (g cm^{-2})	Δ WVP (g cm^{-2})	Number of Points
1	14:46	14:52	0.77	0.04	7
2	15:34	15:48	0.70	0.05	15
3	16:05	16:10	0.64	0.04	6

The CSRs and WVPs measured during the three clear periods are summarised in Table 4.18. It is immediately apparent that the calculated WVP of 1.26 g cm^{-2} is too high when compared with the MWR-retrieved result. Similarly, the calculated clear sky radiances are higher than the IRR-measured values. The IRR-measured CSRs and MWR-retrieved WVPs are known with a certainty that could not explain such high values for the calculated quantities. Inspection of the raw (unaveraged)

aerological measurements revealed the most likely cause for the discrepancy: the variability of humidity with height. It is likely that the profile of the water vapour mixing ratio averaged over a long track over the sea to the west of Cape Grim was significantly different from that which occurred directly over the Cape. (There were no aircraft measurements of a water vapour profile directly over Cape Grim). Thus, the average profile of the water vapour mixing ratio was adjusted and the resulting changes in the calculated infrared properties investigated to determine whether various calculated values of WVPs and CSRs could be brought to match those measured at Cape Grim.

Table 4.18. Measured WVPs and CSRs during the Three Clear Periods

Clear Period	Measured WVP (g cm^{-2})	Measured CSR ($\text{W m}^{-2} \text{sr}^{-1}$)
1	0.73-0.81	0.45-0.53
2	0.65-0.75	0.38-0.46
3	0.60-0.68	0.35-0.43

The surface water vapour mixing ratio measured at Cape Grim was observed to be about about 5 g kg^{-1} . The raw (unaveraged) aerological data showed that there was little variation in the mixing ratio in the boundary layer, and, it was also about 5 g kg^{-1} . So the boundary layer measurements of the water vapour mixing ratio were assumed to be accurate. In fact only one adjustment to the mixing ratio profile could be found that enabled a good match between the measured and calculated CSRs and WVPs, and that was to reduce the amount of water vapour in the free troposphere. This involved two steps - selection of the height of the top of the boundary layer, (TBL), and selection of a factor for reducing the mixing ratio above that height.

When the atmosphere above the lidar was clear or nearly clear of clouds, the TBL was about 1000-1100 m ASL, and this was determined easily from the lidar returns from either the boundary layer aerosol backscatter, or the cloud tops of partially transparent clouds. Up to about 16:30 AEST, the TBL ranged in height from about 1100-1150 m (thin clouds or clear), and after that time the TBL increased to about 1100-1250 m or higher (thicker clouds).

To simplify the calculations with the available aerological data, the TBL was initially taken as 1180 m. The points in the water vapour mixing ratio profile above the TBL were reduced by a single factor until the calculated clear sky radiance and water vapour path matched the measured values, as closely as possible. The results for 5 water vapour continuum mass absorption coefficients ($k_w, \text{cm}^2 \cdot \text{g}^{-1} \cdot \text{atm}^{-1}$) are shown in Table 4.19.

Table 4.19. Calculated CSRs and WVPs after reduction of the mixing ratio above the TBL.

<i>k_w</i>	<i>0.5</i>	<i>0.4</i>	<i>0.3</i>	<i>0.2</i>	<i>0.1</i>	<i>0.05</i>	<i>0.0</i>
7.0	0.403	0.396	0.390	0.384	0.380	0.378	0.376
7.5	0.414	0.407	0.400	0.395	0.390	0.388	0.386
8.0	0.425	0.417	0.410	0.405	0.400	0.398	0.396
8.5	0.436	0.428	0.421	0.415	0.410	0.408	0.406
9.0	0.447	0.438	0.431	0.425	0.420	0.418	0.416
WVP (g.cm ⁻²)	0.941	0.877	0.814	0.751	0.688	0.656	0.625

The numbers in the top row of Table 4.19, in italics, show the factors by which the free tropospheric water vapour mixing ratios were reduced..

A comparison between the new (calculated) results in this table and the results of the measurements shown in Table 4.18, shows better agreement between the calculated and measured results where the free tropospheric water vapour was multiplied by a factor between 0 - 0.2. However, the measured CSR for clear period 1 now appears too high, and no reasonable adjustments of the aerological profiles could force a match between the measured and calculated CSRs and WVPs of this period. As there was some rain just prior to this period, the IRR and MWR measurements may have been affected by precipitation.

Inspection of both Tables 4.18 and 4.19 show that a good match occurs between the calculated and measured WVPs and CSRs for the clear periods 2 and 3, if the mixing ratio profile in the free troposphere is reduced by a significant fraction. The results of this process are shown graphically in Figure (4.21); the calculated WVPs and CSRs initially overestimated the measured values (RHS of plot). These calculated quantities and their uncertainties fell within those of the measured values (LHS of plot), once the water vapour mixing ratio profile above the TBL was reduced by a factor of 0 - 0.2. The three sets of lines, close together, are the results for three TBL heights: 1180 m, 1230 m, and 1270 m. It can be seen that an imprecise choice for the height of the TBL has little effect on the results.

Measured and Calculated Clear Sky Radiances

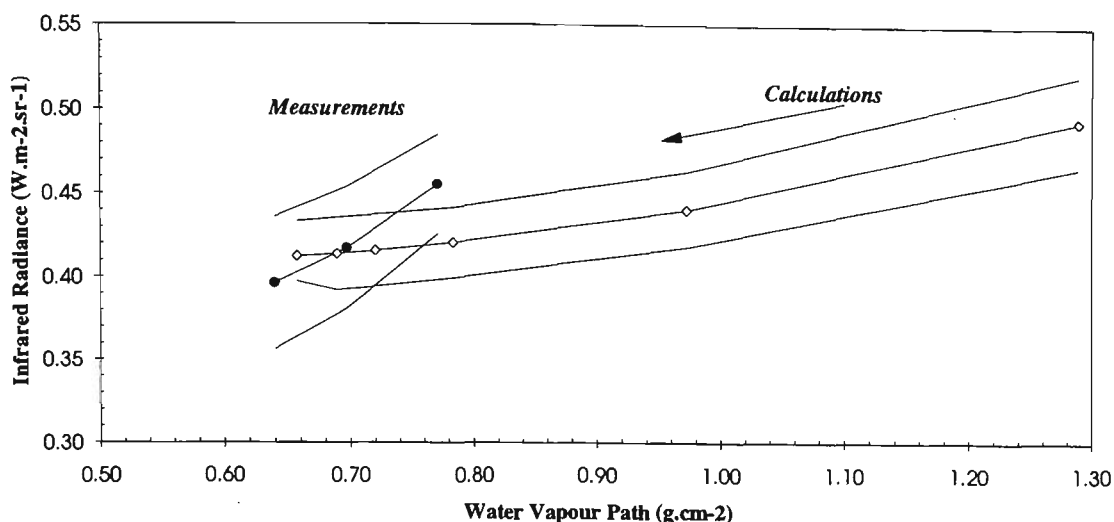


Figure 4.21. This plot shows values of CSR and WVP calculated from height profiles of the water vapour mixing ratios, and measured CSRs and WVPs by IRR and MWR (filled circles). The variabilities are represented by the solid lines.

Now, with a more realistic profile of the water vapour established, the clear air infrared transmittances and clear sky radiances were calculated, via the methods developed by Platt *et al.* (1984). These quantities were calculated with the following parameters varied to represent the full range of conditions expected on the afternoon of 16th July: (1) the TBL heights (1180 m, 1230 m, 1270 m), (2) the water vapour continuum mass absorption coefficients (k_w), 7.0 - 9.0 $\text{cm}^2 \text{g}^{-1} \text{atm}^{-1}$, in steps of 0.5 $\text{cm}^2 \text{g}^{-1} \text{atm}^{-1}$, (3) profiles of the water vapour mixing ratio above the TBL multiplied by the factors 0, 0.1, 0.2.

The resulting calculated infrared transmittances of the cloud-free air (T_{air}) and the clear sky radiances are shown in Figure (4.22), as well as the line of best fit used to parameterise the T_{air} as a function of CSR:

$$T_{\text{air}} = -0.2834 \times \text{CSR} + 0.9859. \quad (4.19)$$

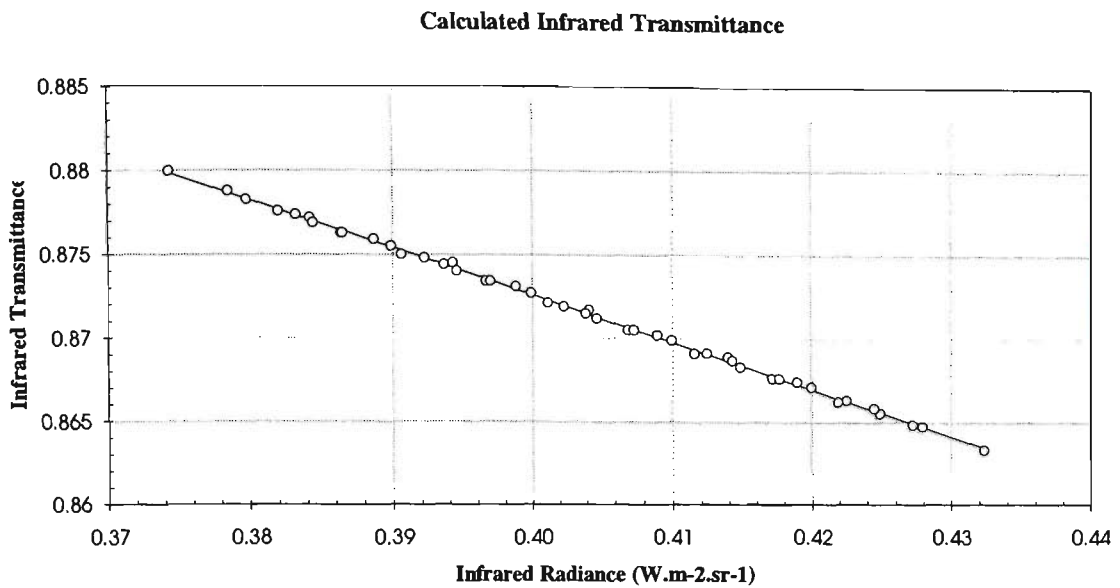


Figure 4.22. Infrared transmittances and clear sky radiances calculated for a number of modelled height profiles of water vapour. Also shown is the line of best fit.

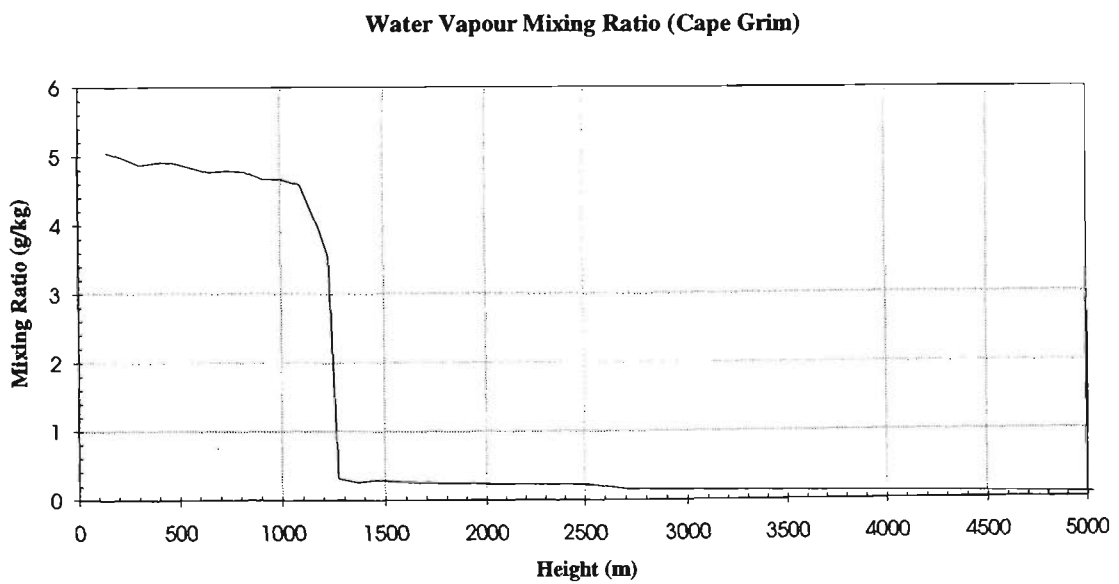


Figure 4.23. Height profile of the water vapour mixing ratio over Cape Grim on the afternoon of 16 July 1993, determined from both CSRs (IRR) and WVPs (MWR) measured at Cape Grim, and aircraft measurements made over the sea to the west of Cape Grim.

The parameterised T_{air} is not forced to equal unity when the CSR is zero, as the calculated T_{air} is only required for the LIRAD analysis for the range of CSRs shown in Figure (4.21): that is, for radiances from 0.37 to 0.44 $\text{W m}^{-2} \text{sr}^{-1}$.

The resulting profile of the water vapour mixing ratio over Cape Grim is shown in Figure (4.23), and the profile of cumulative water vapour path (integrated from the elevation of Cape Grim upwards) is shown in Figure (4.24). It was from these profiles that a profile of the cumulative clear air radiance {Figure (4.25)}, and a profile of the cumulative clear air infrared transmittance were calculated {Figure (4.26)}. These profiles of the clear air radiance and transmittance were necessary for determining the transfer of the clear air infrared emission from above the stratocumulus clouds, through the clouds and to the surface. The calculated profiles of clear air radiance and transmittance were parameterised as a linear function of height and covering the heights of cloud base, to enable ease of computation for analysis of the LIRAD data: these parameterisations are also shown in Figures (4.25) and (4.26).

Cumulative Water Vapour Path

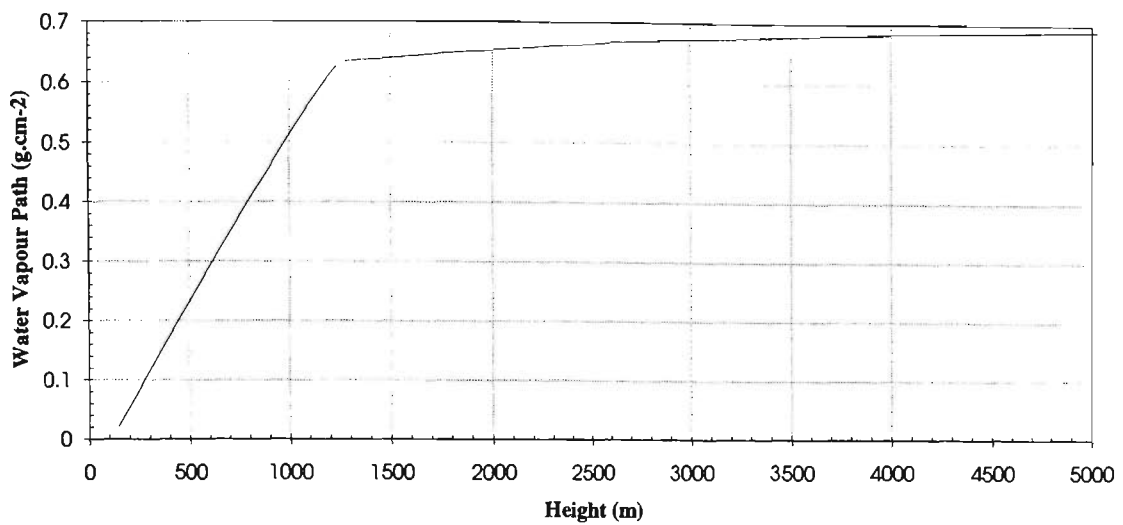


Figure 4.24. Cumulative water vapour path (g cm^{-2}) (integrating upwards from the elevation of Cape Grim), versus height in metres, and calculated from the profile of mixing ratio shown in Figure (4.23).

Cumulative Clear Sky Radiance

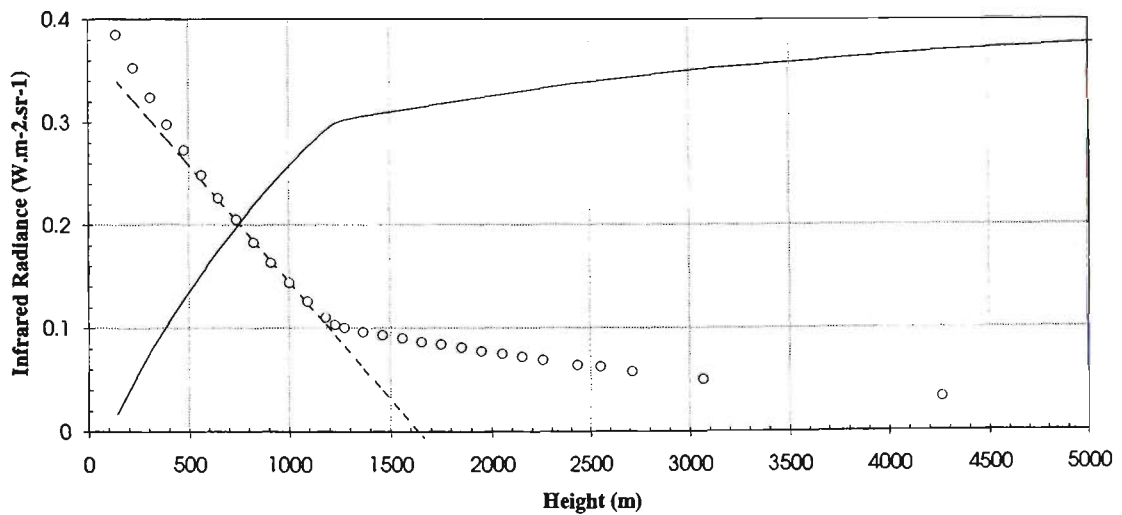


Figure 4.25. Cumulative clear sky radiance ($\text{W m}^{-2} \text{sr}^{-1}$) integrated from the surface and upwards (solid line increasing from a height of 90 metres, the elevation of Cape Grim). The cumulative radiances (open circles) decreasing from above $0.4 \text{ (W m}^{-2} \text{sr}^{-1})$ are those integrated from the top of the atmosphere and downwards. Also shown is a parameterisation of the decreasing radiances (dashed line).

Cumulative Clear Air Infrared Transmittance

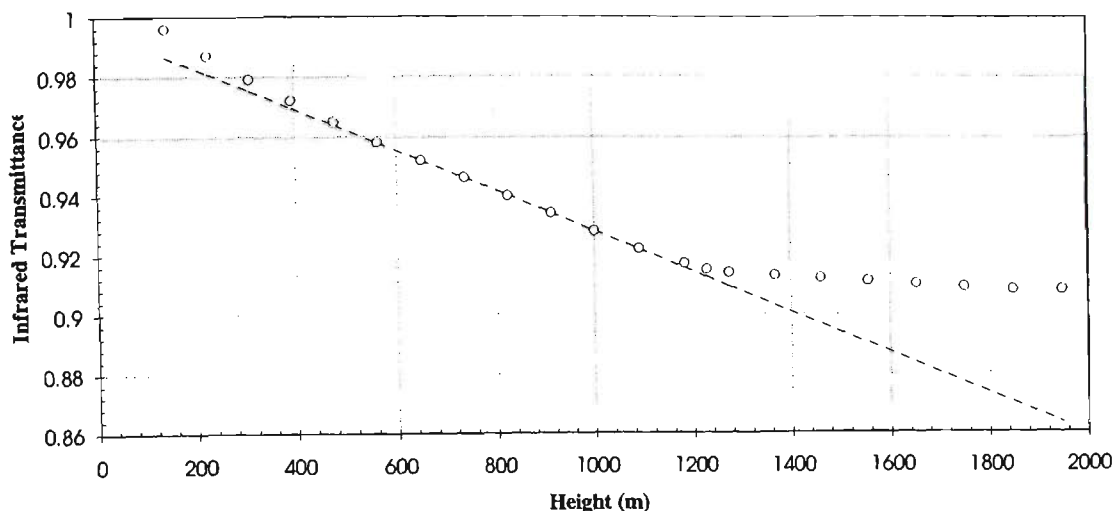


Figure 4.26. Cumulative infrared transmittance of the clear air, integrated upwards from the surface (elevation of Cape Grim). A parameterisation of the transmittance in the height regions where the stratocumulus clouds were observed is shown by the dashed line.

4.3.4.7 Estimate of Infrared Scattering using the DISORT Program

The measured infrared radiances of clouds consist of a thermally emitted component, (L_i), a component due to the scattering of infrared radiation within the clouds, ('internal scattering' L_s), and a component due to thermal radiation emitted by the earth's surface and reflected downwards by the clouds (L_r), *e.g.* Platt and Stephens (1980); see also section A2.7.6 of this thesis. Some estimates of these scattered components were required to determine the infrared absorption optical depths (τ_i) and emittances (ϵ) from the LIRAD measurements of the stratocumulus clouds. The radiance components comprised approximately 5 % of the total and so were estimated using the scattering program 'DISORT'.

To estimate the amount of infrared scattering in the measured radiances the DIScrete-Ordinates Radiative Transfer (DISORT) program (Stamnes *et al.*, 1993) was used to model a water droplet cloud with the properties shown in Table 4.20. A Henyey Greenstein phase function was used with the asymmetry parameter (g) varied to investigate the sensitivity of the results to varying degrees of forward scattering {*e.g.*, see Stephens (1979) for typical values of g }. The cloud and earth surface temperatures were chosen to match measured temperatures. The optical depth of the boundary layer was calculated from airborne measurements of water vapour and aerosols.

Table 4.20. Parameter settings for cloud infrared radiances calculated by DISORT.

Quantity:	Value:	References and comments:
Assymetry parameter (g)	0.8, 0.85, 0.9	<i>e.g.</i> Stephens, 1979; Stephens, 1994.
Single scattering albedo (ω)	0.5	See section A2.7.6.
Cloud optical depths (τ_i)	1, 5	
Cloud temperature	274K	
Earth surface temp.	290K	
Boundary layer temp.	282K	
Infrared optical depth of boundary layer	0.05	
Number of streams (scattering angles)	16	See Stamnes <i>et al.</i> , 1993.
Wavelength band for calcs.	10-12 μm	

Following the calculation of the radiances by DISORT the reflectances were determined by,

$$R_L = \frac{L_c - L_c'}{L_c}, \quad (4.20)$$

where L_c is the downward radiance at cloud base for an earth surface temperature of 290K, (recall that $L_c = L_i + L_s + L_r$), and L_c' is the downward radiance for zero upwelling radiance at cloud base; *i.e.*, earth surface temperature set to 0K. The radiances and reflectances calculated by the DISORT program for a thin cloud ($\tau_i = 1$) and a thick cloud ($\tau_i = 5$) are shown in Tables 4.21 and 4.22 respectively. The radiance L_+ is the upwelling radiance at cloud base. The flux reflectances (R_F) are also given in the table. The reflectances shown in Table 4.22 agree reasonably well with those determined in the study of radiative transfer in thick water clouds by Yamamoto *et al.* (1970), and Paltridge and Platt (1976).

Table 4.21. Radiances ($\text{W m}^{-2} \text{sr}^{-1}$) and reflectances for $\tau_i = 1$.

g	T_s (K)	L_+	L_c	R_L	R_F
0.80	0	0.00	5.20		
0.80	290	16.4	5.39	3.46%	6.92%
0.85	0	0.00	5.13		
0.85	290	16.4	5.26	2.49%	5.36%
0.90	0	0.00	5.06		
0.90	290	16.4	5.15	1.59%	3.70%

Table 4.22. Radiances ($\text{W m}^{-2} \text{sr}^{-1}$) and reflectances for $\tau_i = 5$.

g	T_s (K)	L_+	L_c	R_L	R_F
0.80	0	0.00	11.7		
0.80	290	16.4	12.0	2.02%	4.70%
0.85	0	0.00	11.7		
0.85	290	16.4	11.9	1.43%	3.59%
0.90	0	0.00	11.7		
0.90	290	16.4	11.8	0.90%	2.43%

A satisfactory method for determining the amount of internal scattering (L_s) could not be determined. Intuitively, for thin clouds, the value of L_s should be positive because radiances are scattered into the downward beam from longer (slant) path lengths than the shorter zenith path lengths from which radiation is scattered out of the beam. For thick clouds the zenith radiances are black, so as much radiation is scattered out of the downward beam as is scattered into it from slant paths, therefore L_s should be approximately zero. In short, for thick clouds $\epsilon = 1 - r$. This is a basic test that can be applied to any theoretical determinations of L_s . Further theoretical studies of the infrared scattering in water droplet clouds are required to calculate L_s for stratocumulus clouds.

Although little was known about L_s , an estimate of this quantity was required for the analysis of the LIRAD data, because it was found that (by trial and error) the choice of $L_r + L_s$ had a significant effect on the retrieval of $\eta\alpha$ and the statistics of τ_i and ϵ . Thus a lower boundary for $L_r + L_s$ was estimated by inspection of the reflectances given in Tables 4.21 and 4.22. The first trial of the LIRAD algorithm used as a lower boundary for the scattered components,

$$(L_r + L_s) = (0.03 \pm 0.02) \times L_i, \quad (4.21)$$

and as an upper boundary,

$$(L_r + L_s) = (0.05 \pm 0.02) \times L_i. \quad (4.22)$$

This upper boundary allows for a small but significant increase in the fraction of the measured radiances due to internal scattering. The LIRAD results for these two estimates of the infrared scattering will be presented later.

4.3.4.8 Application of the LIRAD Method to Low Water Droplet Clouds

The basic parts of the LIRAD method are standard as described by Platt *et al.* (1998) and in section 2.3 of this thesis, but some modifications were required for the analysis of the LIRAD measurements of the low boundary layer clouds and these are described in the following paragraphs.

The infrared radiometer measured radiances by water vapour from above cirrus clouds is negligible. Thus in LIRAD studies of cirrus clouds the downwelling radiance by the water vapour may be calculated from the entire water vapour column, and the radiances by the clouds are reduced by the water vapour infrared transmittance (T_{air}) also calculated for the entire column. Boundary layer clouds exist at heights of up to about 2000 m ASL and therefore are likely to exist well inside the primary mass of water vapour, and this was found to be so for this study. In this study the transfer of the measured radiances by water vapour above the thinner stratocumulus clouds was significant. A minor change to the LIRAD method was that the downwelling cloud radiances were reduced only by T_{air} calculated up to cloud base, (and not calculated for the entire water vapour column as in the cirrus studies).

In previous LIRAD studies the internal scattering and the reflection of terrestrial radiation were calculated separately (*e.g.* Platt and Stephens, 1980). In this study there was no attempt to calculate these quantities separately: the total effect of infrared scattering was determined for the measured downwelling radiances (section 4.3.4.7). This is a significant improvement to the LIRAD method.

The methods for calculating χ' which accounted for attenuation of the lidar pulse in the clouds due to molecular scattering were new (section 4.3.4.3). These approximations were satisfactory for this study because the boundary layer clouds were thin. The molecular extinction in these (geometrically) thin clouds was small, however for deeper clouds such as cirrus these approximations may not be satisfactory.

The LIRAD analysis method is described here briefly. First, in the preceding sections, the measured total infrared radiances (L_g) were reduced to cloud infrared absorption radiances (L_i) after elimination of the effects due to emission from the clear air below and above the clouds, and by elimination of the effects due to infrared scattering.

The primary inputs to the LIRAD algorithm were then the cloud absorption radiances, and the calibrated lidar profiles of χ . The microphysical properties of the clouds modified by the multiple

scatter factor (η), *i.e.*, the extinction-to-backscatter ratio (ηS) and the visible extinction-to-infrared absorption ratio ($\eta\alpha$), were assumed homogeneous throughout each profile of χ . Initial estimates of ηS and $\eta\alpha$ were used to invert each profile of χ for infrared absorption. The estimate of ηS was already known with good certainty, and obtained from the values of maximum χ' . If the χ' value of a profile was greater than the estimate of ηS , then ηS was increased to equal the value of χ' .

A cloud radiance was calculated from each infrared absorption profile and compared with the simultaneously measured cloud radiance. The estimate of $\eta\alpha$ was adjusted and the absorption profile recalculated until the radiance calculated from this profile matched the measured radiance to a desired accuracy. This was done for all the profiles of χ and the measured radiances. The final results were, for each profile, the microphysical quantities ηS and $\eta\alpha$, visible and infrared optical depths, and the calculated infrared emittances.

4.4 LIRAD Measurements of 8 February 1995 (SOCEX2)

4.4.1 Introduction

The lidar profiles obtained with the Minilidar used during SOCEX2 were of insufficient quality for the detection of backscatter by aerosols and molecules (see Figure (4.1)). Therefore the profiles obtained with the Minilidar could not be calibrated by a fit to a modelled molecular profile, as was done for the SOCEX1 data. However an analysis of some LIRAD data selected from one day of the SOCEX2 dataset was carried out to provide an indication of the distribution of the optical depths of the summer clouds. This was achieved by using the Minilidar returns from the thickest (water droplet) stratocumulus clouds to calibrate the Minilidar. This calibration is described shortly.

The most number of LIRAD measurements of marine boundary layer clouds obtained on a single day for all of SOCEX were those of 8 February 1995 (6189 measurements). There were 3548 LIRAD measurements of stratocumulus clouds and 2641 measurements of lower cumulus clouds. The cumulus cloud measurements were discarded from the LIRAD analysis by inspection of the cloud heights obtained from the Minilidar measurements (5.4.1).

4.4.2 Comparisons Between the Mie Properties of Stratocumulus Clouds for the Nd:YAG Laser Wavelengths 1064 nm and 532 nm

The Minilidar Nd:YAG laser operated at the fundamental wavelength 1064 nm, twice that of the Maxilidar used during SOCEX1. The method of calibration of the Minilidar (see next section) assumed that the differences in the optical properties of the stratocumulus clouds at these two wavelengths were insignificant. There were some differences in the cloud optical properties between the two wavelengths and these are investigated in the following.

The 353 FSSP measured DSDs of the clouds observed on 16 July 1993 were used to compare the cloud properties at the two wavelengths 1064 nm and 532 nm. (These DSDs are given later, section 5.3.3). The DSDs were measured at depths into the clouds ranging from cloud base to about 450 m into the clouds, so there is a wide variation in their properties (e.g. effective radii) for a comparison of the optical properties at the two wavelengths.

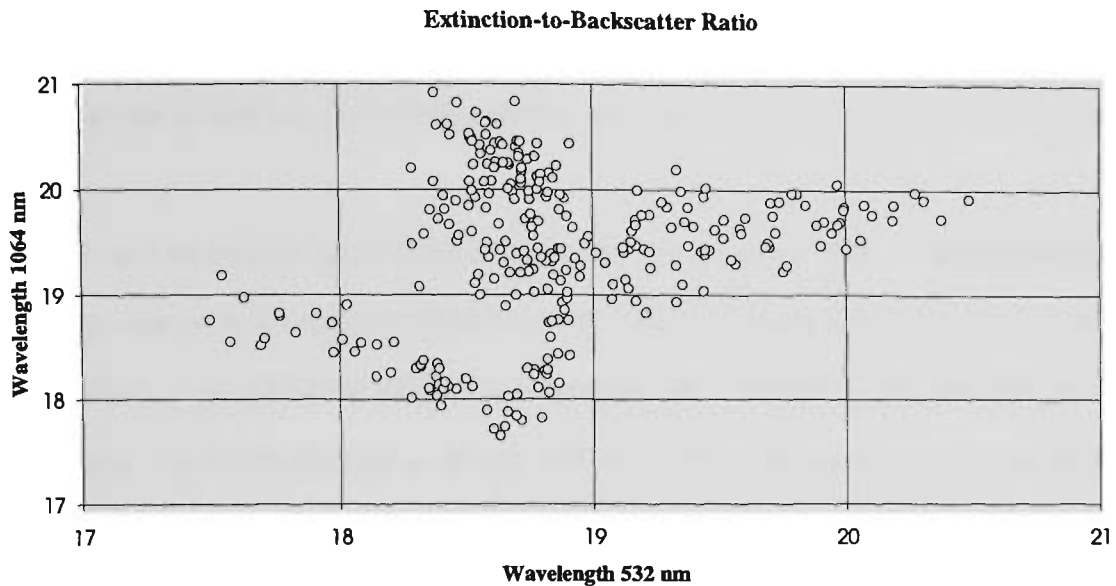


Figure 4.27. Extinction-to-backscatter ratios (S sr) for the wavelength 1064 nm versus those for the wavelength 532 nm. These values were calculated using the FSSP measured DSDs of Flight 8, 16 July 1993. Most of the variation here is due to large variations in the backscatter coefficients.

The visible extinction and backscatter coefficients for these DSDs were determined from Mie computations. Near the heights of cloud base (smaller effective radii) the extinction at the wavelength 1064 nm was about 5% higher than the 532 nm extinction. Deeper into the clouds this difference decreased to about 2% (larger effective radii). The backscatter coefficient at 1064 nm varied between about +6% and -8% of the backscatter at 532 nm. Similarly, the extinction-to-backscatter ratios at 1064 nm varied between -5% and +12% of the values at 532 nm. On average, $S(1064 \text{ nm})$ was greater than $S(532 \text{ nm})$ by +2.9%. A plot of $S(1064 \text{ nm})$ versus $S(532 \text{ nm})$ is shown in Figure (4.27).

The ratios of visible extinction to infrared absorption, (α , wavelengths 1064 nm : 10-84 μm), varied from +5% of α (532 nm : 10-84 μm) near cloud base, to about +2% deeper into the clouds. The variations in these ratios of α were much less than the ratios of S . The larger variations in the values of S was due to the large variations in the backscatter coefficients.

4.4.3 Calibration of the Minilidar

The measurements of the clouds observed on 16 July 1993 showed that there were only small variations in the retrieved ηS for the thicker clouds observed on that day (see later, section 5.3.4.2), as well as only small variations in the microphysical properties S and α determined from the *in situ* measurements (section 5.3.3). These small variations in all of (ηS), S and α meant that the lidar

returns from the thickest water droplet clouds could be used to calibrate the Minilidar. This was done by assuming that the value for ηS for the SOCEX2 clouds was the same as that found for SOCEX1. First, a test was carried out to determine whether this assumption was valid; the test is described below.

To test for possible large changes in S for the summer cloud DSDs, some calculations were made using some of the information from Boers *et al.* (1996) (for Flight 8 of 16 July 1993, SOCEX1), and from Boers *et al.* (1998) (for Flight 9 of 8 February 1995, SOCEX2). The effective radius of a typical winter cloud DSD observed on 16 July 1993 (SOCEX1) was reduced from $9.2 \mu\text{m}$ to $6.2 \mu\text{m}$ and the droplet concentration doubled from 43 cm^{-3} to 86 cm^{-3} , to match the properties of the DSDs observed on 8 February 1995 (SOCEX2), approximately. This decrease in the effective radius combined with a doubled droplet concentration caused an increase in S , but only by about 0.4%. In summary, ηS for the SOCEX2 (summer) clouds was assigned approximately the same value retrieved from the analysis of the LIRAD winter clouds data due to the low signal-to-noise ratio of the Minilidar signal profiles, the small variations in S , and because values of η could not be obtained without further extensive calculations of the multiple scattering in the lidar returns. That is, 14.5 sr (section 5.3.4.2), plus 2.9% to account for the difference due to the wavelength 1064 nm being used. Therefore the final value used for the calibration was 14.9 sr (η was assumed unchanged).

The value of η determined from the LIRAD study of the SOCEX1 data was 0.76 ± 0.03 for cloud depths greater than approximately 1 (see later, section 5.3.4.7). The value of η for $\tau_v > 1$ determined by Platt (1981) for Deirmendjian's (1969) modelled *CI* cloud was approximately 0.7. Some differences between these values of η are expected because the theoretical study by Platt (1981) was different in many respects from the experimental study described in this thesis. (Multiple scattering is discussed in more detail in Chapter 5). So, *prima facie*, at least for the water droplet clouds of about $\tau_v > 1$, it was not an unreasonable assumption that the differences in η between the SOCEX1 and SOCEX2 measurements were insignificant for the analysis of this dataset. Further studies of the multiple scattering in lidar returns from water droplet clouds are required to determine the effects of multiple scattering on the lidar measurements of SOCEX1 and SOCEX2.

4.4.4 Clear Sky Radiances and Infrared Transmittances

The measured clear sky radiances were determined by inspection of the lidar and infrared radiometer data (cf. section 4.3.4.4). A linear regression between these data was used to calculate the cloud-free infrared radiances in terms of the continuously measured water vapour paths (Figure (4.28)). These 'clear sky' radiances were required to determine the cloud radiances.

The measured clear sky radiances are also shown in Figure (4.29) (filled circles), as well as the clear sky radiances derived from the microwave radiometer measurements of water vapour path (noisy curve). The modelled continuous clear sky radiances are shown by the solid lines in the same figure: between 0800EST and 1600EST the radiances have been modelled by a line of best fit through the radiances derived from the microwave radiometer measurements. The average radiance derived from the microwave radiometer measurements after 1830EST were used to model the clear sky radiances after 1830EST. A straight and level line was used to model the radiances between 1600EST and 1830EST by connecting the two other straight lines.

Given that the maximum measured total radiances from the cloudy marine boundary layer was $2.5 \text{ W m}^{-2} \text{ sr}^{-1}$, the errors in the final cloud radiances due to these modelled clear sky radiances are about $\pm 2\%$ for the thickest clouds. The error increases for some of the thinner clouds, and this contributes to the large variability in the LIRAD results for the thinner clouds. (The uncertainties are investigated later in section 5.4).

It is recalled that in the calculations of the water vapour paths and clear sky radiances determined for Cape Grim on 16 July 1993 (SOCEX1), some adjustments were required to the supplied data representing the height profiles of water vapour. The adjustments were required to determine the infrared properties of the water vapour over Cape Grim (section 4.3.4.6), and similar adjustments were made for the SOCEX2 data.

The water vapour mixing ratio data supplied for this study, representing the height profile of the water vapour mixing ratio, was not representative of the water vapour over Cape Grim because above 2300 m (above the maximum height flown by the SOCEX F-27 aircraft), the water vapour mixing ratios were taken from radiosonde measurements made several hundred kilometres away. The height profile of the water vapour mixing ratios obtained from the airborne dataset is shown in Figure (4.30). (The height of the boundary layer was approximately 1760 m).

To achieve a reasonable match between the measured and calculated clear sky radiances and water vapour paths, some combinations of factors were used to reduce the amounts of water vapour in and above the boundary layer. These combinations of factors are shown in Table 4.23 below, as well as the calculated clear sky radiances and water vapour paths. The factors for reducing the mixing ratio (F) are given in the first two columns. The clear sky radiances have been calculated for two water vapour continuum mass absorption coefficients (k_w), (cf. section 4.3.4.6). The units of the Clear Sky Radiances (CSRs) are $W m^{-2} sr^{-1}$, the units of k_w are $cm^2 g^{-1} atm^{-1}$. The measured and calculated quantities are shown in Figure (4.31).

Table 4.23. Calculated Water Vapour Paths (WVPs) and Clear Sky Radiances (CSRs).

$F(\text{B.Layer})$	$F(\text{Free Trop.})$	WVP $g cm^{-2}$	CSR($k_w=7$)	CSR($k_w=9$)
1	0.2	1.1	0.395	0.446
1	0.5	1.33	0.412	0.465
1	0.7	1.48	0.427	0.483
0.9	0.2	1.01	0.356	0.398
0.9	0.5	1.24	0.373	0.417
0.8	0.2	0.912	0.319	0.353
0.8	0.5	1.14	0.337	0.373
0.7	0.5	1.05	0.303	0.333

Water Vapour Path vs. Clear Sky Radiance

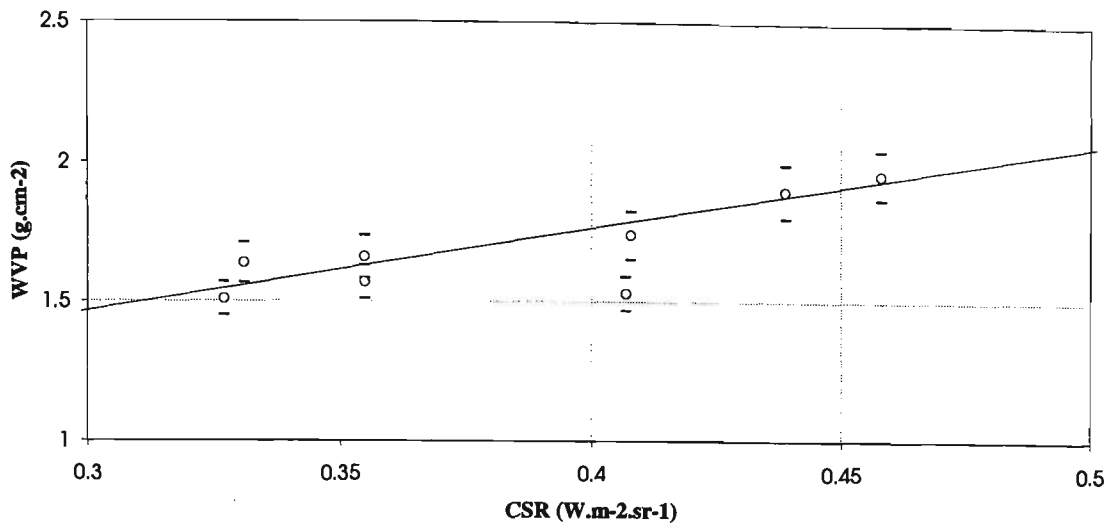


Figure 4.28. WVPs measured by MWR vs. CSRs measured by IRR, (circles), and a linear regression between these data.

Clear Sky Radiances (8 February 1995)

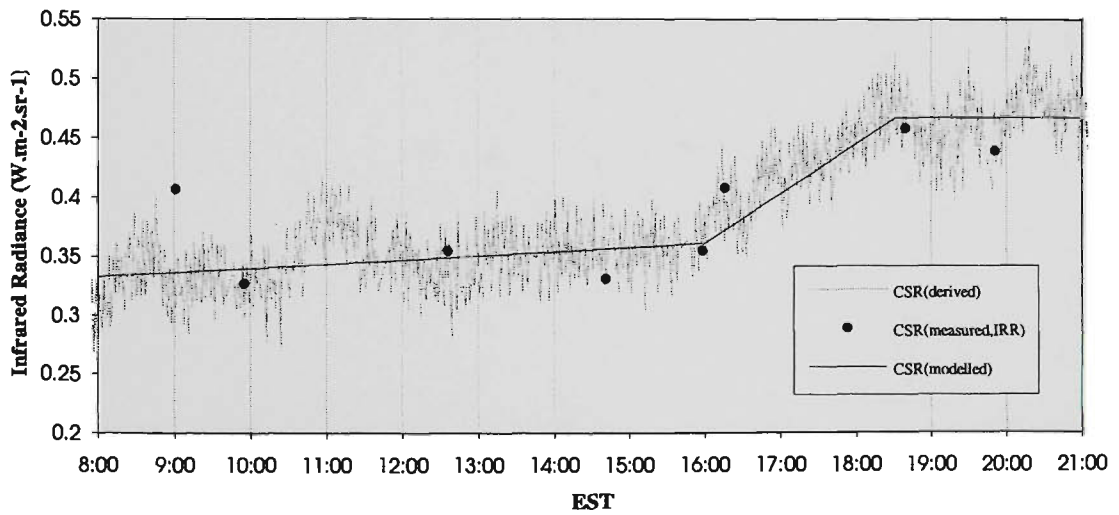


Figure 4.29. Clear sky radiances measured by the infrared radiometer (filled circles), clear sky radiances determined from the microwave radiometer measured water vapour paths (grey and noisy curve), and the modelled continuous clear sky radiance (solid line).

Height Profiles of Water Vapour Mixing Ratio

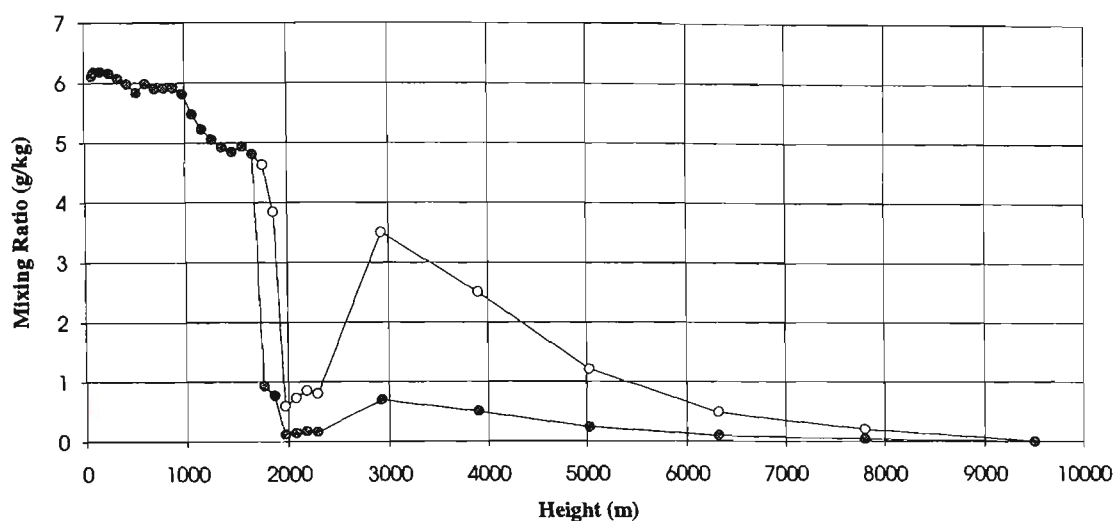


Figure 4.30. Height profiles of the water vapour mixing ratio. The upper profile (open circles) above 2300 m contains is data obtained from distant radiosonde measurements. The lower profile (filled circles) was deduced from aerological measurements made aboard the SOCEX aircraft, and measurements of water vapour paths and clear sky radiances at Cape Grim.

Clear Sky Radiances vs. Water Vapour Paths

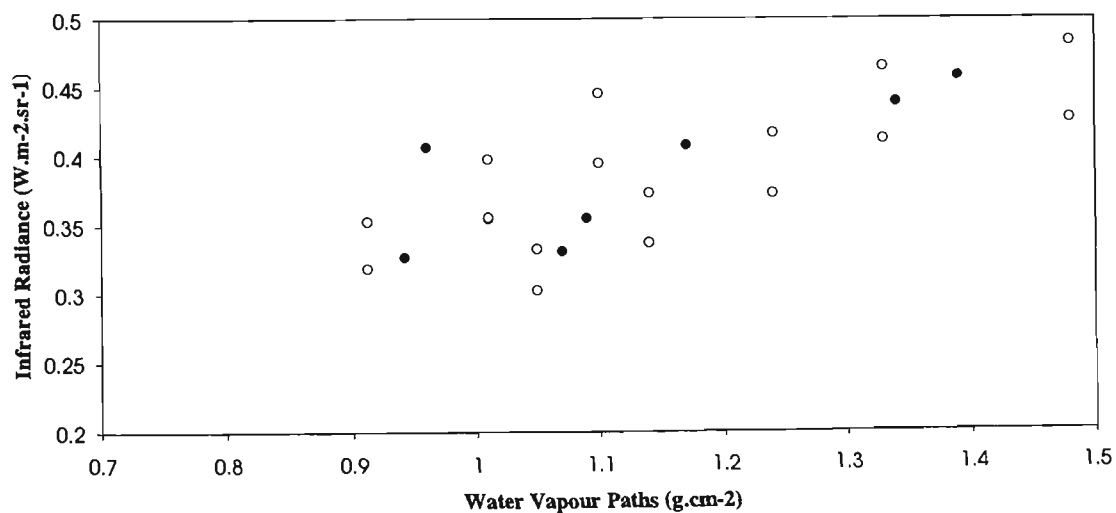


Figure 4.31. Measured clear sky radiances and water vapour paths (filled circles) and calculated values (open circles). The calculated quantities are given in Table 4.23.

The infrared transmittances and clear sky radiances given in Table 4.23 and shown in Figure (4.31), and the parameterisation of the infrared transmittances, are shown in Figure (4.32). This parameterisation was used in the LIRAD analysis method to determine the infrared transmittance of the water vapour up to cloud base (cf. 4.3.4.7).

The analysis of this LIRAD SOCEX2 dataset was basic when compared to that for SOCEX1, and this was because the quality of the SOCEX2 results was limited by the low signal-to-noise ratio of the minilidar. So the downwelling infrared radiances from the water vapour from above these higher clouds, which would only have a small effect on the results, were not considered. The uncertainties in the final LIRAD results are investigated in section 5.4.

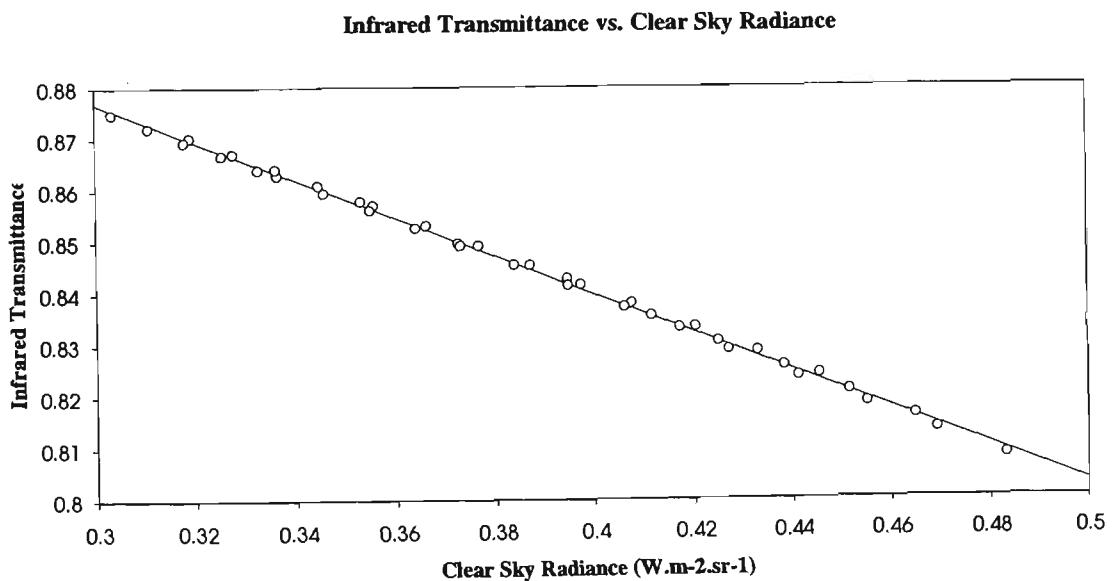


Figure 4.32. Calculated infrared transmittances of cloud-free air versus calculated clear sky radiances (open circles), and a line of best fit. The gradient is -0.370 and the offset 0.988.

5. Results

5.1 Introduction

The results of the analyses of some of the lidar and infrared radiometer measurements of the marine boundary layer clouds observed overhead Cape Grim during the winter and summer phases of SOCEX, are given in this chapter. The heights of these clouds, which were determined from the lidar measurements, are given in section 5.2.

On the afternoon of 16 July 1993 the marine stratocumulus clouds overhead Cape Grim were measured by the lidar and infrared radiometer without interruption from rain. Also, during this period, the microphysics of similar clouds were being measured *in situ* by instruments mounted aboard a Fokker F-27 aircraft, which flew over the sea and upwind to the west of Cape Grim. Thus, because of fine weather conditions at Cape Grim, the simultaneous LIRAD and *in situ* measurements, and the clean air (baseline) conditions, the clouds observed by LIRAD on 16 July 1993 from approximately 1430 - 1700 EST became the focus of study for this thesis. The results for the microphysical and optical properties of the non-precipitating marine stratocumulus clouds determined from the measurements of 16 July 1993 (SOCEX1) are given in section 5.3. The cloud heights determined from the lidar data of this day are shown in more detail in section 5.3.2; these heights by lidar provided an initial inspection of the types, precipitation and geometrical structure of the clouds. The results for some of the microphysical properties of the clouds observed on 16 July 1993 are given in section 5.3.4, and the results of the LIRAD method are given in section 5.3.5.

The microphysics of the clouds observed during SOCEX, including on 16 July 1993, were investigated thoroughly by Boers *et al.* (1996) and Boers *et al.* (1998). The properties of the clouds determined from the *in situ* measurements of 16 July 1993 are presented here, first to assist in the interpretation of the results of the LIRAD measurements (Cape Grim), and secondly for the retrieval of the multiple scatter factor (η) by a comparison of some of the *in situ* properties with the LIRAD results. Also, all these *in situ* results were considered important for any comparisons that may be made in future.

The results of a shorter study of the LIRAD measurements of 8 February 1995 (SOCEX2) are given in section 5.4.

5.2 Lidar Observations of Cloud Heights During SOCEX

The heights of cloud base and apparent cloud top were determined from the lidar measurements made at Cape Grim during SOCEX1 (winter) and SOCEX2 (summer) by Pickett *et al.* (1996). Some of these heights are shown in Figures 5.1a to 5.2c.

The heights of some of the decks of (mainly) non-precipitating stratocumulus clouds observed during SOCEX1 are shown in Figures 5.1a - 5.1c. On 10 July 1993 (Figure 5.1a) at about 1330 EST and about 1600 EST, the large apparent depths caused by the spuriously low heights of cloud base are due to backscatter by precipitation. There is a wider variation in the apparent depths of the non-precipitating clouds observed on 16 July 1993 (Figure 5.1b). There is also a wide variation in the apparent depths of the clouds observed on 18 July 1993 (Figure 5.1c).

The heights of some stratocumulus and cumulus clouds observed for one hour on three days during SOCEX2 are shown in Figures 5.2a - 5.2c. The cloud height regime of a deck of stratocumulus clouds with underlying broken cumulus clouds seen by inspection of these figures was typical for SOCEX2. In Figure 5.2a (6 February 1995) the stratocumulus clouds are seen to occupy the height region 1500 - 2000 m and cumulus exists at approximately 1000 m. On 7 February 1995 from 0630 - 0730 EST the high apparent depths are probably due to precipitation (Figure 5.2b): between 0655 - 0725 EST, the average apparent cloud top of these data is $1660 \text{ m} \pm 200 \text{ m}$.

On 8 February 1995, (Figure 5.2c), the lower heights of cloud base between approximately 1020 - 1040 EST, with no corresponding changes in the apparent depths of the clouds, indicates these thick clouds fully attenuated the lidar pulse.

Cloud Heights and Apparent Depths (10 July 1993)

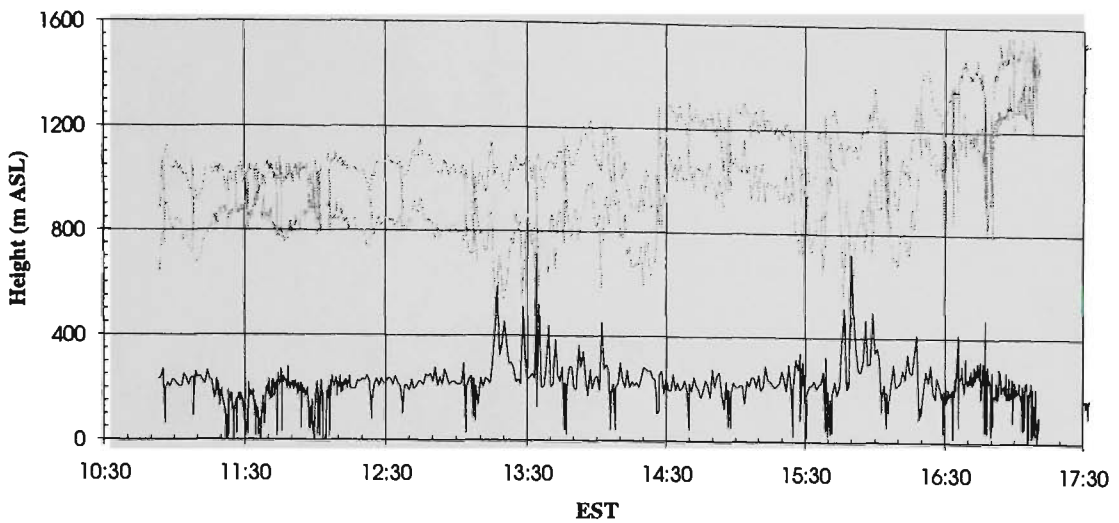


Figure 5.1a. Lidar-retrieved cloud heights of stratocumulus clouds observed over Cape Grim on 10 July 1993 (SOCEX1). The upper curves (grey) show the heights of cloud base and apparent cloud tops. The lower curve (black) shows the apparent depths (m) of the clouds.

Cloud Heights and Apparent Depths (16 July 1993)

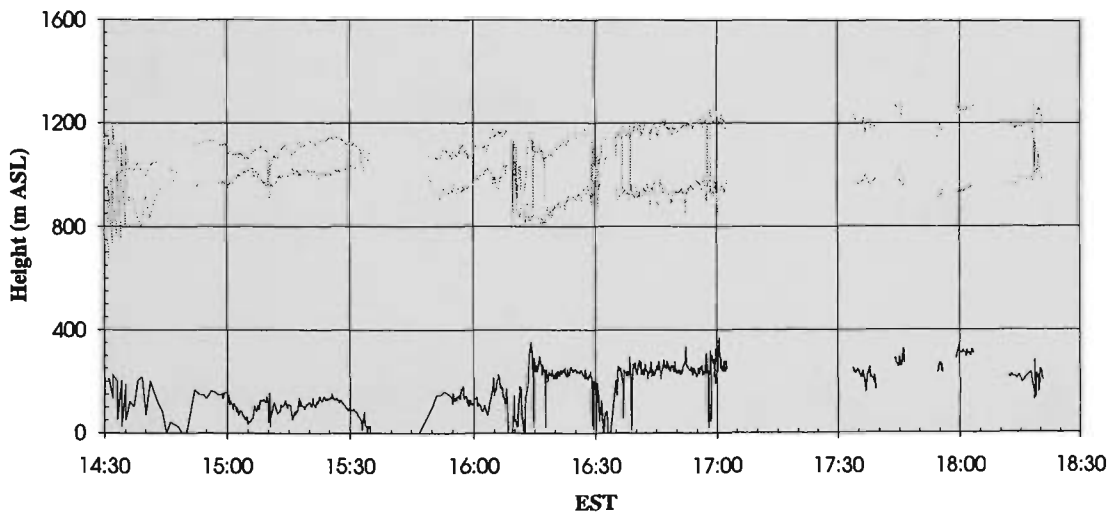


Figure 5.1b. Lidar-retrieved cloud heights of stratocumulus clouds observed over Cape Grim on 16 July 1993 (SOCEX1). The upper curves (grey) show the heights of cloud base and apparent cloud tops. The lower curve (black) shows the apparent depths (m) of the clouds.

Cloud Heights and Apparent Depths (18 July 1993)

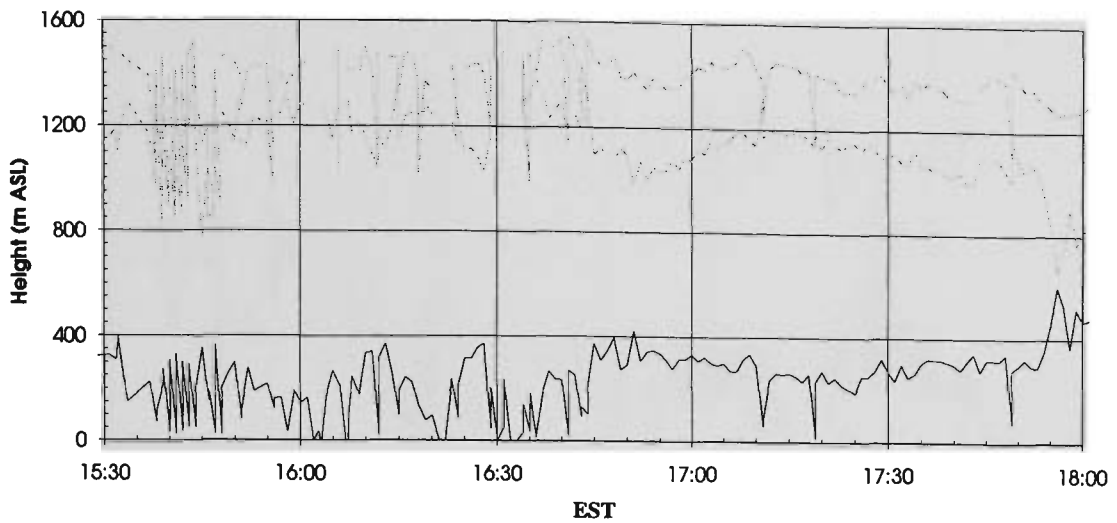


Figure 5.1c. Lidar-retrieved cloud heights of stratocumulus clouds observed over Cape Grim on 18 July 1993 (SOCEX1). The upper curves (grey) show the heights of cloud base and apparent cloud tops. The lower curve (black) shows the apparent depths (m) of the clouds.

Cloud Heights and Apparent Depths (6 February 1995)

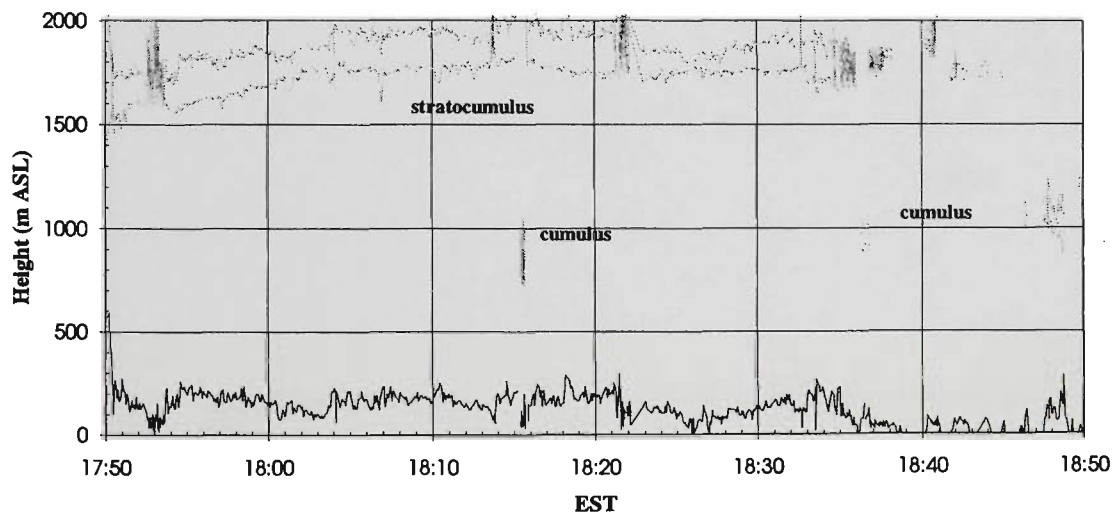


Figure 5.2a. Lidar-retrieved cloud heights of stratocumulus clouds observed over Cape Grim on 6 February 1995 (SOCEX2). The upper curves (grey) show the heights of cloud base and apparent cloud tops. The lower curve (black) shows the apparent depths (m) of the clouds.

Cloud Heights and Apparent Depths (7 February 1995)

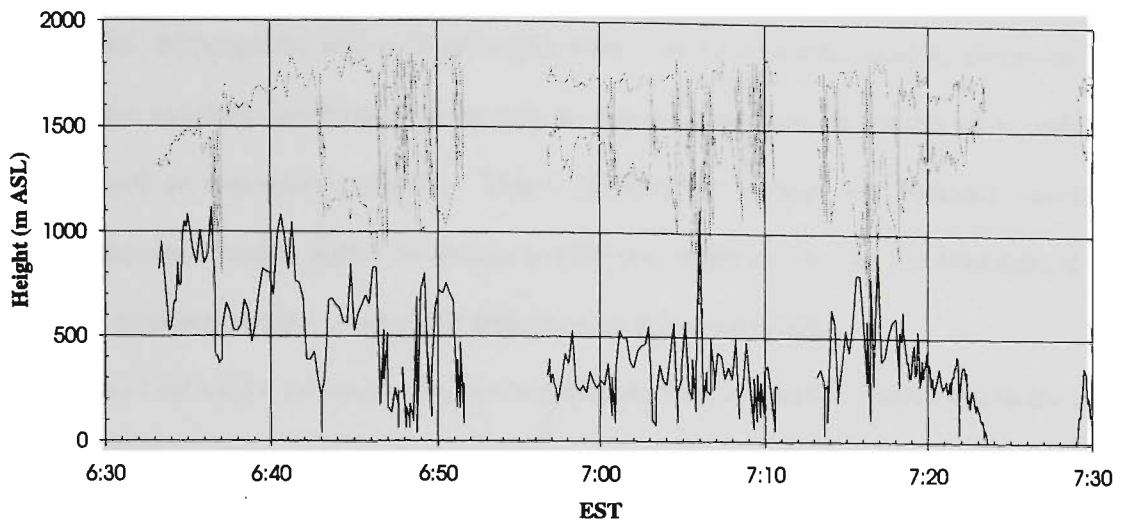


Figure 5.2b. Lidar-retrieved cloud heights of stratocumulus clouds observed over Cape Grim on 7 February 1995 (SOCEX2). The upper curves (grey) show the heights of cloud base and apparent cloud tops. The lower curve (black) shows the apparent depths (m) of the clouds. The lower indicated cloud base of the stratocumulus clouds is probably due to drizzle.

Cloud Heights and Apparent Depths (8 February 1995)

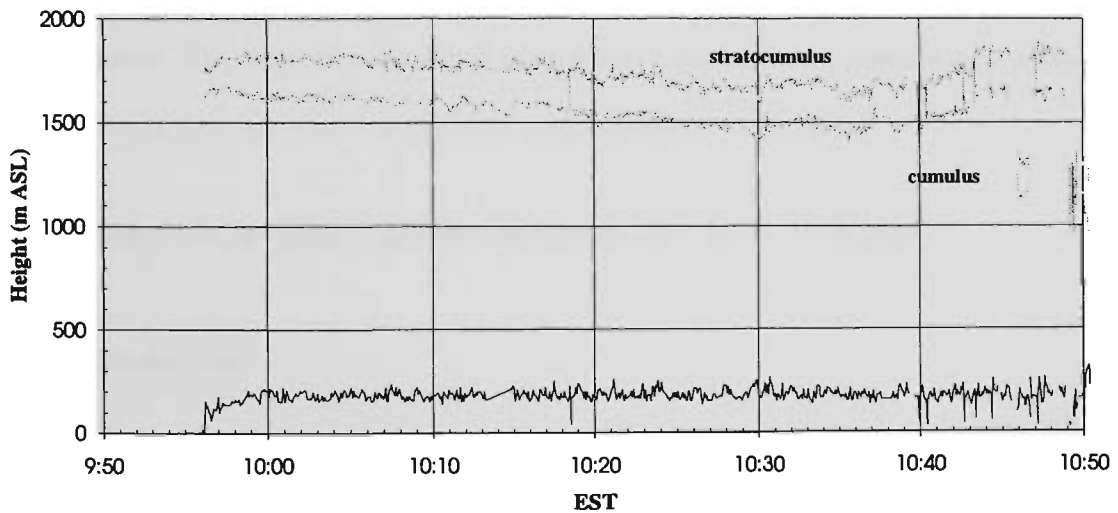


Figure 5.2c. Lidar-retrieved cloud heights of stratocumulus clouds observed over Cape Grim on 8 February 1995 (SOCEX2). The upper curves (grey) show the heights of cloud base and apparent cloud tops. The lower curve (black) shows the apparent depths (m) of the clouds.

The distributions of the heights of lowest cloud base for all the SOCEX data are shown in Figure 5.3. The results of the lowest height bin, 0 - 200 m, were affected by rain interrupting the measurements. Although the winter cloud heights were more heavily influenced by precipitation than in the summer, and these distributions show only the lowest cloud base, the results agree with what is expected based on atmospheric physics. That is, holding air pressure and humidity constant, the lifting condensation level is higher in warmer conditions. However the data set investigated here is too small to draw conclusions on seasonal differences in the cloud heights.

The cloud height statistics were then recalculated only for periods during which the air mass over Cape Grim was of maritime origin ('baseline' conditions; see section 3.1.2). The peaks in the distribution of the heights of cloud base for the summer (1600 - 1800 m) and winter (800 - 1000 m) are due to stratocumulus. The peak in the summer distribution in the 1000 - 1200 m height bin is mainly due to cumulus. Two notable results of the baseline statistics were the lower incidence of clouds and precipitation in the lower height bins and the absence of clouds above about 2000 m (Figure 5.4). The clouds at a height of approximately 3000 m in the all-weather conditions result were altostratus clouds - and they were much less likely to exist in baseline conditions. In general, the free troposphere above the maritime stratocumulus clouds was cloud-free in baseline conditions during both seasonal phases of SOCEX: this was probably due to the subsidence of air under advancing high pressure systems. This result of a cloud-free troposphere in the baseline conditions was verified from extensive photographic and visual observations made aboard the F-27 aircraft.

5.3 Properties of Clouds Observed on 16 July 1993 (SOCEX1)

5.3.1 Introduction

On the afternoon of 16 July 1993 the marine stratocumulus clouds overhead Cape Grim were measured by the lidar and infrared radiometer without interruption from rain (this was illustrated previously in Figure 5.1.b). Thus, because of the fine weather conditions at Cape Grim, the simultaneous LIRAD and *in situ* measurements and the clean air (baseline) conditions, the clouds observed by LIRAD on this day from approximately 1430 - 1700 EST became the focus of study for this thesis.

Heights of Cloud Base (All Air Conditions)

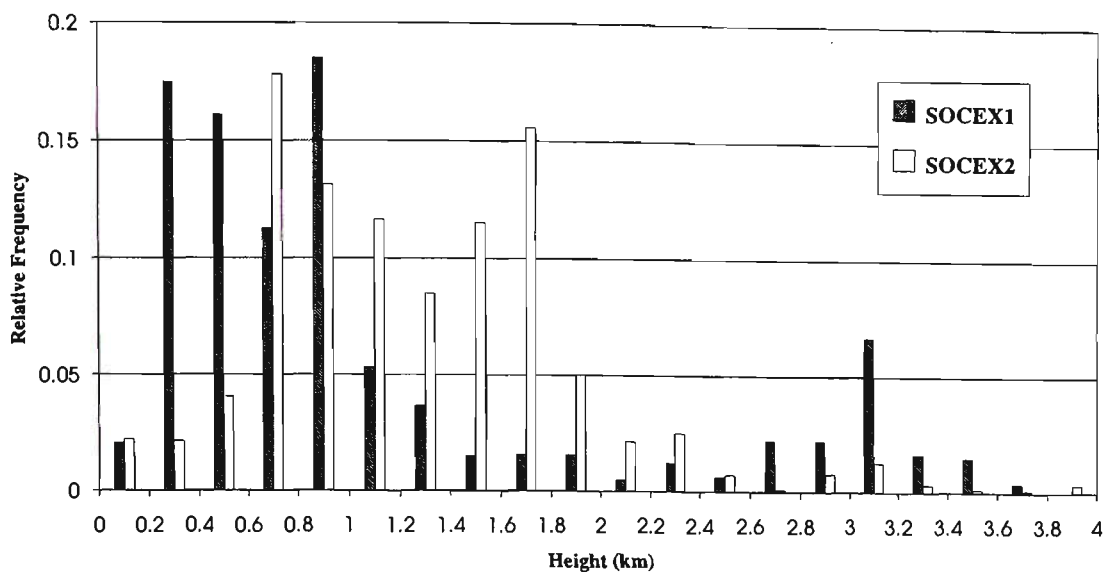


Figure 5.3. Heights of the lowest cloud base for all weather conditions for SOCEX1 and SOCEX2. Heights were recorded up to the 7600-7800 m height bin, but few clouds were detected above 4000 m so these have been excluded from this figure. The areas under the curves have been normalised to unity.

Heights of Cloud Base (Maritime Air)

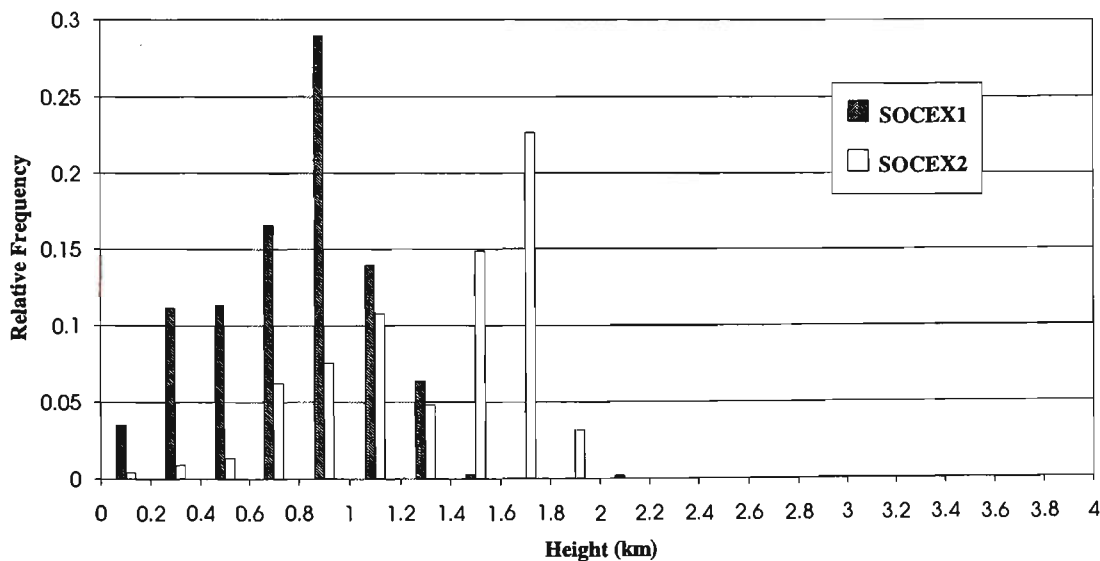


Figure 5.4. Heights of lowest cloud base for maritime-air conditions only, for both phases of SOCEX. The areas under the curves have been normalised to unity.

5.3.2 Lidar Observations of Cloud Heights on 16 July 1993 (In Detail)

The heights of the clouds for the period 1430 - 1700 EST are illustrated in greater detail in Figures 5.5a and 5.5b. Four decks of clouds were identified, separated by 3 cloud-free ('clear') periods: the lidar returns from clear air were used for the calibration (4.3.3.9). Also, the clear periods determined from the lidar measurements were used to identify the infrared radiometer measured radiances of the clear air (4.3.4.4). The clear and cloudy periods analysed are given in Table 5.1.

Table 5.1. Cloud decks and clear periods observed on 16 July 1993.

Deck	Start time	End time	Period	Lidar shots
1	14:52:04	15:34:48	0:42:44	216
clear	15:34:59	15:46:49	0:11:50	20
2	15:48:59	16:08:13	0:19:14	83
clear	16:08:23	16:09:23	0:01:00	7
3	16:09:33	16:32:49	0:23:16	145
clear	16:32:59	16:33:39	0:00:40	3
4	16:34:56	17:02:29	0:27:33	170

Some statistics of the cloud heights were calculated for each of the four cloud decks defined by the periods in Table 5.1: (1) average heights of cloud base ($\langle z_b \rangle$), (2) average heights of the peak of the lidar cloud-signal ($\langle z_p \rangle$), (3) the differences $\langle z_p \rangle - \langle z_b \rangle$, (4) average (apparent) cloud depths ($\langle h \rangle$). These results are shown in Table 5.2.

Table 5.2. Cloud heights (z) and depths (h) of the cloud decks. (Units are metres).

Deck	$\langle z_b \rangle$	$\langle z_p \rangle$	$\langle z_p \rangle - \langle z_b \rangle$	$\langle h \rangle$
1	997	1032	35	103
2	972	1035	62	137
3	880	914	33	185
4	939	979	39	241

Stratocumulus Cloud Heights (16 July 1993)

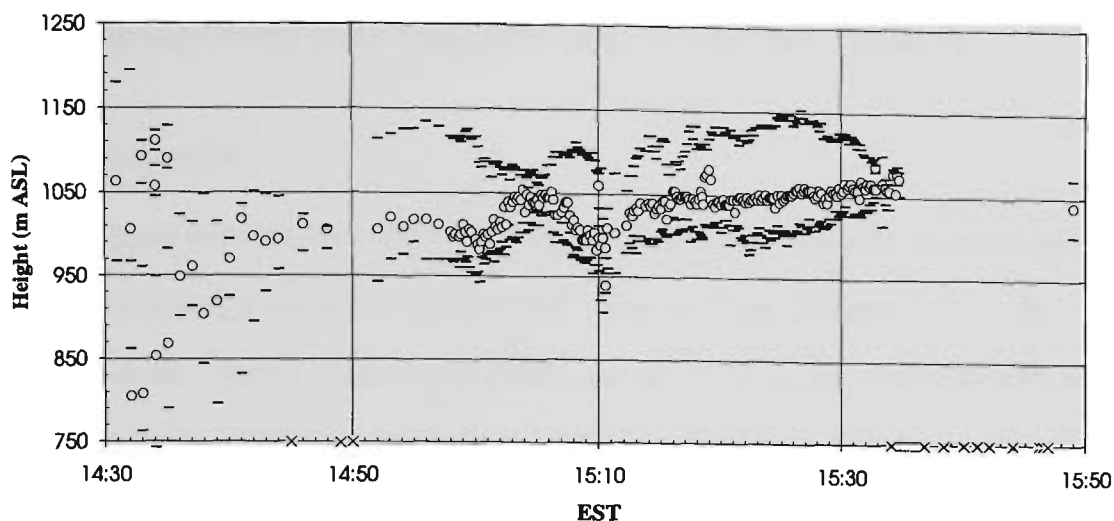


Figure 5.5a. Lidar measured heights of stratocumulus clouds observed on 16 July 1993. Heights of cloud base and apparent cloud tops are represented by horizontal bars, and the heights at which the peak lidar signals occurred are represented by circles. Crosses indicate cloud-free air. There was precipitation prior to approximately 1450 EST.

Stratocumulus Cloud Heights (16 July 1993)

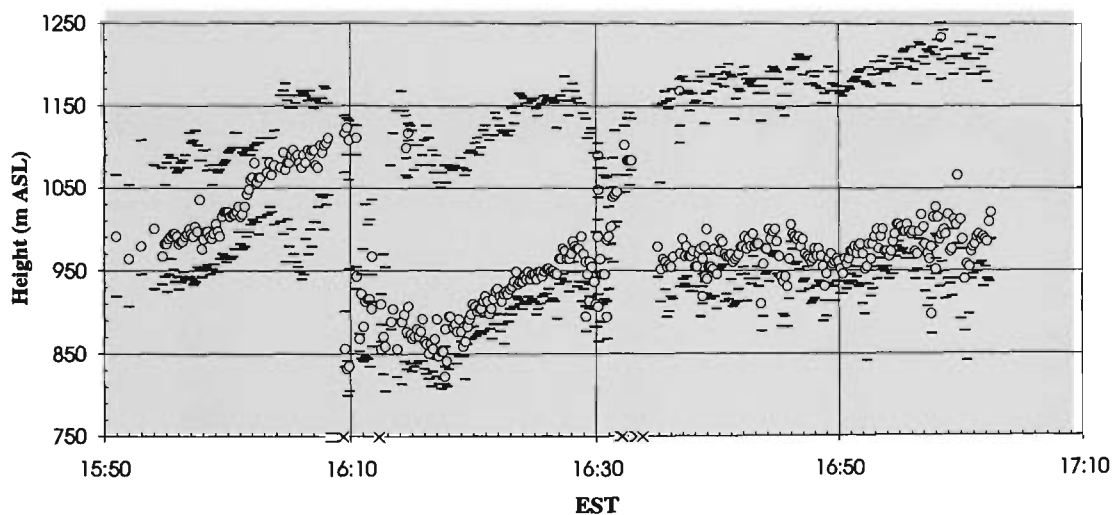


Figure 5.5b. Lidar measured heights of marine stratocumulus clouds observed on 16 July 1993 (1550 - 1710 EST). Heights of cloud base and apparent cloud tops are represented by horizontal bars, and the heights at which the peak lidar signals occurred are represented by circles. Crosses indicate cloud-free air. A deeper cloud deck passed overhead Cape Grim at approximately 1610 EST.

5.3.3 Microphysical and Optical Properties of Stratocumulus Clouds by the In Situ Scattering Probes (FSSP and 2D-C) On 16 July 1993 (Flight 8)

5.3.3.1 Introduction

The *in situ* liquid water and optical properties of the clouds calculated from the measured Droplet Size Distributions (DSDs) are presented in this section. The DSDs were measured continually at various heights (z) in the boundary layer, in the clouds, and above the clouds by the Forward Scattering Spectrometer Probe (FSSP) and drizzle probe (2D-C) (see Chapter 3). The cloud measurements had to be extracted first from these supplied spectrometer probe datasets. To do this, total droplet concentrations (N) were calculated for every DSD measured at height z . The FSSP-measured N were used to identify eight separate passes through the clouds, and these height-sections were labelled 'cloud 1' through to 'cloud 8'.

The cloud heights and depths are shown below in Table 5.3. The column labelled ' $n(\text{DSDs})$ ' indicates the numbers of DSDs recorded. The measured DSDs were determined from layers of cloud approximately 7 m deep (see last column of the table). Averages (x) and variabilities (\pm one standard deviation) are shown in the last row of the table.

Table 5.3. Airborne FSSP-measured cloud heights (SOCEX1, 16 July 1993, Flight 8).

Cloud section	Cloud base (m)	Cloud top (m)	Depth (m)	$n(\text{DSDs})$	DSD depth (m)
1	952	1251	300	43	7.0
2	997	1219	222	20	11
3	978	1126	148	21	7.1
4	1026	1321	295	53	5.6
5	1087	1353	267	45	5.9
6	993	1382	388	79	4.9
7	1063	1202	139	19	7.3
8	454	904	451	73	6.2
$x \pm s$	1014 ± 48	1265 ± 91	251 ± 89	44 ± 24	6.9 ± 1.9

These clouds were observed by the F-27 instruments over the sea from 12 to 72 nautical miles to the west of Cape Grim and did not pass over Cape Grim until about 1610 EST. The heights and depths of these clouds correspond well with the clouds measured by lidar (see previous section, 5.3.2). For example, the heights of cloud base of the marine clouds (1 - 7) and those measured over

Cape Grim are both approximately 1000 m ASL. The apparent depths of the four cloud decks measured by lidar ranged from approximately 100 - 240 m and these also match reasonably well to the depths of the marine clouds measured by the FSSP: 140 - 390 m. (The lidar signal was attenuated in the deeper clouds so the true cloud top was not measured in these cases).

Clouds 1-7 were measured over the sea, so that the properties of these clouds were deduced separately from those of cloud 8, which was measured over land approximately 240 nm to the east and downwind of Cape Grim. The *in situ* data shows that Cloud 8 was broken, lower and deeper than clouds 1-7. In the sections to follow, sometimes only the *in situ* properties of the non-precipitating clouds, 1-3 and 5-7 were determined. This was to enable better comparisons with the LIRAD and microwave radiometer results for the non-precipitating clouds observed overhead Cape Grim. In the following the *in situ* liquid water properties of the clouds are given in sections (5.3.3.2) to (5.3.3.6), and the *in situ* optical properties in sections (5.3.3.7) to (5.3.3.13).

5.3.3.2 Droplet Size Distributions

The DSDs of the cloud height-sections of clouds 1 - 8 are shown in the eight pairs of figures labelled Figure 5.6 through to Figure 5.21. The first figures of the pairs (*e.g.* Figure 5.6) show the entire DSDs measured by both the FSSP and 2D-C, and these show the more numerous 'cloud droplet' mode with droplet radii ranging from about 1- 20 μm and mode radii near 10 μm , and the less numerous 'drizzle droplet' mode with radii ranging from about 20 - 1000 μm . The DSDs over the FSSP measurement-range only are shown in the second figures of the pairs (*e.g.* Figure 5.7). These figures clearly show the mode radii of the droplets increasing with height into the clouds. Later this will be seen to cause an almost linear increase of extinction with height into the clouds. There appeared to be no 2D-C measurements for cloud 7: the data were all zero and the reason for this was not determined. Note the greater quantities of drizzle in cloud 4 (Figures 5.12 and 5.13) and the cloud observed over land, cloud 8 (Figures 5.20 and 5.21). The DSDs for the 7 marine clouds were used to determine the Mie scattering properties of the clouds, which were important for understanding the lidar and LIRAD measurements and retrievals of the backscatter, extinction and optical depths of the clouds observed over Cape Grim. Retrievals of the microphysical properties from these DSDs, combined with some of the LIRAD results enabled a retrieval of the multiple scatter factor (η) for the clouds. These results will be described later in this chapter.

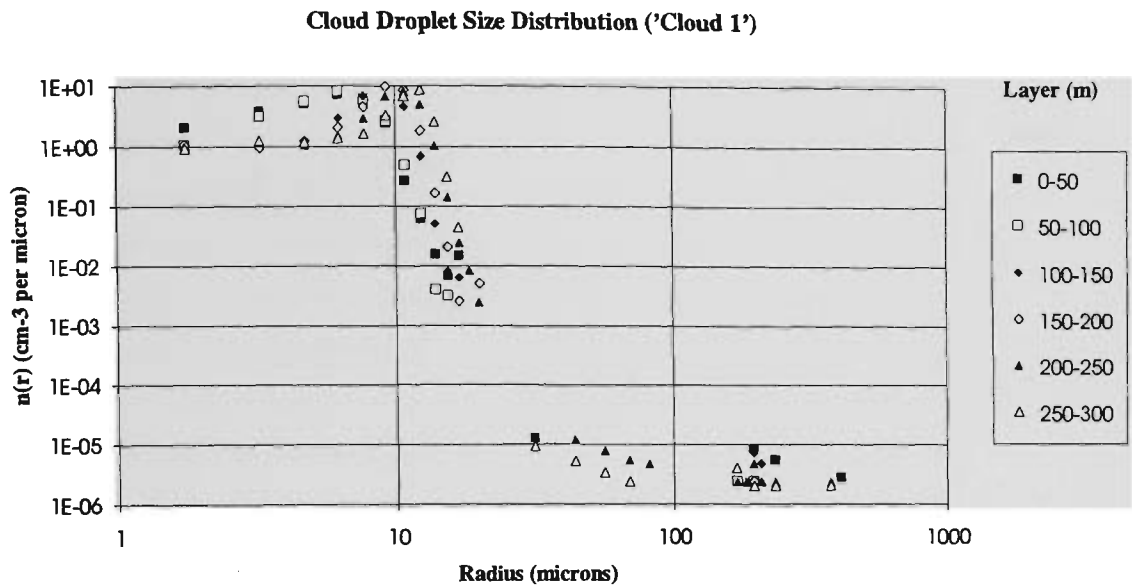


Figure 5.6. Cloud droplet size distributions measured by the FSSP and drizzle (2D-C) probes, of the cloud height-section labelled 'cloud 1'. The droplet concentrations $n(r)$ ($\text{cm}^{-3} \cdot \mu\text{m}^{-1}$) versus droplet radius (μm) have been divided into 50 metre-deep layers into the cloud, starting with the lowest height layer (0 - 50 m).

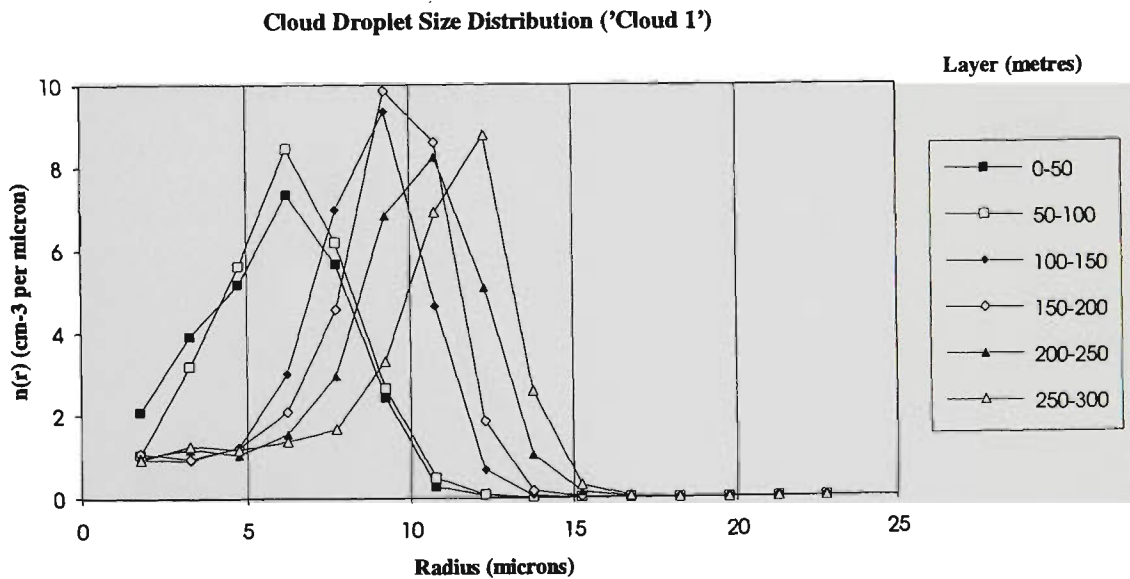


Figure 5.7. Cloud droplet size distributions measured by the FSSP for the cloud height-section labelled 'cloud 1'. The droplet concentrations $n(r)$ ($\text{cm}^{-3} \cdot \mu\text{m}^{-1}$) versus droplet radius (μm) have been divided into 50 metre-deep layers into the cloud, starting with the lowest height layer (0 - 50 m).

Cloud Droplet Size Distribution ('Cloud 2')

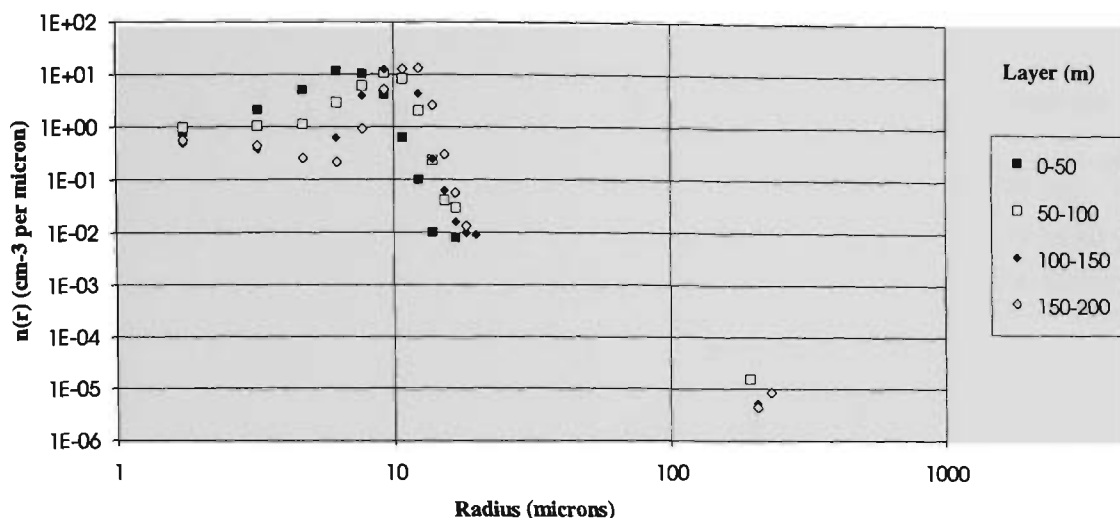


Figure 5.8. Cloud droplet size distributions measured by the FSSP and drizzle (2D-C) probes, of the cloud height-section labelled 'cloud 2'. The droplet concentrations $n(r)$ ($\text{cm}^{-3} \cdot \mu\text{m}^{-1}$) versus droplet radius (μm) have been divided into 50 metre-deep layers into the cloud, starting with the lowest height layer (0 - 50 m).

Cloud Droplet Size Distribution ('Cloud 2')

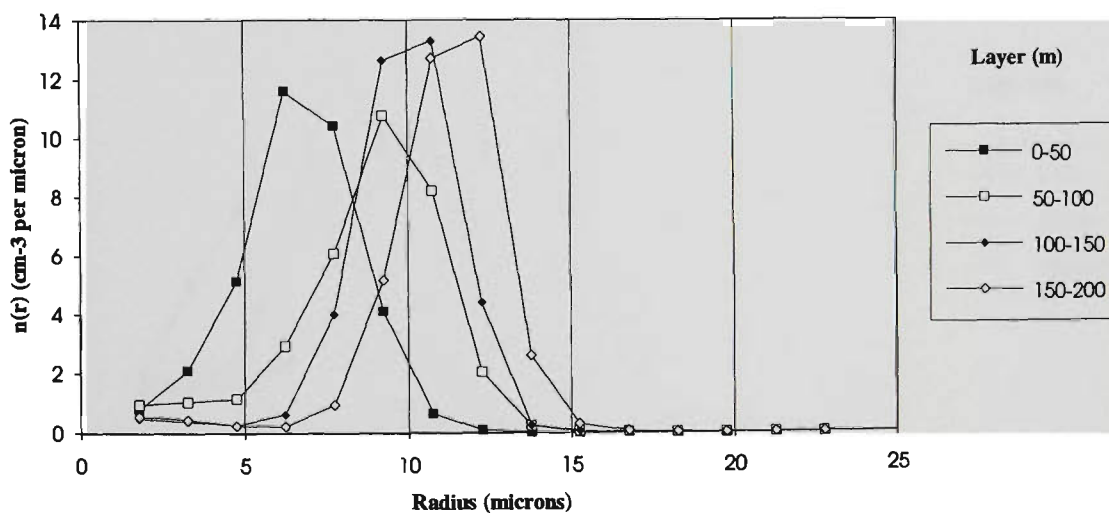


Figure 5.9. Cloud droplet size distributions measured by the FSSP for the cloud height-section labelled 'cloud 2'. The droplet concentrations $n(r)$ ($\text{cm}^{-3} \cdot \mu\text{m}^{-1}$) versus droplet radius (μm) have been divided into 50 metre-deep layers into the cloud, starting with the lowest height layer (0 - 50 m).

Cloud Droplet Distribution ('Cloud 3')

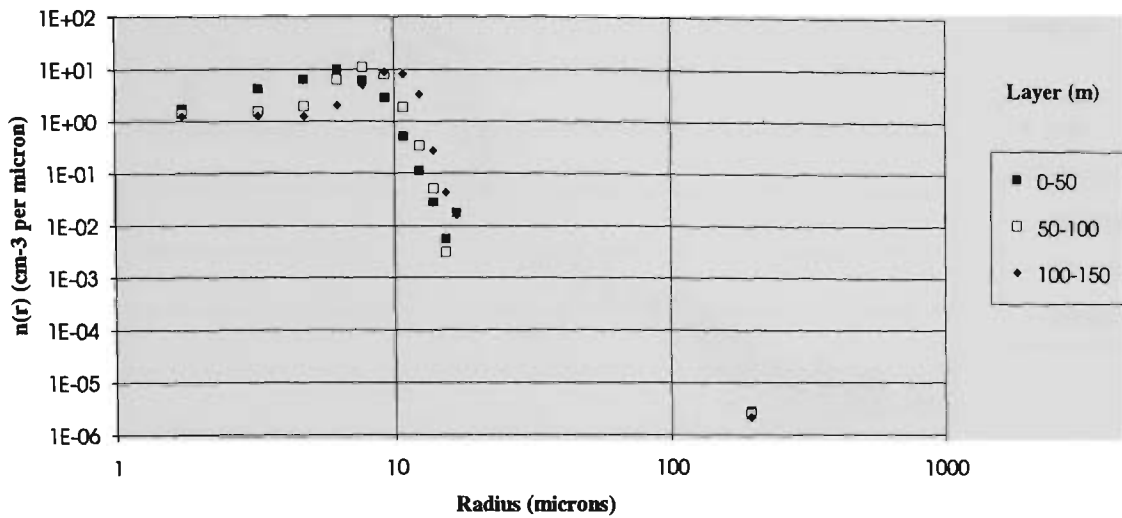


Figure 5.10. Cloud droplet size distributions measured by the FSSP and drizzle (2D-C) probes, of the cloud height-section labelled 'cloud 3'. The droplet concentrations $n(r)$ ($\text{cm}^{-3} \cdot \mu\text{m}^{-1}$) versus droplet radius (μm) have been divided into 50 metre-deep layers into the cloud, starting with the lowest height layer (0 - 50 m).

Cloud Droplet Size Distribution ('Cloud 3')

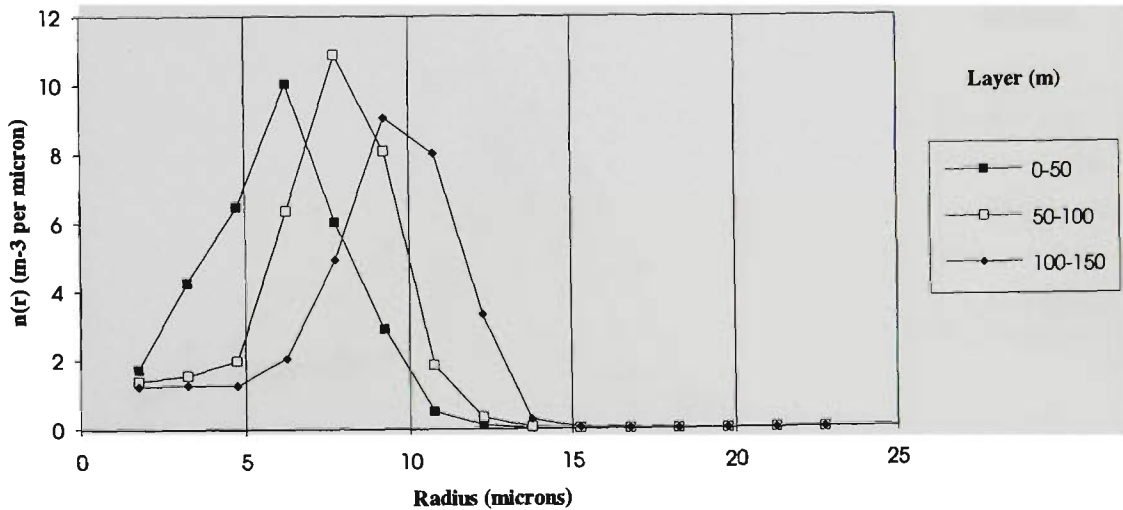


Figure 5.11. Cloud droplet size distributions measured by the FSSP for the cloud height-section labelled 'cloud 3'. The droplet concentrations $n(r)$ ($\text{cm}^{-3} \cdot \mu\text{m}^{-1}$) versus droplet radius (μm) have been divided into 50 metre-deep layers into the cloud, starting with the lowest height layer (0 - 50 m).

Cloud Droplet Size Distribution ('Cloud 4')

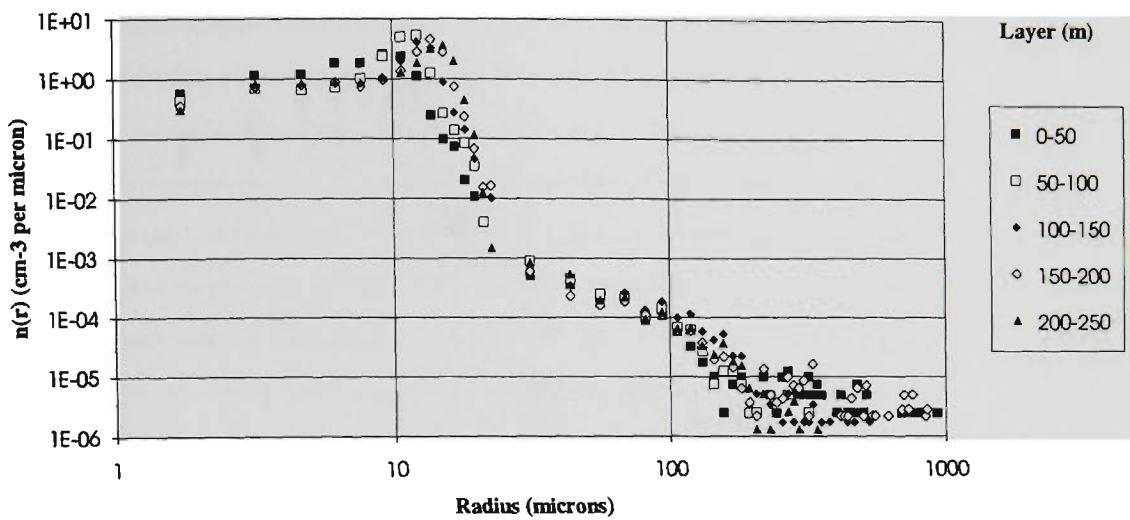


Figure 5.12. Cloud droplet size distributions measured by the FSSP and drizzle (2D-C) probes, of the cloud height-section labelled 'cloud 4'. The droplet concentrations $n(r)$ ($\text{cm}^{-3} \cdot \mu\text{m}^{-1}$) versus droplet radius (μm) have been divided into 50 metre-deep layers into the cloud, starting with the lowest height layer (0 - 50 m).

Cloud Droplet Size Distribution ('Cloud 4')

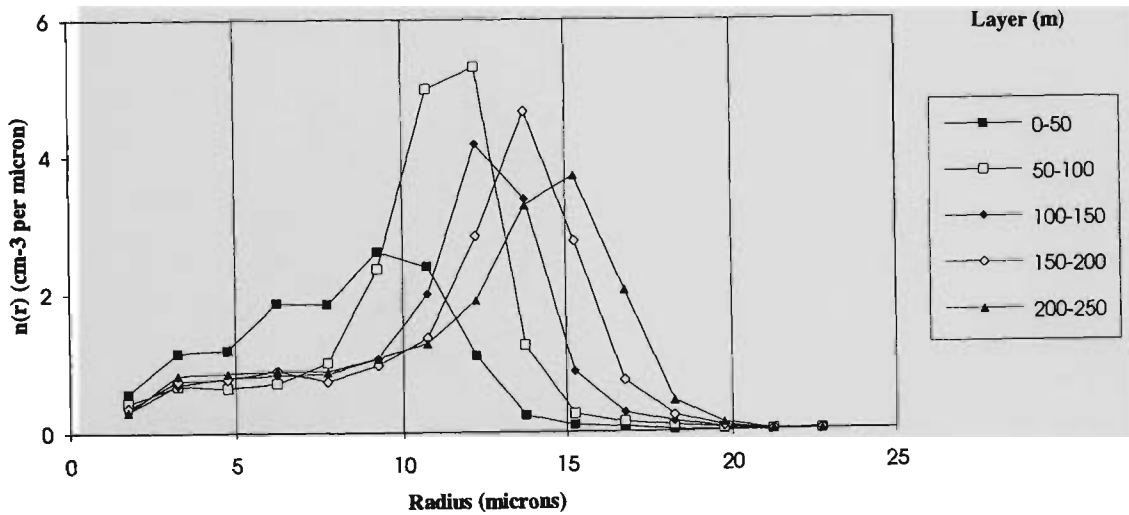


Figure 5.13. Cloud droplet size distributions measured by the FSSP for the cloud height-section labelled 'cloud 4'. The droplet concentrations $n(r)$ ($\text{cm}^{-3} \cdot \mu\text{m}^{-1}$) versus droplet radius (μm) have been divided into 50 metre-deep layers into the cloud, starting with the lowest height layer (0 - 50 m).

Cloud Droplet Size Distribution ('Cloud 5')

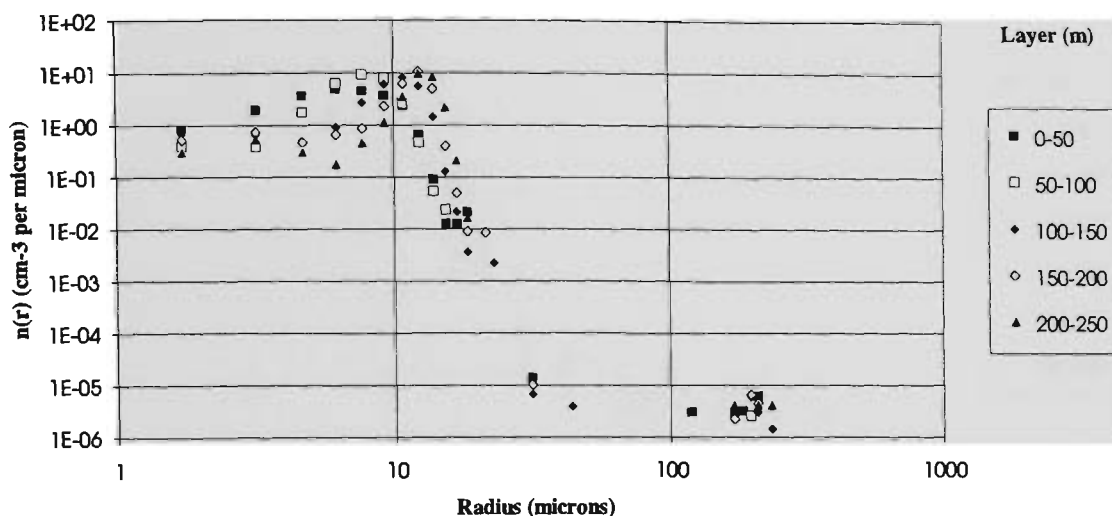


Figure 5.14. Cloud droplet size distributions measured by the FSSP and drizzle (2D-C) probes, of the cloud height-section labelled 'cloud 5'. The droplet concentrations $n(r)$ ($\text{cm}^{-3}\cdot\mu\text{m}^{-1}$) versus droplet radius (μm) have been divided into 50 metre deep layers into the cloud, starting with the lowest height layer (0 - 50 m).

Cloud Droplet Size Distribution ('Cloud 5')

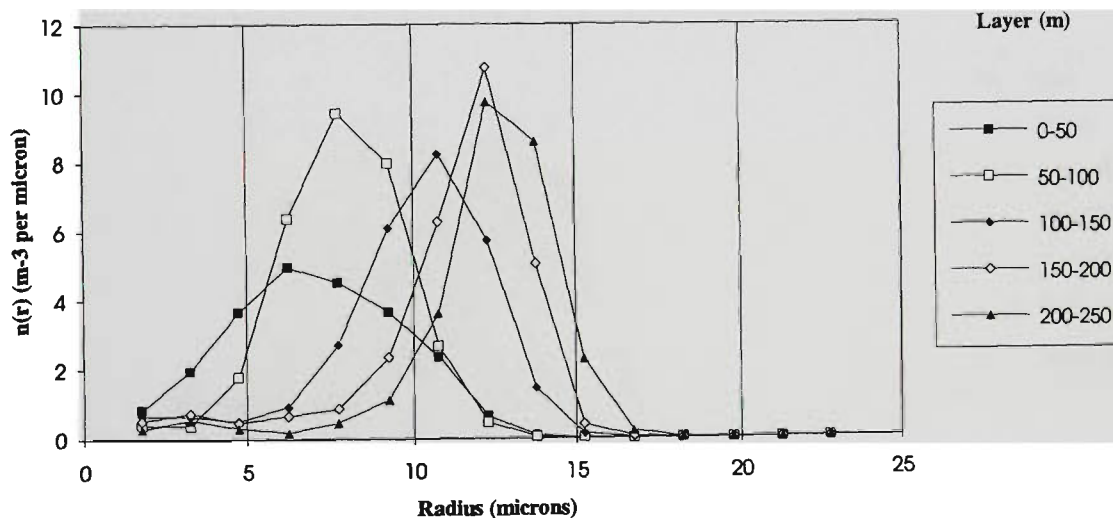


Figure 5.15. Cloud droplet size distributions measured by the FSSP for the cloud height-section labelled 'cloud 5'. The droplet concentrations $n(r)$ ($\text{cm}^{-3}\mu\text{m}^{-1}$) versus droplet radius (μm) have been divided into 50 metre-deep layers into the cloud, starting with the lowest height layer (0 - 50 m).

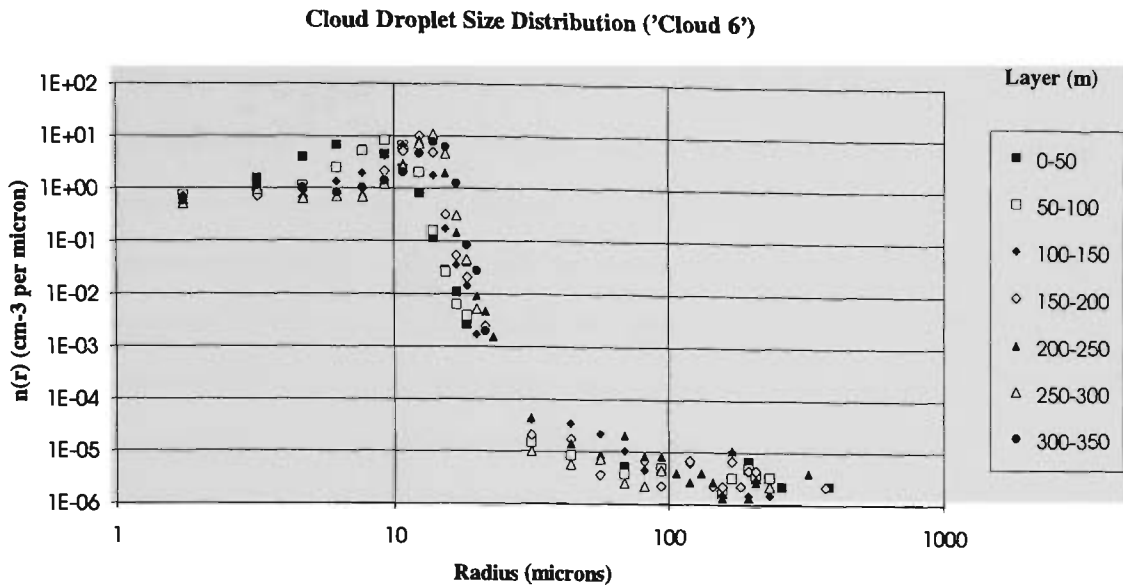


Figure 5.16. Cloud droplet size distributions measured by the FSSP and drizzle (2D-C) probes, of the cloud height-section labelled 'cloud 6'. The droplet concentrations $n(r)$ ($\text{cm}^{-3} \cdot \mu\text{m}^{-1}$) versus droplet radius (μm) have been divided into 50 metre-deep layers into the cloud, starting with the lowest height layer (0 - 50 m).

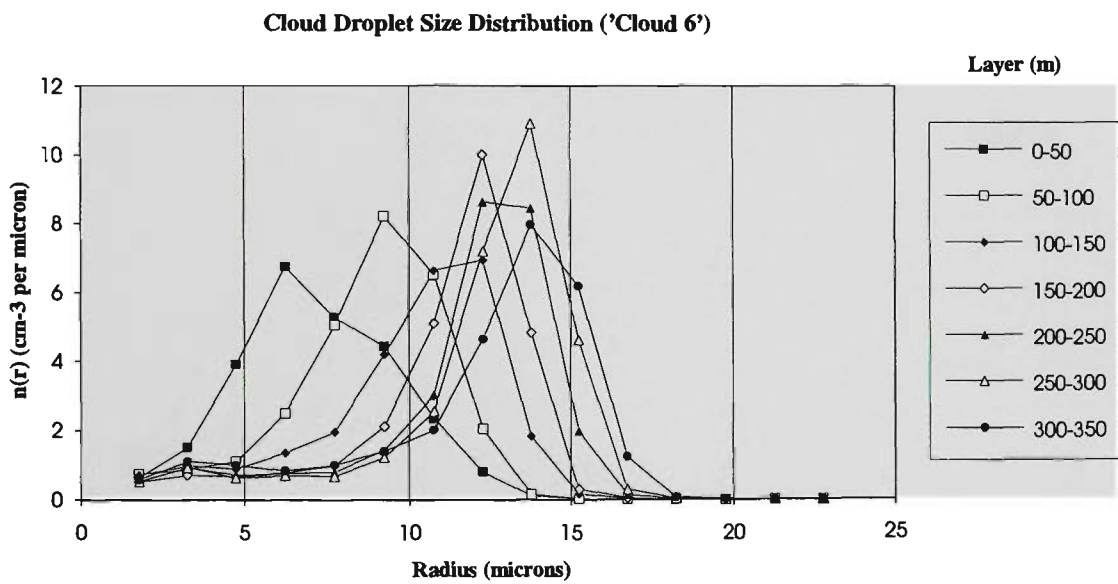


Figure 5.17. Cloud droplet size distributions measured by the FSSP for the cloud height-section labelled 'cloud 6'. The droplet concentrations $n(r)$ ($\text{cm}^{-3} \cdot \mu\text{m}^{-1}$) versus droplet radius (μm) have been divided into 50 metre-deep layers into the cloud, starting with the lowest height layer (0 - 50 m).

Cloud Droplet Size Distribution ('Cloud 7')

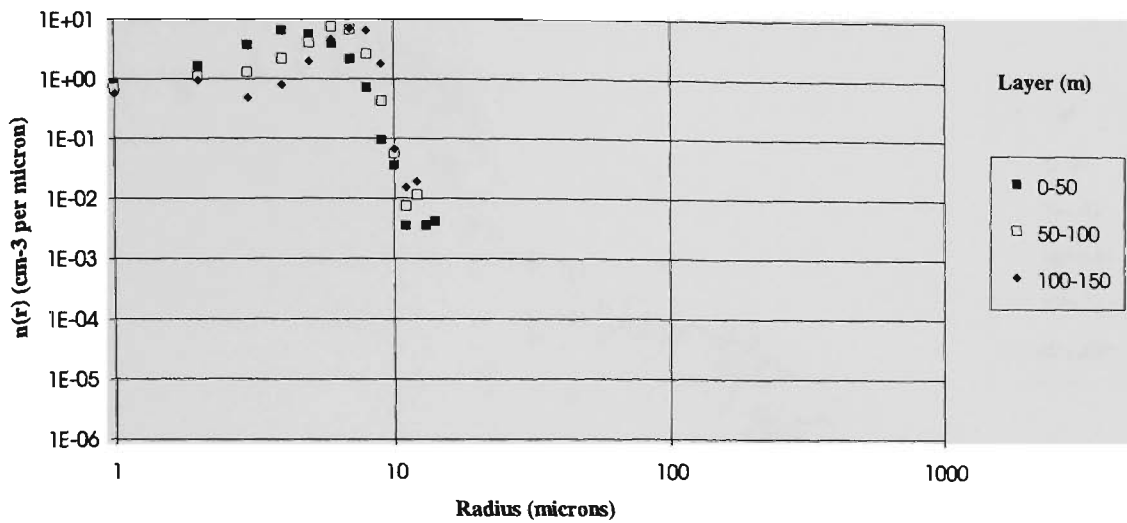


Figure 5.18. Cloud droplet size distributions measured by the FSSP of the cloud height-section labelled 'cloud 7'. There were no data for $r > 25 \mu\text{m}$; this may have been due to equipment failure. The droplet concentrations $n(r)$ ($\text{cm}^{-3} \cdot \mu\text{m}^{-1}$) versus droplet radius (μm) have been divided into 50 metre-deep layers into the cloud, starting with the lowest height layer (0 - 50 m).

Cloud Droplet Size Distribution ('Cloud 7')

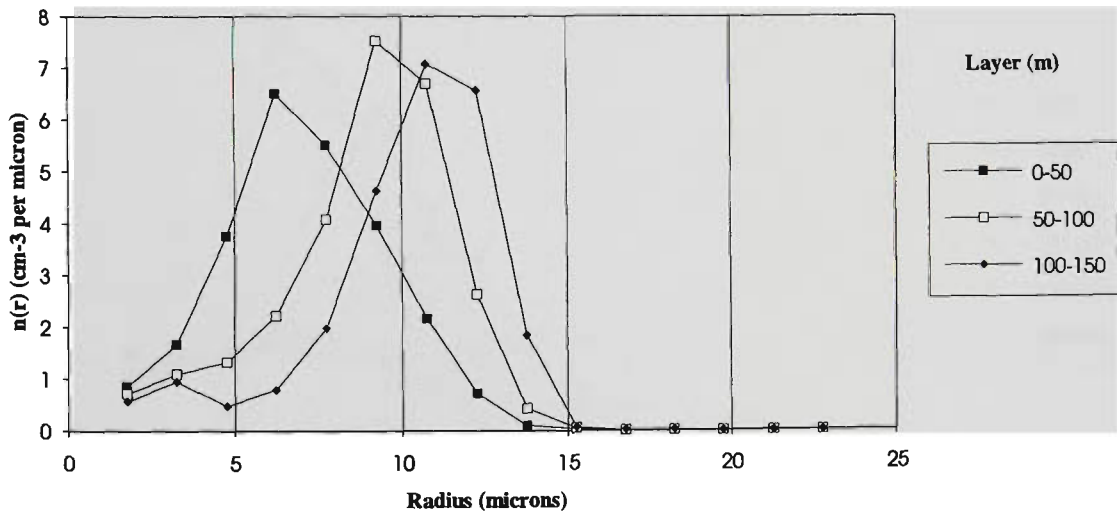


Figure 5.19. Cloud droplet size distributions measured by the FSSP for the cloud height-section labelled 'cloud 7'. The droplet concentrations $n(r)$ ($\text{cm}^{-3} \cdot \mu\text{m}^{-1}$) versus droplet radius (μm) have been divided into 50 metre deep layers into the cloud, starting with the lowest height layer (0 - 50 m).

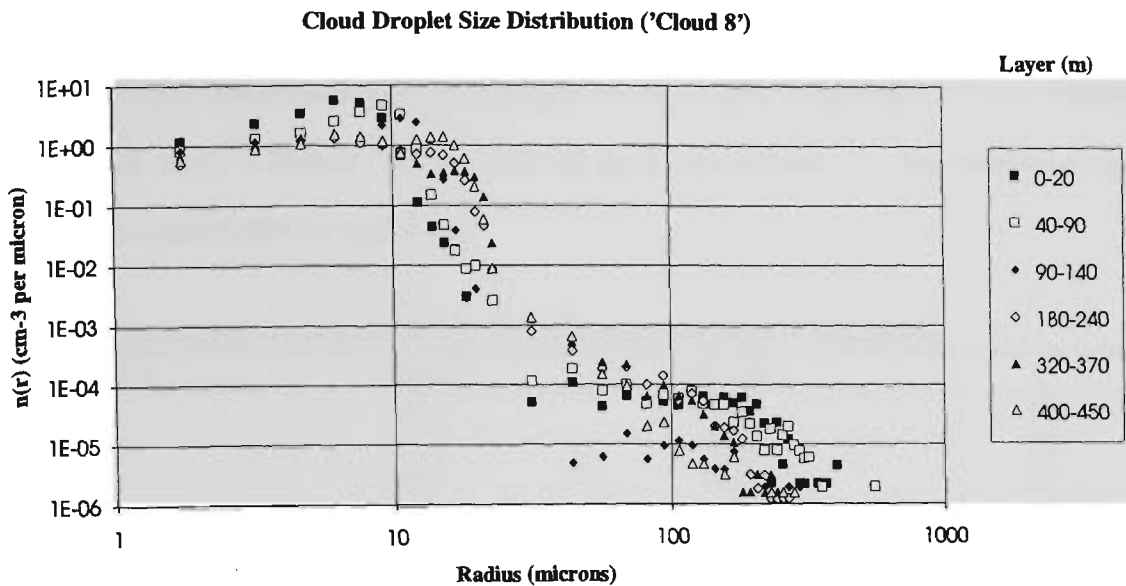


Figure 5.20. Cloud droplet size distributions measured by the FSSP and drizzle (2D-C) probes, of the cloud height-section labelled 'cloud 8'. The droplet concentrations $n(r)$ ($\text{cm}^{-3} \cdot \mu\text{m}^{-1}$) versus droplet radius (μm) have been divided into 50 metre deep layers into the cloud, starting with the lowest height layer (0 - 50 m).

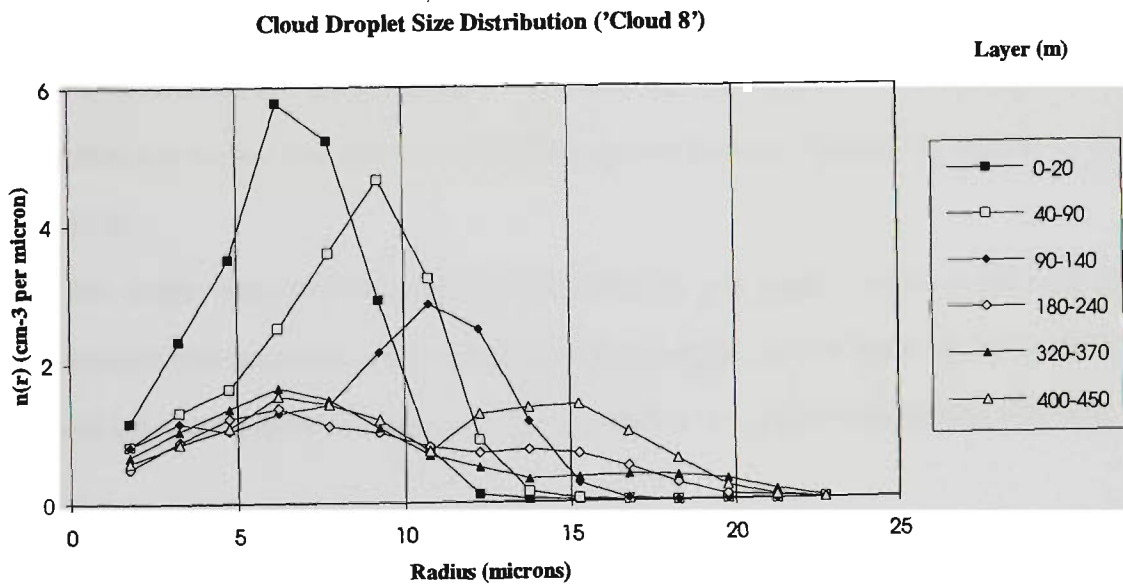


Figure 5.21. Cloud droplet size distributions measured by the FSSP for the cloud height-section labelled 'cloud 8'. The droplet concentrations $n(r)$ ($\text{cm}^{-3} \cdot \mu\text{m}^{-1}$) versus droplet radius (μm) have been divided into 50 metre deep layers into the cloud, starting with the lowest height layer (0 - 50 m).

5.3.3.3 Droplet Concentrations

The average droplet concentrations (N) and standard deviations (ΔN) of the clouds 1-8 were calculated from the DSDs shown in Figures (5.6) to (5.21) and are shown in Table 5.4. The numbers n are the numbers of measured DSDs for each cloud.

Table 5.4. Total droplet concentrations (N) for each measured cloud height-section.

Cloud #	N (cm^{-3})	ΔN (cm^{-3})	n
1	42.3	6.51	43
2	51.4	6.65	20
3	48.1	10.7	21
4	23.9	5.24	53
5	40.4	8.11	45
6	41.4	6.32	79
7	38.7	7.93	19
8	20.2	9.32	73

The drizzling clouds, 8 (the inland cloud), and 4 (one of the marine clouds), had much lower droplet concentrations: the lower droplet concentrations in the drizzling clouds are probably due to the water in those clouds existing in larger and therefore fewer droplets.

Average droplet concentrations were calculated from all the measured DSDs for each 50 m layer from cloud base and are shown in Table 5.5. The results for the inland cloud 8 have been separated from those of the marine clouds 1-7; the average concentrations for all clouds over each depth are shown in the last row. Data from this table are also shown in Figures 5.22 (clouds 1 - 7) and 5.23 (cloud 8).

The droplet concentrations are reasonably constant with height. As the mode radii of the droplets increase with height into the clouds, the increasing extinction with depth into these clouds (as will be seen later) is due to the increasing droplet size, and not to increasing droplet concentration.

Table 5.5. Total droplet concentrations ($N \pm \Delta N$) for clouds 1-7, and cloud 8.

Depth (m)	Clouds 1-7			Cloud 8		
	N (cm ⁻³)	ΔN (cm ⁻³)	n	N (cm ⁻³)	ΔN (cm ⁻³)	n
000-050	37.5	11.8	47	20.0	4.5	10
050-100	41.0	9.9	50	16.2	5.2	9
100-150	39.3	10.1	58	16.6	3.0	7
150-200	40.8	10.6	39	15.1	3.5	12
200-250	36.9	8.7	40	16.5	9.9	15
250-300	35.6	12.3	28	-	-	-
300-350	42.0	11.0	9	24.7	4.7	7
350-400	45.8	9.6	9	29.7	11.7	5
400-450	-	-	-	32.8	12.0	8
000-450	39.1	10.6	280	20.2	9.3	73

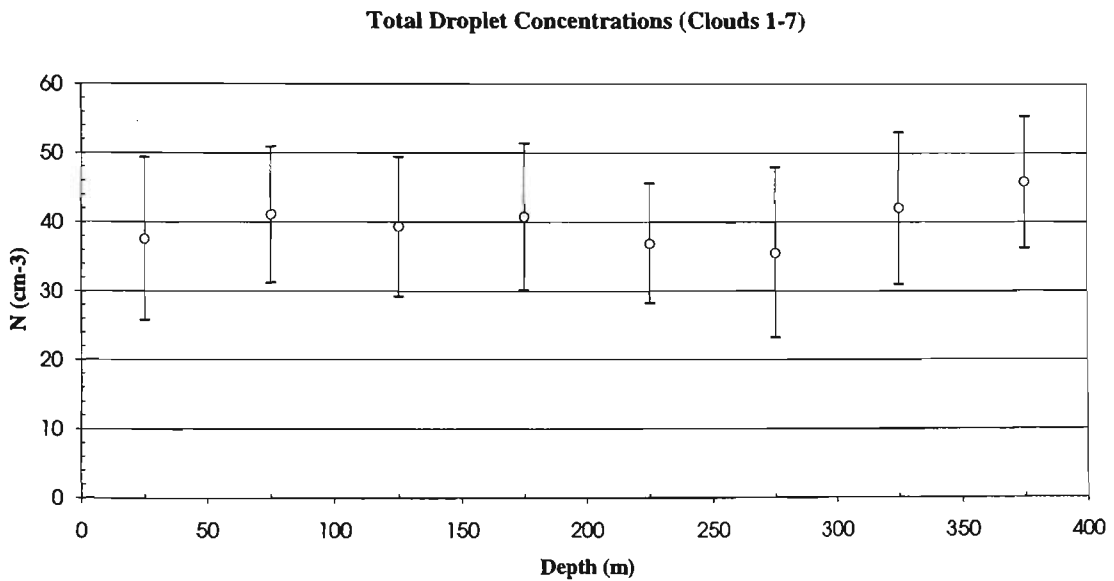


Figure 5.22. Averaged total droplet concentrations (N) of the cloud height-sections 'clouds 1-7', which were observed over the sea. The measures of variability ($\pm \Delta N$) are \pm one standard deviation.

Total Droplet Concentrations (Cloud 8)

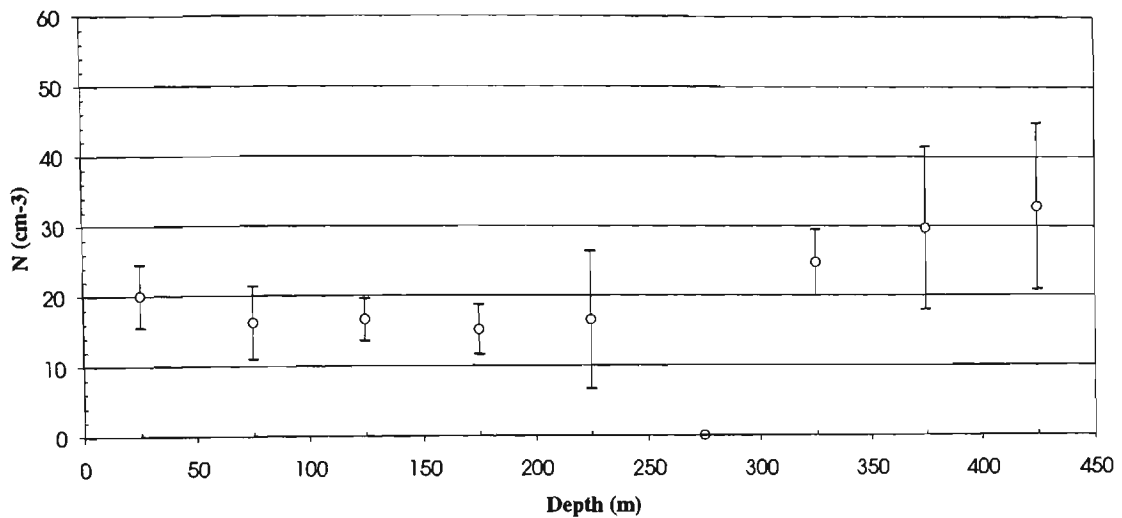


Figure 5.23. Averaged total droplet concentrations (N) of the cloud layers in 'cloud 8', which was observed over the land. There were no measurements in the 250-300 m layer. The last datum shows the average $N \pm \Delta N$ over all heights.

5.3.3.4 Cloud Droplet Effective Radius

The effective droplet radii (a_{eff} , see equation A2.4) of clouds 1- 8 were calculated for all the FSSP-measured DSDs only, (Figure 5.24), and also for the combined FSSP and 2D-C-measured DSDs (Figure 5.25). Note the larger effective radii of the water droplets in the drizzling clouds 4 (marine) and cloud 8 (observed over land), particularly near cloud base (Figure 5.25). The FSSP appears to have measured larger droplets in the drizzling marine cloud 4, (Figure 5.24), however this could be due to an error in the determination of the height of cloud base by (the airborne) FSSP.

These values of a_{eff} were then averaged over 50 m deep layers into the clouds starting from cloud base. The average effective radii were calculated for the marine clouds 1-7 and the results are shown in Table 5.6 and Figure 5.26. The effective radii were recalculated with the data for the drizzling (marine) cloud (4) data eliminated from the calculations. These results for the non-precipitating clouds (1-3 and 5-7) are shown in Figure 5.27.

Water Droplet Effective Radius (FSSP)

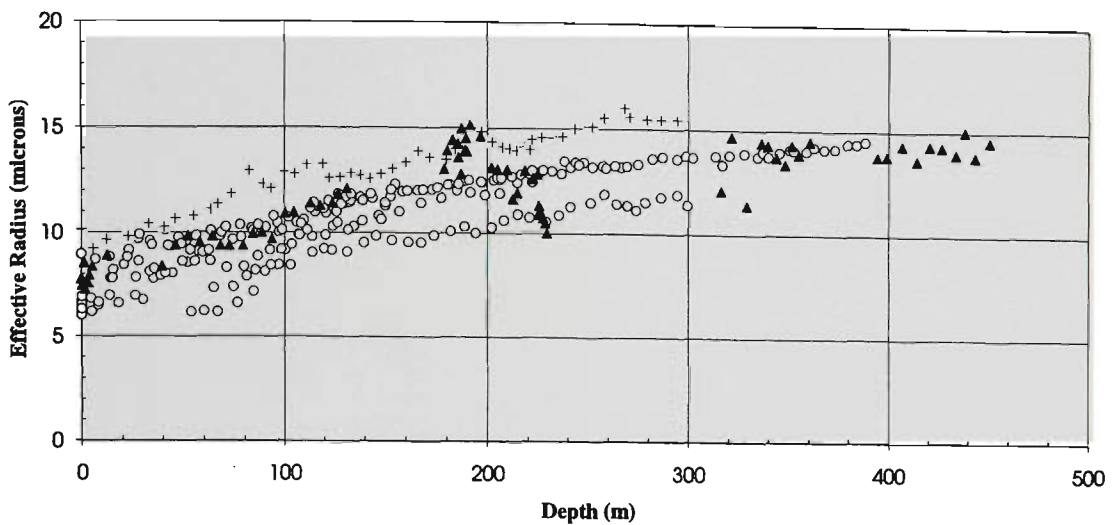


Figure 5.24. Water droplet effective radius (a_{eff}) for clouds 1-3 and 5-7 (open circles), the drizzling marine cloud 4 (crosses), and the cloud observed over land, cloud 8 (filled triangles). These a_{eff} s were calculated from the FSSP measured DSDs only. Depths are measured from cloud base.

Water Droplet Effective Radius (FSSP and 2D-C)

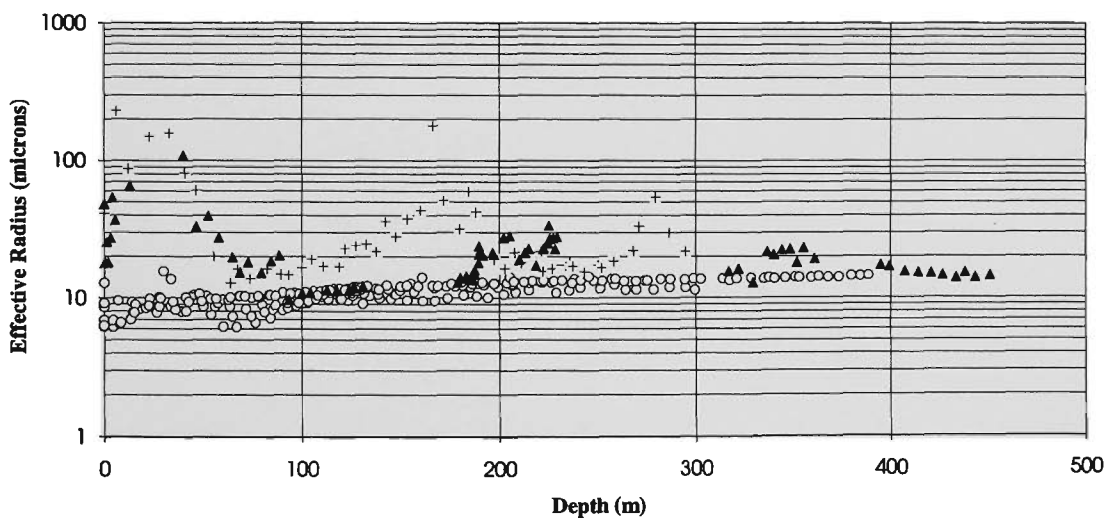


Figure 5.25. Water droplet effective radii (a_{eff}) for the marine clouds 1-3 and 5-7 (open circles), the drizzling marine cloud 4 (crosses), and the drizzling cloud 8 observed over land (filled triangles). These effective radii were calculated from the FSSP and 2D-C measured DSDs. Depths are measured from cloud base.

Water Droplet Effective Radius (FSSP and 2D-C, Clouds 1-7)

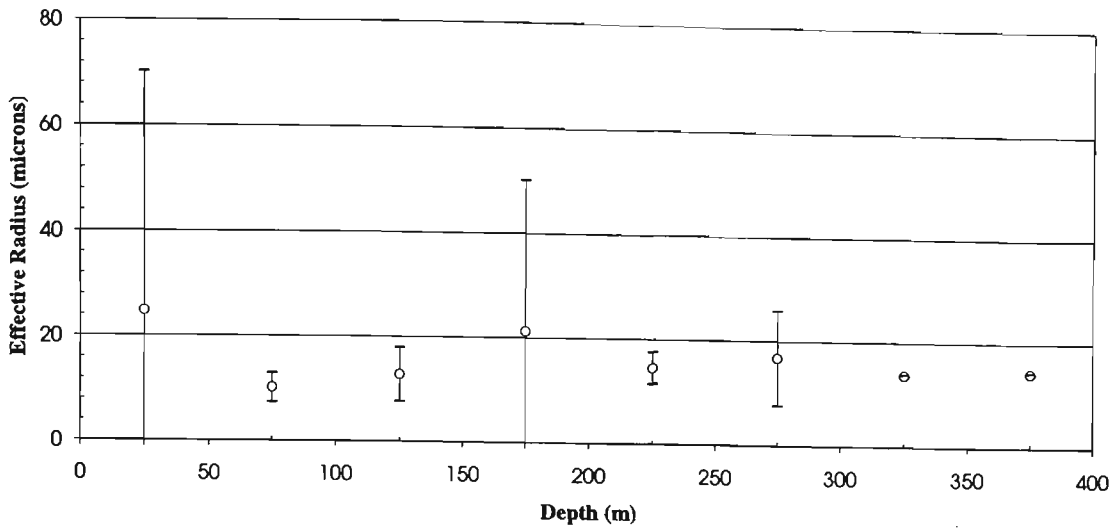


Figure 5.26. Water droplet effective radii calculated from both the FSSP and 2D-C-measured DSDs, averaged over 50 m deep layers into the clouds starting at cloud base, for clouds 1-7. The measures of variability in the calculated a_{eff} are \pm one standard deviation.

Water Droplet Effective Radius (FSSP and 2D-C, Clouds 1-3, 5-7)

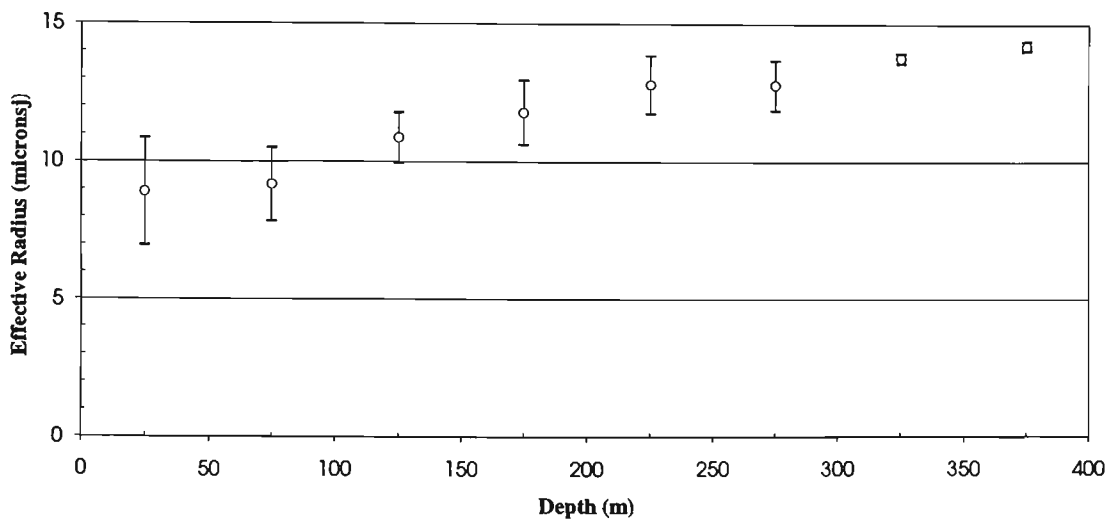


Figure 5.27. The water droplet effective radii (a_{eff}) determined in the same way as for the data shown in the previous figure, except with the data from the drizzling marine cloud, 4, eliminated from the calculations. The measures of variability in the calculated a_{eff} are \pm one standard deviation.

Table 5.6. Water droplet effective radii (a_{eff}) for clouds 1-7 (see Figures 5.25 and 5.26).

Layer (m)	FSSP		FSSP and 2D-C	
	a_{eff} (μm)	Δa_{eff} (μm)	a_{eff} (μm)	Δa_{eff} (μm)
0-50	8.35	1.33	24.8	45.4
50-100	9.44	1.63	10.2	2.81
100-150	11.0	1.16	12.8	5.17
150-200	12.0	1.29	21.3	28.8
200-250	13.0	1.29	14.6	3.05
250-300	13.4	1.58	16.8	9.15
300-350	13.8	0.19	13.8	0.19
350-400	14.2	0.17	14.2	0.17

The variabilities in a_{eff} were significantly less for the clouds 1-3 and 5-7 (Figure 5.27). This indicates that there was a clear difference in the microphysical properties of the non-precipitating marine clouds (1-3, 5-7) and the precipitating marine cloud 4. The a_{eff} of the non-precipitating clouds 1-3 and 5-7 increased with depth into the cloud, as may be expected from the increase in the mode radii seen by inspection of the DSDs in Figures 5.6 - 5.21. The values of a_{eff} calculated from the FSSP measurements only of the precipitating clouds 4 and 8 also increased with depth into these clouds. The most drizzle was observed in cloud 8, and the values of the calculated a_{eff} of that cloud are shown in Table 5.7.

Table 5.7. Water droplet effective radii (a_{eff}) for cloud 8 (see Figures 5.28 and 5.29).

Layer (m)	FSSP		FSSP and 2D-C	
	a_{eff} (μm)	Δa_{eff} (μm)	a_{eff} (μm)	Δa_{eff} (μm)
0-50	8.18	0.68	43.54	27.91
50-100	9.67	0.26	20.45	8.61
100-150	11.42	0.44	11.42	0.44
150-200	14.09	0.70	17.07	3.70
200-250	11.90	1.07	24.85	4.23
250-300	-	-	-	-
300-350	13.44	1.24	18.83	3.84
350-400	14.06	0.33	18.98	2.47
400-450	14.25	0.44	14.79	0.59

These results for cloud 8 (Figures 5.28 and 5.29) show that even for the drizzling clouds, the FSSP measurements showed the typical mode radii of 10 μm , with those droplets also increasing in size with depth into the clouds.

Water Droplet Effective Radius (FSSP, Cloud 8)

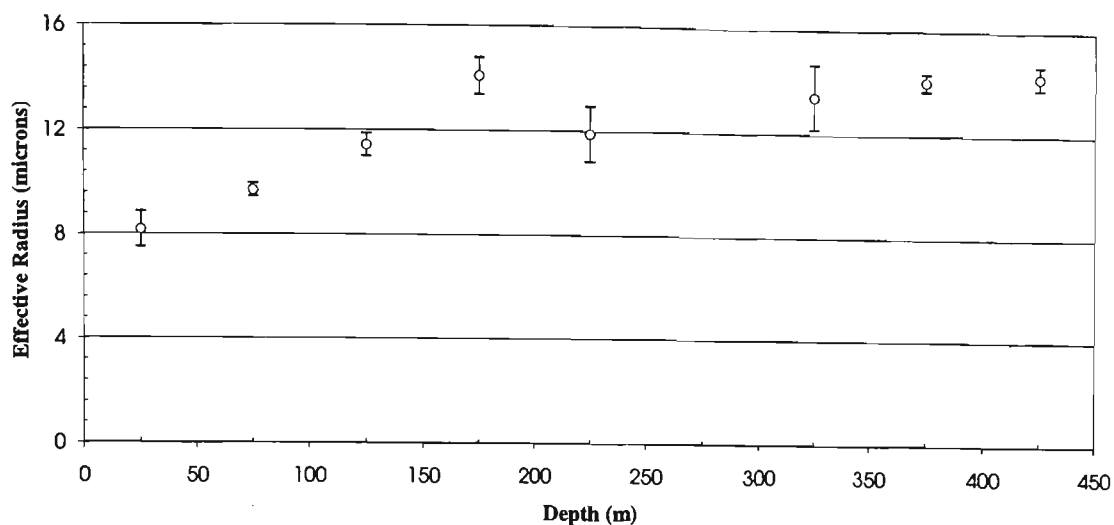


Figure 5.28. Water droplet effective radii of cloud 8 calculated from the FSSP measurements only, averaged over 50 m deep layers into the clouds starting at cloud base, for clouds 1-7. The measures of variability in the calculated a_{eff} are \pm one standard deviation.

Water Droplet Effective Radius (FSSP and 2D-C, Cloud 8)

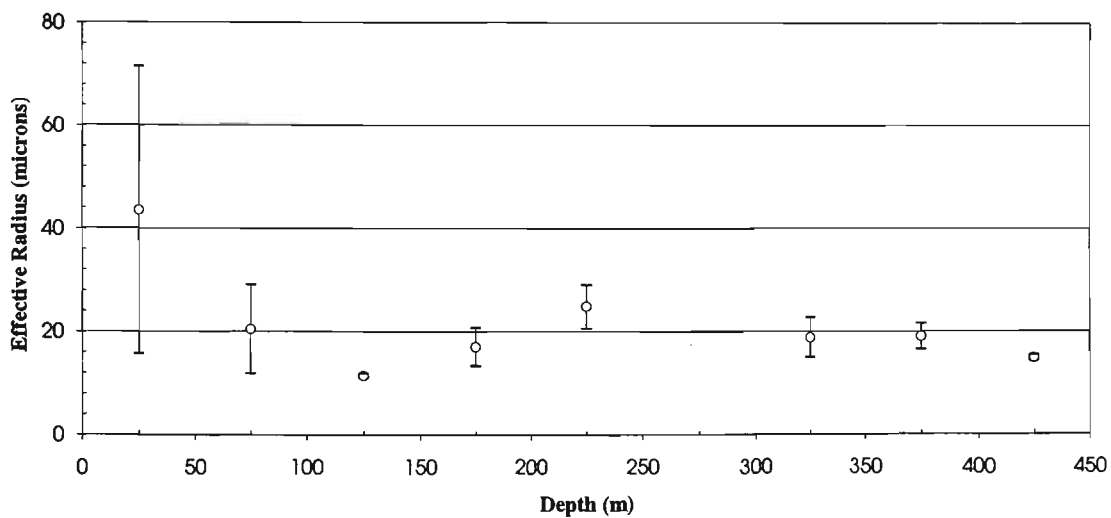


Figure 5.29. Water droplet effective radii of cloud 8 calculated from the FSSP and 2D-C measurements, averaged over 50 m deep layers into the clouds starting at cloud base. The measures of variability in the calculated a_{eff} are \pm one standard deviation.

5.3.3.5 Liquid Water Content

The liquid water contents (w) of the clouds 1-8 were calculated from the measured DSDs using equation (A2.6). Values of w were calculated for the FSSP-measured DSDs (see Figure 5.30), and also from the combined FSSP and 2D-C-measured DSDs (see Figure 5.31).

The values of w determined for both the FSSP and combined FSSP and 2D-C measured DSDs were then averaged over 50 m deep layers into the clouds from cloud base; the results for clouds 1-7 are shown in Table 5.8. These data are plotted in Figures 5.32 and 5.33.

Table 5.8. Liquid water contents (w) for clouds 1-7.

Layer (m)	FSSP		FSSP and 2D-C	
	w (g.m^{-3})	Δw (g.m^{-3})	w (g.m^{-3})	Δw (g.m^{-3})
0-50	0.071	0.031	0.201	0.353
50-100	0.124	0.047	0.135	0.057
100-150	0.183	0.045	0.211	0.081
150-200	0.252	0.073	0.428	0.495
200-250	0.282	0.067	0.316	0.073
250-300	0.287	0.103	0.345	0.162
300-350	0.388	0.114	0.388	0.114
350-400	0.472	0.102	0.472	0.102

The liquid water contents for cloud 8 are shown in Table 5.9 (see also Figures 5.34 and 5.35).

Table 5.9. Liquid water contents (w) for cloud 8.

Layer (m)	FSSP		FSSP and 2D-C	
	w (g.m^{-3})	Δw (g.m^{-3})	w (g.m^{-3})	Δw (g.m^{-3})
0-50	0.052	0.021	0.294	0.142
50-100	0.084	0.023	0.206	0.131
100-150	0.101	0.038	0.101	0.038
150-200	0.112	0.092	0.134	0.095
200-250	0.065	0.018	0.150	0.029
250-300	-	-	-	-
300-350	0.080	0.031	0.123	0.056
350-400	0.139	0.055	0.193	0.056
400-450	0.146	0.022	0.155	0.028

Liquid Water Content (FSSP, Clouds 1-8)

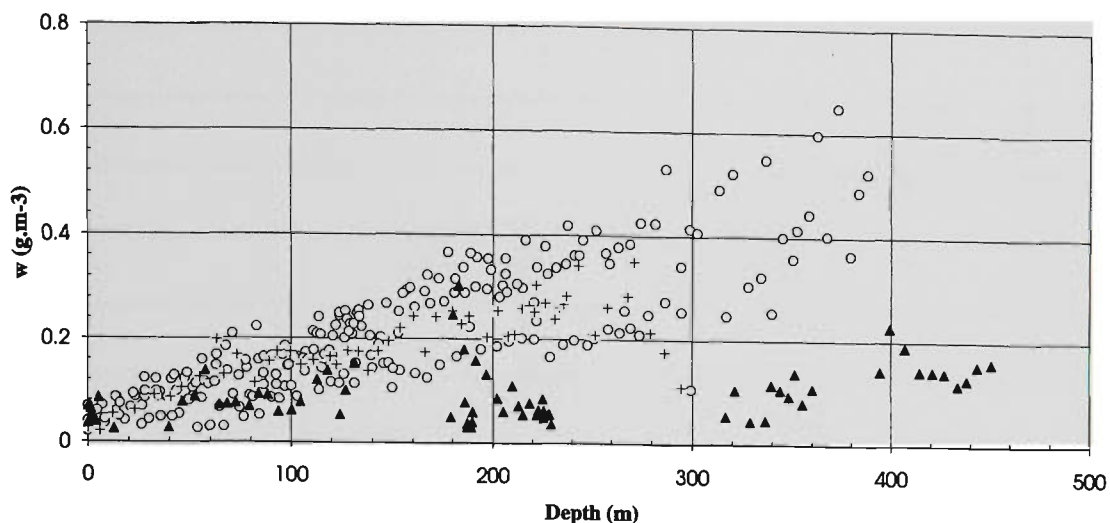


Figure 5.30. Liquid water contents (w $\text{g}\cdot\text{m}^{-3}$) for clouds 1-3 and 5-7 (open circles), the precipitating marine cloud 4 (crosses), and cloud 8 (filled triangles), calculated from the DSDs measured by the FSSP only. Depths are measured from cloud base.

Liquid Water Content (FSSP and 2D-C, Clouds 1-8)

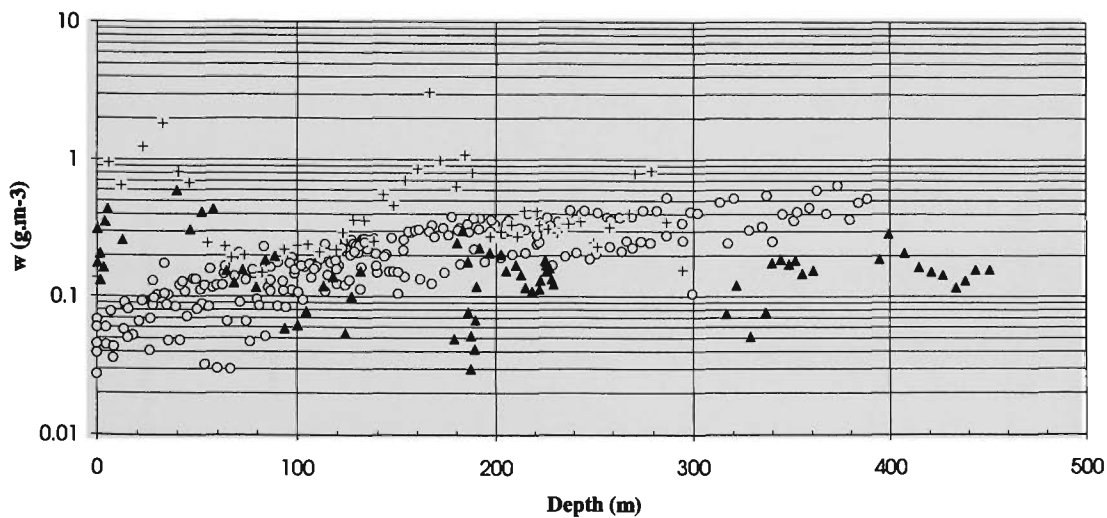


Figure 5.31. Liquid water contents (w $\text{g}\cdot\text{m}^{-3}$) of clouds 1-3 and 5-7 (open circles), the precipitating marine cloud 4 (crosses), and cloud 8 observed over land (filled triangles). These liquid water contents were calculated from the DSDs measured by the FSSP and 2D-C. Depths are measured from cloud base.

Liquid Water Content (FSSP, Clouds 1-7)

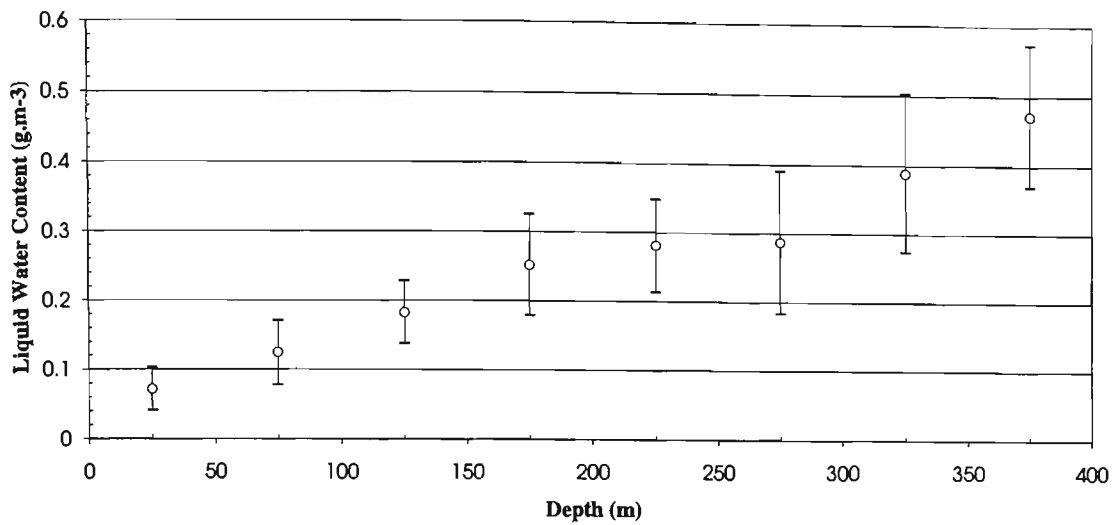


Figure 5.32. Liquid water content (w) calculated from the FSSP-measured DSDs, averaged over 50 m deep layers into the clouds starting at the height of cloud base, for clouds 1-7. The measures of variability in the calculated w are \pm one standard deviation.

Liquid Water Content (FSSP and 2D-C, Clouds 1-7)

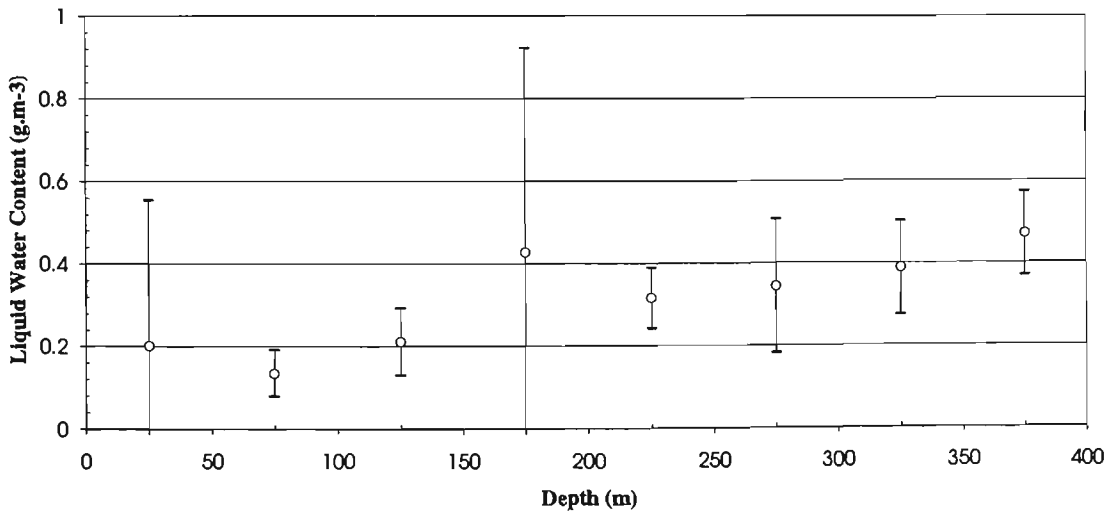


Figure 5.33. Liquid water content (w) calculated from both the FSSP and 2D-C-measured DSDs, averaged over 50 (m)-deep layers into the clouds starting at cloud base, for clouds 1-7. The measures of variability in the calculated w are \pm one standard deviation.

Liquid Water Content (FSSP, Cloud 8)

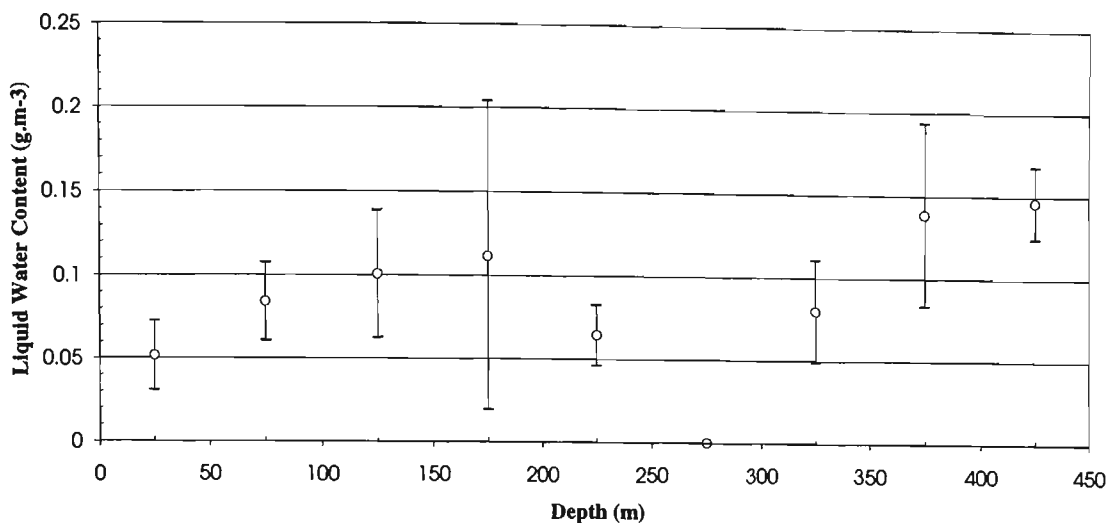


Figure 5.34. Liquid water content (w) of cloud 8 calculated from the FSSP-measured DSDs, averaged over 50 m deep layers into the clouds starting at the height of cloud base. The measures of variability in the calculated w are \pm one standard deviation.

Liquid Water Content (FSSP and 2D-C, Cloud 8)

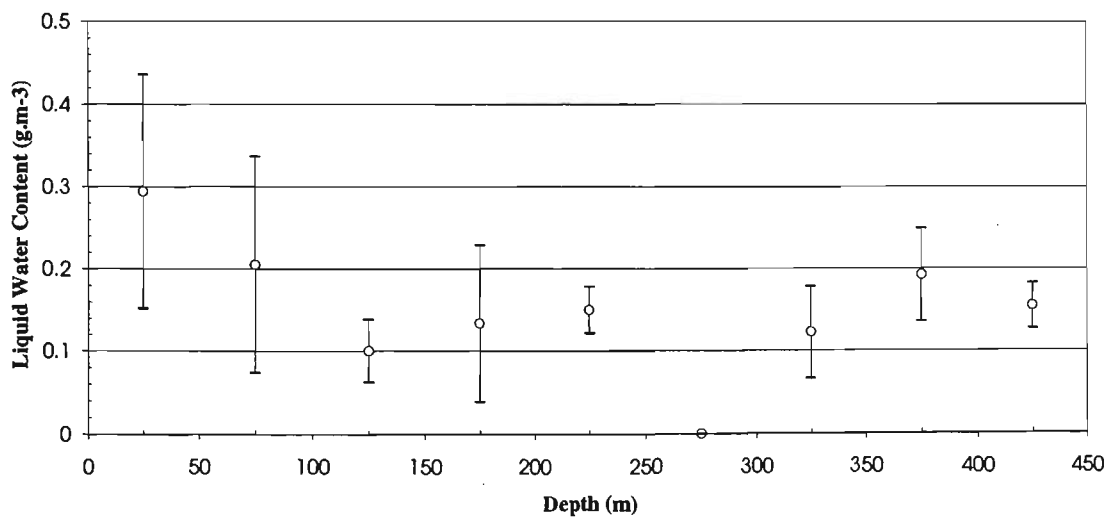


Figure 5.35. Liquid water content (w) for cloud 8 calculated from both the FSSP and 2D-C-measured DSDs, averaged over 50 m deep layers into the clouds starting at cloud base. The measures of variability in the calculated w are \pm one standard deviation.

5.3.3.6 Liquid Water Path

The liquid water paths (W) of clouds 1-8 were calculated from the FSSP-measured DSDs (Figure 5.36), and also from the combined FSSP and 2D-C-measured DSDs (Figure 5.37). The values of W were linearly interpolated at 50 m deep intervals into the clouds, starting from cloud base. The values of W for clouds 1-8 are shown in Table 5.10; the variabilities are single standard deviations. The values of W calculated from the FSSP measurements are shown in Figure 5.38, and for the FSSP and 2D-C measurements combined, see Figure 5.39.

Table 5.10.a. Liquid water paths (W) for clouds 1-8, by FSSP.

Height (m)	clouds 1-7 W (g.m^{-2})	ΔW (g.m^{-2})	cloud 8 W (g.m^{-2})
50	3.6	0.76	1.35
100	9.9	2.7	5.50
150	18.6	4.6	8.67
200	31.8	8.2	11.76
250	43.8	10.9	13.91
300	55.3	15.8	12.60
350	90.9	-	16.55
400	-	-	18.63
450	-	-	26.24

Table 5.10.b. Liquid water paths (W) for clouds 1-8, by FSSP and 2D-C.

Height (m)	clouds 1-7 W (g.m^{-2})	ΔW (g.m^{-2})	cloud 8 W (g.m^{-2})
50	10.5	17.3	8.09
100	17.4	19.5	17.88
150	28.8	24.2	21.04
200	52.1	42.8	25.00
250	70.2	50.3	29.38
300	93.9	64.2	27.75
350	93.7	-	33.25
400	-	-	36.21
450	-	-	44.50

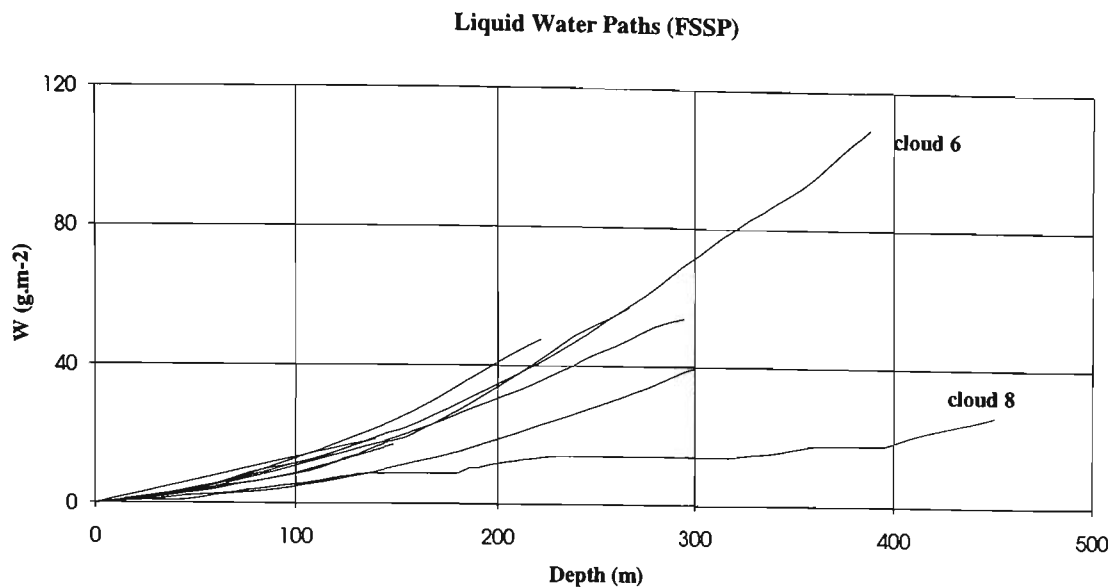


Figure 5.36. Liquid water paths ($W \text{ g}\cdot\text{m}^{-2}$) of clouds 1-8, calculated from the FSSP measured DSDs only. Depths start at height of cloud base.

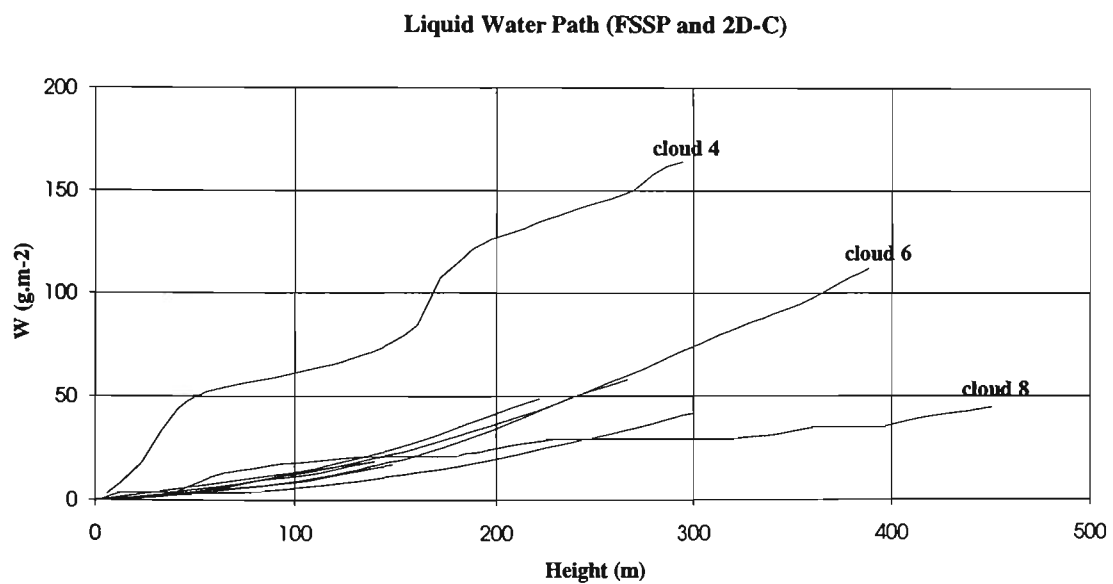


Figure 5.37. Liquid water paths ($W \text{ g}\cdot\text{m}^{-2}$) of clouds 1-8, calculated from the combined FSSP and 2D-C measured DSDs. Depths start at height of cloud base. The 2D-C measurements significantly affect the profiles of W of clouds 4 and 8.

Liquid Water Paths (FSSP, Clouds 1-8)

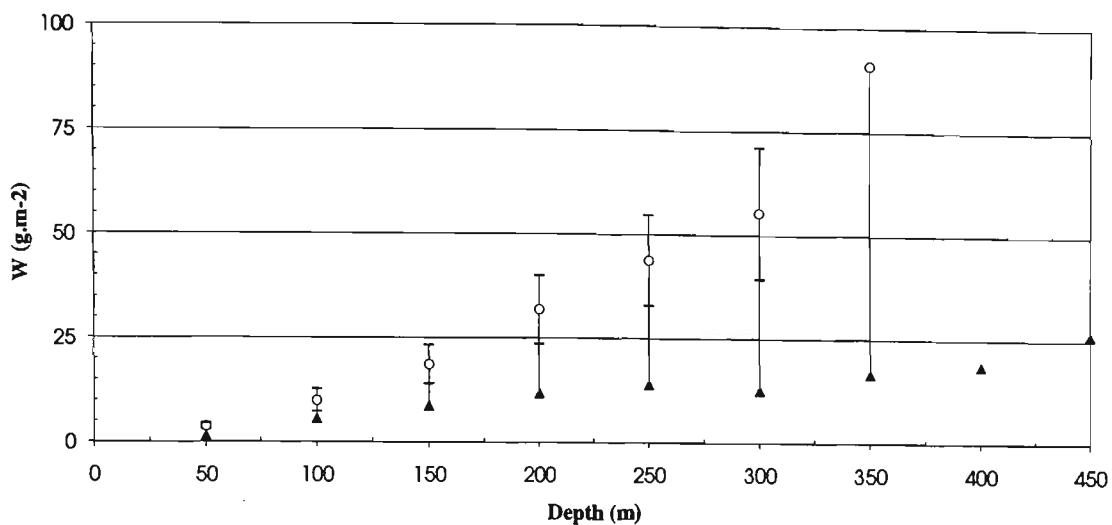


Figure 5.38. Average liquid water paths (W) of clouds 1-7 (open circles) and cloud 8 (filled triangles), linearly interpolated at 50 m height intervals from cloud base. These results were determined from the FSSP measurements only. The variabilities in W for clouds 1-7 are \pm one standard deviation.

Liquid Water Path (Clouds 1-8, FSSP and 2D-C)

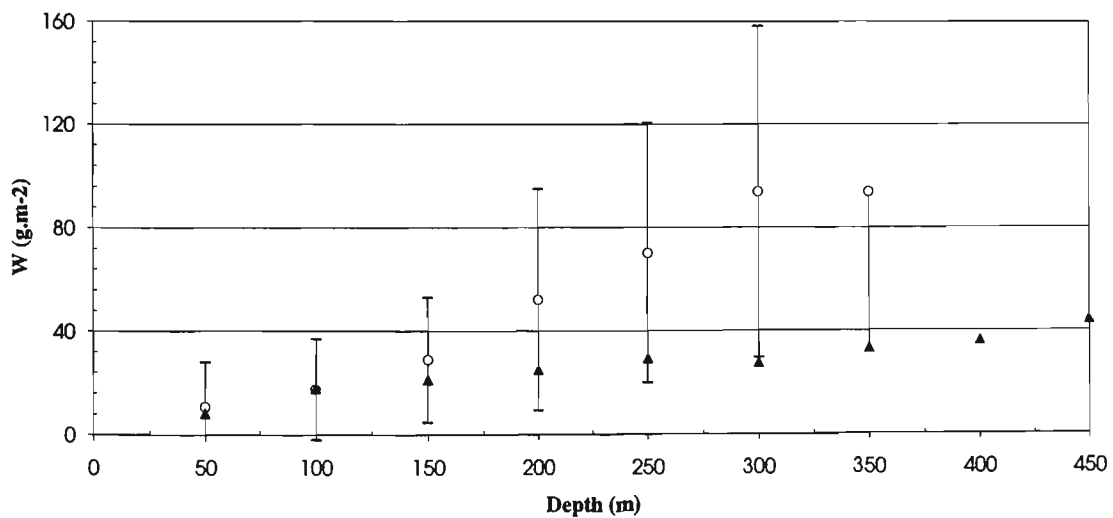


Figure 5.39. Average liquid water paths (W) of clouds 1-7 (open circles) and cloud 8 (filled triangles), linearly interpolated at 50 m height intervals from cloud base. These results were determined from the FSSP and 2D-C measurements combined. The variabilities in W for clouds 1-7 are \pm one standard deviation.

5.3.3.7 Visible Extinction

The visible (532 nm) volume extinction coefficients (σ_v) were calculated for all DSDs of clouds 1-8 (4.3.2.2 and 4.3.2.3). The results calculated from the combined FSSP and 2D-C measured DSDs are shown in Figure 5.40. These results were averaged over 50 m depths into the clouds starting from cloud base. Average σ_v and variabilities (standard deviations, $\Delta\sigma_v$) for the marine clouds, clouds 1-7, are shown in Table 5.11. Similar results for cloud 8 are shown in Table 5.12. Numbers of DSDs (n) used in the calculations are shown in the last columns. The results shown in Tables 5.11 and 5.12 are plotted in Figures 5.41 and 5.42 respectively.

Table 5.11. Visible extinction for clouds 1-7.

Layer (m)	FSSP		FSSP and 2D-C		n
	σ_v (m^{-1})	$\Delta\sigma_v$	σ_v (m^{-1})	$\Delta\sigma_v$ (m^{-1})	
000-050	1.36E-02	4.41E-03	1.31E-02	4.55E-03	47
050-100	2.02E-02	6.02E-03	2.01E-02	6.01E-03	50
100-150	2.62E-02	5.79E-03	2.59E-02	5.97E-03	58
150-200	3.34E-02	8.52E-03	3.28E-02	8.94E-03	39
200-250	3.41E-02	7.32E-03	3.38E-02	7.52E-03	40
250-300	3.38E-02	1.17E-02	3.36E-02	1.18E-02	28
300-350	4.37E-02	1.26E-02	4.37E-02	1.26E-02	9
350-400	5.14E-02	1.11E-02	5.14E-02	1.11E-02	9

Table 5.12. Visible extinction for cloud 8.

Layer (m)	FSSP		FSSP and 2D-C		n
	σ_v (m^{-1})	$\Delta\sigma_v$	σ_v (m^{-1})	$\Delta\sigma_v$ (m^{-1})	
000-050	1.17E-02	3.67E-03	9.95E-03	3.86E-03	10
050-100	1.47E-02	4.35E-03	1.36E-02	3.79E-03	9
100-150	1.37E-02	4.90E-03	1.37E-02	4.90E-03	7
150-200	1.26E-02	9.85E-03	1.22E-02	9.96E-03	12
200-250	9.51E-03	1.80E-03	8.39E-03	1.84E-03	15
250-300	-	-	-	-	-
300-350	9.84E-03	3.34E-03	9.15E-03	3.09E-03	7
350-400	1.62E-02	6.30E-03	1.54E-02	6.31E-03	5
400-450	1.62E-02	2.53E-03	1.59E-02	2.39E-03	8

Visible Extinction (FSSP and 2D-C, Clouds 1-8)

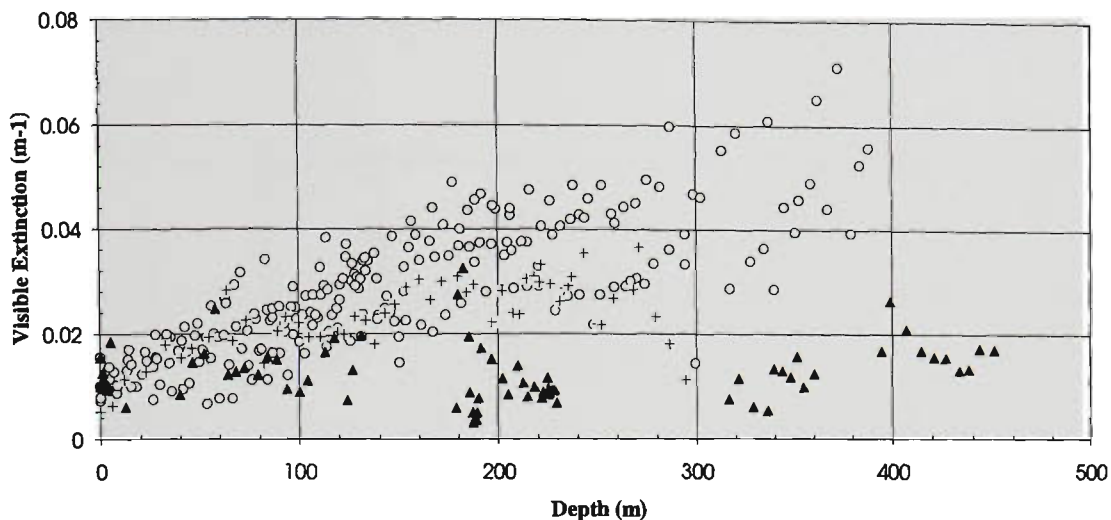


Figure 5.40. Visible Extinction of clouds 1-3 and 5-7 (open circles), the marine cloud 4 (crosses), and the cloud observed over land, cloud 8 (filled triangles). The 2D-C measurements had only a small effect on the calculated visible extinction.

Visible Extinction (FSSP and 2D-C, Clouds 1-7)

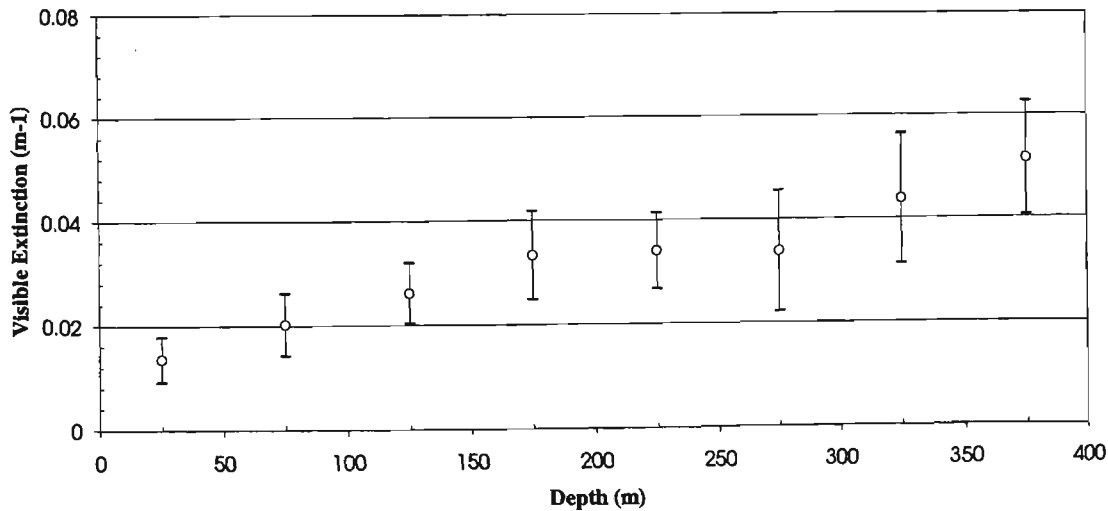


Figure 5.41. Visible (532 nm) extinction of clouds 1-7 averaged over 50 m deep layers into the clouds. The statistics were calculated from the combined FSSP and 2D-C measured DSDs.

Visible Extinction (FSSP and 2D-C, Cloud 8)

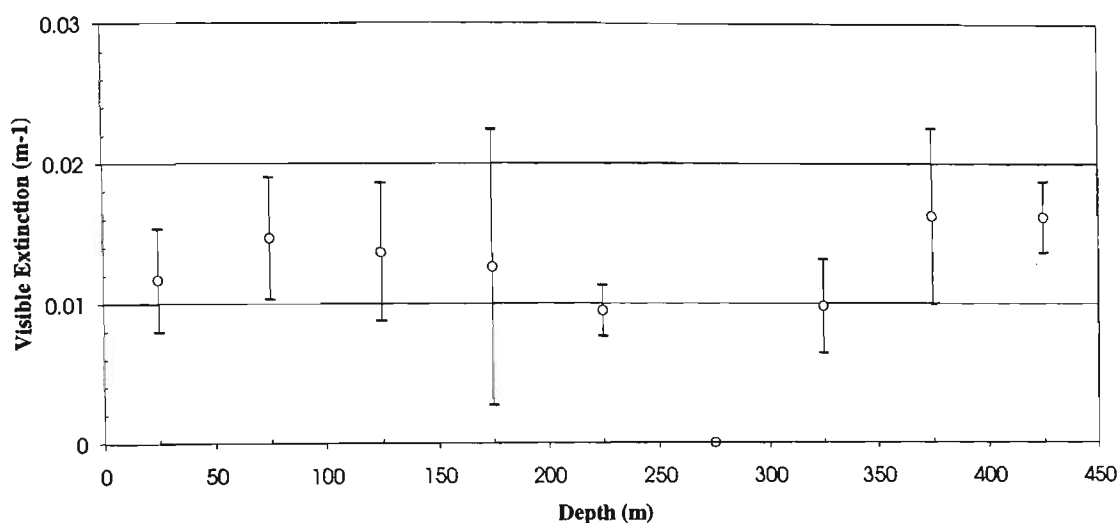


Figure 5.42. Visible (532 nm) extinction of cloud 8 averaged over 50 m deep layers into the cloud. The statistics were calculated from the combined FSSP and 2D-C measured DSDs.

5.3.3.8 Visible Backscatter

The visible (532 nm) volume backscatter coefficients (β) were calculated for all DSDs of clouds 1-8 (4.3.2.2 and 4.3.2.3). The results calculated from the combined FSSP and 2D-C measured DSDs are shown in Figure 5.43. These results were averaged over 50 m depths into the clouds starting from cloud base. Average β and variabilities (standard deviations, $\Delta\beta$) for the marine clouds, clouds 1-7, are shown in Table 5.13. Similar results for cloud 8 are shown in Table 5.14. Numbers of DSDs used in the calculations are the same as used for the calculations of visible extinction (see Tables 5.11 and 5.12). The results shown in Tables 5.13 and 5.14 are plotted in Figures 5.44 and 5.45 respectively.

Table 5.13. Visible backscatter for clouds 1-7.

Layer (m)	FSSP		FSSP and 2D-C	
	β (m ⁻¹ .sr ⁻¹)	$\Delta\beta$ (m ⁻¹ .sr ⁻¹)	β (m ⁻¹ .sr ⁻¹)	$\Delta\beta$ (m ⁻¹ .sr ⁻¹)
000-050	6.94E-04	2.30E-04	6.77E-04	2.36E-04
050-100	1.05E-03	3.28E-04	1.05E-03	3.27E-04
100-150	1.39E-03	3.20E-04	1.38E-03	3.28E-04
150-200	1.78E-03	4.67E-04	1.76E-03	4.84E-04
200-250	1.83E-03	3.79E-04	1.81E-03	3.87E-04
250-300	1.82E-03	6.08E-04	1.81E-03	6.14E-04
300-350	2.36E-03	6.80E-04	2.36E-03	6.80E-04
350-400	2.81E-03	6.01E-04	2.81E-03	6.01E-04

Table 5.14. Visible backscatter for cloud 8.

Layer (m)	FSSP		FSSP and 2D-C	
	β ($\text{m}^{-1}.\text{sr}^{-1}$)	$\Delta\beta$ ($\text{m}^{-1}.\text{sr}^{-1}$)	β ($\text{m}^{-1}.\text{sr}^{-1}$)	$\Delta\beta$ ($\text{m}^{-1}.\text{sr}^{-1}$)
000-050	5.78E-04	1.86E-04	5.07E-04	1.94E-04
050-100	7.58E-04	2.23E-04	7.16E-04	2.00E-04
100-150	7.31E-04	2.63E-04	7.31E-04	2.63E-04
150-200	6.91E-04	5.49E-04	6.75E-04	5.53E-04
200-250	4.97E-04	1.02E-04	4.52E-04	1.04E-04
250-300	-	-	-	-
300-350	5.29E-04	1.83E-04	5.02E-04	1.73E-04
350-400	8.81E-04	3.45E-04	8.47E-04	3.46E-04
400-450	8.88E-04	1.36E-04	8.78E-04	1.31E-04

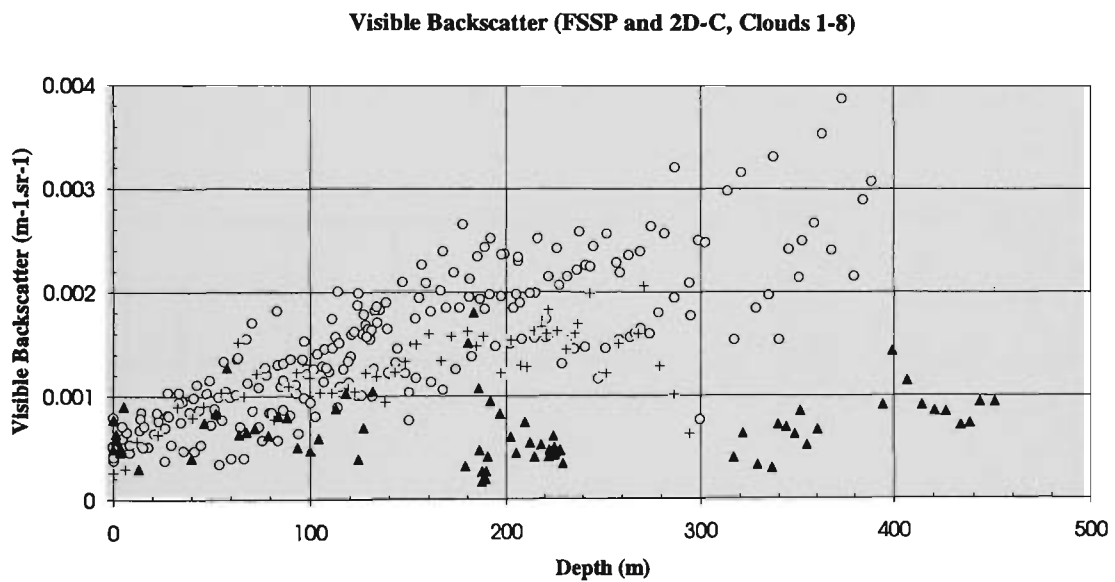


Figure 5.43. Visible (532 nm) backscatter (β $\text{m}^{-1}.\text{sr}^{-1}$) of clouds 1-3 and 5-7 (open circles), cloud 4 (crosses), and cloud 8 (filled triangles).

Visible Backscatter (FSSP and 2D-C, Clouds 1-7)

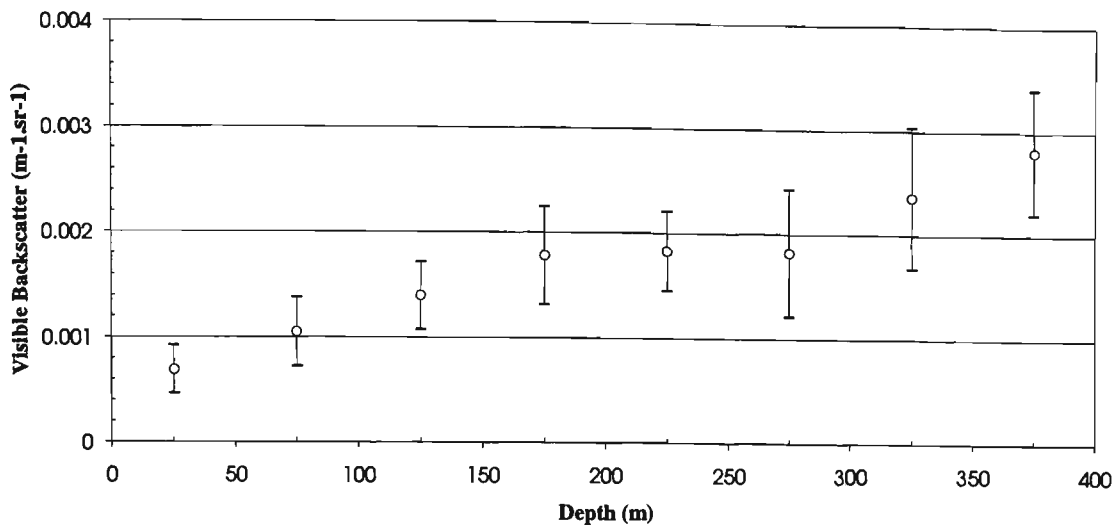


Figure 5.44. Visible (532 nm) backscatter of clouds 1-7 averaged over 50 m deep layers into the clouds. The statistics were calculated from the combined FSSP and 2D-C measured DSDs.

Visible Backscatter (FSSP and 2D-C, Cloud 8)

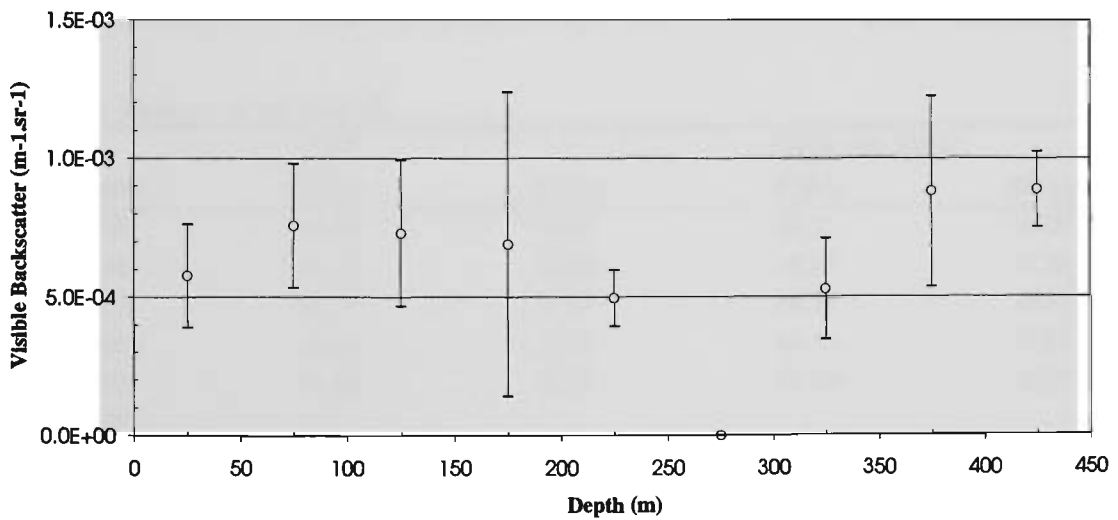


Figure 5.45. Visible (532 nm) backscatter of cloud 8 averaged over 50 m deep layers into the clouds. The statistics were calculated from the combined FSSP and 2D-C measured DSDs.

5.3.3.9 Visible Extinction-to-Backscatter Ratio (S)

The visible (532 nm) extinction-to-backscatter ratios (S) were calculated for all DSDs of clouds 1-8, simply by dividing the σ_v by β obtained for each DSD. The results calculated from the combined FSSP and 2D-C measured DSDs are shown in Figure 5.46. These results were averaged over 50 m depths into the clouds starting from cloud base. Averages S and variabilities (standard deviations, ΔS) for the marine clouds, clouds 1-7, are shown in Table 5.15. Similar calculations for cloud 8 are shown in Table 5.16. Numbers of DSDs used in the calculations are the same as used for the calculations of visible extinction (see Tables 5.11 and 5.12). The results shown in Tables 5.15 and 5.16 are plotted in Figures 5.47 and 5.48 respectively.

Table 5.15. Ratios S sr for clouds 1-7.

Layer (m)	FSSP		FSSP and 2D-C	
	S (sr)	ΔS (sr)	S (sr)	ΔS (sr)
000-050	19.41	0.42	19.58	0.47
050-100	19.22	0.60	19.26	0.56
100-150	18.77	0.36	18.83	0.37
150-200	18.67	0.24	18.77	0.28
200-250	18.57	0.34	18.63	0.29
250-300	18.42	0.51	18.48	0.43
300-350	18.54	0.10	18.54	0.10
350-400	18.32	0.10	18.32	0.10

Table 5.16. Ratios S sr for cloud 8.

Layer (m)	FSSP		FSSP and 2D-C	
	S (sr)	ΔS (sr)	S (sr)	ΔS (sr)
000-050	19.58	0.31	20.31	0.46
050-100	19.05	0.20	19.35	0.23
100-150	18.74	0.07	18.74	0.07
150-200	18.09	0.21	18.36	0.33
200-250	18.60	0.31	19.20	0.39
250-300	-	-	-	-
300-350	18.29	0.29	18.63	0.29
350-400	18.17	0.12	18.47	0.22
400-450	18.14	0.13	18.22	0.16

Visible Extinction-to-Backscatter Ratio

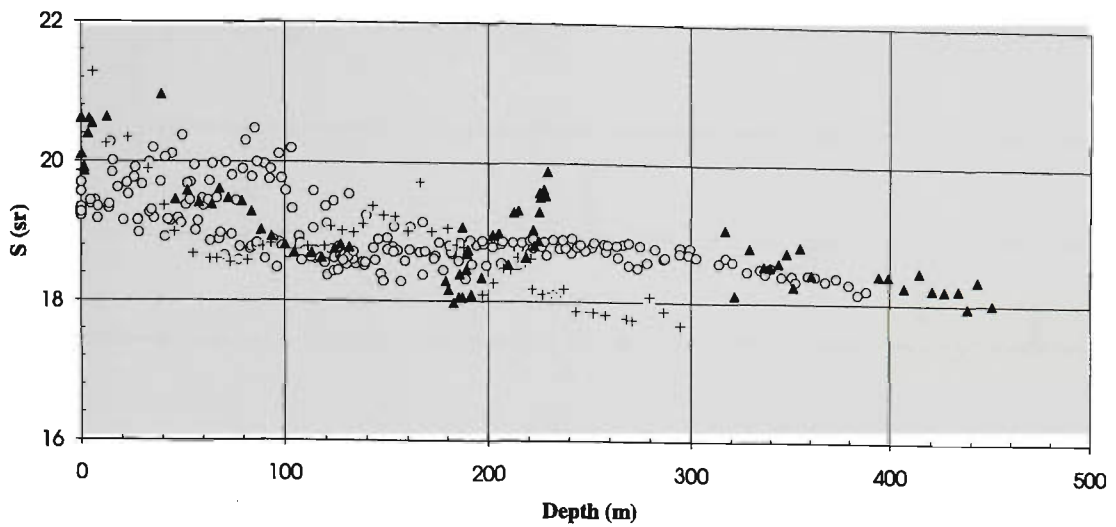


Figure 5.46. Visible extinction-to-backscatter ratio (S sr) of clouds 1-3 and 5-7 (open circles), cloud 4 (crosses) and cloud 8 (filled triangles), calculated from the combined FSSP and 2D-C measured DSDs.

Visible Extinction-to-Backscatter Ratio (FSSP and 2D-C, Clouds 1-7)

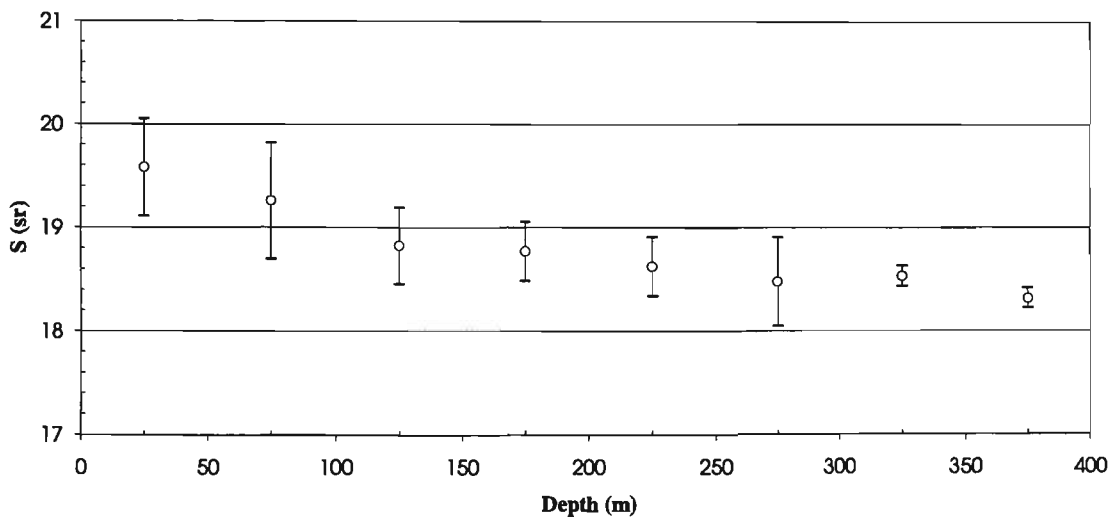


Figure 5.47. Visible (532 nm) extinction-to-backscatter ratio of clouds 1-7 averaged over 50 m deep layers into the clouds. Variability is indicated by \pm one standard deviation. The statistics were calculated from the combined FSSP and 2D-C measured DSDs.

Visible Extinction-to-Backscatter Ratio (FSSP and 2D-C, Cloud 8)

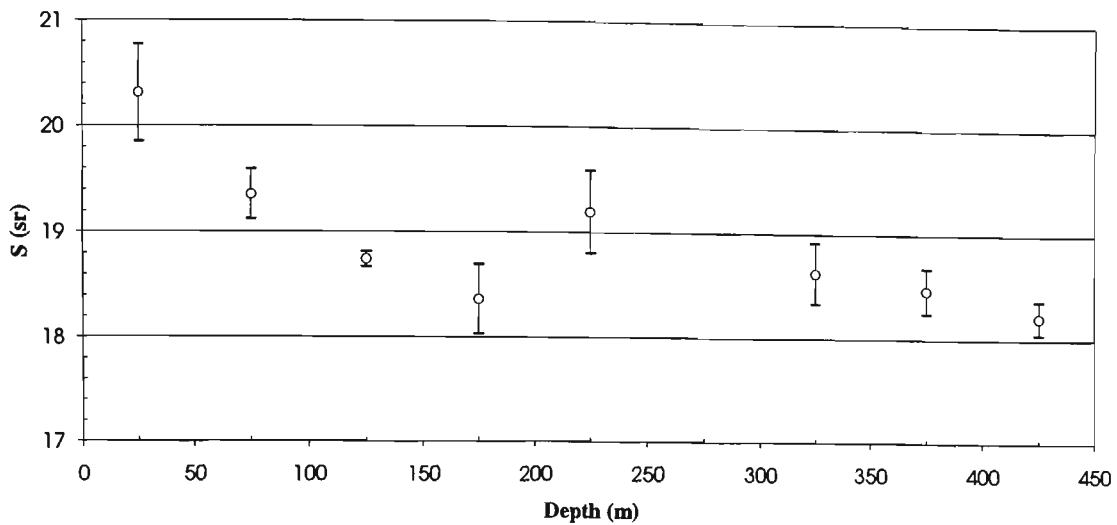


Figure 5.48. Visible (532 nm) extinction-to-backscatter ratio of cloud 8 averaged over 50 m deep layers into the clouds. Variability is indicated by \pm one standard deviation. The statistics were calculated from the combined FSSP and 2D-C measured DSDs.

5.3.3.10 Infrared Absorption

The infrared (10-84 μm) volume absorption coefficients (σ_a) were calculated for all DSDs of clouds 1-8 (4.3.2.4 and 4.3.2.5). The results calculated from the combined FSSP and 2D-C measured DSDs are shown in Figure 5.49. These results were averaged over 50 m depths into the clouds starting from cloud base. Averages σ_a and variabilities (standard deviations, $\Delta\sigma_a$) for the marine clouds, clouds 1-7, are shown in Table 5.17. Similar results for cloud 8 are shown in Table 5.18. Numbers of DSDs used in the calculations are the same as used for the calculations of visible extinction (see Tables 5.11 and 5.12). The results shown in Tables 5.17 and 5.18 are plotted in Figures 5.50 and 5.51 respectively.

Table 5.17. Infrared (10-84 μm) absorption (σ_a) for clouds 1-7.

Layer (m)	FSSP		FSSP and 2D-C	
	σ_a (m^{-1})	$\Delta\sigma_a$ (m^{-1})	σ_a (m^{-1})	$\Delta\sigma_a$ (m^{-1})
000-050	5.08E-03	2.00E-03	5.28E-03	1.99E-03
050-100	8.35E-03	2.83E-03	8.43E-03	2.85E-03
100-150	1.15E-02	2.72E-03	1.16E-02	2.66E-03
150-200	1.51E-02	4.24E-03	1.54E-02	4.08E-03
200-250	1.59E-02	3.66E-03	1.61E-02	3.58E-03
250-300	1.60E-02	5.71E-03	1.61E-02	5.64E-03
300-350	2.11E-02	6.13E-03	2.11E-02	6.13E-03
350-400	2.51E-02	5.42E-03	2.51E-02	5.42E-03

Table 5.18. Infrared (10.84 μm) absorption (σ_a) for cloud 8.

Layer (m)	FSSP		FSSP and 2D-C	
	σ_a (m^{-1})	$\Delta\sigma_a$ (m^{-1})	σ_a (m^{-1})	$\Delta\sigma_a$ (m^{-1})
000-050	3.75E-03	1.50E-03	4.63E-03	1.44E-03
050-100	5.67E-03	1.58E-03	6.20E-03	1.86E-03
100-150	6.14E-03	2.27E-03	6.14E-03	2.27E-03
150-200	5.86E-03	4.85E-03	6.08E-03	4.79E-03
200-250	3.70E-03	9.09E-04	4.28E-03	8.86E-04
250-300	-	-	-	-
300-350	4.22E-03	1.47E-03	4.59E-03	1.60E-03
350-400	7.26E-03	3.04E-03	7.71E-03	3.04E-03
400-450	7.62E-03	1.14E-03	7.76E-03	1.21E-03

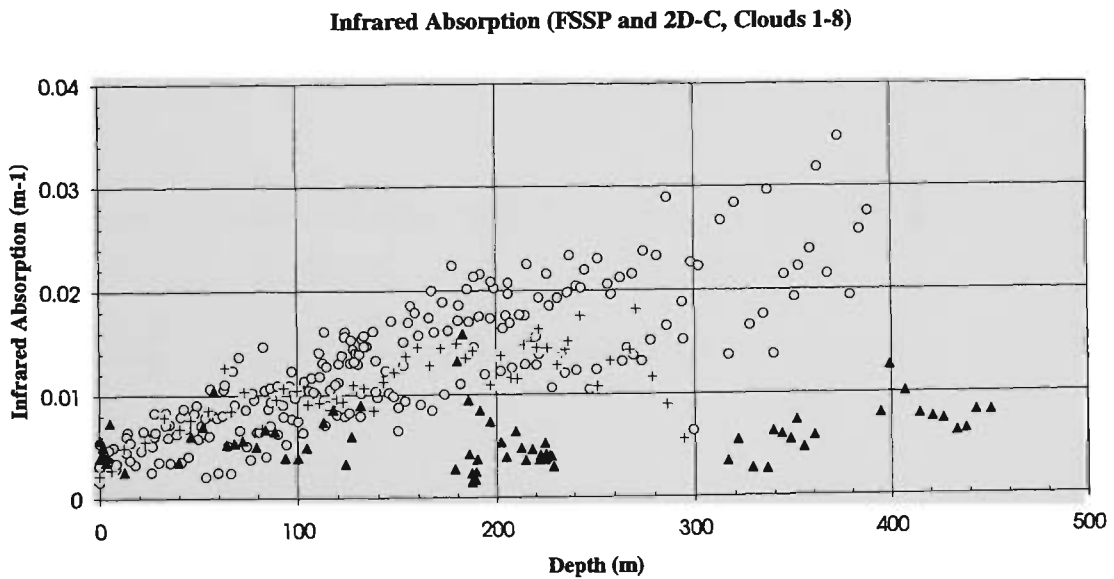


Figure 5.49. Infrared (10.84 μm) absorption (σ_a) of clouds 1-3 and 5-7 (open circles), cloud 4 (crosses), and cloud 8 (filled triangles), calculated from the combined FSSP and 2D-C measured DSDs.

Infrared Absorption (FSSP and 2D-C, Clouds 1-7)

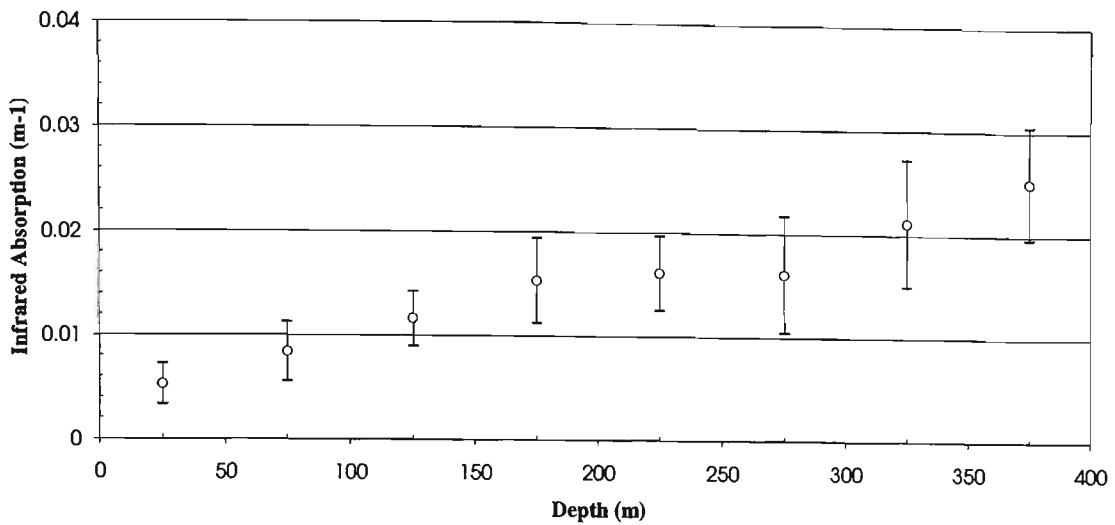


Figure 5.50. Infrared (10-84 μm) absorption of clouds 1-7 averaged over 50 m deep layers into the clouds. Variability is indicated by \pm one standard deviation. The statistics were calculated from the combined FSSP and 2D-C measured DSDs.

Infrared Absorption (FSSP and 2D-C, Cloud 8)

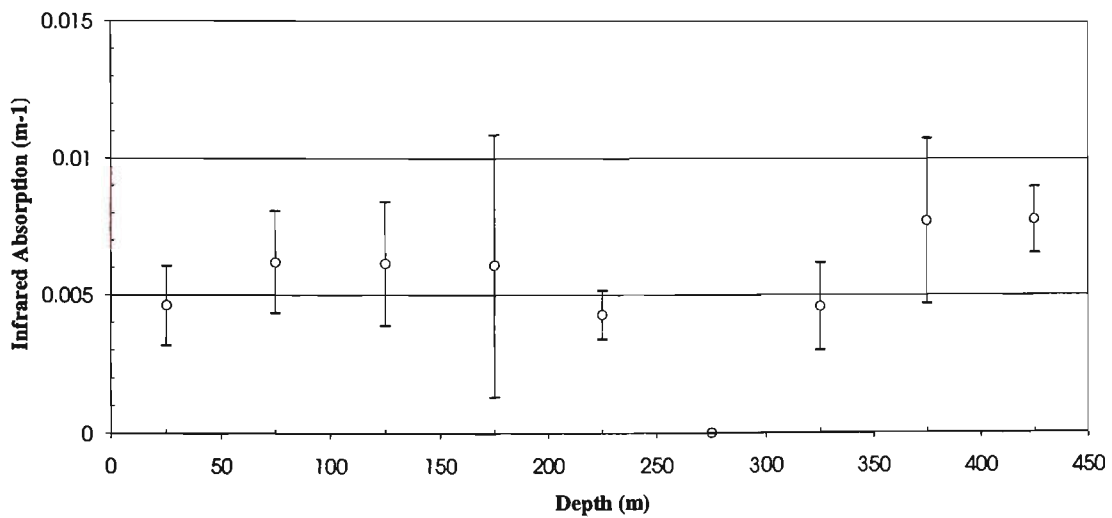


Figure 5.51. Infrared (10-84 μm) absorption of cloud 8 averaged over 50 m deep layers into the cloud. Variability is indicated by \pm one standard deviation. The statistics were calculated from the combined FSSP and 2D-C measured DSDs.

5.3.3.11 Ratio of Visible Extinction to Infrared Absorption (α)

The visible (532 nm) extinction-to-infrared (10.84 μm) absorption ratios (α) were calculated for all DSDs of clouds 1-8. This was done by simply calculating σ_v/σ_a for each measured DSD. The results calculated from the combined FSSP and 2D-C measured DSDs are shown in Figure 5.52. These results were averaged over 50 m depths into the clouds starting from cloud base. Averages α and variabilities (standard deviations, $\Delta\alpha$) for the marine clouds, clouds 1-7, are shown in Table 5.19. Similar results for cloud 8 are shown in Table 5.20. Numbers of DSDs used in the calculations are the same as used for the calculations of visible extinction (see Tables 5.11 and 5.12). The results shown in Tables 5.19 and 5.20 are plotted in Figures 5.53 and 5.54 respectively.

Table 5.19. The ratio (α) for clouds 1-7.

Layer (m)	FSSP		FSSP and 2D-C	
	α	$\Delta\alpha$	α	$\Delta\alpha$
000-050	2.65	0.25	2.63	0.27
050-100	2.47	0.25	2.46	0.25
100-150	2.27	0.10	2.27	0.11
150-200	2.19	0.10	2.18	0.10
200-250	2.12	0.08	2.12	0.08
250-300	2.10	0.08	2.10	0.08
300-350	2.07	0.01	2.07	0.01
350-400	2.05	0.01	2.05	0.01

Table 5.20. The ratio (α) for cloud 8.

Layer (m)	FSSP		FSSP and 2D-C	
	α	$\Delta\alpha$	α	$\Delta\alpha$
000-050	2.66	0.12	2.52	0.13
050-100	2.41	0.03	2.37	0.04
100-150	2.24	0.03	2.24	0.03
150-200	2.09	0.04	2.08	0.03
200-250	2.28	0.09	2.23	0.07
250-300	-	-	-	-
300-350	2.17	0.06	2.15	0.06
350-400	2.13	0.02	2.11	0.02
400-450	2.09	0.02	2.09	0.02

Ratio of Visible Extinction to Infrared Absorption

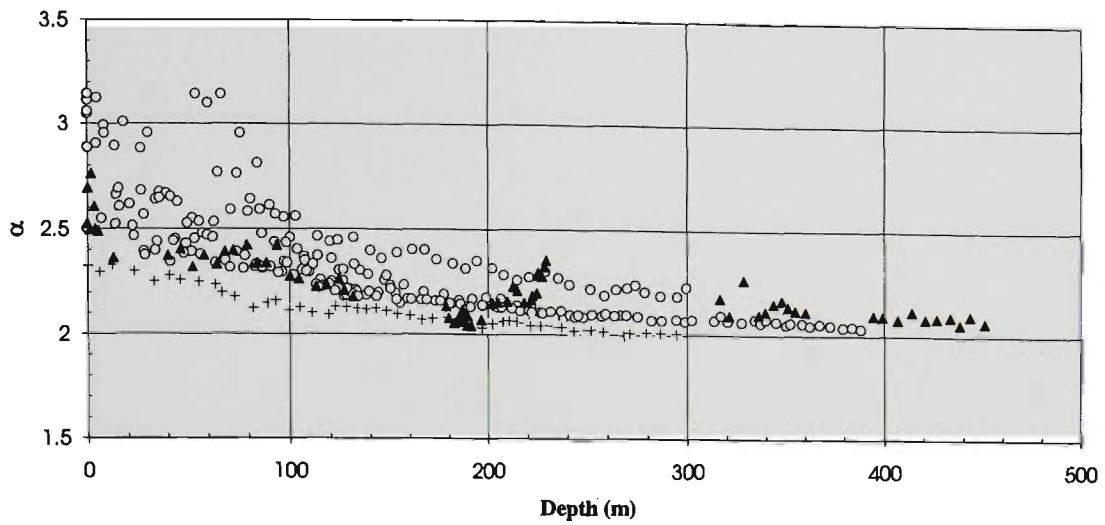


Figure 5.52. Visible extinction-to-infrared absorption ratio (α) of clouds 1-3 and 5-7 (open circles), cloud 4 (crosses) and cloud 8 (filled triangles), calculated from the combined FSSP and 2D-C measured DSDs.

Ratio of Visible Extinction to Infrared Absorption

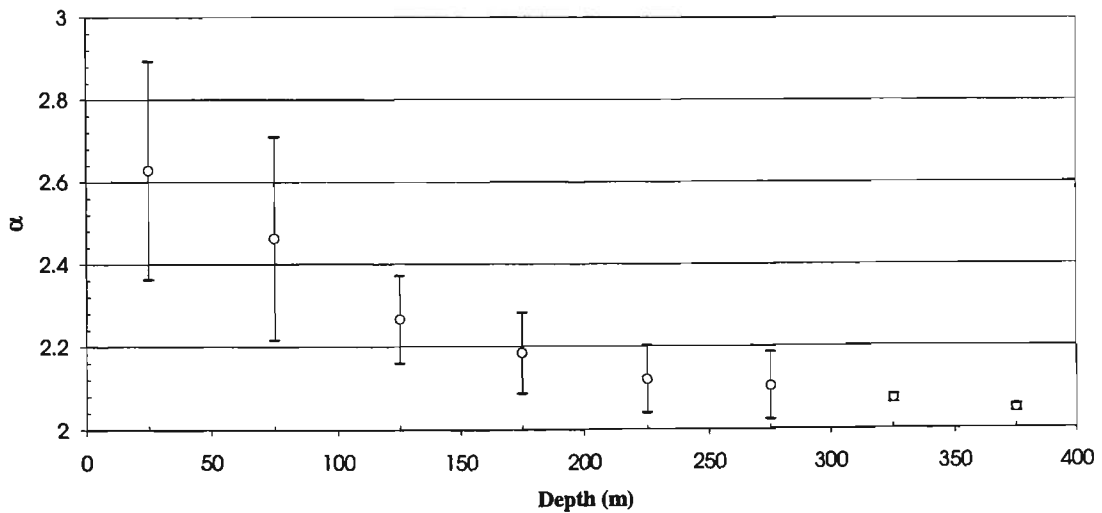


Figure 5.53. Visible extinction-to-infrared absorption ratio (α) of clouds 1-7, averaged over 50 m deep layers into the clouds. Variability is indicated by \pm one standard deviation. The statistics were calculated from the combined FSSP and 2D-C measured DSDs.

Ratio of Visible Extinction to Infrared Absorption

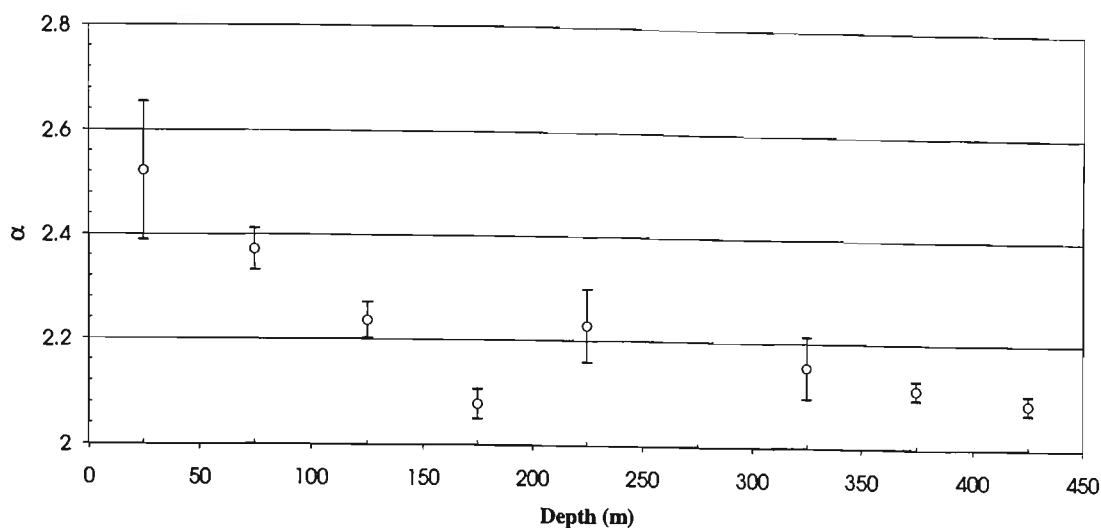


Figure 5.54. Visible extinction-to-infrared absorption ratio (α) of cloud 8, averaged over 50 m deep layers into the clouds. Variability is indicated by \pm one standard deviation. The statistics were calculated from the combined FSSP and 2D-C measured DSDs.

5.3.3.12 Visible Optical Depths

Visible (532 nm) optical depths (τ_v) were calculated by integrating the height profiles of σ_v with respect to height z for clouds 1-8, and the results calculated from the combined FSSP and 2D-C measurements are shown in Figure 5.55. Values for τ_v were calculated at 50 m intervals into the clouds by linear interpolation. The averages (τ_v) and variabilities (one standard deviation, $\Delta\tau_v$) of clouds 1-7 and the interpolated τ_v for the cloud 8 profile, are shown in Table 5.21. The results of Table 5.21 for the combined FSSP and 2D-C results are plotted in Figure 5.56.

Table 5.21. Visible optical depths (τ_v) for clouds 1-8.

Depth (m)	FSSP		FSSP and 2D-C			
	clouds 1-7		cloud 8	clouds 1-7		cloud 8
	τ_v	$\Delta\tau_v$	τ_v	τ_v	$\Delta\tau_v$	τ_v
0	0.00	0.00	0.00	0.00	0.00	0.00
50	0.68	0.13	0.24	0.70	0.11	0.29
100	1.69	0.37	0.91	1.72	0.36	1.01
150	2.96	0.65	1.34	3.00	0.62	1.44
200	4.64	1.12	1.68	4.73	1.06	1.79
250	5.98	1.21	1.95	5.10	1.14	2.08
300	7.27	1.73	1.95	7.44	1.62	2.08
350	11.47	-	2.25	11.49	-	2.41
400	-	-	2.48	-	-	2.65
450	-	-	3.31	-	-	3.50

Visible Optical Depths, Clouds 1-8

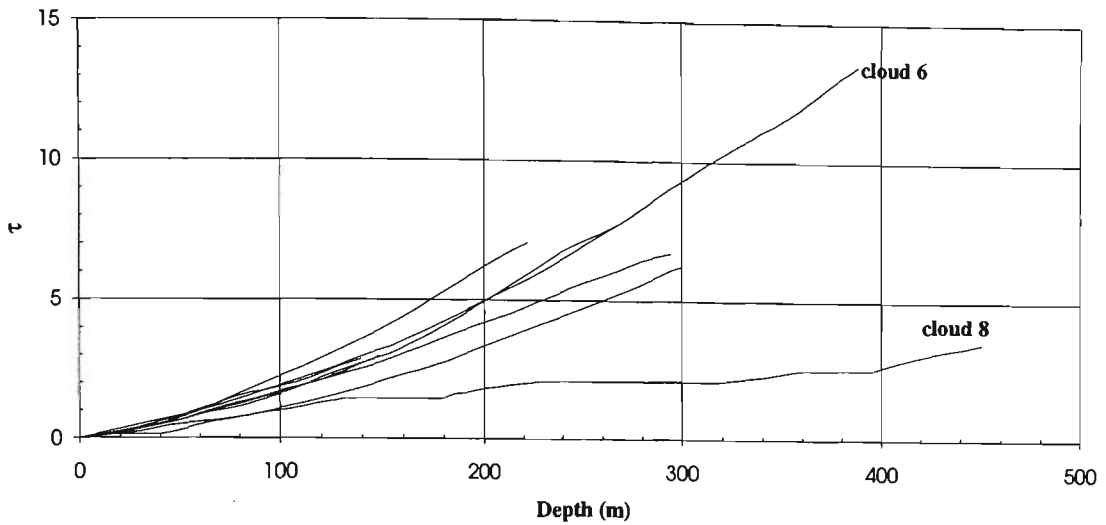


Figure 5.55. Visible (532 nm) optical depths (τ_v) of clouds 1-8. These profiles were calculated from the combined FSSP and 2D-C measured DSDs.

Visible Optical Depths, Clouds 1-8

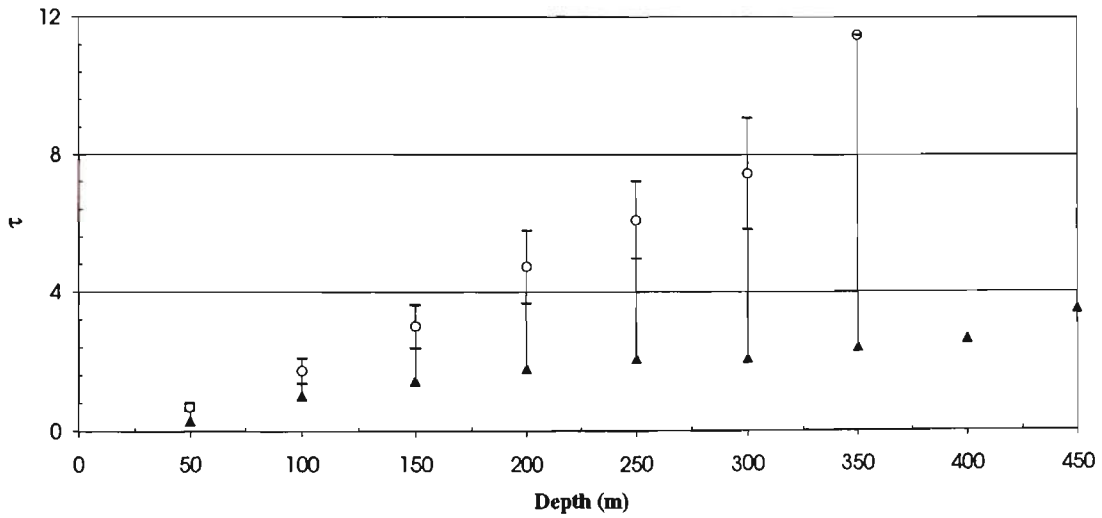


Figure 5.56. Visible (532 nm) optical depths (τ_v) calculated at 50 m intervals into the clouds by linear interpolation. Average τ_v of the clouds 1-7 are shown by circles with variabilities \pm one standard deviation, and τ_v of cloud 8 is shown by triangles. These profiles were calculated from the combined FSSP and 2D-C measured DSDs.

5.3.3.13 Infrared Absorption Optical Depths

Infrared (10-84 μm) optical depths (τ_i) were calculated from the height-profiles of infrared absorption for clouds 1-8, and the results calculated from the combined FSSP and 2D-C measurements are shown in Figure 5.57. Values for τ_i were calculated at 50 m intervals into the clouds by linear interpolation. The averages (τ_i) and variabilities (one standard deviation, $\Delta\tau_i$) of clouds 1-7 and the interpolated τ_i for the cloud 8 profile, are shown in Table 5.22. The results of Table 5.22 for the combined FSSP and 2D-C results are plotted in Figure 5.58.

Table 5.22. Infrared optical depths (τ_i) for clouds 1-7, and τ_i for cloud 8 in columns 4 and 7.

Depth (m)	<i>FSSP</i>		cloud 8	<i>FSSP and 2D-C</i>		cloud 8
	clouds 1-7			clouds 1-7		
	τ_i	$\Delta\tau_i$	τ_i	τ_i	$\Delta\tau_i$	τ_i
0	0	0	0	0	0	0
50	0.26	0.05	0.09	0.27	0.05	0.12
100	0.68	0.17	0.37	0.69	0.17	0.42
150	1.23	0.29	0.57	1.26	0.28	0.61
200	2.02	0.51	0.73	2.06	0.49	0.78
250	2.67	0.59	0.85	2.73	0.58	0.92
300	3.29	0.85	0.85	3.37	0.82	0.92
350	5.31	-	0.99	5.32	-	1.07
400	-	-	1.10	-	-	1.18
450	-	-	1.49	-	-	1.59

Infrared Optical Depths, Clouds 1-8

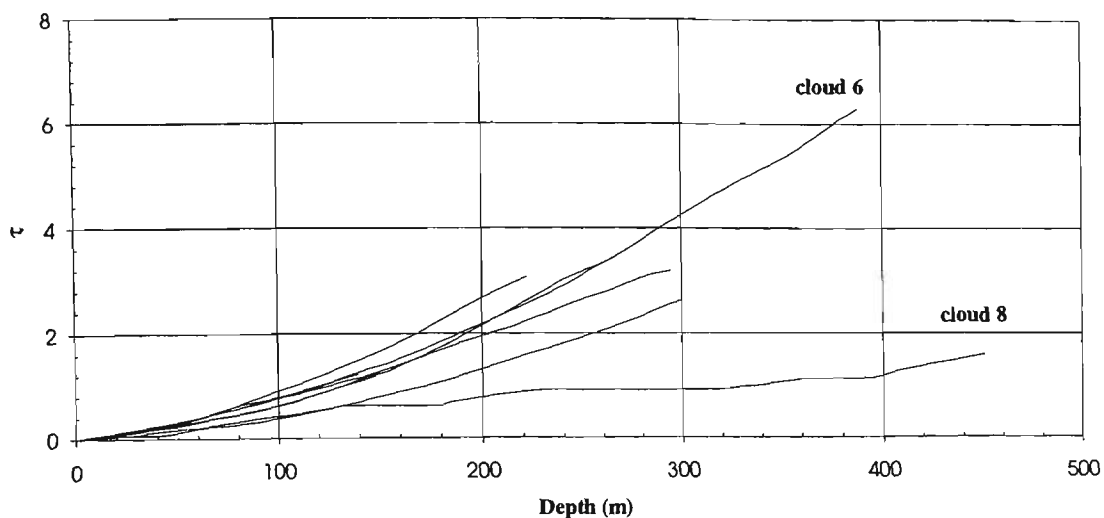


Figure 5.57. Infrared (10-84 μm) optical depths (τ_i) of clouds 1-8. These profiles were calculated from the combined FSSP and 2D-C measured DSDs.

Infrared Optical Depths, Clouds 1-8

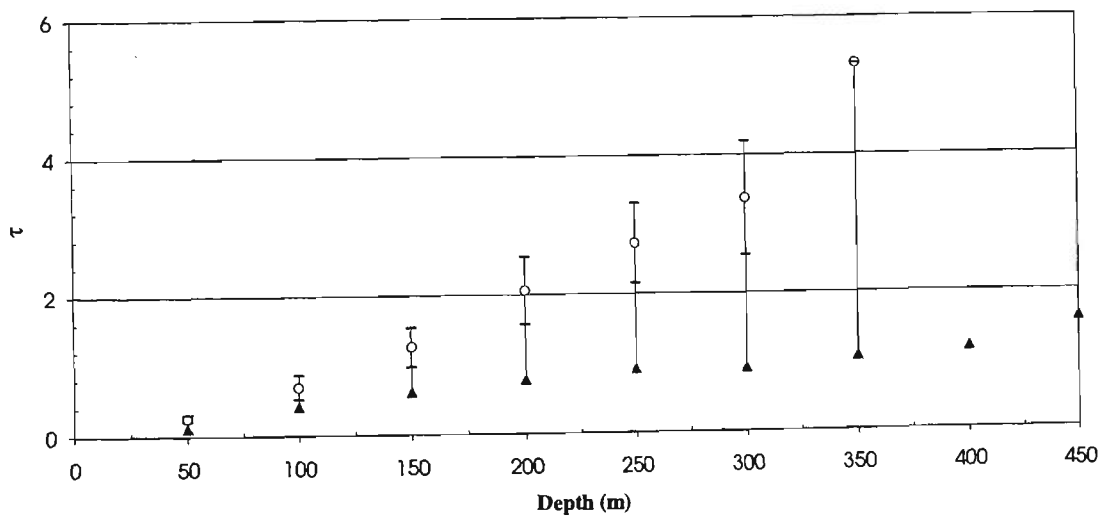


Figure 5.58. Infrared (10-84 μm) optical depths (τ_a) calculated at 50 m intervals into the clouds by linear interpolation. Average τ_a of the clouds 1-7 are shown by circles with variabilities \pm one standard deviation, and τ_v of cloud 8 is shown by triangles. These profiles were calculated from the combined FSSP and 2D-C measured DSDs.

5.3.4 LIRAD Study of Stratocumulus Clouds Observed On 16 July 1993 (SOCEX1)

5.3.4.1 Introduction

The LIRAD results for the marine stratocumulus clouds observed on 16 July 1993 during SOCEX1 are presented in the following sections. The primary inputs to the LIRAD analysis technique were the calibrated lidar profiles of attenuated backscatter, from which the integrated values (χ') were calculated, {section 4.3.4.3, and Figure (5.59)}, and the measured infrared radiances, {section 4.3.4.2, and Figure (5.60)}, from which the cloud radiances due to infrared absorption (L_i) were determined. Note that the radiances shown in the latter figure include the effects of spectral filtering by the radiometer (section 3.2.3): the infrared radiances of water droplet clouds integrated over the 10 - 12 μm wavelength band of the spectrum increase from approximately $5 \text{ W m}^{-2} \text{ sr}^{-1}$ for an infrared optical depth (τ_i) of 1, to approximately $12 \text{ W m}^{-2} \text{ sr}^{-1}$ for $\tau_i = 5$ (see section 4.3.4.7).

The LIRAD results presented in the following sections are: the infrared emittances (ϵ_i) and τ_i and estimates of the maximum errors in these quantities (5.3.4.2), the extinction-to-backscatter ratio modified by the multiple scatter factor (ηS , section 5.3.4.3.), and the visible optical depths modified by η , ($\eta\tau_v$, section 5.3.4.4). These latter two sections demonstrate that some useful visible optical properties of boundary layer (water droplet) clouds can be determined from calibrated lidar measurements only, and with only a little analysis effort. (This is provided that the fully attenuating clouds can be clearly identified). In section 5.3.4.5 a comparison of the LIRAD-retrieved ηS and $\eta\alpha$ with the values of S and α determined from the *in situ* measurements enabled retrievals of η .

Integrated Attenuated Backscatter (16 July 1993)

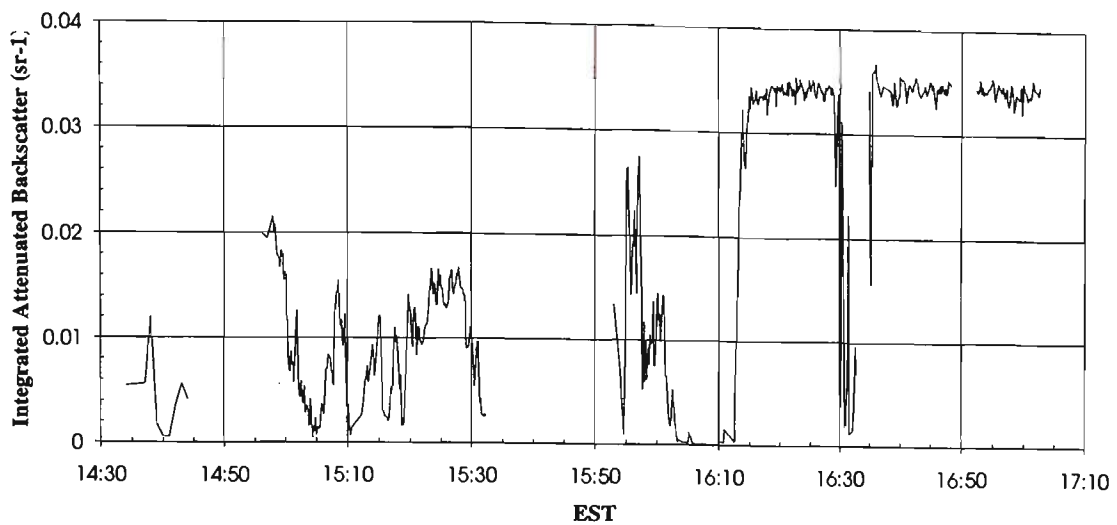


Figure 5.59. Integrated attenuated backscatter (χ' sr⁻¹) for the marine stratocumulus clouds measured by lidar at Cape Grim on the afternoon of 16 July 1993.

Measured Infrared Radiances (16 July 1993)

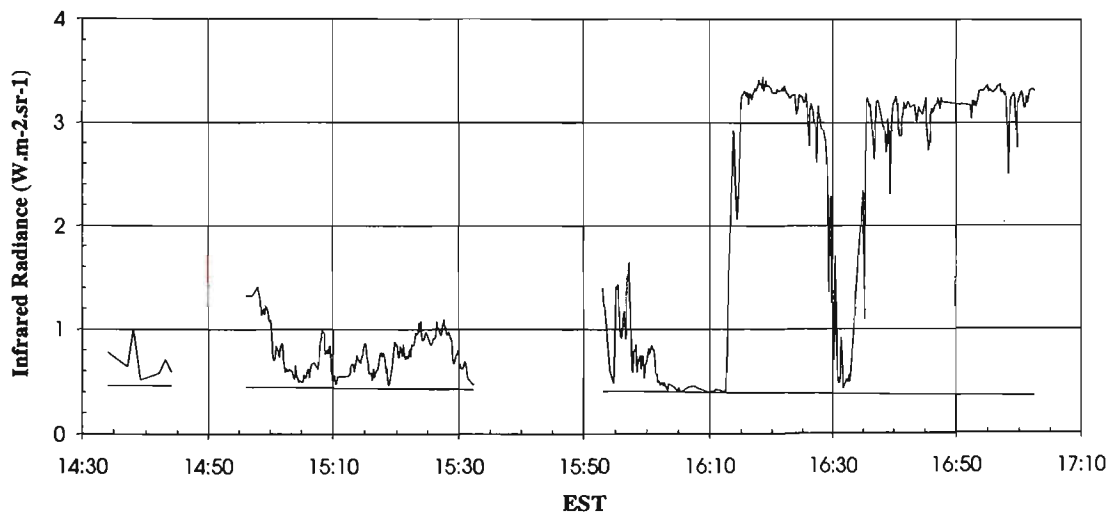


Figure 5.60. Total infrared radiances (L_g W m⁻² sr⁻¹) measured by radiometer (upper lines), and calculated cloud-free radiances (lower straight lines), obtained over the same period as shown in the previous figure. These radiances represent the radiometer filter spectral band.

5.3.4.2 Infrared Properties of the Clouds by LIRAD

Estimates of the errors for infrared emittances (ϵ) and infrared absorption optical depths (τ_i) are presented in section (i), followed by the LIRAD results for ϵ and τ_i in section (ii).

(i) Errors

The equation (2.40) was used to determine the error in the cloud radiances ΔL_c , and equation (2.43) to determine the error in the cloud infrared absorption radiance (ΔL_i). Estimates of the errors used to determine these quantities are shown in Table 5.23. These errors in the radiances were estimated by inspection of the variabilities in the measured infrared radiances as well as the various parameterisations presented in sections 4.3.4.4. to 4.3.4.7.

Table 5.23. Estimates of maximum errors in infrared radiances and transmittances.

<i>Error</i>	<i>Magnitude</i>
ΔL_g	0.04 W m ⁻² sr ⁻¹
ΔL_{air}	0.04 W m ⁻² sr ⁻¹
$\Delta L_{air}^{(a)}$	0.04 W m ⁻² sr ⁻¹
$\Delta L_{air}^{(b)}$	0.08 W m ⁻² sr ⁻¹ (= $\Delta L_{air} + \Delta L_{air}^{(a)}$)
$\Delta T_{air}^{(b)}$	0.002
ΔT_i	≈ 0.08 (maximum determined by iteration)
$\Delta(L_r + L_s)$	≈ 0.02 × L_i (see 4.3.4.7).

The relative errors $\Delta\epsilon/\epsilon \approx \Delta L_i/L_i$, (e.g. Platt *et al.*, 1998), and as ϵ were calculated from τ_i , the errors $\Delta\tau_i$ were determined from,

$$\Delta\tau_i = \frac{\Delta\epsilon + \Delta\epsilon_r + \Delta\epsilon_s}{\exp(-\tau_i)}, \quad (5.1)$$

where ($\epsilon_r + \epsilon_s$) is the (small) contribution to the measured emittances due to reflection and internal scattering, and ($\Delta\epsilon_r + \Delta\epsilon_s$) was estimated to be approximately 3% of ϵ . The relative errors $\Delta\epsilon/\epsilon$ and $\Delta\tau_i/\tau_i$ were then determined for all the LIRAD results for ϵ and τ_i {see Figures (5.61) and (5.62)}.

(ii) Results

The results for $\epsilon \pm \Delta\epsilon$ and $\tau_i \pm \Delta\tau_i$ are shown in Figures (5.63) and (5.64) respectively. Frequency distributions of the emittances and infrared absorption optical depths are shown in Figures (5.65) and (5.66) respectively. These results used the estimate of $(L_r + L_s) = (0.05 \pm 0.02) \times L_i$ (see section 4.3.4.7).

Relative Errors in Infrared Emittances

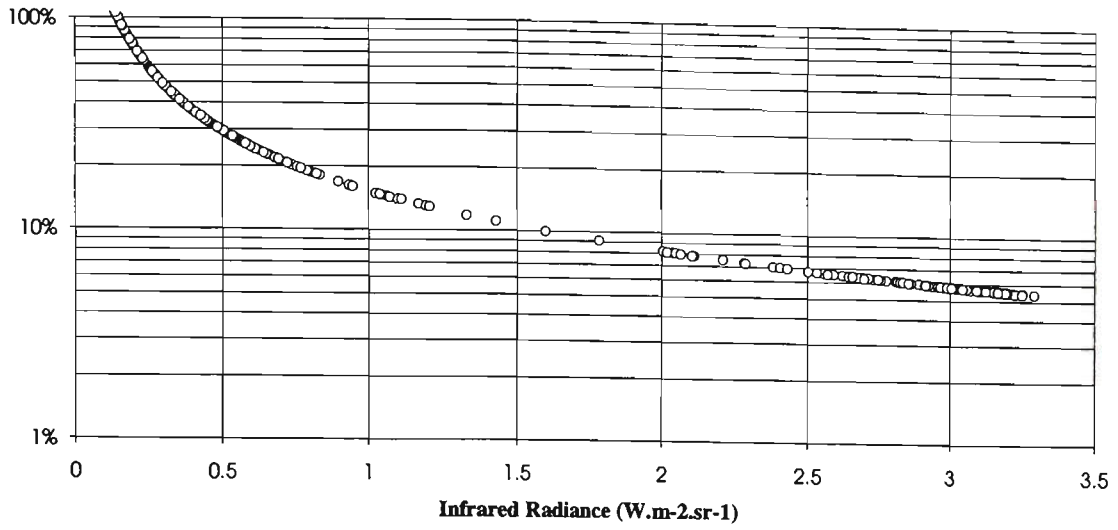


Figure 5.61. Relative errors $\Delta\epsilon/\epsilon$ versus L_i for each LIRAD result.

Relative Errors in Infrared Absorption Optical Depths

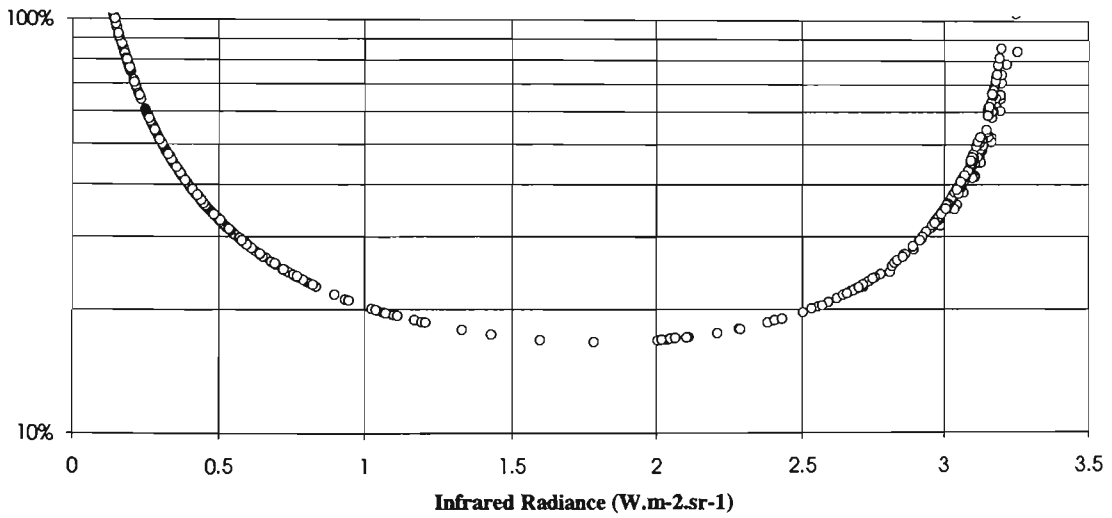


Figure 5.62. Relative errors $\Delta\tau_i/\tau_i$ versus L_i for each LIRAD result.

Infrared Emittances by LIRAD

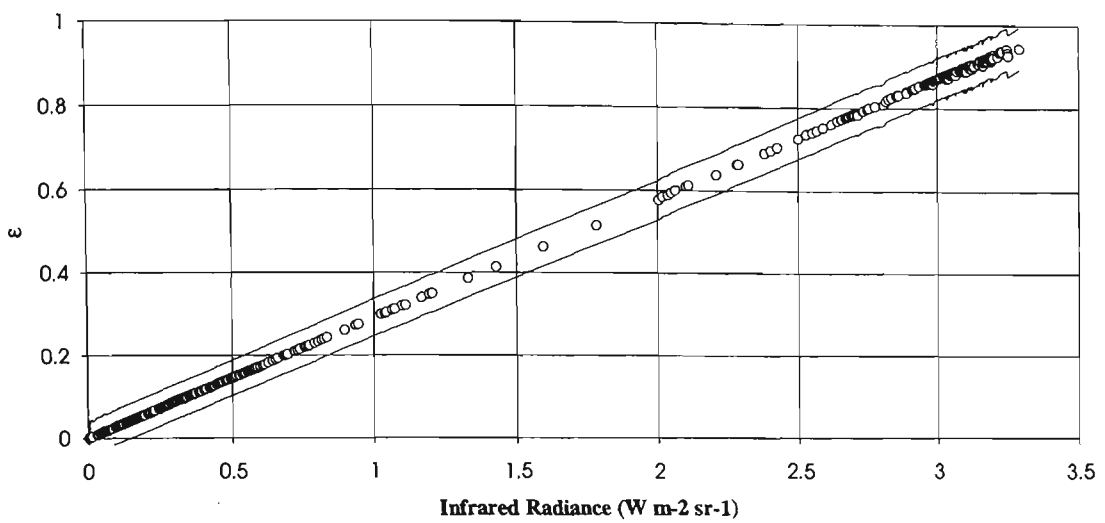


Figure 5.63. LIRAD results for $\epsilon \pm \Delta\epsilon$ versus the measured cloud infrared absorption radiance (L_i) for the stratocumulus cloud temperature of approximately 1°C .

Infrared Absorption Optical Depths by LIRAD

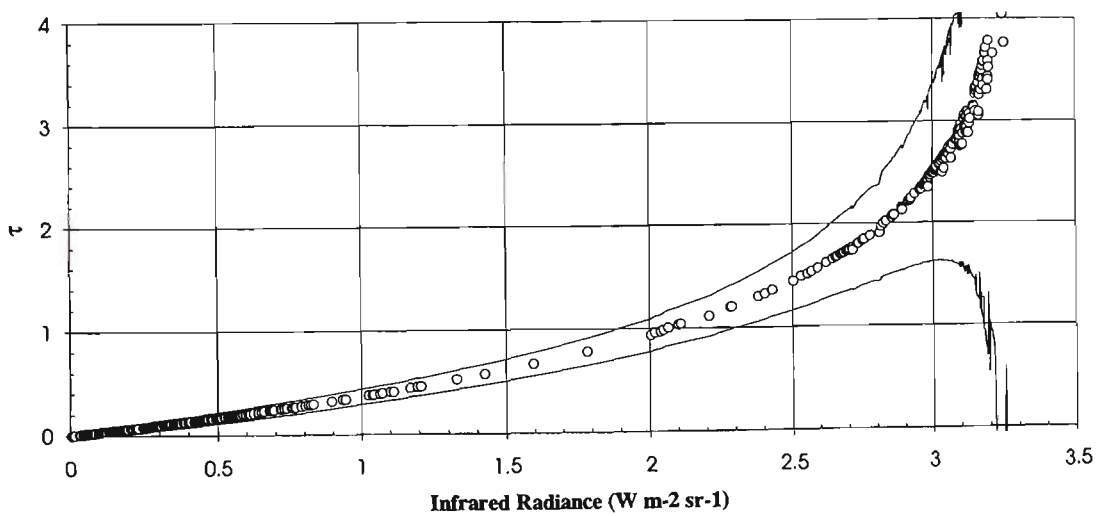


Figure 5.64. LIRAD results for $\tau_i \pm \Delta\tau_i$ versus the measured L_i for a stratocumulus cloud temperature of approximately 1°C .

Normalised Frequency Distribution of Infrared Emittances

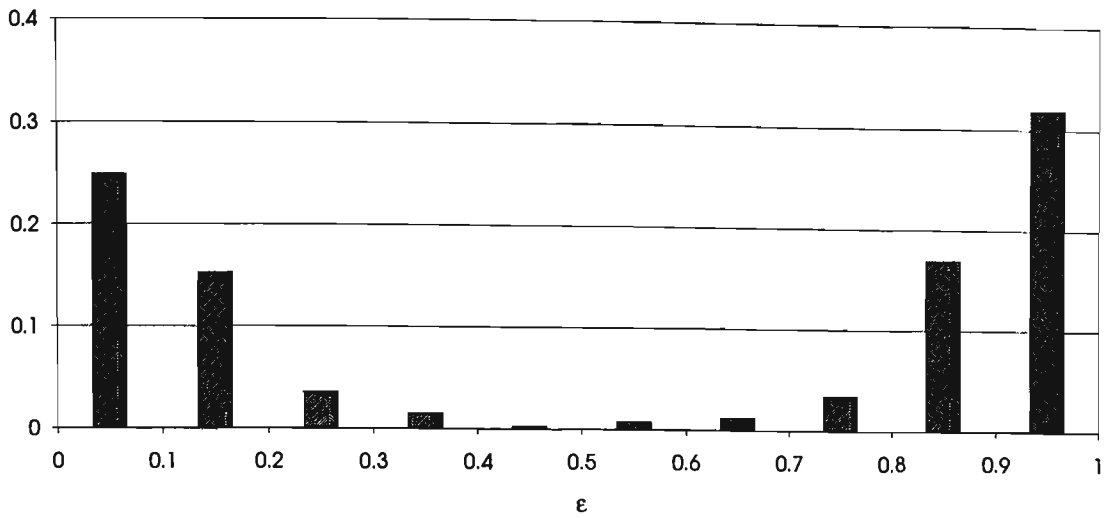


Figure 5.65. Normalised frequency distribution for the infrared emittances (ϵ) of the clouds measured by LIRAD between approximately 1430 EST to 1700 EST on 16 July 1993. Some of the LIRAD measurements of the thickest clouds could not be analysed; these were assumed to have $\epsilon > 0.9$.

Distribution of Infrared Absorption Optical Depths

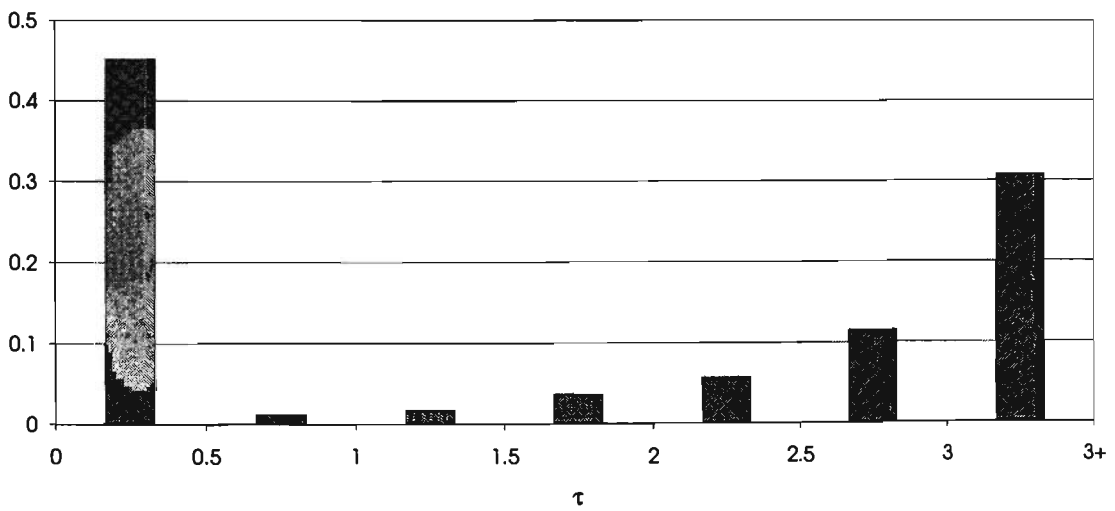


Figure 5.66. Normalised frequency distribution of the infrared absorption optical depths (τ_i) measured by LIRAD between approximately 1430 EST to 1700 EST on 16 July 1993.

5.3.4.3 Extinction-to-Backscatter Ratio Modified by The Multiple Scatter Factor (ηS)

The first estimate of $(2\eta S)^{-1}$ which was obtained from the lidar backscatter and measured radiances prior to applying the LIRAD method to the data, (section 4.3.4.3), is checked in the following. It is recalled that by inspection of the LIRAD equation (2.30a),

$$\chi' = \frac{1}{2\eta S} (1 - \exp(-2\eta\tau_v)), \quad \text{\{equation (2.30a)\}}$$

as,

$$\tau_a \rightarrow \infty, \chi' \rightarrow \frac{1}{2\eta S}. \quad \text{\{equation (2.31)\}}$$

The values of χ' approached a maximum for infrared emittances of approximately $\epsilon_i > 0.80$; {see Figure (5.67)}. For $\epsilon_i > 0.80$ the average $\chi' \pm$ one standard deviation was $0.0345 \pm 0.0007 \text{ sr}^{-1}$ ($\pm 2.2\%$); {Figure (5.68)}. This result compared well with the value of $\chi' = 0.0344 \pm 0.0007 \text{ sr}^{-1}$; (section 4.3.4.3). The value of ηS that results from the new maximum χ' value is $14.5 \pm 0.3 \text{ sr}$ ($\pm 2.2\%$).

The variability in the retrieved maximum χ' is due to uncertainties in the signal offsets of each profile, the digital signal-resolutions, and variations in the microphysical and multiple scattering properties of the clouds. The uncertainty in χ' due to molecular scattering is about $\pm 0.6\%$, and that due to the lidar system constant about $\pm 2.2\%$. Thus the maximum χ' and the resulting ηS are,

$$\chi' = 0.0345 \pm 0.001 \text{ sr}^{-1} (\pm 3\%), \quad (5.2)$$

and,

$$\eta S = 14.5 \pm 0.5 \text{ sr} (\pm 3\%). \quad (5.3)$$

Integrated Attenuated Backscatter vs. Infrared Emittance

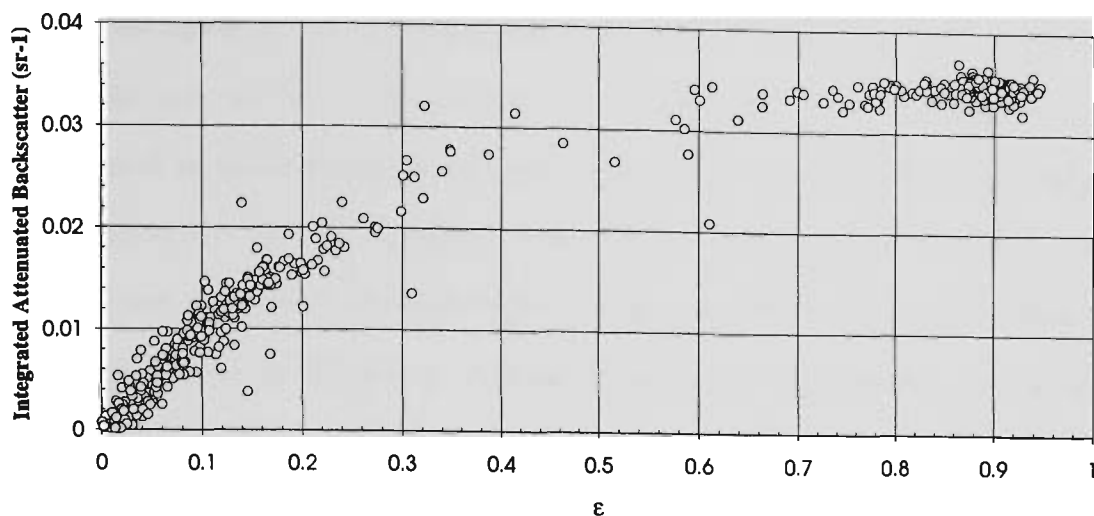


Figure 5.67. Integrated attenuated backscatter (χ' sr⁻¹) vs. ϵ {cf. Figure (2.2)}. The traditional presentation of LIRAD results, *i.e.* γ vs. ϵ , is obtained by multiplying these results by 4π .

Maximum Integrated Attenuated Backscatter

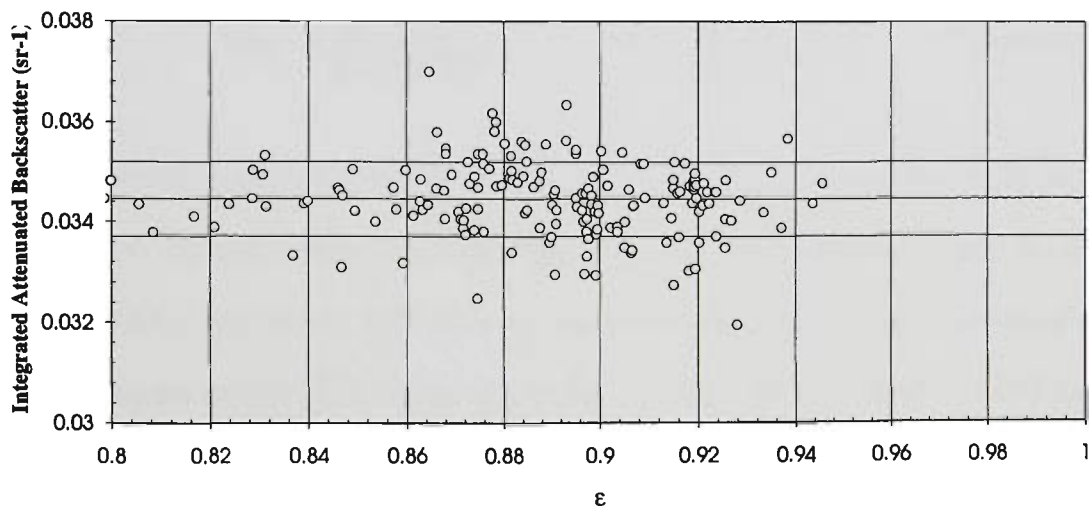


Figure 5.68. Maximum values of measured χ' and the average \pm one standard deviation obtained from the points with $\epsilon_i > 0.80$. An estimate of ηS is obtained from these results (see text).

5.3.4.4 Visible Optical Depths Modified by the Multiple Scatter Factor ($\eta\tau_v$)

Laser pulses are rapidly attenuated in water droplet clouds due to volume extinction coefficients (σ_v) of magnitudes such as those seen in Figures (5.40) and (5.41). By inspection of the lidar measurements of the marine stratocumulus clouds studied for this thesis the lidar pulses penetrated an apparent depth of only 200 - 250 m into the thickest clouds. The detection of the slight backscatter from deeper into these clouds was limited by the sensitivity of the lidar detector/digitiser, which limited the precision of the retrieved χ' . This meant that the lidar measurements could be used for retrieving only $\eta\tau_v$ for the optically thin clouds, illustrated in the following. The measured ηS and χ' obtained from the previous section were used to calculate visible optical depths modified by the multiple scatter factor ($\eta\tau_v$) by the method described in section 2.2.3.1: *i.e.*,

$$\eta\tau_v = \frac{1}{2} \ln \left(\frac{1}{1 - 2\eta S \chi'} \right), \quad \{\text{equation (2.32)}\}$$

with the standard deviation of $\eta\tau_v$ determined by,

$$s_{(\eta\tau_v)} = \sqrt{\left(\frac{\chi'}{1 - 2\eta S \chi'} \right)^2 s_{(\eta S)}^2 + \left(\frac{\eta S}{1 - 2\eta S \chi'} \right)^2 s_{\chi'}^2}. \quad \{\text{equation (2.35)}\}$$

The use of these equations assumes that the parameters χ' and ηS are independent but this is not the case - the value of χ' for a single lidar measurement of a cloud is dependent on, in part, the value of ηS (section 5.3.4.2). However, for these measurements of water droplet clouds S was found to vary by only a small amount with depth into the clouds {see Figures (5.46), (5.47) and (5.48)}. Thus, here, the values of χ' were assumed to be independent of ηS . It is known that η varies with optical depth but is relatively constant for larger optical depths {*e.g.* Platt (1981)}.

Visible Optical Depths Modified by Eta

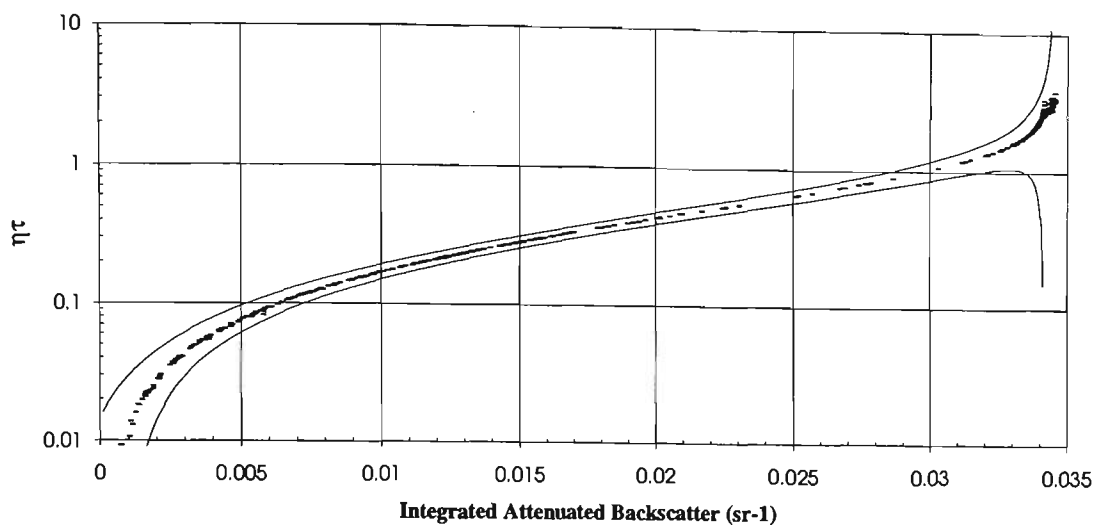


Figure 5.69. Visible optical depths modified by the multiple scatter factor ($\eta\tau_v$), determined by the LIRAD method, versus integrated attenuated backscatter ($\chi' \text{ sr}^{-1}$). The uncertainties indicated by the solid lines were calculated from the lidar measured quantities ηS and χ' only.

Visible Optical Depths Modified by Eta (Thicker Clouds)

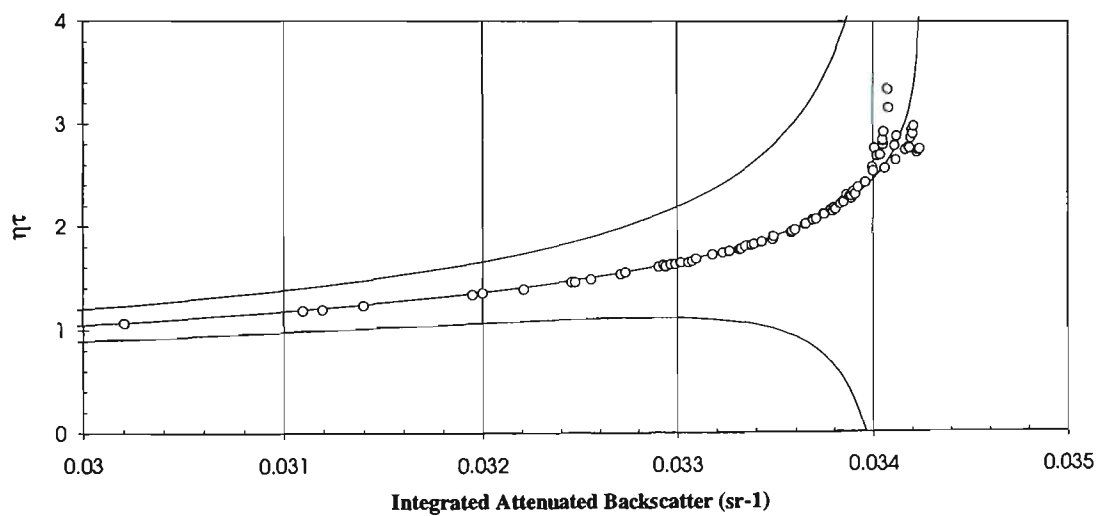


Figure 5.70. The same data as in the previous figure but showing only those with $\chi' > 0.03 \text{ sr}^{-1}$. Note the linear scale for $\eta\tau_v$ in this figure. $\Delta(\eta\tau_v)/(\eta\tau_v) = 100\%$ where $\chi' \approx 0.0340 \text{ sr}^{-1}$.

The calculated results for $\eta\tau_v \pm s_{\eta\tau}$ are shown in Figure (5.69) as well as the values of $\eta\tau_v$ determined by the LIRAD method. An expanded view showing the results for the thicker clouds with $\chi' > 0.03 \text{ sr}^{-1}$ is shown in Figure (5.70). Inspection of these figures highlights the difficulties in obtaining accurate values of $\eta\tau_v$ by lidar only: the accuracy of the calculated $\eta\tau_v$ was limited for the thin clouds by the large values of $\Delta\chi'/\chi'$, and, as χ' approached $(2\eta S)^{-1}$, the retrieval of the optical depths of the thicker clouds was limited by attenuation of the laser beams in the clouds. Over the range,

$$0.014 < \chi' < 0.025 \text{ sr}^{-1}, \quad (5.4)$$

the retrieval of $\eta\tau_v$ was reasonably accurate with relative errors less than 10%.

5.3.4.5 The Multiple Scatter Factor (η) and Distributions of the Visible Optical Depths

In this section estimates of the multiple scatter factor (η) are made by comparing the LIRAD retrievals for ηS and $\eta\alpha$ with values of S and α determined from the *in situ* microphysical measurements of the clouds. The LIRAD results ηS and $\eta\alpha$ were determined from the measurements of the thicker clouds and thinner clouds respectively, and the values for S and α were calculated via the Mie theory using measured cloud droplet size distributions (section 5.2.3).

A value of ηS was obtained from the LIRAD measurements of clouds that were fully attenuating to the lidar. That is, for $\epsilon > 0.8$,

$$\eta S = 14.5 \pm 0.5 \text{ sr}, \quad \{\text{result (5.3)}\}$$

(section 5.2.4.3). The average apparent depth \pm one standard deviation of these 166 LIRAD measurements was approximately $281 \pm 27 \text{ m}$. The backscatter and extinction of the 263 DSDs measured *in situ* up to a depth of 308 m into these clouds were determined by Mie calculations, and the average $S \pm$ one standard deviation of these results was (5.3.3.9),

$$S = 18.9 \pm 0.5 \text{ sr}. \quad (5.5)$$

Ratio of Visible Extinction to Infrared Absorption

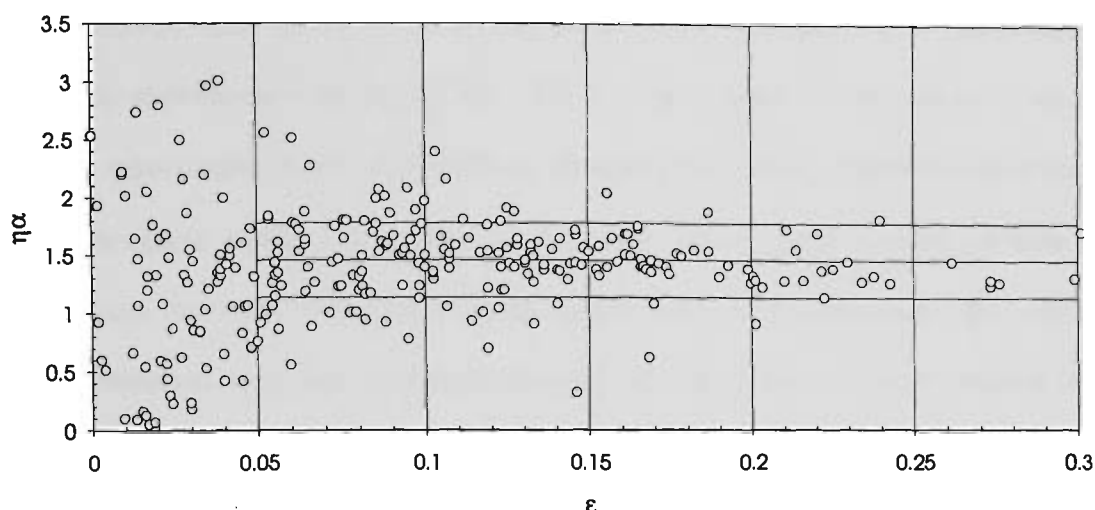


Figure 5.71. Values of $\eta\alpha$ versus ϵ_i . The average $\eta\alpha \pm$ one standard deviation over the range of ϵ where the errors $\Delta\eta\alpha$ were smallest, *i.e.*, $0.05 < \epsilon < 0.3$, are indicated by the horizontal lines.

Division of the result (5.3) by (5.5) produced,

$$\eta = 0.77 \pm 0.05. \quad (5.6)$$

Values of $\eta\alpha$ were determined for all τ_i and $\eta\tau_v$, determined by the LIRAD method. The errors in $\eta\alpha$ were smallest over the range of ϵ of approximately 0.05 to 0.3. Over this range the variability in $\eta\alpha$ was approximately the same as the relative errors in $\eta\alpha$, and the average $\eta\alpha \pm$ one standard deviation over this range was,

$$\eta\alpha = 1.5 \pm 0.3 (\pm 20\%), \quad (5.7)$$

{see Figure (5.71)}. Outliers with $\eta\alpha > 3$ were discarded from this result. The average geometrical depth for these 205 LIRAD measurements was 105 ± 35 m. For the 148 DSDs measured *in situ* up to a depth of 140 m into these clouds the average $\alpha \pm$ one standard deviation was,

$$\alpha = 2.5 \pm 0.25 (\pm 10\%), \quad (5.8)$$

(section 5.3.3.11). Division of the result (5.7) by result (5.8) gives,

$$\eta = 0.6 \pm 0.2 (\pm 30\%). \quad (5.9)$$

As seen in Figure (5.67), χ' reaches a maximum for the thickest clouds, for which signals are received from approximately the lowest 200 - 250 m in the clouds. As the average S was nearly constant for water droplet clouds of all depths, and because there were no significant variations in χ' for the larger optical depths, then η must also have been approximately constant for these deeper clouds. (Unless, that is, the thicker stratocumulus clouds were all of approximately the same optical depth). Distributions of τ_v were determined by using the upper limit of $\eta = 0.8$ obtained from the measurements of the thickest clouds, and the lower limit of $\eta = 0.4$ obtained from the measurements of the moderately thick clouds. The values of τ_v were simply obtained by dividing the LIRAD retrieved values of $\eta\tau_v$ (section 5.3.4.4) by both values of η (0.4 and 0.8). The resulting distributions of τ_v are shown in Figure (5.72). By inspection of this figure, note that the choice of η has little effect on the major result: that a significant fraction of the clouds were optically thin; *i.e.*, 40% to 42% had $\tau_v < 1$. The effects of multiple scattering and the lack of knowledge about the variation of η with τ_v did not have a big impact on the results of this study.

Lastly, it was found that the retrievals of the cloud optical properties were sensitive to changes in the estimates of both L_r and L_s . To test the sensitivity of the results to these estimates a trial of the LIRAD algorithm was performed with the estimate of the infrared scattering doubled, *i.e.*,

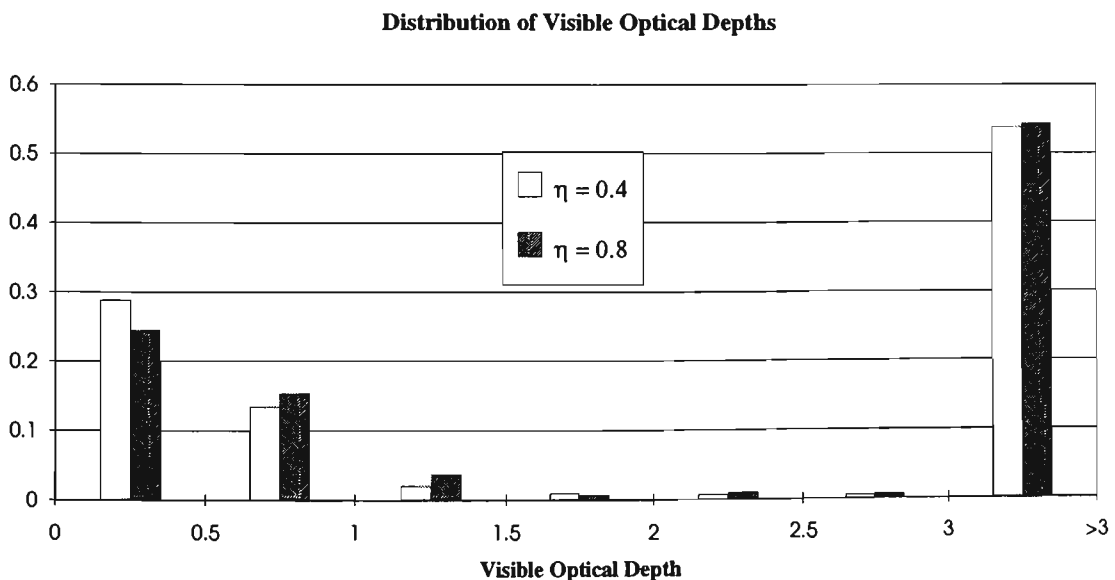


Figure 5.72. Normalised frequency distributions of the cloud visible optical depths determined for a multiple scatter factor (η) of 0.8, (hashed bars), and for $\eta = 0.4$ (open bars).

$(L_r + L_s) = 0.10 \times L_i$. With this reasonably large increase in the estimate of the infrared scattering the corresponding increase in the retrieved $\eta\alpha$, from the measurements of the moderately thick clouds with $0.12 < \tau_v < 0.88$, was approximately 5% - an insignificant increase when compared to the error of 33%. Thus for the moderately thin clouds $\eta = 0.6 \pm 0.2$, as per result (5.9), and this is strong evidence that the value of η retrieved from the measurements of these clouds was indeed less than that retrieved from the measurements of the thickest clouds for which $\eta = 0.77 \pm 0.05$ (result 5.6). The latter value of η is for visible optical depths of approximately $1.3 < \tau_v < 3.9$. To this author's knowledge these are the first measurements of η and these as well as future similar measurements should prove a valuable adjunct to the most recent theoretical studies of the multiple scattering in lidar returns (*e.g.*, Bissonette *et al.*, 1995). Also, an improved knowledge of the effects of scattering on infrared measurements of stratocumulus clouds should make some improvements to the LIRAD retrievals of cloud optical properties.

5.3.5 Microwave Radiometer Results

5.3.5.1 Introduction

The optical depths retrieved by LIRAD were limited to optically thin clouds because of the strong attenuation of visible and infrared radiation by these boundary layer clouds (5.3.4 and 5.4). However simultaneous measurements of the more highly penetrating microwave radiation emitted by the clouds were also available (3.2.4), and this meant that some information about the deeper clouds could also be obtained. Thus the purpose of 5.3.5 is to obtain a better perspective of the total range of cloud optical depths than could be provided by the LIRAD results alone, and also to investigate the utility of the MicroWave Radiometer (MWR) for retrieving optical depths of boundary layer clouds.

5.3.5.2 Limitations of the Measurements

Microwave radiation penetrates water droplet clouds more deeply than shorter-wavelength infrared and visible radiation, provided the droplets are not too much larger than approximately $10 \mu\text{m}$ (typical mode radii). The attenuation of microwave radiation due to scattering becomes more important if the clouds are precipitating; that is, there are droplets with radii of approximately $100 \mu\text{m} - 1 \text{mm}$. The effects of scattering by these large droplets on the MWR retrieved liquid water paths (W) will be illustrated shortly. By inspection of the lidar observations of 16 July 1993, (and from observations

made by the author), there was no precipitation overhead Cape Grim during the period of the LIRAD measurements: *i.e.*, approximately 1430EST to 1700EST.

A more obvious effect of precipitation on the MWR measurements was that sometimes the values of W were spuriously large due to water collected on the MWR receiving dish and mylar screen shield (Boers, 1996a; Boers, 1996b). On 16 July many of the MWR measurements were affected by rain up to 1406EST. Guided by the work of Boers (1996a) and Boers (1996b) an attempt was made to eliminate all the bad data from the study that follows. However, the possibility remains that unevaporated liquid water on the MWR after 1406EST affected some of the results for W .

5.3.5.3 Liquid Water Paths by Microwave Radiometer

The values of W derived from the MWR measurements of the stratocumulus clouds overhead Cape Grim on the afternoon of 16 July 1993 are shown in Figure (5.73) (Boers, 1996a; Boers, 1996b; Boers and O'Brien, 1996). For comparison, also shown are the variations in the infrared emittances obtained by LIRAD (5.3.4.2 of this thesis). Visible optical depths were calculated from these values of W (following sections).

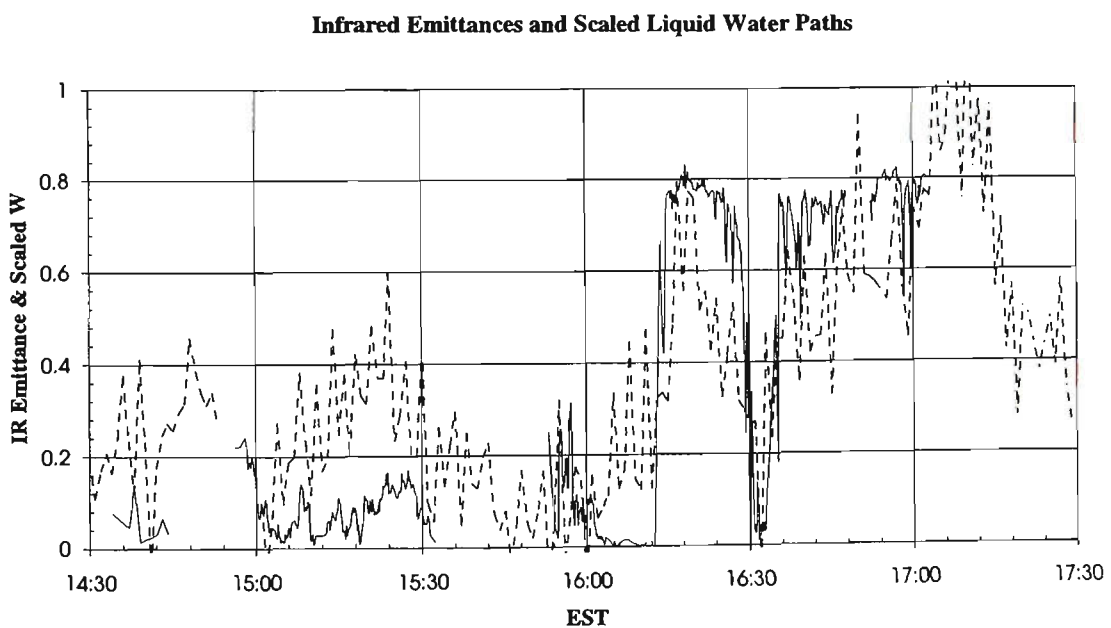


Figure 5.73. Infrared emittances by LIRAD (solid lines) and $W \text{ g m}^{-2}$ derived by MWR, the latter scaled by $0.008 \text{ g}^{-1} \text{ m}^2$ (dashed lines).

5.3.5.4 LIRAD and *In Situ* Measurements by FSSP and 2D-C (16 July 1993)

The purpose of this section is to give the basic LIRAD and *in situ* results to assist with the interpretation of the MWR-retrieved optical depths in the sections to follow. A large fraction of the non-precipitating stratocumulus clouds observed by LIRAD over Cape Grim on 16 July 1993 from 1430EST to 1700EST were optically thin: approximately 50% of these clouds had $\tau_v < 1$ (5.3.4.5). The values of the average visible extinction (σ_v) and average infrared absorption (σ_i) for the thin clouds observed by LIRAD prior to 1610EST are shown in Table 5.24. These averages were determined by dividing the optical depth of each measured cloud by the geometrical depth (also shown in Table 5.24). The thin clouds were not precipitating so the extinction and optical depths determined by LIRAD were compared with the same optical properties determined from the lowest 100 m of the non-precipitating marine stratocumulus clouds observed *in situ* (clouds 1-3, 5-7; see section 5.3.3). The properties of these 100 m layers are also shown in Table 5.24.

Inspection of the results shown in Table 5.24 shows that the extinction of the thin clouds measured over Cape Grim by LIRAD was much less than the extinction of the lowest 100 m depths of the clouds observed over the sea. An explanation of the discrepancy follows. Thicker stratocumulus clouds passed overhead Cape Grim at approximately 1610EST, as determined by inspection of the lidar cloud heights {see Figures (5.1b), (5.5a), (5.5b)}. The satellite image NOAA-11 {Figure (3.3)} shows these thicker clouds in a band and crossing the Tasmanian coast at approximately 1618EST. The times and positions of the *in situ* measurements of the 7 height sections of the clouds show that all the marine clouds 1-7 (5.3.3) were measured in the thick band of clouds seen in the satellite image.

Table 5.24. Optical properties of stratocumulus clouds over Cape Grim (LIRAD) and over the sea to the west of Cape Grim (FSSP and 2D-C).

Depth (m)	Property:	Average	Variability (std. dev.)
93 ± 33	(LIRAD)		
	σ_v	0.0021 m ⁻¹	0.001 m ⁻¹
	τ_v	0.22	0.2
	σ_i	9.4 × 10 ⁻⁴ m ⁻¹	5 × 10 ⁻⁴ m ⁻¹
	τ_i	0.094	0.07
	(FSSP and 2D-C)		
0 - 100	σ_v	0.017 m ⁻¹	0.006 m ⁻¹
100	τ_v	1.72	0.4
0 - 100	σ_i	0.0068 m ⁻¹	0.003 m ⁻¹
100	τ_i	0.68	0.2

The optical depths of the thicker clouds observed over Cape Grim after 1610EST, (those also measured by the airborne instruments), could not be determined by the LIRAD method. However, although there were no *in situ* results for the optically thinner clouds, an attempt was made to determine the optical depths of the clouds of all depths by combining all the MWR measurements with the *in situ* measurements of the thicker clouds. The variations in the cloud droplet size distributions were not expected to have a large effect on the optical properties of the different droplet distributions.

5.3.5.5 Visible Optical Depths from Liquid Water Paths (16 July 1993)

The calculation of visible (532 nm) optical depths (τ_v) in terms of the values of W derived from the MWR measurements is described in the following. Cloud visible optical depths are sometimes calculated in terms of W as described by equation (A2.61). This equation assumes that the Mie extinction efficiency $Q_{ex} = 2$. The *in situ* results for a_{eff} , W and τ_v obtained over 50 m intervals into the non-precipitating clouds 1-3 and 5-7 (5.3.3) were used to determine an effective Q_{ex} . A least squares method was used to obtain the Q_{eff} that gave the best fit between the values of τ_v retrieved from the *in situ* measurements and those calculated by,

$$\tau_v = \frac{3WQ_{eff}}{4\rho a_{eff}} \quad (5.10)$$

Given the variabilities in a_{eff} , W and τ_v of $\pm 10\%$, $\pm 25\%$ and $\pm 20\%$ respectively, (from the results of section 5.3), a range of Q_{eff} was obtained using 3 combinations of these relative errors: (1) all negative errors, (2) no errors, (3) all positive errors. The ranges of values for the 3 error conditions are shown in Table 5.25, as well as the 3 retrieved Q_{eff} . The values used to form the ranges in the middle row of this table are shown in Figure (5.74).

Table 5.25. Ranges of the values used for the parameterisations, and retrieved Q_{eff} .

Error condition	a_{eff} (μm)	W (g m^{-2})	τ_v	Q_{eff}
(1)	9.00 - 13.3	2.96 - 70.2	0.55 - 8.76	2.21
(2)	10.0 - 14.8	3.95 - 93.7	0.68 - 11.0	2.30
(3)	11.0 - 16.2	4.94 - 117	0.77 - 12.4	2.43

Parameterisation of Visible Optical Depth

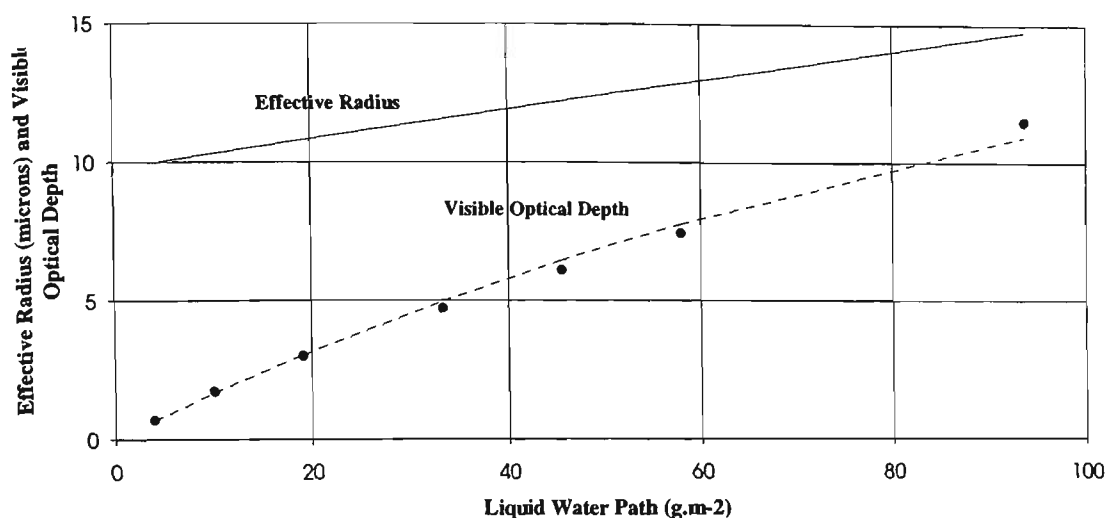


Figure 5.74. Average effective radii determined from the *in situ* measurements and modelled by a straight line of best fit (solid line, top), visible optical depths determined from the *in situ* measurements (filled circles) and a modelled τ_v (dashed line).

Note that the results for $\tau_v(W)$ shown in Figure (5.74) compare well with the results of Boers *et al.* (1998) for $\tau_v(W)$, for the stratocumulus clouds observed during all of SOCEX1, (with a_{eff} approximately 11 - 14 μm ; see Figure 5 of that paper).

5.3.5.6 Visible Optical Depths by Microwave Radiometer (16 July 1993)

Values of τ_v were obtained from the MWR-retrieved W using equation (5.10), with a value for a_{eff} of 13 μm , and using the values of Q_{eff} determined in the previous section. The resulting distributions in the MWR-retrieved τ_v are shown in Figure (5.75), for the LIRAD measurement period 1434EST to 1702EST (filled bars), and for the period 1430EST to 2350EST (open bars). Approximately 18% of these results for τ_v were less than 2. According to the lidar measurements, the cloud-free periods amounted to approximately 13.5 minutes. Taking this into account approximately 16% of the MWR results had $\tau_v < 2$. This is significantly less than that found from the LIRAD results ($\approx 50\%$). The higher quality LIRAD results for the optically thinner clouds are presumed to be more accurate. As previously mentioned, there is a possibility that erroneously large values of W obtained from the MWR measurements after the rainfall earlier in the day could have caused the spuriously large $\tau_v(\text{MWR})$. Although, it should be pointed out that the values of a_{eff} for the thinner clouds were larger than those obtained for the thicker clouds that arrived over Cape Grim at approximately 1610EST.

Distribution of Visible Optical Depths (Microwave Radiometer)

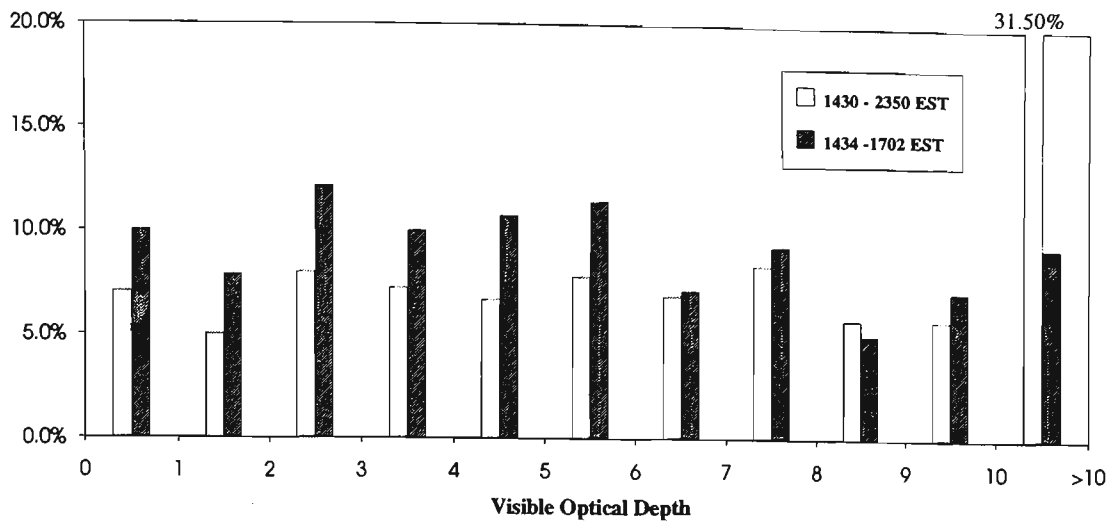


Figure 5.75. Distribution of τ_v obtained from the MWR retrievals of W , for the same period for which the LIRAD results were obtained, 1434 - 1702 EST (filled bars), and also for the period 1430 - 2350 EST (open bars).

This was checked as follows. To match the LIRAD results, with $Q_{eff} = 2$, the value of a_{eff} was adjusted until the average $\tau_v(MWR)$ was equal to the average τ_v of the thin clouds measured by LIRAD from 1434EST to 1613EST. The results for a_{eff} are shown in Table 5.26.

Table 5.26. Effective radii (MWR) by a comparison with the LIRAD results (thin clouds).

τ_v	a_{eff} (μm)
0.42	95
0.22	182
0.02	2000

The values of a_{eff} shown in Table 5.26 are too large, indicating that inaccuracies in the MWR retrievals of W probably were the cause of the inaccuracies of the retrievals of τ_v . Clearly, the MWR retrievals of W need to be improved for future MWR studies of the optical properties of these clouds. At the very least, the MWR results for τ provide a perspective on the optical depths of the thick clouds that could not be obtained by LIRAD alone.

5.3.5.7 Infrared Optical Depths from Liquid Water Paths (10 July 1993)

For completeness, the calculations for $\tau_i(W)$ were investigated briefly; *i.e.*, those given by equations (A2.65) and (A2.68) (see section A2.7.7). Here, these parameterisations are described as the Small Droplet Approximation (SDA) and the Large Droplet Approximation (LDA) respectively.

The values of τ_i used to test these parameterisations were determined from the same FSSP and 2D-C *in situ* measurements of the droplet size distributions used in section 5.3.5.3; *i.e.*, the non-precipitating marine stratocumulus clouds 1-3 and 5-7. The value of a_2 in the LDA is an effective Mie efficiency for absorption (Q_{eff}). Using the same relative errors of a_{eff} , W and τ_i used in section 5.3.5.3, and by using a method of least squares, the value of Q_{eff} for these data was 1.04 ± 0.2 (The LDA shown in Figure (5.76) uses this Q_{eff}). This range of Q_{eff} corresponds to an $a_{eff} > 10 \mu\text{m}$ {see Figure (A2.10) for example}. The values of τ_i calculated from the SDA and the LDA are shown in Figure (5.76). In this figure, the effective radii (solid line, top) are the same as those shown in Figure (5.73). The results shown in Figure (5.76) indicate that the LDA models the increasing τ_i more accurately than the SDA in this case. This is because a significant number of the droplets had radii larger than approximately $10 \mu\text{m}$.

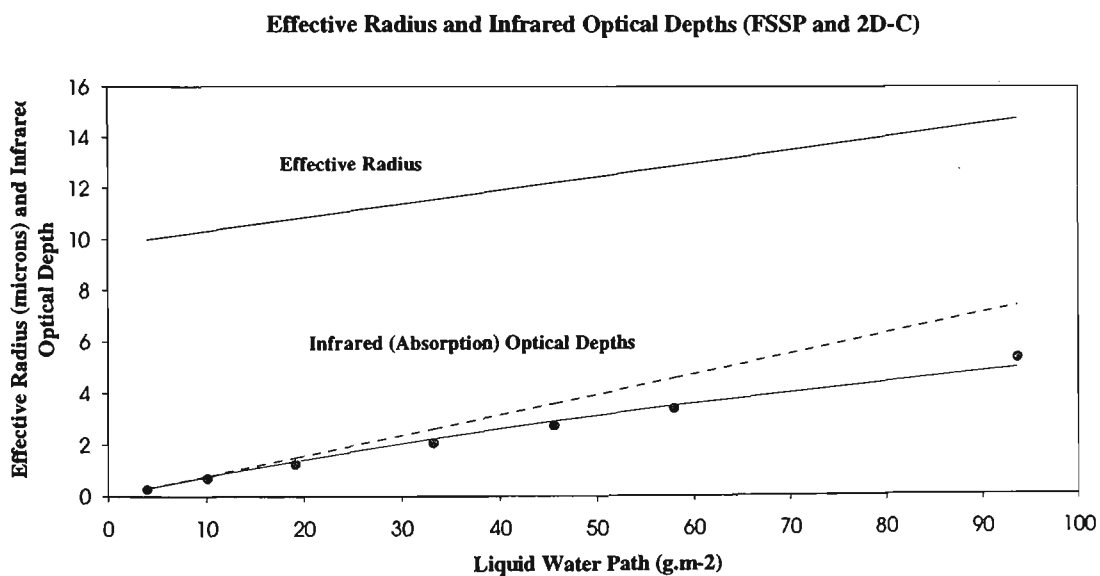


Figure 5.76. Effective radii (solid line, top) and infrared optical depths (τ_i) determined from the *in situ* measurements of 16 July 1993. For these data, the Small Droplet Approximation (SDA, dashed line) is not as accurate as the Large Droplet Approximation (LDA, solid line, bottom).

As an aside, to further investigate the utility of the MWR to retrieve values of τ , the values of $\tau_i(W)$ were determined for another period of lidar measurements not previously investigated in detail. At Cape Grim on 10 July 1993 (SOCEX1) marine stratocumulus clouds were observed by lidar {Figure (5.77) below; see also Figure (5.1a)}, as well as by MWR (there were no infrared radiometer measurements made on this day). Using the parameterisations $\tau_i(W)$ just described, values of τ_i were calculated from W . The lidar results in Figure (5.77) clearly show precipitation at approximately 1320EST, and also between about 1530EST and 1650EST. The effect of these large droplets on the MWR retrievals for W is evident by the spuriously large peaks in $\tau_i(W)$ shown in Figure (5.78). (Similarly, the errors in the parameterised visible optical depths, $\tau_v(W)$, would be large and positive). Clearly, these results (10 July 1993) provide a valuable insight into the effects of large droplets on MWR retrievals of τ , and should be investigated further in future.

- Note: Figures 5.77 and 5.78 are shown together on the next page for easier comparison of the lidar and microwave radiometer results.

Cloud Heights by Lidar

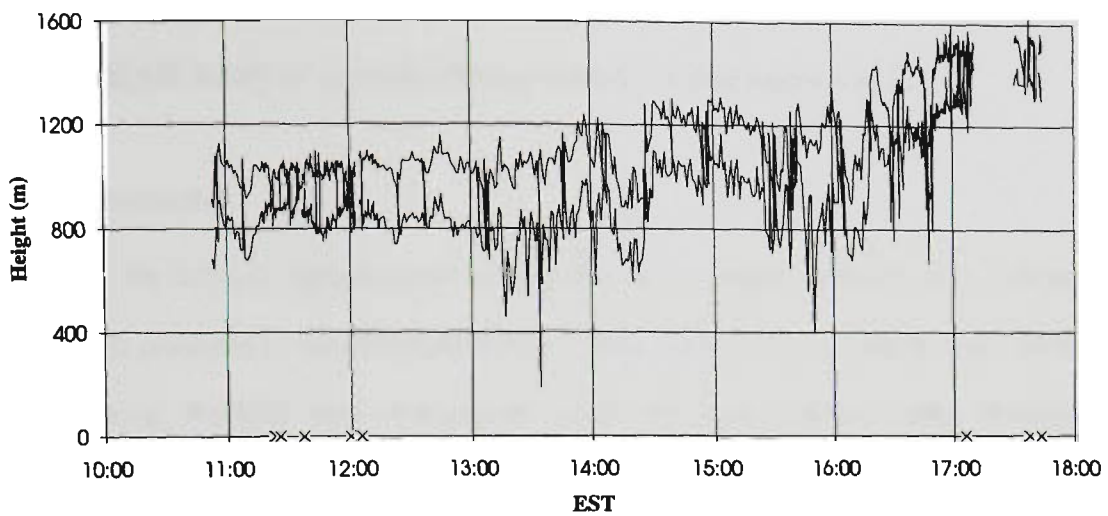


Figure 5.77. Cloud heights measured by the maxilidar at Cape Grim on 10 July 1993 (SOCEX1). The crosses at 0 m (ASL) indicate a lidar shot but no detected cloud signal. The clouds begin to precipitate at approximately 1320 EST.

Infrared Optical Depths by Microwave Radiometer (Overestimated)

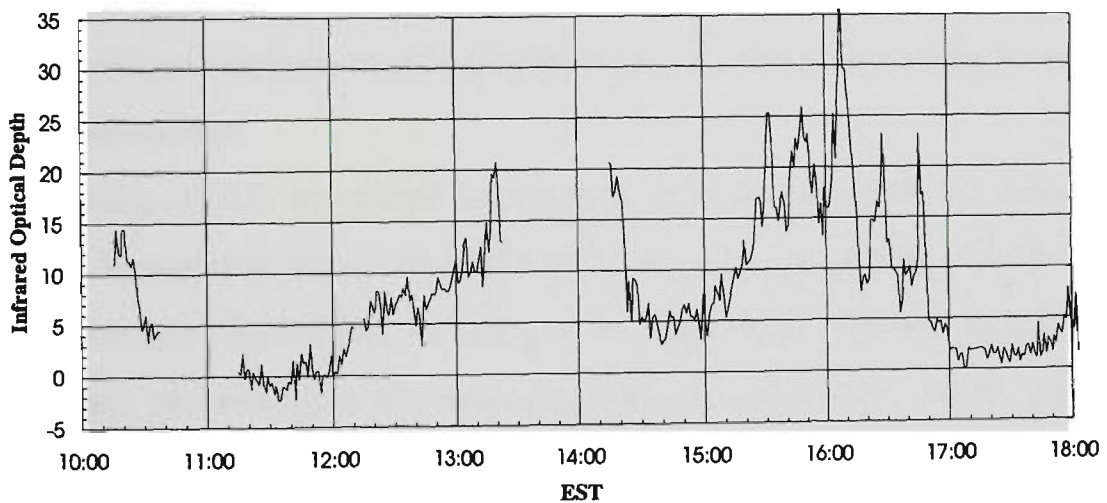


Figure 5.78. Values $\tau_i(W)$ calculated from the values of W retrieved from the microwave radiometer measurements of 10 July 1993. Some of the data are missing. Variations in Q_{eff} had only a small effect on these results. Note the sharp and spurious increases in optical depth that occur where precipitation was present.

5.4 Properties of Clouds Observed on 8 February 1995 (SOCEX2)

5.4.1 LIRAD Study of Stratocumulus Clouds (8 February 1995)

5.4.1.1 Introduction

A study of the LIRAD measurements of boundary layer clouds observed on 8 February 1995 (SOCEX2) is presented in the following sections. This study was kept brief because the lidar data obtained during SOCEX2 were of a poorer quality than those obtained during SOCEX1. The SOCEX2 lidar data could not be calibrated using measurements of cloud-free air as was done for the SOCEX1 data (see 4.4). However in the study of droplet size distributions measured *in situ* on 16 July 1993 it was found that the extinction-to-backscatter ratio (S) of these boundary layer clouds varied by only a small amount (section 5.3.3.9), regardless of the depth into the clouds. Thus the minilidar was calibrated by assuming that ηS (and therefore the maximum χ') for the SOCEX2 stratocumulus clouds was the same as that obtained for SOCEX1 (5.3.4.3). Further higher quality lidar measurements of optically thick boundary layer clouds are required to determine the validity of this calibration method.

During SOCEX2 the minilidar was optimised for the returned signals from stratocumulus clouds and because of this the cumulus cloud signals were saturated in amplitude. Thus the cumulus cloud signals were discarded from the analysis of the LIRAD data, achieved by inspection of the cloud heights. This left a total of 3523 measurements of stratocumulus clouds for analysis. Note that, as well the LIRAD studies of stratocumulus clouds presented in this thesis, a LIRAD study of cumulus clouds is long overdue and could provide valuable insights into the optical properties of boundary layer clouds: *e.g.*, see Platt and Gambling, (1971a).

To provide an initial view of the LIRAD measurements of the stratocumulus clouds made on 8 February 1995, the heights of cloud base and the apparent cloud tops obtained from the minilidar signals are illustrated in Figures (5.79) to (5.83). Some of the simultaneously measured cloud infrared radiances are also shown in these figures.

Stratocumulus Cloud Heights and Infrared Radiances (1 of 5)

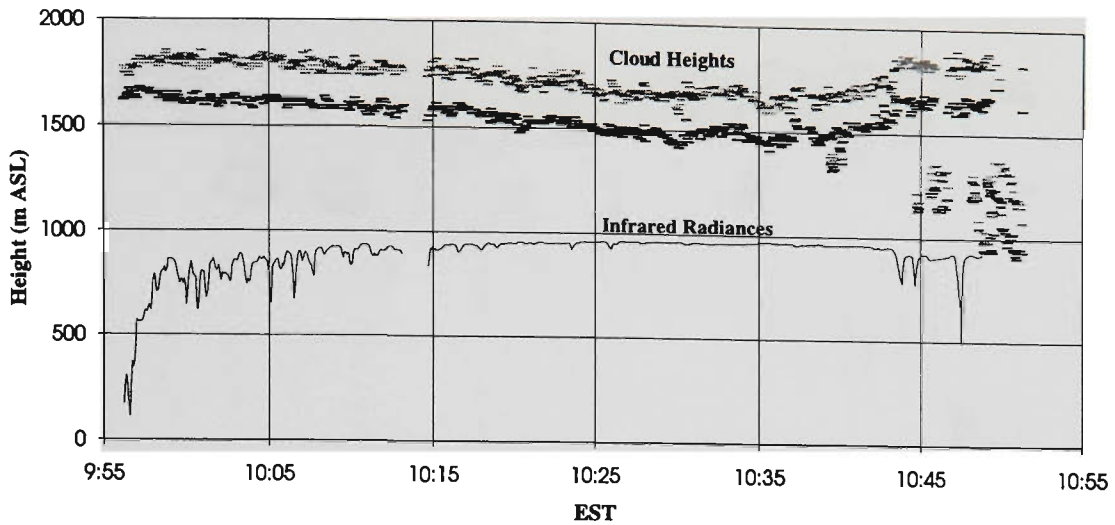


Figure 5.79. Stratocumulus cloud heights (m ASL) obtained from lidar measurements (upper dashes). After 1045 EST cumulus clouds lie in the region 1000 - 1500 m ASL. The simultaneously measured infrared radiances of the stratocumulus clouds are shown by the solid lines (arbitrary units). The radiances reached a maximum where the cloud base of the stratocumulus clouds dropped to ≈ 1500 m. Obviously the clouds are black to infrared radiation at that point.

Stratocumulus Cloud Heights and Infrared Radiances (2 of 5)

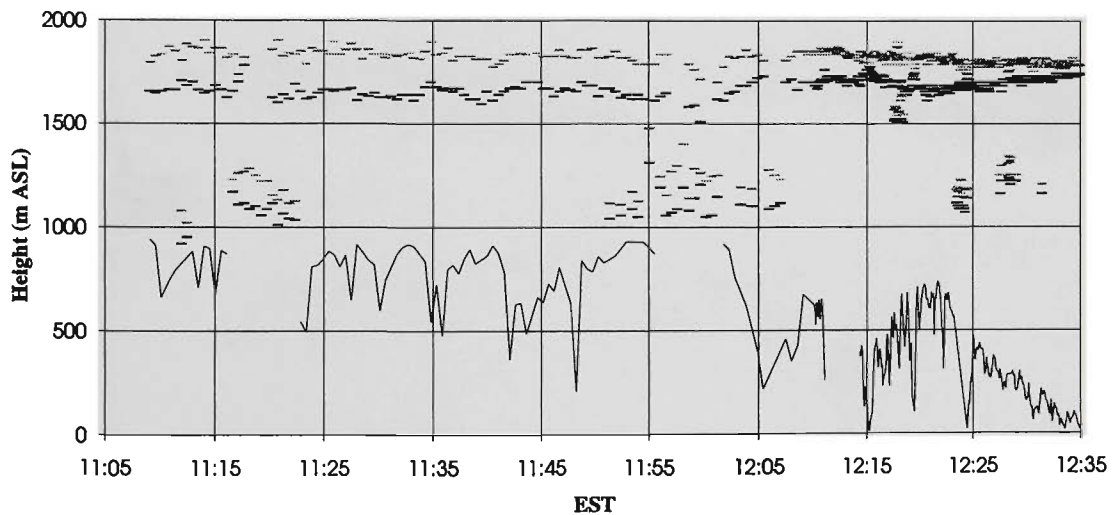


Figure 5.80. Cloud heights of cumulus and stratocumulus clouds (m ASL) indicated by the upper dashes, and simultaneously measured infrared radiances shown by the solid lines below (arbitrary units). The radiances are to the same scale as in the previous plot. Only the radiances of the stratocumulus clouds used for the LIRAD analysis are shown.

Stratocumulus Cloud Heights and Infrared Radiances (3 of 5)

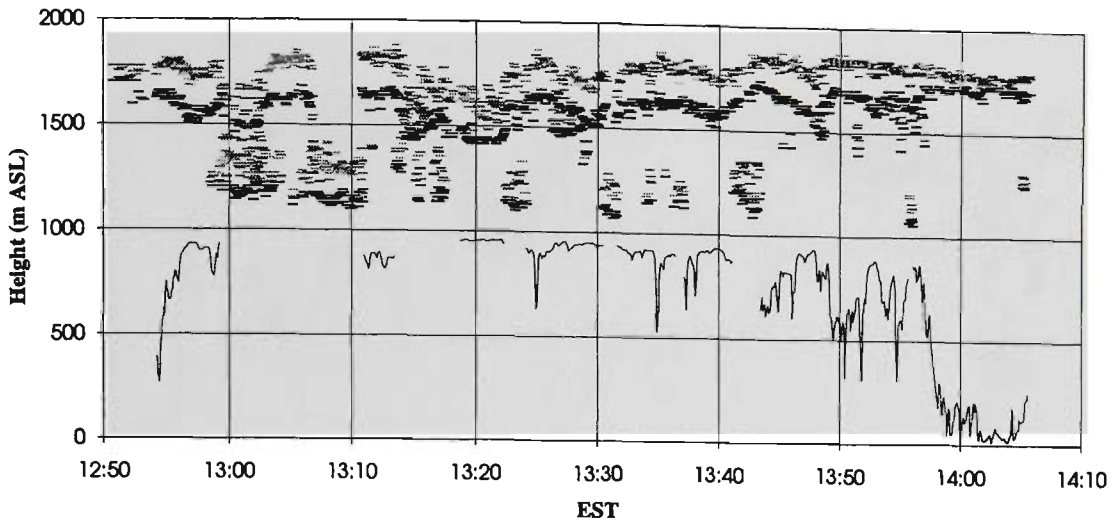


Figure 5.81. Cloud heights of cumulus and stratocumulus clouds (m ASL) indicated by the upper dashes, and simultaneously measured infrared radiances shown by the solid lines (arbitrary units). The radiances of the lower cumulus clouds have been excluded from this plot.

Stratocumulus Cloud Heights and Infrared Radiances (4 of 5)

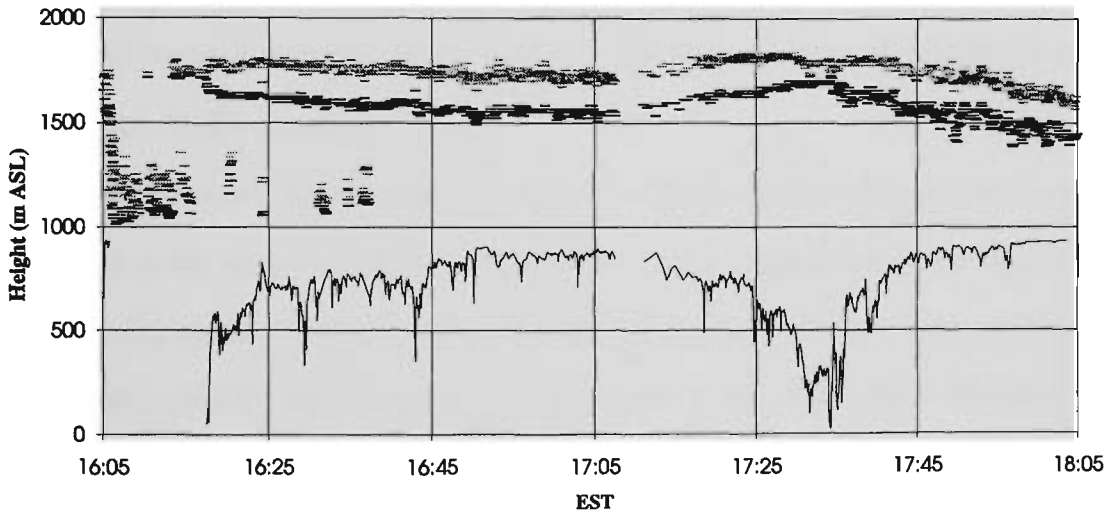


Figure 5.82. Cloud heights of cumulus and stratocumulus clouds (m ASL) indicated by the upper dashes, and simultaneously measured infrared radiances of the stratocumulus clouds shown by the solid lines (arbitrary units).

Stratocumulus Cloud Heights and Infrared Radiances (5 of 5)

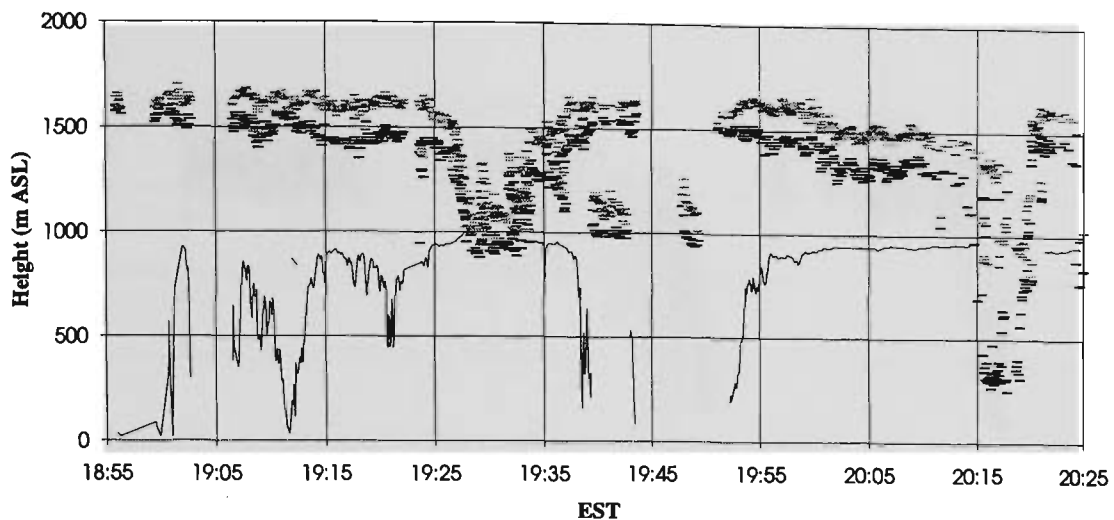


Figure 5.83. Cloud heights of cumulus and stratocumulus clouds (m ASL) indicated by the upper dashes, and simultaneously measured infrared radiances of the stratocumulus clouds shown by the solid lines (arbitrary units).

Time series plots for the values of χ' determined from the minilidar measurements of the stratocumulus clouds, (which used the estimate of η_S found for SOCEX1), are shown in Figures (5.84) and (5.85). In Figure (5.85) the period 1720 EST to 1745 EST is interesting because of the drop in cloud depth that occurred over this period; the measurements of the cloud radiances and χ' are shown in more detail in Figure (5.86).

Apart from the assumption that the value of η_S for these clouds measured during SOCEX2 was the same as that found for SOCEX1, the optical properties of the stratocumulus clouds presented in the following sections (SOCEX2) were determined in a similar manner to those obtained for the SOCEX1 dataset (5.3.4). The calculated visible optical depths modified by the multiple scatter factor ($\eta\tau_v$) are given in section 5.4.2, and the values of the ratios of visible extinction to infrared absorption, modified by the multiple scatter factor ($\eta\alpha$), are given in section 5.4.3. An estimate of η is used to determine a distribution in the visible optical depths (τ_v). The infrared optical depths (τ_i) determined by the LIRAD method are given in 5.4.4. The infrared emittances (ϵ_i) are presented in section 5.4.5.

Lidar Measurements of Stratocumulus Clouds (1 of 2)

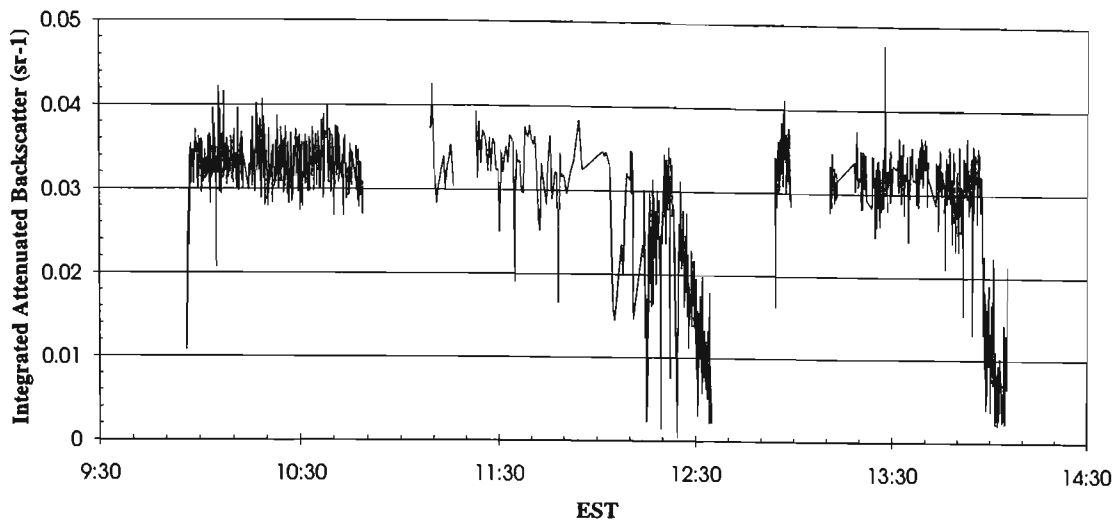


Figure 5.84. Integrated attenuated backscatter (χ') of the stratocumulus clouds observed on 8 February 1995 versus time. These values were obtained using the maximum values of χ' obtained from the SOCEX1 data.

Lidar Measurements of Stratocumulus Clouds (2 of 2)

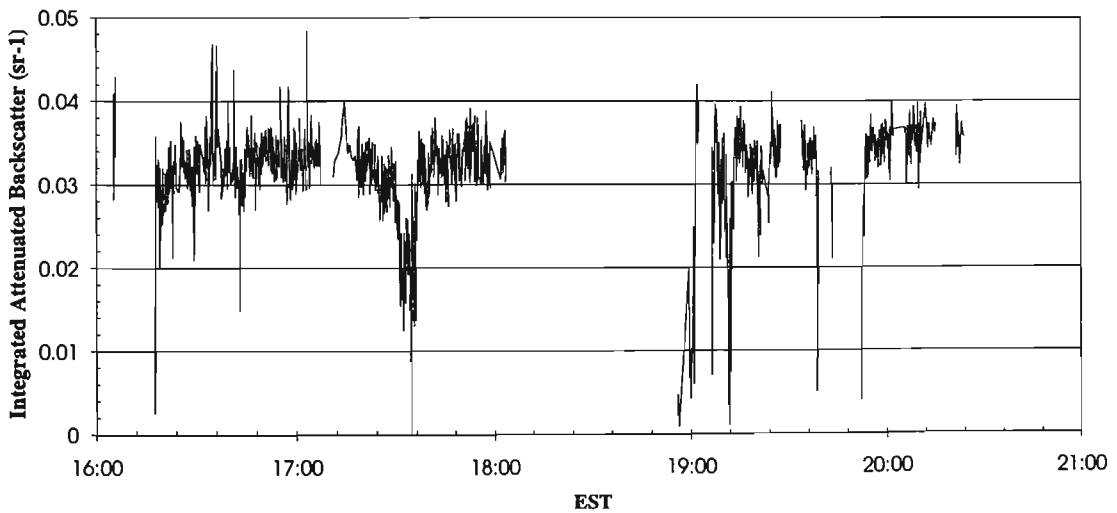


Figure 5.85. Integrated attenuated backscatter (χ') of stratocumulus clouds observed on 8 February 1995. These values were obtained using the maximum values of χ' obtained from the SOCEX1 data. See Figure (5.86) for another view of the values of χ' during the period 1730 - 1735 EST.

LIRAD Measurements of Stratocumulus Clouds

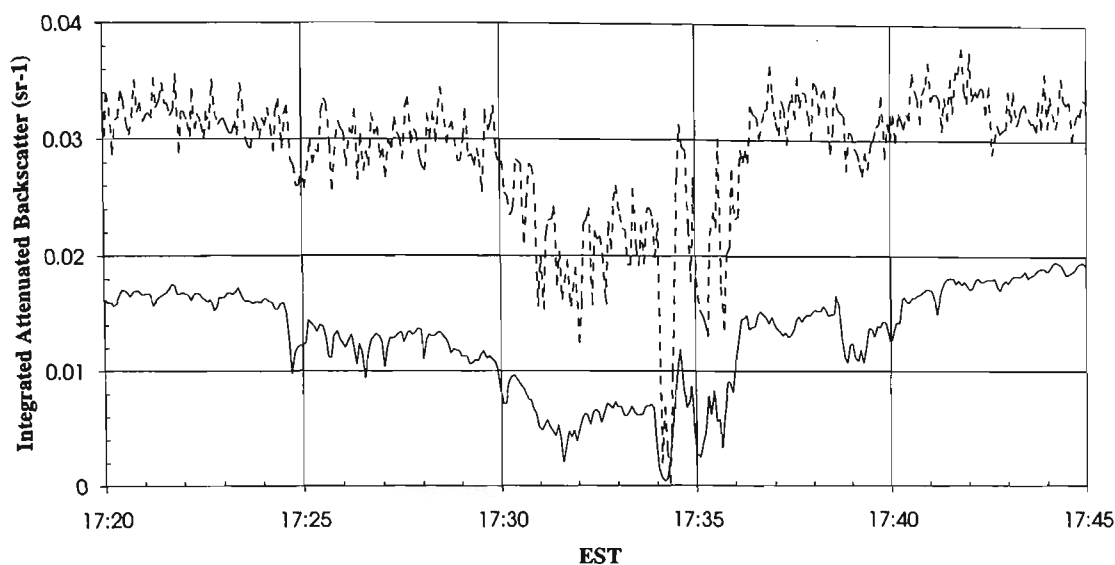


Figure 5.86. A larger-scale plot of some of the data shown in Figures (5.85) and (5.82): $\chi' \text{ sr}^{-1}$ (upper line), and simultaneously measured cloud radiances (lower line, arbitrary units).

5.4.1.2 Infrared Properties of the Clouds by LIRAD

Estimates of the errors for infrared emittances (ϵ_i) and infrared absorption optical depths (τ_i) are presented in the section (i), followed by the LIRAD results for ϵ_i and τ_i in section (ii).

(i) Errors

The equation (2.42) was used to determine the error in the cloud radiances ΔL_c , and equation (2.43) to determine the error in the cloud infrared absorption radiance (ΔL_i). Estimates of the errors used to determine these quantities are shown in Table 5.27. These errors in the radiances were estimated by inspection of the variabilities in the measured infrared radiances as well as the various parameterisations presented in sections 4.3.4.4. to 4.3.4.7.

Table 5.27. Estimates of maximum errors in infrared radiances and transmittances.

<i>Error</i>	<i>Magnitude</i>
ΔL_g	$0.04 \text{ W m}^{-2} \text{ sr}^{-1}$
ΔL_{air}	$0.04 \text{ W m}^{-2} \text{ sr}^{-1}$
ΔT_{air}	0.002
ΔL_s	$\approx 0.05 \times L_i$

The relative errors $\Delta\varepsilon_i/\varepsilon_i$ were found by equating them with $\Delta L_i/L_i$ as for the SOCEX1 results (e.g. Platt *et al.*, 1998), and the errors $\Delta\tau_i$ were determined by equation (5.1). The relative errors $\Delta\varepsilon_i/\varepsilon_i$ and $\Delta\tau_i/\tau_i$ were then determined for all the LIRAD results for ε_i and τ_i {see Figures (5.87) and (5.88)}.

(ii) Results

Plots of $\varepsilon_i \pm \Delta\varepsilon_i$ and $\tau_i \pm \Delta\tau_i$ versus the measured cloud infrared absorption radiances (L_i) are shown in Figures (5.89) and (5.90) respectively. Given the errors just determined, between 46% to 54% of the clouds were optically thin with $\varepsilon_i < 0.5$. Frequency distributions of the emittances and infrared absorption optical depths are shown in Figures (5.91) and (5.92) respectively.

There were a total of 2486 LIRAD measurements, so to avoid clutter in Figure (5.83), the results for the thickest clouds (where the uncertainties were large) were excluded from this plot. These discarded points were those with $\chi' > 0.03355 \text{ sr}^{-1}$, or $\tau_i > 1.2$. There remain 1200 points in the plot.

The results shown in Figures (5.89) and (5.90) provide a good indication of the high occurrence of optically thin boundary layer clouds observed on 8 February 1995. According to the LIRAD results approximately 20% of the clouds observed on this day had $\tau_i < 0.8$. Given the estimate of α for SOCEX2 determined in the previous section, this means that approximately 20% of the visible optical depths of these clouds were less than approximately 3.

Relative Errors in Infrared Emittance (SOCEX2)

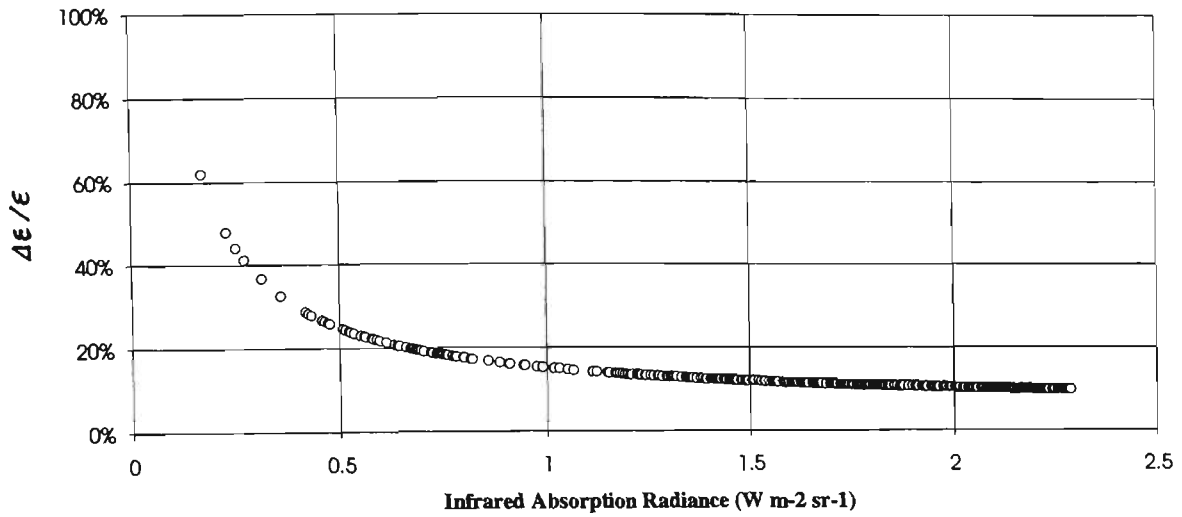


Figure 5.87. Relative errors $\Delta\epsilon_i/\epsilon_i$ versus radiance (L_i) for a sample of the LIRAD measurements obtained on 8 February 1995 (SOCEX2).

Relative Errors in Infrared Absorption Optical Depths (SOCEX2)

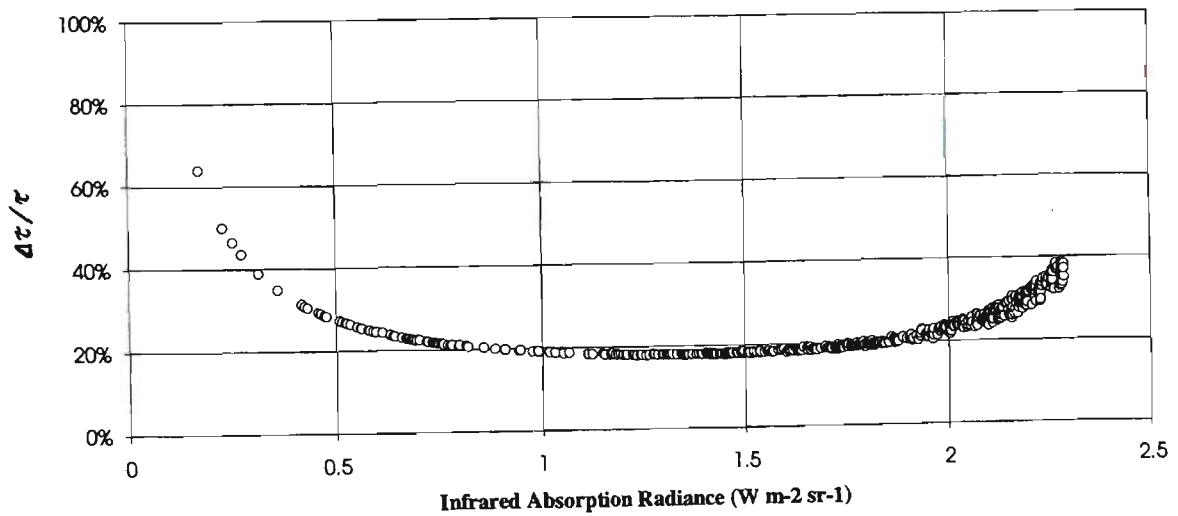


Figure 5.88. Relative errors $\Delta\tau_i/\tau_i$ versus radiance (L_i) for the same sample of LIRAD measurements shown in the previous figure.

Infrared Emittances (SOCEX2)

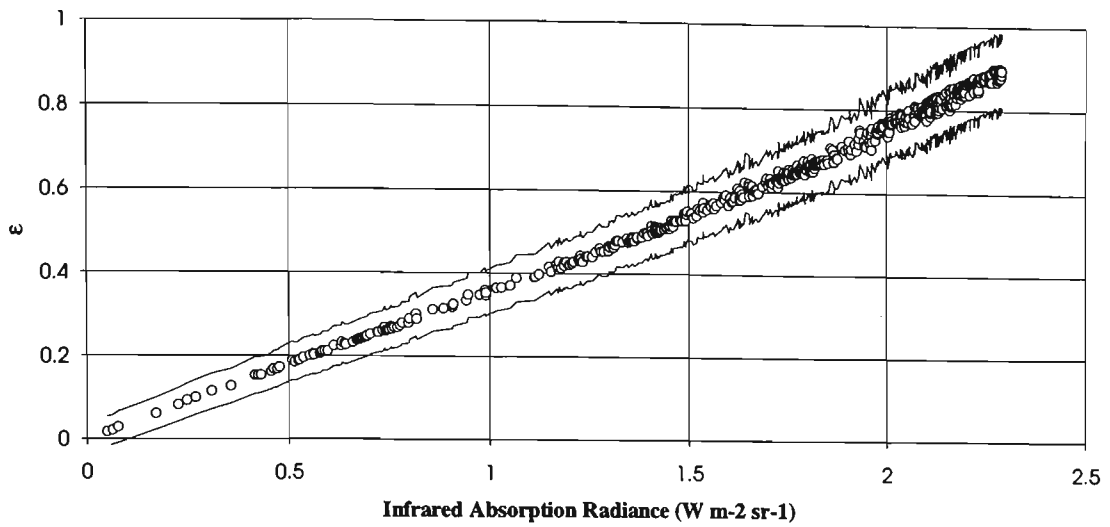


Figure 5.89. Emittances and calculated uncertainties versus radiance (L_i) for a sample of the LIRAD measurements obtained on 8 February 1995 (SOCEX2).

Infrared Absorption Optical Depths (SOCEX2)

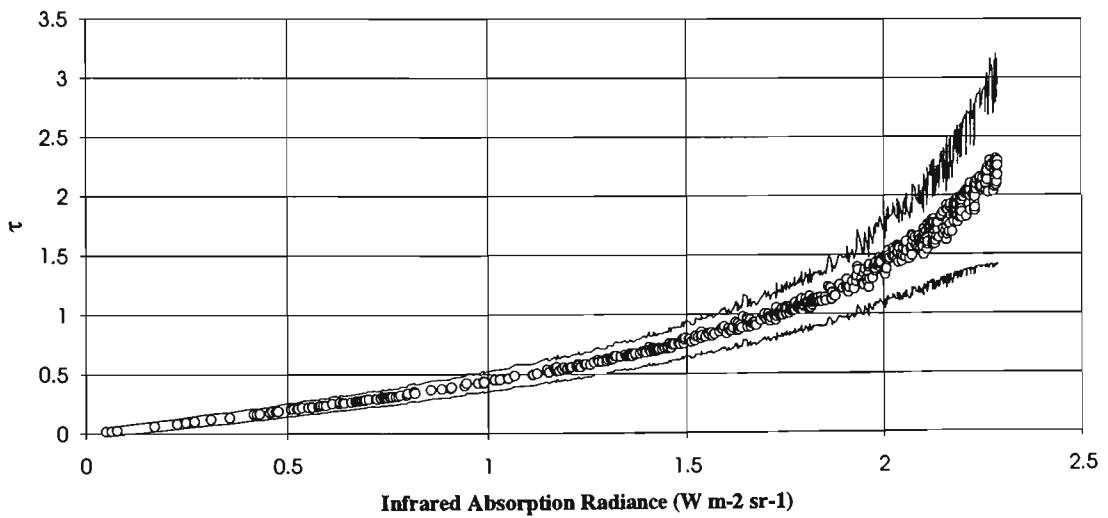


Figure 5.90. Infrared absorption optical depths (τ_i) and calculated uncertainties versus radiance (L_i) for a sample of the LIRAD measurements obtained on 8 February 1995 (SOCEX2).

Distribution of Infrared Emittances (SOCEX2)

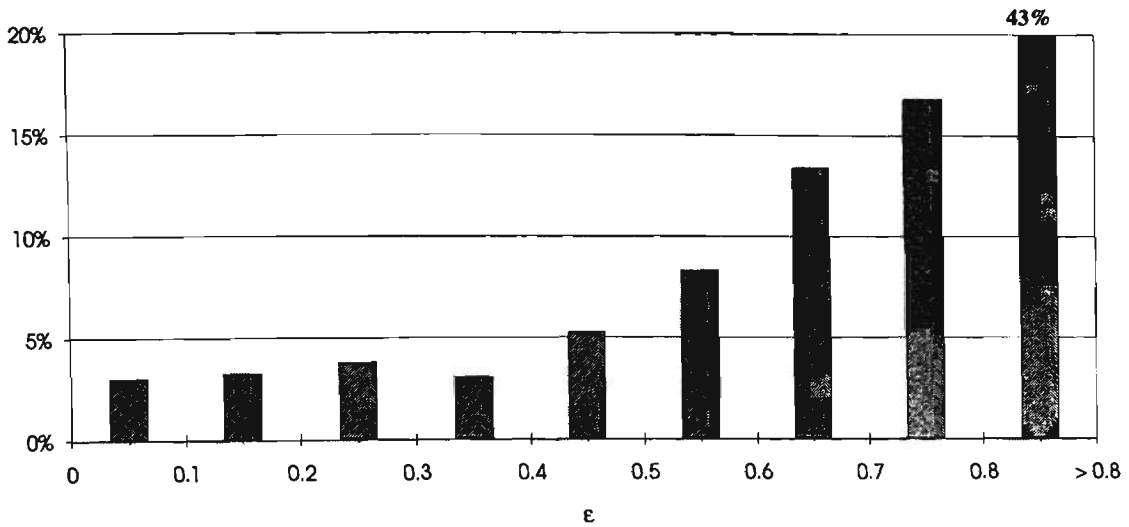


Figure 5.91. Distribution of the infrared emittances (ϵ_i) determined by the LIRAD method for the measurements obtained on 8 February 1995 (SOCEX2). There were 2023 values of $\epsilon_i < 0.8$ (57% of the total).

Distribution of Infrared Absorption Optical Depths (SOCEX2)

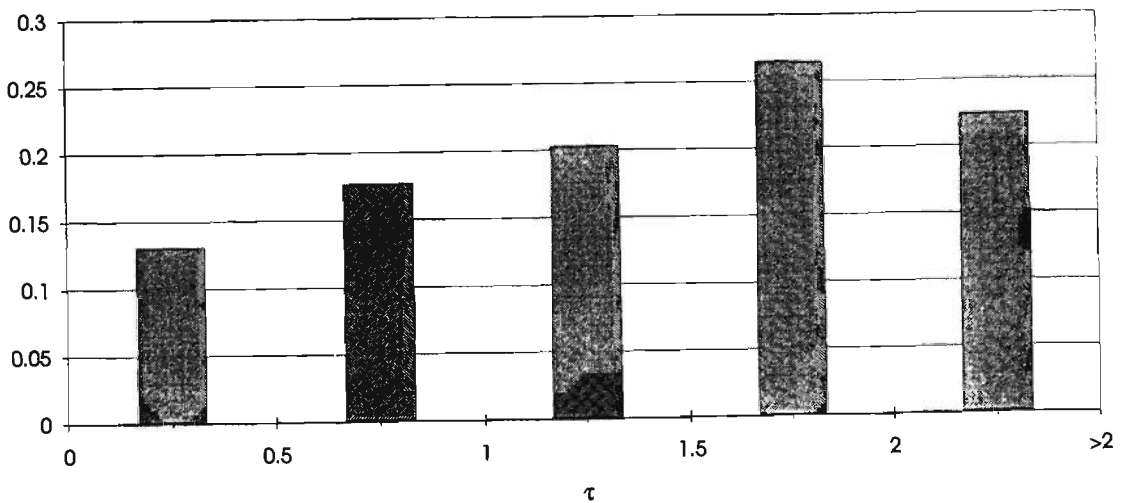


Figure 5.92. Distribution of the infrared optical depths determined by the LIRAD method for the measurements obtained on 8 February 1995 (SOCEX2). There were 1093 values of $\tau_i < 1.0$ (31% of the total).

5.4.1.3 Estimate of the Multiple Scatter Factor

In the application of the LIRAD method to the SOCEX2 data, if a match between the measured and calculated radiances could not be achieved to a reasonable precision by adjustments to $\eta\alpha$ only, then those data were discarded from the analysis of the main group of LIRAD data. That is, in this application of the LIRAD method there were no adjustments made to the original ηS used to calibrate the lidar. (See section 2.3.5 for a description of the iteration processes in the LIRAD algorithm). These discarded data were all of measurements of thick clouds with $\chi' > 0.0340 \text{ sr}^{-1}$, so the uncertainties in retrieving their optical properties were large. There were 1037 measurements of these thicker clouds, and the remaining 2486 LIRAD measurements were used for analysis.

The uncertainties in the calculated $\eta\tau_v$ for the SOCEX2 data were less than 25% over the range of χ' , 0.016 - 0.025 sr^{-1} . Over this range of χ' the average $\eta\alpha$ and the variability determined by the LIRAD method was,

$$\eta\alpha = 1.5 \pm 0.6. \quad (5.11)$$

Outlying points with $\eta\alpha > 4$ were discarded from this result. This value of $\eta\alpha$ and the variabilities are shown in Figure (5.93). In the figure, for $\chi' > 0.025 \text{ sr}^{-1}$, the clustering of the values of $\eta\alpha$ near $\chi' = 0.03 \text{ sr}^{-1}$ is an artifact of the LIRAD computer algorithm. The spurious clustering observed here is related to the initial estimates used for $\eta\alpha$ in the LIRAD analysis process, and occurs in a region where the uncertainties in determining absorption profiles from the lidar data were very large.

For comparison, the value of $\eta\alpha$ for the SOCEX1 data was determined in the same way as the result (5.11), (*i.e.* uncertainties in $\eta\tau_v$ less than 25%):

$$\eta\alpha = 1.5 \pm 0.3 \text{ (SOCEX1)}. \quad (5.12)$$

Given that the value of α at the wavelength 1064 nm is (at most) about 5% more than α for 532 nm, and about 20% more than α (SOCEX1) due to the different microphysics of the summer clouds observed on 8 February 1995 (see section 4.4.3), then α (1064 nm) for the SOCEX2 results was approximately

$$\alpha = 3.0 \pm 0.3 \text{ (SOCEX2)}. \quad (5.13)$$

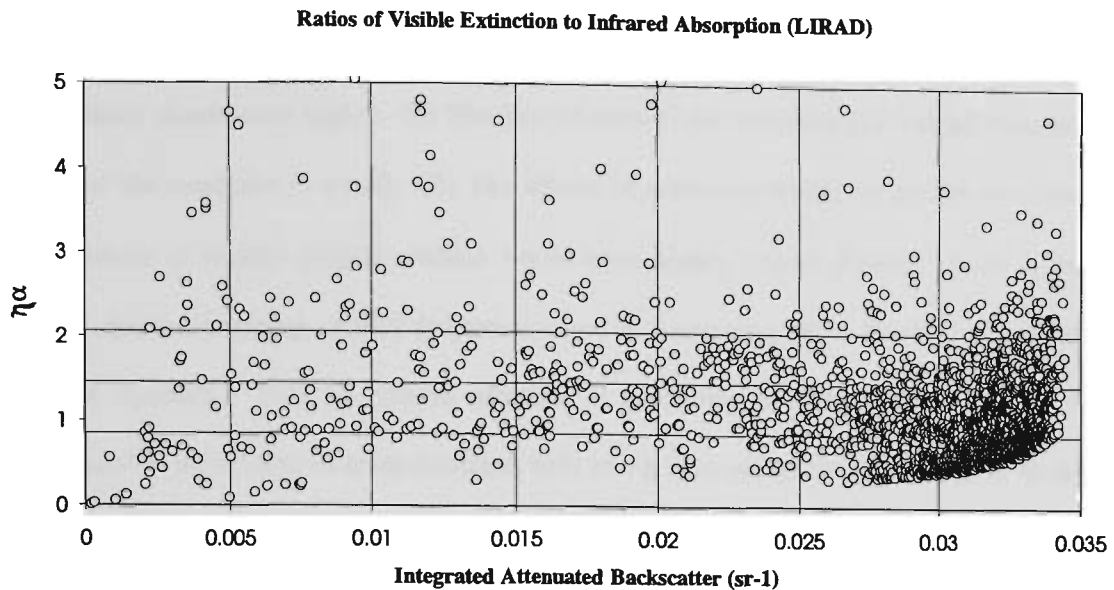


Figure 5.93. The values of $\eta\alpha$ determined by the LIRAD method. The average $\eta\alpha$ and the variabilities are also shown, which were calculated over the range $0.016 < \chi' < 0.025 \text{ sr}^{-1}$. Outlying points with $\eta\alpha > 4$ were discarded from these calculations. The clustering of points near $\chi' = 0.03 \text{ sr}^{-1}$ is erroneous - an artifact of the LIRAD algorithm (see text).

(Using the same relative uncertainty for α found for SOCEX1). Therefore, using the results (5.11) and (5.13) and assuming random errors, the value of the multiple scatter factor for the thinner stratocumulus clouds observed during SOCEX2 was,

$$\eta = 0.5 \pm 0.3 \text{ (SOCEX2)}, \quad (5.14)$$

The multiple scatter factor for the SOCEX2 (summer) thin clouds is less than the value found for the thin clouds measured in the winter (SOCEX1):

$$\eta = 0.6 \pm 0.2 \text{ (SOCEX1)}. \quad (5.15)$$

The effect of overestimating the radiance due to scattering (L_s) is to increase the retrieved value of $\eta\alpha$. The SOCEX2 results for the emittances strongly suggest that L_s has been overestimated, therefore $\eta\alpha$ (SOCEX2) is likely to be too large, therefore the retrieval of η shown above (5.14) is also likely to be too large. However the value of η obtained from the SOCEX1 results is believed to be closer to the correct value, thus it seems very likely that the value of η obtained from the SOCEX1 data is indeed larger than that for SOCEX2, as shown by the results (5.14) and (5.15).

The smaller η for the summer clouds (5.15) meant that the effect of multiple scattering on the minilidar measurements was greater and there are a number of reasons why this should be the case: (1) The summer clouds were higher. (2) The field of view of the minilidar (11.5 mrad) was more than twice that of the maxilidar (5 mrad). (3) The effects of scattering would be greater for clouds with greater numbers of smaller droplets (which would have higher optical depths). Also, η would be smaller for clouds containing smaller droplets because the scattering phase function is peaked less in the forward direction. Thus the greater amounts of scattering in other directions other than the forward direction would lead to more scattered light being detected by the lidar. Higher quality lidar or LIRAD studies of water droplet clouds combined with theoretical studies of the multiple scattering in clouds are required to check the accuracy of these results for η , for both SOCEX1 and SOCEX2.

5.4.2 Visible Optical Depths by Microwave Radiometer (8 February 1995)

This section is a brief investigation into the visible optical depths derived from the MWR measurements of 8 February 1995 (Boers, 1996b; Boers and O'Brien, 1996). The liquid water paths retrieved from the MWR measurements of 8 February 1995 are shown in Figure (5.94). (At the time of this study, the available numerical resolution of these measurements was 10 g m^{-2}). The microphysical and optical properties of the clouds determined from the *in situ* measurements of SOCEX2 were studied in detail by Boers *et al.* (1998), and that study included a comparison between the results obtained for the winter and summer phases of SOCEX.

The visible optical depths $\tau_v(W)$ were calculated using equation 5.10 with estimates of the various parameters shown below in Table 5.28. The uncertainties in the parameters were treated as random errors. The results for $W < 100 \text{ g m}^{-2}$ are shown in Figure (5.95).

Table 5.28. Parameters used for calculation of $\tau_v(W)$.

Parameter	Estimate	
Q_{eff}	2.9 ± 0.3	Section 5.4.3.
a_{eff}	$9.5 \pm 1.5 \mu\text{m}$	Boers <i>et al.</i> (1998)
δW	10 g m^{-2}	Numerical res. of W

A distribution for $\tau_v(W)$ was determined using intervals of τ_v of 5, and formed for the LIRAD measurement periods only to enable a comparison with the LIRAD results (see later, 5.5). This meant that only the stratocumulus cloud periods were considered, with cloud-free periods also eliminated

from the distribution (Figure (5.96)). The optically thin clouds with $\tau_v(W) < 5$ comprised 28% of the data.

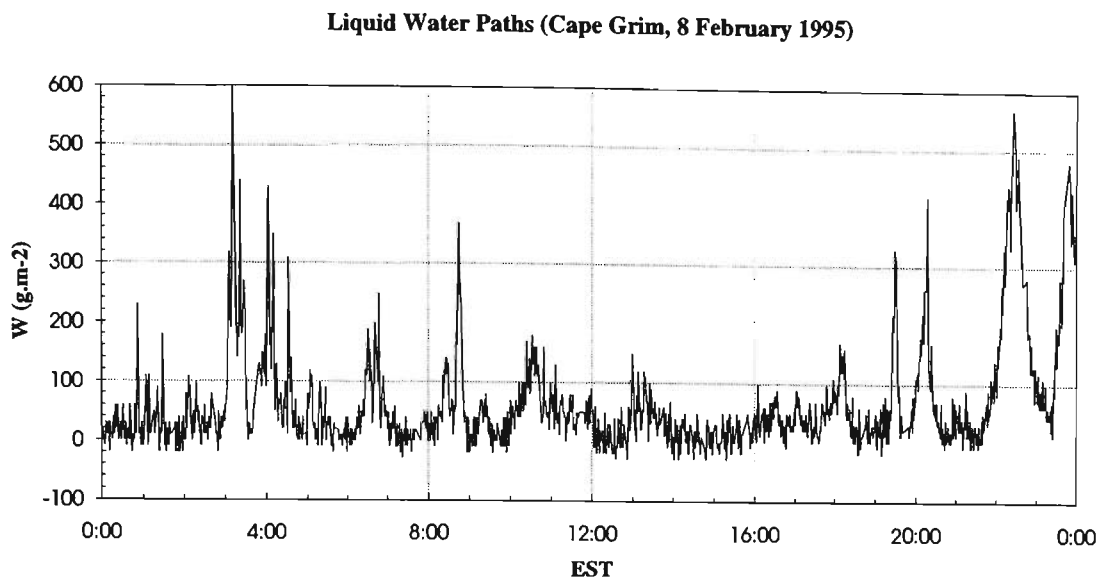


Figure 5.94. Values of the cloud liquid water paths (W , g m^{-2}) obtained from microwave radiometer measurements at Cape Grim on 8 February 1995.

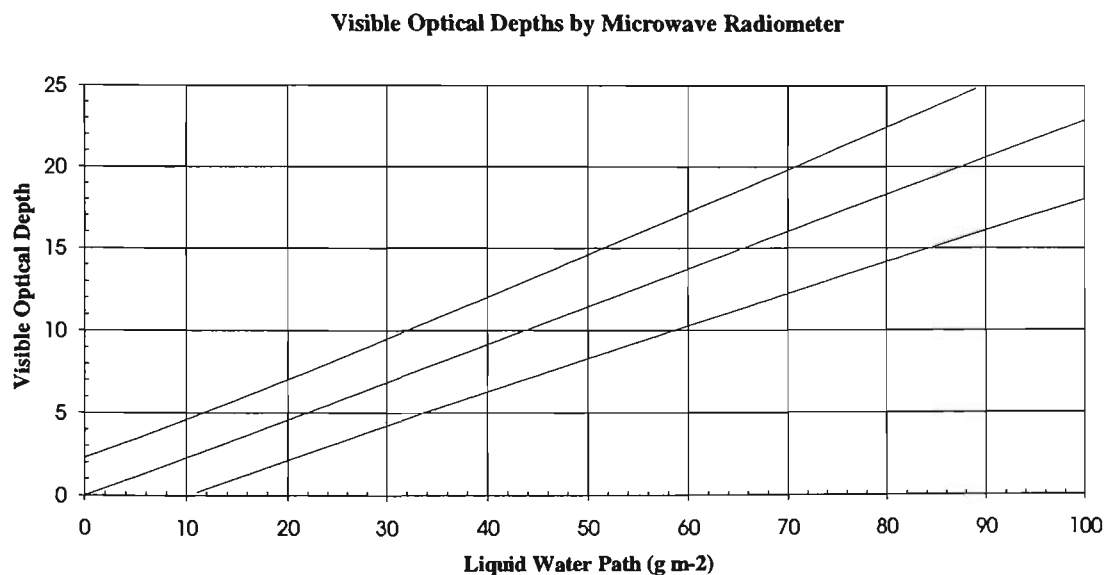


Figure 5.95. Values of the visible optical depth $\tau_v(W)$ calculated for the summer stratocumulus clouds, for liquid water paths $W < 100 \text{ g m}^{-2}$. The high uncertainties are mostly due to the uncertainties in the microwave radiometer retrievals of W (cf. Figure 5 of Boers *et al.*, 1998).

Distribution of Visible Optical Depths by Microwave Radiometer

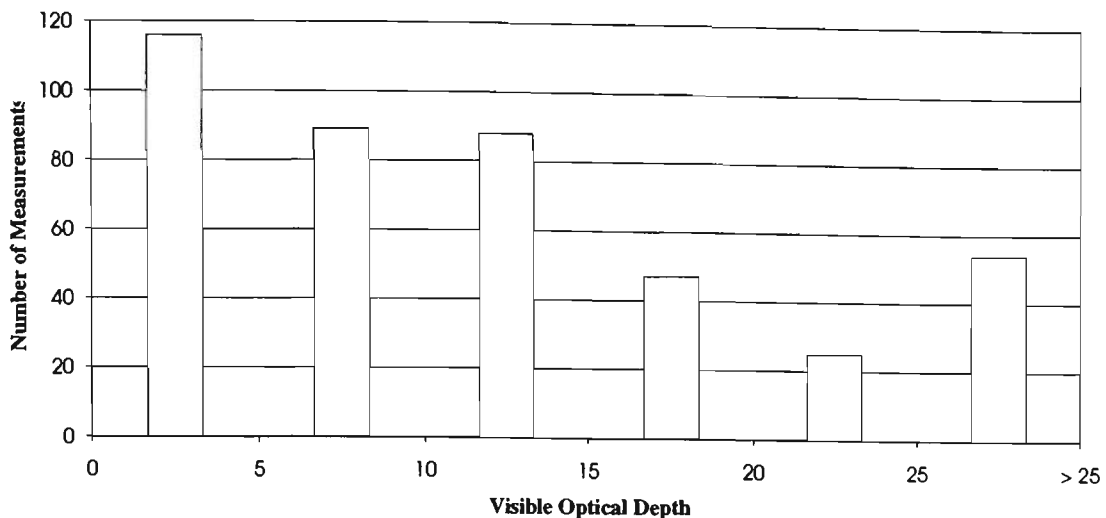


Figure 5.96. Distribution of visible optical depths determined from MWR measurements for the LIRAD measured clouds only, of 8 February 1995.

5.5 Discussion of Results

5.5.1 Introduction

Primarily, the results of this thesis given in this chapter represent the information that was required for and obtained from the first application of the LIRAD technique to stratocumulus clouds. The results were divided into three main sections, the lidar measured cloud heights obtained over the full duration of the SOCEX (5.2), the properties of clouds observed on 16/7/1993 during SOCEX1 (5.3), and the properties of clouds observed on 8/2/95 during SOCEX2 (5.4). The properties of the clouds were determined from several sources: *in situ* measurements obtained some miles to the west of Cape Grim (over the sea), and from lidar, infrared radiometer and microwave radiometer measurements obtained at Cape Grim (over land and directly downwind from the airborne measurements). These final sections discuss the important relationships between the various results, their limitations, and identify the primary geophysical results of the thesis. These discussions are extensions of those presented throughout this chapter.

5.5.2 Lidar Measured Cloud Heights (SOCEX)

The marine stratocumulus and cumulus clouds measured by lidar during SOCEX were all located in or near the top of the boundary layer. There were some limitations on these measurements. Very little information could be obtained about any of the properties of the precipitating clouds as rain often interrupted the lidar measurements – rain was a problem particularly during the winter phase of the experiment (SOCEX1). Where lidar measurements were obtained during periods of rain the measured heights were less accurate due to backscatter from rain droplets. The other limitation was that the lidar could not measure clouds deeper than approximately 200–250 m due to the total attenuation of the lidar return. This meant that multiple layers of cloud above a deep cloud layer were not observed. This would have biased the cloud heights down.

Even with these limitations the lidar measured cloud heights showed with reasonable certainty that, for the observation days under consideration, the stratocumulus clouds observed during the summer phase of SOCEX were higher than those observed during the winter phase. One possible reason for this was that during the summer phase the boundary layer air was not always dynamically coupled to the surface air. This meant that, in the summer, the main cloud layer was often warmer and dryer than the layer immediately above the sea surface, leading to the formation of higher clouds.

Cloud heights were also measured during the lidar study of cloud optical properties by Pal *et al.* (1995). A comparison of results from that study with those of this thesis is made with caution, because of possible differences in the cloud detection algorithms, and also because of the small amounts of data obtained in both studies. Pal *et al.* found that low-level clouds with bases below an altitude of 2 km were more frequent during ECLIPS 1, the (Canadian) autumn phase of the ECLIPS experiment, than during ECLIPS 2 (Canadian summer). This result does not contradict the findings of this thesis. Further long-term measurements of the heights of low cumulus and stratocumulus clouds are required to confirm whether or not there are seasonal differences in the heights of these cloud types. Any relationships that could be found between the heights and optical properties of boundary layer clouds would also be useful in parameterisations for climate models.

5.5.3 Properties of Clouds Observed on 16/7/93 (SOCEX1)

5.5.3.1 Aircraft *In Situ* Measurements

The *in situ* properties of the clouds determined from the aircraft measurements made on Flight 08 of 16/7/93 were calculated from the measured Droplet Size Distributions (DSDs) shown in Figures 5.6 to 5.21. The clouds '1' to '7' were measured over the sea whereas cloud '8' was measured over the land. Thus the properties of cloud '8' were not used in the analyses of the LIRAD and MWR data as the remote sensing instruments measured clouds that had just reached the coast after forming at sea. Note that the droplet concentrations of clouds '4' and '8', were approximately 20 cm^{-3} (5.3.3.3), about half the other concentrations. This is because the liquid water in these clouds was taken up by fewer numbers of larger droplets ('drizzle') with radii ranging from approximately $100 \mu\text{m}$ to 1 mm . Evidence of these larger droplets may be seen in Figures 5.12 and 5.20.

The measured cloud droplet concentrations (n) were approximately constant with height (Figure 5.22). However, the effective radii of the droplets increased with height (Figure 5.27). Therefore the increasing extinction with height, as seen in Figure 5.41, was due to an increasing droplet size with height and not increasing n . The *in situ* results for liquid water content (5.3.3.5) were used to calculate the cloud liquid water paths, W (Figures 5.36 and 5.37). The values of W and cloud droplet effective radius (5.3.3.4) were used to determine the parameterisation of optical depth, to enable optical depths to be calculated from the microwave radiometer measurements of W .

The *in situ* results for visible extinction (5.3.3.7) and backscatter (5.3.3.8) represent the results of the steps taken to calculate the visible extinction-to-backscatter ratio, S (5.3.3.9). Similarly, the *in situ* results for infrared absorption (5.3.3.10) and visible extinction were used to calculate the ratio of visible extinction-to-infrared absorption ratio, α (5.3.3.11). Subsequently the comparisons of these values of S and α with the LIRAD retrieved values of ηS and $\eta \alpha$ provided the multiple scatter factors (5.3.4.3 and 5.4.1.3). There were only small variations in S with depth into the clouds and this led to the calculations of optical depth (modified by η) directly from the calibrated lidar returns (5.3.4.4).

The visible and infrared optical depths of the clouds '1' to '8' (5.3.3.12 and 5.3.3.13) were calculated from the *in situ* results for visible extinction and infrared absorption, and comparisons of

these depths were made with the LIRAD results (about which more will be said in a following section).

Primarily, the *in situ* data presented in this chapter represented the results at the end of each of the steps taken to provide *in situ* data for comparisons with the LIRAD results, and for calculating optical depths from the microwave radiometer measurements. Also, these *in situ* results provide a detailed database of the *in situ* properties of the clouds that may be useful for future investigations of the results of this thesis.

5.5.3.2 LIRAD Study of Stratocumulus Clouds Observed on 16/7/93

The stratocumulus clouds observed by LIRAD on 16/7/93 could be separated into two 'decks' of cloud. One deck consisted of optically thin clouds that passed overhead Cape Grim between approximately 14:30 and 16:10 hours EST. The second deck was measured between approximately 16:10 and 17:05 hours EST. The two decks provided a wide range of optical depths that enabled a successful study of the LIRAD data by the LIRAD analysis technique. The LIRAD results can be summarised by the single plot of integrated attenuated backscatter (χ') versus infrared emittance (ϵ), shown in Figure 5.67. There is very little scatter in the data of this result, and inspection of previous LIRAD results (for cirrus clouds) shows that this result (for stratocumulus clouds) may be the 'tightest' fit of χ' versus ϵ data of any LIRAD study of clouds. This is because the stratocumulus clouds contained only water droplets with only small variations in their microphysical properties, whereas the microphysical properties of high clouds vary more widely due to the different shapes of their ice crystals.

Comparisons of the *in situ* extinction-to-backscatter ratios (S) with the LIRAD-retrieved ηS delivered the multiple scattering factors (η). The measured values of η compared reasonably well with theoretical values of η determined for water droplet clouds (Platt, 1981). The retrievals of η made for this thesis represents very new work. In the literature, there are very few reports on the value of η , and where information is available, there is little agreement on the magnitude of lidar multiple scattering even for the simplest modelled clouds (Bissonnette *et al.* 1995). With η accounted for in the work for this thesis, the primary results of the analyses of the lidar and infrared radiometer measurements could be given: that is, cloud infrared emittances and visible and infrared optical depths.

5.5.3.3 Optical Depths of Stratocumulus Clouds by Microwave Radiometer (16/7/93)

The detection of aerosols and clouds of low optical depth is a strength of the lidar/LIRAD methods, but this is offset by their inability to determine the optical depths of deeper clouds. Thus where the total range of optical depths is required, lidar/LIRAD methods should be used in conjunction with measurements by instruments that penetrate clouds more deeply. During SOCEX simultaneous measurements by a microwave radiometer were available for investigation. Again, the *in situ* data proved invaluable for 'calibrating' ground-based measurements so that optical properties could be calculated from them.

The quality of the microwave radiometer data was limited by uncertainties associated with data resolution and scattering of the microwave radiation by larger droplets. With respect to the latter problem, the correlation between the lidar measured heights of cloud base and the microwave radiometer measurements of liquid water path obtained on 10 July 1993 (Figures 5.77 and 5.78), at least gave some indication of the size of the errors involved. (This error was of the order of positive 100% where precipitation was present). The cloud optical depths obtained by the MWR during the daylight hours of 16/7/93 ranged from zero to approximately 10. This agrees reasonably well with the range of optical depths of zero to approximately 10 obtained by Boers *et al.* (1998), for stratocumulus clouds measured *in situ* during the entire winter experiment. At least, the microwave radiometer measurements at Cape Grim provided a broad overview of the total range of the optical depths of the clouds observed on 16/7/93 that could not be provided by the LIRAD method alone.

5.5.4 Properties of Clouds Observed on 8/2/95 (SOCEX2)

5.5.4.1 LIRAD Study of Stratocumulus Clouds Observed on 8/2/95 (SOCEX2)

The 'minilidar' used during the summer phase of SOCEX was a less sensitive instrument than the 'maxilidar' used during SOCEX1. However, the cloud measurements by the minilidar had adequate signal-to-noise ratios, and so an attempt was made to analyse the SOCEX2 LIRAD dataset. The minilidar could not detect a molecular backscatter profile for calibration purposes, and the absence of a molecular signal in the free troposphere meant that a novel method of 'calibration' was required. The only practical option available was to determine the (uncalibrated) maximum integrated attenuated backscatter for these clouds measured by the lidar, then equate that with an estimate of $(2\eta S)^{-1}$. The value of $(2\eta S)^{-1}$ used for this 'calibration' was obtained from the previous part of the

thesis, (the LIRAD study of the SOCEX1 data), but with the value of S corrected for the wavelength difference between the lidars (532 nm, SOCEX1, versus 1.06 μm , SOCEX2; see 4.4.2). The assumption of no changes in η between the datasets was discussed in 4.4.3.

The results of the analysis of this second LIRAD dataset proved fruitful, and once again, there was a strong representation by optically thin stratocumulus clouds (Figures 5.89 to 5.92). Furthermore, an estimate of the multiple scatter factor (η) could also be made from the dataset. The value of η of 0.5 that was obtained from the SOCEX2 dataset indicated that there was more multiple scattering detected from the measurements of the summer clouds than for the SOCEX1 result. This can be explained in part by the greater field of view of the minilidar (11.5 mr versus 5 mr), and the greater heights of the summer clouds from the minilidar. Also, it is possible that there was more multiple scattering occurring in the summer clouds with their higher concentrations of smaller droplets (Boers *et al.*, 1998). Whether the latter explanation is true needs to be answered by further rigorous theoretical studies of the multiple scattering in lidar returns from these clouds.

5.5.4.2 Optical Depths of Stratocumulus Clouds by Microwave Radiometer (8/2/95)

As with the SOCEX1 dataset, the quality of the microwave radiometer data was limited by uncertainties associated with data resolution and scattering of the microwave radiation by larger droplets. The optical depths of the clouds measured on 8/2/95 calculated from the MWR data that were not contaminated by rain ranged from zero to just above 20. This result, that the optical depths of the stratocumulus clouds measured by MWR on 8/2/95 (summer) were greater than those observed on 16/7/93 (winter), is not inconsistent with the results of Boers *et al.* (1998). In that study it was determined that the higher optical depths of the summer stratocumulus clouds was due to the higher extinction of the higher concentrations of smaller droplets that existed in the summer clouds.

5.5.5 Cloud Optical Depths

In order to place all the results for the optical properties of the clouds in perspective, a simple equation linking cloud microphysics with visible optical depth (τ_v) was used to provide comparisons between the various τ_v of the stratocumulus clouds obtained in this thesis, with those obtained in other studies. Attention was focussed on the visible part of the spectrum because, climatologically, the solar fluxes of stratocumulus clouds are more important than their thermal infrared fluxes. Attention was focussed

on visible optical depths because it is this quantity that appears most often in the literature, and is most easily compared with other results. (Approximations for the cloud infrared optical depths may be obtained by dividing the τ_v by 2). The equation used for the comparisons is,

$$\tau_v = 2\pi N a_{eff}^2 h, \quad (5.17)$$

where N is the droplet concentration, a_{eff} is the effective droplet radius, and h is the geometrical cloud depth (Twomey, 1977).

A modelled stratocumulus cloud that is sometimes used for radiative studies is the so-called 'Sc II' model (Stephens, 1978; Slingo and Schrecker, 1982). In Table 5.29 the values of τ_v obtained from equation (5.17) are shown for Sc II; the a_{eff} was calculated by Slingo and Schrecker (1982). The values for τ_v calculated from the a_{eff} and N obtained from the SOCEX airborne study by Boers *et al.* (1998) are also shown. (Transmittances calculated from τ_v are also shown).

Table 5.29. Calculated optical depths of the 'Sc II' stratocumulus cloud.

Depths of Cloud Layer (m)	a_{eff} (μm)	N (cm^{-3})	τ_v	T_v
'Sc II'				
300	9.9	120	22.2	2×10^{-10}
200	9.9	120	14.8	4×10^{-7}
100	9.9	120	7.4	6×10^{-4}
SOCEX1				
300	11.5	28	5.9	2.7×10^{-3}
200	10	31	3.5	3.0×10^{-2}
100	9	31	1.6	2.0×10^{-1}
SOCEX2				
300	6.5	89	6.8	1.1×10^{-3}
200	6.5	89	4.5	1.1×10^{-2}
100	6	93	2.1	1.2×10^{-1}

Inspection of Table 5.29 shows that the optical depths of Sc II are large when compared to the *in situ* SOCEX results because of the high droplet concentrations of Sc II. Note that a significant result of SOCEX, that the summer clouds were optically deeper than the winter clouds (Boers *et al.*, 1998), is borne out even in this limited extraction of properties of the lowest 100 m - 300 m layers of the clouds. Also note that the stratocumulus clouds observed by the airborne team were often optically thin primarily due to the low droplet concentrations measured in the clean marine Southern Ocean atmosphere, with its relatively fewer numbers of CCN.

The LIRAD results for τ_v of the stratocumulus clouds approximately 100 m thick (observed on 16 July 1993) are shown in Table 5.30. Transmissions calculated from τ_v are also shown, as well as some of the *in situ* results for comparison. These are not direct comparisons: the clouds 1-7 were hundreds of metres thick and observed further out to sea. However, clearly, the LIRAD measurements were of unusually thin layers of cloud. If the cloud droplets in these LIRAD measured clouds had typical radii of 10 μm , then the concentrations must have been very small – of the order of 10 cm^{-3} ; or, the cloud droplets were unusually small.

Table 5.30. Cloud optical depths by LIRAD and *in situ* measurements.

	$\tau_v \pm \delta\tau_v$	$T_v \pm \delta T_v$	Depth from Cloud Base (m)
LIRAD	0.22 ± 0.2	0.80 ± 0.16	93 ± 33 m
'Clouds 1 – 7' (<i>in situ</i>)	1.7 ± 0.4	0.18 ± 0.07	0 – 100 m

The detection of optically thin clouds is also highlighted in other lidar studies. For example, from the extinction profiles of stratocumulus clouds determined by Carnuth and Reiter (1986), the cloud optical thicknesses varied from approximately 0.1 to 1 over 100 metre layers. Pal *et al.* (1995) presented some statistics on cloud optical properties that were obtained by lidar, and these showed a prevalence of thin clouds or cloud 'fragments'. For the low clouds, (heights 0 - 2 km), the average $\tau_v \approx 0.651$ (ECLIPS 1, Canadian autumn), and $\tau_v \approx 0.125$ (ECLIPS 2, Canadian summer). That study was limited by its few measurements and a bias towards thinner clouds (about 10 - 15% of the clouds were not penetrated by the lidar and omitted from the study). However, Pal *et al.* (1995) concluded that the ECLIPS observations indicated the fractions of clouds (of all heights) with fractions of $\tau_v < 1.2$ was "much greater" than the global 10 - 15% suggested by Rossow and Lacis (1990). In keeping with the cut-off figure of 1.2, the fractions of stratocumulus clouds with $\tau_v < 1.2$ obtained from the LIRAD analyses of this thesis are $\approx 43\%$ ($\eta = 0.6$, 16 Jul '93), and $\approx 12\%$ ($\eta = 0.5$, 8 Feb '95).

The MWR measurements were very imprecise for the optically thin clouds, however for completeness the fractions of $\tau_v < 1.2$ obtained by MWR were: $\approx 7\%$ ($Q_{\text{eff}}: 2.2 - 2.4$; $a_{\text{eff}}: 10 - 15 \mu\text{m}$), and $\approx 18\%$ ($Q_{\text{eff}}: 2.6 - 3.2$; $a_{\text{eff}}: 8 - 11 \mu\text{m}$). Although obtained from small datasets only, the LIRAD results of 43% and 12% are pointing to significantly large fractions of optically thin boundary layer clouds and so support the findings of other lidar studies.

Thus, the primary geophysical result of the thesis was that many of the observed boundary layer clouds, composed of water droplets only, were optically thin. These "thin clouds" ranged from

layers of swelling aerosols near the top of the boundary layer to clouds with visible optical depths less than approximately 1. This is an important geophysical result because it is usual, especially in climatological studies of the interaction of clouds on climate, for boundary layer clouds to be considered optically thick. In fact, often they are considered to be of the maximum optical thickness (or maximum infrared emittance). It is emphasised that the datasets investigated for this thesis were relatively small considering the amounts of data that would be required to draw conclusions about cloud properties on oceanic or global scales. However, the LIRAD results of this thesis as well as other lidar studies are pointing to a prevalence of optically thin low clouds in the atmosphere that may not have been previously recognised. An investigation dedicated to this problem would seem worthwhile.

5.5.6 Lidar Multiple Scattering Factor

Multiple scattering in the lidar signals in most lidar studies of clouds is appreciable, and this can be shown by simple approximations (see, for example, Nicholas *et al.*, 1997). The multiple scattering intensity is a function of telescope field of view, cloud range, cloud optical depth and cloud depth. The multiple scattering in the backscatter depends on the shape of the scattering phase function in the backwards direction, and also varies with depth into the cloud (Kunkel and Weinman, 1976; Platt, 1981). Platt (1981) found that in a stratocumulus cloud, η increases rapidly above cloud base and then levels off. However, because the infrared emittance is for the whole cloud depth and the integrated backscatter is also an integral through the cloud, only an average representative value of η is obtained in the present study. Based on this result, and the approximations of Nicholas *et al.*, (1997), it is concluded that the assumption of a constant value of η , averaged through the cloud depth, will not lead to large errors in the situations reported in this thesis. The average values of η estimated for this thesis can be compared with those of Platt (1981), and other authors (Bissonnette *et al.*, 1995). In the present case, η is found to be lower for lower optical depths (Table 5.31). This does not contradict what Platt found, and the values of η are similar to his (≈ 0.7).

Table 5.31. Lidar multiple scattering factors (η) obtained for this thesis.

<i>Experiment</i>	<i>Height; Depth</i>	<i>Field Of View</i>	τ_v	η
SOCEX1, 16/7/93	≈ 1000 m; $\approx 200 - 300$ m	5 mr	$1.3 < \tau_v < 3.9$	0.77 ± 0.05
SOCEX1, 16/7/93	≈ 1000 m; $\approx 50 - 200$ m	5 mr	$0.12 < \tau_v < 0.88$	0.6 ± 0.2
SOCEX2, 8/2/95	≈ 1500 m; $\approx 50 - 200$ m	11.5 mr	$0.5 < \tau_v < 1.5$	0.5 ± 0.3

Values of η can also be calculated from the results from a number of authors given by Bissonnette *et al.* (1995), for Deirmendjian's (1969) model cumulus cloud 'C1'. Using their values of total scattering and single scattering and optical depth, values of η can be calculated from a formula given by Platt (1981). Values are shown in Table 5.32 (C. M. Platt, private communication).

Table 5.32. Lidar multiple scattering factors (η) calculated for cloud type 'C1'.

<i>Cloud</i>	<i>Height; Depth</i>	<i>Field Of View</i>	τ_v	η
<i>C1</i>	1000 m; 300 m	10 mrad	5.125	0.82 - 0.89
<i>C1</i>	1000 m; 300 m	1 mrad	5.125	> 0.9

Considering that the calculations were made for a standard cloud, there is considerable variation, depending on the computer codes employed. All the values appear to be higher than those found by Platt, and also in the present study. Thus, of all the models, the Platt values seem to be closer to the truth.

6. Conclusions

Introduction

The major outcomes of the work described in this thesis were, referring to the aims (1.5): 1) The distribution of the heights of the boundary layer clouds measured in limited periods during the winter of 1993 and the summer of 1995 showed differences that require further investigation before conclusions on seasonal differences can be drawn. 2) The first LIRAD study of stratocumulus clouds revealed that many of the clouds observed were not always optically thin (or 'black' in the infrared), as they are often assumed to be for climate studies. 3) The effects of multiple scattering on the lidar returns were determined by comparisons with *in situ* measurements of the clouds, providing rare (if not the first) measurements of the lidar multiple scatter factor (η). 4) The more deeply penetrating cloud measurements by a microwave radiometer were used to obtain a better perspective of the total range of optical depths observed during SOCEX. 5) In addition, the method of calibrating the lidar led to the finding that large aerosols were very important for determining the optical properties of the cloud-free marine boundary layer. Each of these outcomes is addressed in the conclusions given in the following sections. It should be noted that the Experimental Cloud Lidar Pilot Study (ECLIPS) program attempted to acquire lidar measurements of clouds on a large scale (Platt *et al.*, 1994; Pal *et al.*, 1995). By providing cloud heights and optical properties the work described in this thesis has also contributed further to the ECLIPS program and its aims.

6.1 Lidar Measured Heights of Boundary Layer Clouds

The boundary layer clouds observed by lidar during SOCEX2 (summer) had bases that were approximately 600 m higher than those observed during SOCEX1 (winter). The peaks of the cloud height frequency distributions occurred between the heights 800 - 1000 m for SOCEX1, and 1600 - 1800 m for SOCEX2. These findings were obtained from measurements that were limited in some ways. First, the measurements were interrupted by precipitation during SOCEX1. Secondly, the fact that the lidar penetrated only 200 - 250 m into these clouds meant that above a layer of this depth or greater, clouds could not be detected. However, reports from the observers aboard the SOCEX aircraft indicated that during baseline conditions the air above the boundary layer clouds was cloud-free. Therefore it seems reasonable, allowing for errors in cloud top from the effects of attenuation, that the peaks in the cloud

height frequency distributions of the clouds of approximately 900 m for SOCEX1 and 1700 m for SOCEX2, are likely to be representative of the marine stratocumulus clouds observed at Cape Grim during SOCEX.

6.2 Lidar and Infrared Radiometer (LIRAD) Studies of Boundary Layer Clouds

Prior to the studies of this thesis the LIRAD method was used as a technique for studying the optical properties of high and mid-level clouds, (*e.g.* Platt, 1979; Platt and Dilley, 1979; Platt *et al.*, 1984; Platt *et al.*, 1987; Platt *et al.*, 1998). In the study reported in this thesis, the LIRAD method was successfully adapted to the analysis of some LIRAD measurements of marine stratocumulus clouds that had formed over the Southern Ocean south and west of the coast of Tasmania {Young, (1995); Young *et al.*, (1996); Pickett *et al.*, (1996a); Pickett *et al.*, (1996b)}.

There were two primary reasons for the success of the application of the LIRAD method to these low clouds. First, the stratocumulus clouds contained only water droplets, as determined from the airborne measurements (Boers *et al.*, 1996; Boers *et al.*, 1998). From the *in situ* measurements the cloud microphysical properties, the extinction-to-backscatter ratio (S) and the ratio of visible extinction to infrared absorption (α), could be determined from Mie scattering theory. It was found that these microphysical properties varied only a little between cloud droplet size distributions. This meant that there was only one LIRAD function of integrated attenuated backscatter (χ' or γ') versus emittance (ϵ) to investigate, as opposed to the several LIRAD functions that would have been required had there been ice in the clouds (one LIRAD function per ice crystal shape). The lack of variation in S and α means that it may be possible to 'calibrate' a lidar from measurements of fully attenuating water droplet clouds, thus dispensing with the need for independent measurements of the clouds. This could be done by equating the measured values of the maximum χ' (or γ') to the calculated $(2\eta S)^{-1}$ (or $k/2\eta$) via equation (2.22).

The second reason for the success of the LIRAD method was that the clouds observed on 16 July 1993 (SOCEX1) and 8 February 1995 (SOCEX2) covered a wide range of optical depths; this is a requirement for accurate retrievals of $\eta\alpha$ by the LIRAD analysis technique. From this wide range of depths the detection of optically thin clouds by LIRAD during both phases of SOCEX was an important observation; this is discussed in the next section.

The successful application of the LIRAD method to boundary layer clouds shows that further similar studies could provide valuable statistics of the optical properties of these clouds. Statistics on the

optical properties of these clouds, seasonally and monthly averaged, could be obtained by ground-based LIRAD measurements. This would be a simpler and cheaper alternative to mounting instruments on aircraft and satellites, for example.

6.3 Optically Thin Boundary Layer Clouds

One of the important results of the thesis was the finding of a large fraction of optically thin clouds in the marine boundary layer. The fractions of the non-precipitating stratocumulus clouds with infrared (10 - 12 μm) optical depths less than 1 were approximately 40% (16 July 1993, SOCEX1) and 20% (8 February 1995, SOCEX2). This finding of a high incidence of optically thin clouds in the boundary layer supports that of Pal *et al.* (1995). The fact that significant fractions of these stratocumulus clouds were optically thin, whether they occurred in widespread decks as on 16 July 1993, or whether they were formed by cumulus rising to and then spreading out at the top of the boundary layer as on 8 February 1995 (Krummel, 1998), was surprising. This is because in studies of the impact of clouds on climate, low clouds are normally considered to be optically thick.

These optically thin clouds warrant further investigation. If thin boundary layer clouds are more common in the atmosphere than previously known, it is possible they have an effect on climate that has not been previously considered. If the coverage of stratocumulus clouds has been underestimated in the past because thin clouds have not been detected, then consideration of the interaction of these clouds with both solar and terrestrial radiation would produce an additional cooling effect due to their high solar albedos. Alternatively, if the stratocumulus cloud coverage has been correctly estimated but the optical depths overestimated, the 'thin cloud correction' would allow more solar radiation to penetrate the cloud cover thereby producing a warming effect. Further measurements of boundary layer clouds are required to determine whether the occurrence of thin boundary layer clouds has an impact on climate that has not been previously considered.

6.4 Multiple Scattering in Lidar Returns from Stratocumulus Clouds

With the aid of the *in situ* aircraft measurements of drop size distribution it was found that it was possible to retrieve the lidar multiple scatter factors (η). This was accomplished by comparisons of the retrieved values of ηS and $\eta\alpha$ obtained by LIRAD, with values of S and α obtained from the *in situ* measurements. To the author's knowledge this was the first time the lidar multiple scatter factor has been measured in this way. The measured values of η compared reasonably well with the values expected from theoretical

calculations (Platt, 1981). These retrievals of η meant that the LIRAD results were freed of any significant effects due to multiple scattering in the lidar returns. Also, these measured values of η provide rare experimental results for the lidar multiple scattering in clouds that should provide valuable input to future theoretical studies.

6.5 Cloud Optical Depths by Lidar, *In Situ* Measurements and Microwave Radiometer

The LIRAD study of the stratocumulus clouds was limited to retrieving the properties of optically thin clouds. To obtain a better perspective on the optical depths of the thicker clouds, the utility of the more deeply penetrating MicroWave Radiometer (MWR) measurements was examined. There were risks associated with the quality of the MWR data due to the possibility of contamination by water on the receiver, and errors in the measurements due to the effects of precipitation on the measured radiation (see 5.5.4). However, if the MWR measurements were affected in these ways, the errors in the retrieved liquid water paths and optical depths would be positive. If that was the case for this study, the MWR results would show a significant fraction of the clouds were optically thin (see Table 6.1).

Table 6.1. Fractions of thin clouds determined by LIRAD and MWR.

<i>Equipment</i>	<i>16 July 1993 (SOCEX1)</i>	<i>8 February 1995 (SOCEX2)</i>
LIRAD	$\tau_v < 2, \approx 50\%$	$\tau_v < 5, \approx 20\%$
MWR	$\tau_v < 2, \approx 18\%$	$\tau_v < 5, \approx 28\%$

As a minimum, the study of the MWR measurements of the clouds provided a perspective on the larger optical depths that could not be obtained by LIRAD or lidar methods alone. The optical depths of the thicker clouds ranged up to approximately 10 on 16/7/93 (SOCEX1) and up to approximately 25 on 8/2/95 (SOCEX2). Finally, it is recalled that the optical depths of the deeper clouds were obtained in part from values of Q_{eff} and a_{eff} obtained from the *in situ* measurements. These two parameters do not vary significantly in stratocumulus clouds, so in future it should be possible to obtain useful cloud properties from MWR measurements without *in situ* measurements.

6.6 Optical Properties of Moist Boundary Layer Aerosols

The *in situ* ASASP and FSSP measurements of the aerosols in the boundary layer and free troposphere, and measurements of the ambient humidity, were used to calculate height profiles of aerosol backscatter and extinction. There was excellent agreement between the aerosol backscatter determined from the *in*

situ measurements, after corrections for hydration, and that determined by the lidar. This contributed to a quality calibration and validation of the lidar results. From this came the discovery that for the marine boundary layer aerosols observed on 16 July 1993 (SOCEX1), the majority of the aerosol backscatter was due to scattering by the few large particles measured by the FSSP - those with radii larger than approximately 1 μm . The magnitude of the aerosol backscatter measured by lidar during SOCEX1 could only be explained by the light scattering properties of these hydrated swollen aerosols.

6.7 Recommendations for Future Work

The studies of the cloud measurements made for this thesis point to opportunities for further advances to be made using the LIRAD method or lidar alone. First, with the information on the *in situ* properties of stratocumulus clouds obtained from the results of this thesis, the LIRAD method could be applied to water droplet clouds without incorporating results from *in situ* measurements every time. Enough has been learnt about the *in situ* properties of the water droplet clouds to predict the cloud microphysics and multiple scattering. More practical or routine monitoring by LIRAD should be possible.

The analysis of the LIRAD data could be made more efficient by taking advantage of recent advances in theoretical studies of the multiple scattering in lidar returns (Bissonnette *et al.*, 1995) and in radiative transfer algorithms (Stamnes *et al.*, 1993). These new methods could be used to form a new platform for an improved LIRAD algorithm, for example. In such a program the LIRAD measurements could form some of the constraints on the solutions calculated by the new methods. The design of such a program should ensure that the measurements from any lidar and infrared radiometer equipment, as well as any new advances in the theoretical studies of multiple scattering and radiative transfer, could be transferred efficiently into the program. Such a program should help to advance our knowledge of the optical properties of clouds.

It is recognised that a LIRAD study of clouds is costly in terms of the analysis of data, and often only a lidar may be available. The work done for this thesis showed that without an infrared radiometer, a calibrated lidar could be used to retrieve the visible extinction and optical depths of thin water droplet clouds. For water droplet clouds only small variations in the extinction-to-backscatter ratio (S) with depth occur, assuming that there are not significant variations in the multiple scatter factor. It is recalled that as $\tau \rightarrow \infty$, $\chi' \rightarrow (2\eta S)^{-1}$ (2.21a). Thus ηS may be retrieved from the maximum χ' values, provided the lidar returns from the clouds that fully attenuate the lidar pulse can be identified. This is a relatively simple

exercise as the maximum χ' from the thickest water droplet clouds is easily identified in large datasets of χ' . Given a value of the maximum χ' from the fully attenuating clouds a result for ηS may be determined such as the result achieved for this thesis, $\eta S \approx 14.5 \pm 0.5$ sr {result (5.2)}, determined for clouds approximately 250 m in depth. Where there are only small variations in ηS , $\eta \tau$, can be calculated from lidar measurements by a re-arrangement of equation (2.21a) {e.g., see Figures (5.69) and (5.70)}. Further studies are required to determine the variations in S in water droplet clouds, as well as further studies of the multiple scattering to determine the variation in η with depth into these clouds.

Appendix A1. Radiative Quantities and List of Symbols

A list of the important quantities and the adopted symbols used in this thesis are shown in the following tables. Table A1.1 shows the quantities used for radiative transfer theory, and Table A1.2 shows the quantities used for the analysis of the lidar and LIRAD measurements. Here, 'infrared' refers to the infrared radiometer-measured band of the spectrum, over the range of wavelengths 10 - 12 μm . Some symbols that appear only briefly in the thesis may not be in the list.

. . .

Table A1.1. List of quantities for radiative transfer and scattering theory.

<i>Symbol</i>	<i>Description</i>	<i>Units</i>
a	droplet radius	m
a _{eff}	effective droplet radius	m
A	surface	m ²
β _{sc}	volume angular scattering coefficient	m ² m ⁻³ sr ⁻¹
C	cross section	m ²
E	irradiance	W m ⁻²
ε	beam emittance	nil
ε _f	flux emittance	nil
g	asymmetry parameter	nil
G	geometrical cross section	m ²
I	intensity	W sr ⁻¹
j	emission coefficient	W sr ⁻¹ g ⁻¹
κ _{ab}	mass absorption coefficient	m ⁻² g ⁻¹
κ _{ex}	mass extinction coefficient	m ⁻² g ⁻¹
L	radiance	W m ⁻² sr ⁻¹
m	refractive index	nil
n	refractive index (real part)	nil
n'	refractive index (complex part)	nil
n _p	number of photons	nil
N	number density per wavelength interval	m ⁻³ μm ⁻¹
N'	number density or concentration	m ⁻³
M	exitance	W m ⁻²
ν	frequency	Hz
ω	solid angle	sr
ω̄	single scattering albedo	nil
Ω	solid angles integrated over all directions	sr
φ	azimuthal scattering angle	radians
Φ	radiant flux	W
p	phase function	sr ⁻¹
P	air pressure	Pa
Q	radiant energy	J
Q _{ab}	absorption efficiency	nil
Q _{sc}	scattering efficiency	nil
Q _{ex}	extinction efficiency	nil
r	range	m
ρ	mass density	g m ⁻³
σ	volume extinction coefficient (total extinction)	m ² m ⁻³
σ _{ab}	volume absorption coefficient	m ² m ⁻³
σ _{ex}	volume extinction coefficient	m ² m ⁻³
σ _{sc}	volume scattering coefficient	m ² m ⁻³
ℑ	source function	W m ⁻² sr ⁻¹
t	time	s
T	temperature	K
τ	optical thickness or depth	nil
θ	scattering angle	radians
w	liquid water content	g m ⁻³
W	liquid water path	g m ⁻²
x	size parameter (2πa/λ)	nil
z	height	m

Table A1.2. List of quantities for analysis of lidar and LIRAD measurements.

<i>Symbol</i>	<i>Description</i>	<i>Units</i>
α	visible extinction-to-infrared absorption ratio ($\sigma_v : \sigma_i$)	nil
B	isotropic volume backscatter coefficient	m^{-1}
β_m	volume visible backscatter coefficient (molecular)	$\text{m}^{-1} \text{sr}^{-1}$
β_a	volume visible backscatter coefficient (aerosol)	$\text{m}^{-1} \text{sr}^{-1}$
β_c	volume visible backscatter coefficient (cloud)	$\text{m}^{-1} \text{sr}^{-1}$
C	lidar system constant	$\text{V m}^3 \text{sr}$
χ	attenuated β	$\text{m}^{-1} \text{sr}^{-1}$
χ'	integrated attenuated β	sr^{-1}
ε_i	infrared absorption emittance	nil
η	multiple scatter factor	nil
γ	attenuated B	m^{-1}
γ'	integrated attenuated B	nil
k	isotropic backscatter-to-extinction ratio (B : σ)	nil
k_w	water vapour continuum mass absorption coefficient	$\text{cm}^2 \text{g}^{-1} \text{atm}^{-1}$
L_g	total measured radiance (at ground)	$\text{W m}^{-2} \text{sr}^{-1}$
L_i	infrared absorption radiance	$\text{W m}^{-2} \text{sr}^{-1}$
L_c	cloud radiance, $L_c = L_i + L_s + L_r$	$\text{W m}^{-2} \text{sr}^{-1}$
L_s	cloud internal-scattering infrared radiance	$\text{W m}^{-2} \text{sr}^{-1}$
L_r	reflection of earth surface infrared radiance from cloud	$\text{W m}^{-2} \text{sr}^{-1}$
L_{air}	radiance by cloud-free air, or clear sky radiance	$\text{W m}^{-2} \text{sr}^{-1}$
ϕ	returned optical power (lidar)	W
p_π	phase function at 180°	sr^{-1}
P	pressure	hPa
S	extinction-to-backscatter ratio ($\sigma : \beta$)	sr
σ_a	volume visible extinction coefficient (aerosol)	m^{-1}
σ_m	volume visible extinction coefficient (molecular)	m^{-1}
σ_i	volume infrared absorption coefficient (cloud)	m^{-1}
σ_v	volume visible extinction coefficient (cloud)	m^{-1}
Δt	laser pulse duration	s
T	temperature	K
T_m	visible transmittance (molecular)	nil
T_a	visible transmittance (aerosol)	nil
T_v	visible transmittance (cloud)	nil
T_{air}	transmittance of cloud-free air (infrared)	nil
T_i	transmittance (cloud, infrared absorption)	nil
τ_i	infrared absorption optical depth	nil
τ_v	visible optical depth	nil
V	measured signal voltage	V
z	height	m
z_b	height of cloud base	m
z_t	height of apparent (lidar-measured) cloud top	m
ζ	ratio of σ_i to B	nil

Appendix A2. Optical Properties of Air Molecules, Spherical Aerosols and Cloud Droplets

A2.1 Introduction

This appendix collects together all the important equations used to develop the theory on which the thesis 'Lidar and Infrared Radiometer Studies of Stratocumulus Clouds' was formed. Some basic microphysical properties of aerosols and cloud water droplets are presented in the next section. Primary radiative quantities are presented in section A2.3, and basic radiative transfer in section A2.4. The absorption by air molecules of infrared radiation in the 10 - 12 μm region of the spectrum is described in section A2.5. The molecular absorption of visible light at the Nd:YAG laser wavelengths of 532 nm and 1.064 μm is investigated briefly, also in section A2.5. Outlines of the Rayleigh and Mie scattering theories are given in sections A2.6 and A2.7 respectively.

A2.2 Microphysical Properties and Measures of Cloud Water

The microphysical properties, composition, size, shape and number density determine the optical properties of air molecules, aerosols and cloud droplets. The composition of the particles determines the complex refractive index (m) and this is given by,

$$m = n + in' . \quad (\text{A2.1})$$

where n and n' are the real and complex parts of the refractive index respectively. The size of particles is usually given in relation to the wavelength of light (λ) being scattered (or absorbed) by them, by the size parameter (x):

$$x = \frac{2\pi a}{\lambda} , \quad (\text{A2.2})$$

where a is the radius of a particle and λ is the wavelength of the incident light.

In the atmosphere, aerosols and cloud particles exist as ensembles of particles of different sizes - polydispersions. The total number of particles per unit volume of air in a polydispersion is,

$$N' = \int_0^{\infty} N(a) da, \quad (\text{A2.3})$$

where the function $N(a)$ describes the number distribution of particles of radius a . For studies of the microphysical and optical properties of water droplet clouds, the cloud effective droplet radius (a_{eff}) defined by,

$$a_{eff} = \frac{\int_0^{\infty} a^3 N(a) da}{\int_0^{\infty} a^2 N(a) da}, \quad (\text{A2.4})$$

is often used (*e.g.* Hansen and Travis, 1974). The liquid water content (w) is the mass of water per unit volume of air,

$$w = \rho \int_0^{\infty} \frac{4}{3} \pi a^3 N(a) da, \quad (\text{A2.5})$$

where ρ is the density of water, *i.e.* 10^6 g m^{-3} . The liquid water content (w) integrated from cloud base (z_b) to cloud top (z_t) is the liquid water path (W , units g m^{-2}),

$$W = \int_{z_b}^{z_t} w(z) dz. \quad (\text{A2.6})$$

Another quantity sometimes used in cloud studies is the liquid water column, the depth of a volume of liquid water that would cover any unit surface area. The liquid water column in units of microns is numerically equal to the liquid water path given in units g m^{-2} .

A2.3 Radiative Quantities

Although there have been many remote sensing studies of the optical properties of the atmosphere, inspection of the literature reveals no firm agreement over the symbols used to describe radiative and optical quantities, and also, occasionally inconsistencies arise over the meanings and the units of terms used to describe quantities of radiation themselves; for example, 'intensity' and 'radiance' are sometimes used to describe the same quantity.

The names and symbols of the radiative quantities used throughout this thesis adopt some of the conventions set out for studies in radiative transfer and atmospheric optics (*e.g.* CRC Handbook of Chemistry and Physics, 63rd ed., 1982-1983; Horvath, 1994). Also, an attempt is made here to strike a balance between the use of the quantities and symbols adopted in the review of lidar by Collis and Russell (1976), and those used in the lidar studies by Klett (1981), Fernald (1984), Young, (1995), and also by the authors of the LIRAD studies of clouds: Platt (1979) through to Platt *et al.* (1998). A summary of all the important quantities and symbols adopted for use in this thesis are presented in Appendix A1.

The primary radiative quantities are defined as follows: the radiative energy Q of n_p photons of frequency ν is,

$$Q = n_p h \nu, \quad (\text{A2.7})$$

where h is Planck's constant. The radiant flux (W) is,

$$\Phi = \frac{dQ}{dt}. \quad (\text{A2.8})$$

The radiant exitance is the radiant flux emitted by a surface ($W \text{ m}^{-2}$),

$$M = \frac{d\Phi}{dA}, \quad (\text{A2.9})$$

and the irradiance is the radiant flux intercepted by a surface ($W \text{ m}^{-2}$),

$$E = \frac{d\Phi}{dA}. \quad (\text{A2.10})$$

Intensity is the radiant flux per unit solid angle ($W \text{ sr}^{-1}$),

$$I = \frac{d\Phi}{d\omega}, \quad (\text{A2.11})$$

and the radiance, with units $W \text{ m}^{-2} \text{ sr}^{-1}$, is a measure of the intensity of a beam of radiation across a unit surface area:

$$L = \frac{dI \cos \theta}{dA}, \quad (\text{A2.12})$$

where θ is the angle between the surface vector and the direction of the beam.

The flux emittance (ϵ_f) is defined by the ratio of the radiant exitance (M) of a medium at temperature T to the radiant exitance emitted by a blackbody at the same temperature,

$$\epsilon_f = \frac{M}{M_B(T)}. \quad (\text{A2.13})$$

Similarly the beam emittance (abbreviated in this work to emittance, ϵ) is defined by the ratio of a radiance (L) emitted by a medium at a temperature T to the radiance that would be emitted in the same beam by a blackbody at the temperature T ,

$$\epsilon = \frac{L}{L_B(T)}. \quad (\text{A2.14})$$

A2.4 Basic Radiative Transfer Theory

A2.4.1 Extinction

In the following and throughout this thesis the transfer of radiation in vertical beams only is considered. The extinguishing processes of (single) scattering and absorption reduce the optical power of a beam of radiation propagating through a medium. The loss in radiant flux $d\Phi$ of a beam with irradiance E that intercepts a small surface with an extinction cross section dC_{ex} is,

$$d\Phi = -EdC_{ex}. \quad (\text{A2.15})$$

Here the surface vector of the intercepted surface is assumed parallel to the incident beam, and C_{ex} is the extinction cross section. The ratio of the extinction cross section to the geometrical cross section (G) is known as the efficiency factor for extinction (*e.g.* van de Hulst, 1981),

$$Q_{ex} = \frac{C_{ex}}{G}. \quad (\text{A2.16})$$

The loss in radiant flux $d\Phi$ in a vertically directed beam through a height dz in a small volume (dV) of a material is,

$$d\Phi = -E(z)\sigma_{ex}(z)dV. \quad (\text{A2.17})$$

where σ_{ex} is the extinction cross section per unit volume and known as the volume extinction coefficient, or equivalently, the linear extinction coefficient. Equation (A2.17) is sometimes known as Bouguer's Law, but only where the extinction is assumed to be due to absorption only. Extinction may also be described by the extinction of a beam per unit mass of a material, and the quantity used for this purpose is the mass extinction coefficient, κ_{ex} ($\text{m}^2 \text{g}^{-1}$). The mass extinction coefficient is related to the volume extinction coefficient thus,

$$\sigma_{ex}(z) = \kappa_{ex}(z)\rho(z), \quad (\text{A2.18})$$

where ρ (g m^{-3}) is the mass density of the medium.

The total extinction (σ_T) of a beam of monochromatic radiation may be separated into its various components, such as that due to absorption (σ_{ab}) and scattering (σ_{sc}), or the extinction by different types of particles (*e.g.* air molecules (σ_m) and aerosols (σ_a)): for example,

$$\sigma_T = \sigma_i + \sigma_{i+1} + \dots, \quad (\text{A2.19})$$

where the subscript ' i ' stands for the i th extinction process or particle type. Assuming the effects of multiple scattering to be negligible and proceeding from equation (A2.17), the loss in radiance of an incident beam is proportional to the incident radiance,

$$dL(z) = -L(z)\sigma_T(z)dz, \quad (\text{A2.20})$$

and the solution of this equation is,

$$L(z) = L_o \exp\left(-\int_{z_o}^z \sigma_T(z')dz'\right). \quad (\text{A2.21})$$

The integral term in equation (A2.21) is defined as the optical depth (or thickness) of the medium for radiation propagating vertically from the boundary (z_0) to a height z in the medium:

$$\tau_T(z_0, z) = \int_{z_0}^z \sigma_T(z') dz' . \quad (\text{A2.22})$$

Transmittance is defined by,

$$T_T(z_0, z) = \exp(-\tau_T(z_0, z)) . \quad (\text{A2.23})$$

For monochromatic radiation, the separation of extinction described by equation (A2.19) is easily transferred into transmittance terms:

$$T_T(z_0, z) = T_1(z_0, z) T_2(z_0, z) \dots \quad (\text{A2.24})$$

A2.4.2. Extinction by Scattering

Following the notation of Chandrasekhar (1960), a beam of radiation incident from a direction defined by $d\omega$ is scattered by an elemental volume into a direction defined by $d\omega'$, the latter defined by

$$d\omega' = \sin \theta d\theta d\phi , \quad (\text{A2.25})$$

where θ is the angle between the directions of the incident and scattered photons, and ϕ defines the azimuthal scattering direction. {Equation (A2.25) integrated over all directions delivers a value of 4π }. The loss to the radiance of an incident beam (L_i) due to scattering at a height z in a single direction ω and through an elemental volume $dAdz$ is,

$$dL(\omega) = -L_i(z) p(\omega') \frac{d\omega'}{4\pi} \sigma_{sc}(z) dz , \quad (\text{A2.26})$$

where p is the phase function and describes the intensity of the scattered radiation as a function of direction. The loss to an incident beam through an elemental volume from scattering in all directions is

$$dL = -L_i(z) \int_{\Omega} p(\omega') \frac{d\omega'}{4\pi} \sigma_{sc}(z) dz. \quad (\text{A2.27})$$

The term 4π is introduced so that the phase function is normalised to unity: (*e.g.* Chandrasekhar, 1960; van de Hulst, 1981),

$$\int_{\Omega} p(\omega') \frac{d\omega'}{4\pi} = 1. \quad (\text{A2.28})$$

The solution to equation (A2.27) is the same as equation (A2.21) and represents the loss to an incident beam due to scattering in all directions.

A2.4.3 Thermal Emission

The spectral distribution of the radiation emitted by a blackbody depends only on the temperature of the medium, and the radiance (L_B) emitted by a blackbody at temperature T , is described by the Planck function (*e.g.* Reif, 1965):

$$L_B(\nu, T) = \frac{2h\nu^3}{c^2} \frac{1}{\exp(h\nu/kT) - 1}. \quad (\text{A2.29})$$

In terms of wavelength the same function is,

$$L_B(\lambda, T) = \frac{2hc^2}{\lambda^5} \frac{1}{\exp(hc(\lambda kT)^{-1}) - 1}. \quad (\text{A2.30})$$

A2.4.4 The Equation of Radiative Transfer

The Radiative Transfer Equation (RTE) is an equation of the conservation of radiative energy in a scattering and absorbing medium. Three quantities in the RTE characterise a problem in radiative transfer: the extinction coefficient, the scattering phase function, and the emission coefficient (Chandrasekhar, 1960).

The emission coefficient (j) is defined by the product of the mass extinction coefficient (κ) with the radiance emitted into the beam (e.g. Chandrasekhar, 1960). The source function (\mathfrak{S}) is defined as,

$$\mathfrak{S} = \frac{j}{\kappa}. \quad (\text{A2.31})$$

{equation (40) of Chandrasekhar, 1960}. The differential form of the RTE can be written as,

$$-\frac{dL}{dz} = \sigma(z)L(z) - \sigma(z)\mathfrak{S}(z), \quad (\text{A2.32})$$

{equivalent to equation (47) of Chandrasekhar (1960)}, and this equation is solved by substituting

$$d\tau = \sigma(z)dz \quad (\text{A2.33})$$

into equation (A2.32) so that,

$$\frac{dL}{d\tau} + L(z) = \mathfrak{S}(z). \quad (\text{A2.34})$$

Equation (A2.34) is solved by the use of the integrating factor,

$$\exp(\tau), \quad (\text{A2.35})$$

so,

$$\frac{d(L \exp(\tau))}{d\tau} = \mathfrak{S} \exp(\tau). \quad (\text{A2.36})$$

The integral form of the RTE is obtained by integrating equation (A2.36) from z_0 to z ,

$$L(z) = L_0 \exp(-\tau(z_0, z)) + \exp(-\tau(z_0, z)) \int_{z_0}^z \mathfrak{S}(z') \exp(\tau(z_0, z')) \sigma(z') dz', \quad (\text{A2.37})$$

{cf. equation (4.11) of Measures, 1984}. This is equivalent to,

$$L(z) = L_o \exp(-\tau(z_o, z)) + \int_{z_o}^z \mathfrak{S}(z') \exp(-\tau(z', z)) \sigma(z') dz', \quad (\text{A2.38})$$

{cf. equation (50) of Chandrasekhar, 1960}.

A2.4.5 Calculation of Beam Emittance from an Absorption Profile

The downwelling radiance of a beam of radiation of wavelength λ , incident at the top of a slab consisting of a purely absorbing medium, $L(z_t)$, is diminished as radiation is absorbed by the slab. By inspection of the RTE the downwelling radiance at the base of the slab, $L(z_o)$, is related to the height profile of absorption by,

$$L(z_o) = \int_{z_o}^{z_t} L_B(z) \exp\left(-\int_{z_o}^z \sigma_\lambda(z') dz'\right) \sigma_\lambda(z) dz + L(z_t) \exp\left(-\int_{z_o}^{z_t} \sigma_\lambda(z'') dz''\right). \quad (\text{A2.39})$$

From Kirchoff's Law, the radiative energy of wavelength λ that is emitted by the slab is given by,

$$\varepsilon_\lambda = 1 - \exp(-\tau_\lambda(z_t, z_o)), \quad (\text{A2.40})$$

where ε_λ is the beam (absorption) emittance and equal to the radiative energy absorbed by the slab, and τ_λ is the (absorption) optical depth of the slab determined from the height profile of σ_λ . Thus, as ε_λ is defined here, {as in the previous LIRAD studies: Platt (1979) through to Platt *et al.*, 1998}, the emittance of the slab can be determined from the slab temperature and the downward radiance at the base of the slab. The influence of scattering on cloud infrared optical properties is discussed in section A2.6.7.

A2.5 Absorption of Electromagnetic Radiation by Air Molecules

A2.5.1 Introduction

The absorption of electromagnetic radiation by air molecules occurs by the conversion of incident radiative energy to internal energy of the absorbing molecules. The absorption of electromagnetic radiation by specific atoms and molecules is observed to occur over very narrow regions of the spectrum (spectral lines), and the positions of these lines in the spectrum can be determined by

quantum mechanics (*e.g.* Herzberg, 1950). In the ultraviolet, visible and near-infrared regions of the spectrum ($\approx 10 \text{ nm} < \lambda < 1 \text{ }\mu\text{m}$) the absorption of light is due to transitions between the electronic levels. Absorption that occurs in the infrared region of the spectrum ($\approx 1 \text{ }\mu\text{m} < \lambda < 100 \text{ }\mu\text{m}$) is due to transitions between the vibrational-rotational modes of molecules. Absorption in the far-infrared to the microwave region of the spectrum ($\approx 100 \text{ }\mu\text{m} < \lambda < 1 \text{ cm}$) is due to transitions between rotational states of molecules (Goody and Yung, 1989).

The spectral lines of absorption have linewidths that depend on natural broadening, collision broadening and Doppler broadening, and by treating the collision and Doppler broadening independently the broadening due to both these effects is often determined by calculating Voigt line profiles (*e.g.* Goody and Yung, 1989; Vaughan, 1989).

A2.5.2 Absorption of Visible and Infrared (10 - 12 μm) Radiation by Air Molecules

Ozone (O_3) is a significant absorber of visible light in the atmosphere due to the Chappuis absorption bands that cause absorption between the wavelengths 450 - 750 nm. However most ozone exists in the stratosphere so the absorption by ozone near sea level is slight. For example, the study by Elterman (1964) shows that from sea level to an altitude of 2 km, the absorption coefficient of O_3 is 0.7% of the Rayleigh scattering extinction coefficient for the wavelength 500 nm, and 2.8% for the wavelength 550 nm. (Rayleigh scattering is treated in section A2.6). Thus the absorption by O_3 is negligible for visible Nd:YAG laser (532 nm) lidar studies of the lower troposphere. The absorption of this light by water vapour and oxygen also was assumed to be negligible for the work of this thesis.

Some of the spectral absorption lines in the near-infrared region of the spectrum are close to the fundamental Nd:YAG laser wavelength of 1.064 μm . However in the analysis of the 1.064 μm laser measurements for this thesis the molecular absorption properties were not required to be known, only that the absorption be slight and any variations random. {Some variations in the molecular absorption of near-infrared radiation may be expected due to variations in the water vapour column; *e.g.* see Figure 3.1 of Zuev (1976)}.

In the infrared (10 - 12 μm) wavelength region of the spectrum most of the molecular absorption is due to H_2O (*e.g.* Platt *et al.*, 1984). There is strong absorption by H_2O in a band centred

at 6.3 μm , and very strong absorption near 20 μm and above (*e.g.* Zuev, 1976). The water vapour continuum absorption between 7 - 20 μm is not fully understood (*e.g.* Goody and Yung, 1989). At least some of this absorption is due to water vapour dimers (Gebbie *et al.*, 1969). Platt *et al.* (1998) determined the absorption by dimers to constitute 85% of the 10 - 12 μm absorption by water vapour in a tropical atmosphere.

There is some absorption by CO_2 due to the twin vibrational-rotational bands centred at about 10.6 μm , as well as some absorption by O_3 due to the wing of a strong band centred near 9.6 μm (*e.g.* Herzberg, 1950; Zuev, 1976). However for infrared (10 - 12 μm) radiometer measurements the emission by these gases is small, and in this band measured infrared radiances of cloud-free atmospheres are assumed due to water vapour only (Platt *et al.*, 1984; Platt *et al.*, 1998).

A2.6 Rayleigh Scattering by Air Molecules

A2.6.1 Introduction

Rayleigh scattering theory is the classical theory of elastic scattering of electromagnetic radiation by small oscillating dipoles, and is used to describe the light scattering by air molecules (*e.g.* Chandrasekhar, 1960; McCartney, 1976; van de Hulst, 1981). Basic Rayleigh scattering theory is used to determine the radiation emitted by a non-ionised, non-polar, isotropic, linear, and lightly damped dipole oscillator (*e.g.* McCartney, 1976). For the condition of light damping the incident field should penetrate the particle quickly, or $mx \ll 1$, and also the scattering dipoles are assumed small compared to the incident radiation so the following condition should exist: $x \ll 1$ (van de Hulst, 1981). That is, the whole molecule is assumed to be in a uniform electromagnetic field.

A2.6.2 The Rayleigh Scattering Coefficients

The geometry of scattering is defined here as follows: the positive x-axis is aligned with the direction of the incident (polarised) radiation, and the z-axis is aligned with the electric vector of the incident radiation. The variation of the intensity of the scattered light with direction can be described by the angular scattering coefficient,

$$I(\theta, \phi) = E_o \frac{dC_{sc}(\theta, \phi)}{d\omega}, \quad (\text{A2.41})$$

where θ is the angle between the x-axis and the z-component of the scattering direction, and ϕ is the angle between the x-axis and the y-component of scattering.

The Rayleigh angular scattering coefficient can be shown to be,

$$\frac{dC_R(\theta)}{d\omega} = \frac{\pi^2(n^2 - 1)^2}{N^2 \lambda^4} \cos^2 \theta, \quad (\text{A2.42})$$

(e.g. Measures, 1984), where n is the real part of the complex refractive index of the molecules, N is the concentration of the molecules (units m^{-3}), and λ is the wavelength of the incident radiation. This formulation (A2.42) is an approximation based on the assumption that the refractive index of air is unity (e.g. for standard air $n = 1.000293$ for light of wavelength 550 nm; McCartney, 1976).

The phase function for Rayleigh scattering of polarised light is toroidal with the major axis of the torus parallel to the electric polarisation vector of the incident radiation - so the azimuthal scattering angle (ϕ) has been dropped from equation (A2.42) as the phase function is independent of ϕ .

The volume angular scattering coefficient for polarised light is,

$$\beta_{sc}(\theta) = N \frac{dC_{sc}(\theta)}{d\omega}, \quad (\text{A2.43})$$

so from equation (A2.42), for Rayleigh scattering by air molecules:

$$\beta_R(\theta) = \frac{\pi^2(n^2 - 1)^2}{N\lambda^4} \cos^2 \theta, \quad (\text{A2.44})$$

A quantity important for lidar studies is the volume molecular backscattering coefficient (β_m) which is equivalent to $\beta_R(\pi)$ of (A2.44). The volume scattering coefficient is obtained by integrating equation (A2.44) over all solid angles from which the Rayleigh scattering extinction coefficient is determined:

$$\sigma_R = \frac{8\pi^3(n^2 - 1)^2}{3N\lambda^4}. \quad (\text{A2.45})$$

A2.6.3 Calculation of Attenuated Molecular Backscatter for Lidar Calibration

The method developed by Young (1995) was used for the lidar calibration of the SOCEX1 measurements, (see section 4.3.2), and this method required a known height profile of the attenuated molecular backscatter coefficient. To calculate this profile aerological data were used to determine the molecular concentration (N) with height from which the molecular backscatter (β_m) and extinction coefficients (σ_m) were calculated by the Rayleigh scattering theory.

An example of these molecular scattering coefficients is computed in the following. Employing the equation of state for an ideal gas the number density of molecules at a height z is,

$$N(z) = \frac{1}{k} \frac{P(z)}{T(z)}, \quad (\text{A2.46})$$

where k is the Boltzmann constant, P is the air pressure (Pa), and T is the air temperature (K). At sea level (in standard air),

$$N = \frac{1}{1.380622 \times 10^{-23}} \frac{1.01325 \times 10^5}{(273.15 + 15)} \approx 2.55 \times 10^{25} \text{ m}^{-3}. \quad (\text{ex. A246})$$

Standard air has a refractive index of about 1.000 277 46 for light of the wavelength 532 nm, (CRC Handbook, 63rd Ed.). Substituting these values of N and n into equation (A2.44) gives,

$$\beta_m = \frac{\pi^2 (1.00027746^2 - 1)^2}{2.55 \times 10^{25} \times (532 \times 10^{-9})^4} = 1.488 \times 10^{-6} \text{ m}^{-1} \text{ sr}^{-1}, \quad (\text{ex. A244})$$

and for the molecular extinction coefficient, from equation (A2.45),

$$\sigma_m = \frac{8\pi^3 (1.00027746^2 - 1)^2}{3 \times 2.55 \times 10^{25} \times (532 \times 10^{-9})^4} = 1.247 \times 10^{-5} \text{ m}^{-1}. \quad (\text{ex. A245})$$

Assuming that the Rayleigh angular backscattering cross section {see equation (A2.42)} is constant with height over the limited range of heights studied for this thesis, (the lowest 3 km of the atmosphere), and using equations (A2.44), (A2.45) and (A2.46), a height profile of the attenuated molecular backscatter coefficient is calculated for the lidar calibration as follows:

$$M(z) \equiv z^{-2} \beta_m(z) T_m(z_o, z). \quad (\text{A2.47})$$

$T_m(z_o, z)$ is the molecular transmittance between the heights z_o and z . Another useful quantity for the analysis of lidar returns is the molecular extinction-to-backscatter ratio (S_m), obtained by dividing equation (A2.45) by equation (A2.44):

$$S_m = \frac{\sigma_R}{\beta_R(\pi)} = \frac{8\pi}{3} = 8.378 \text{ sr}. \quad (\text{A2.48})$$

A2.7 Optical Properties of Spherical Aerosols and Cloud Droplets

A2.7.1 Introduction

Rayleigh theory is valid for small scatterers when the whole scatterer can be assumed to be in a uniform electromagnetic field. In this case the cluster of closely spaced molecules in a small droplet of liquid, for example, all vibrate in phase as the incident wave propagates through the droplet. As the droplet increases in size, variations in the electric field across the droplet become important. In this case the scattering can be described by the Mie theory – the formal solution of Maxwell's equations for the scattering of a planar electromagnetic wave by homogeneous spheres (*e.g.* Deirmendjian, 1969; Wiscombe, 1980; van de Hulst, 1981).

It is noted that for the scattering of visible light by air molecules, the size parameter (x) (A2.2) is approximately 0.01 ($x \ll 1$, as required for the application of the Rayleigh scattering theory determined by van de Hulst (1981)). In this thesis the Mie scattering theory is used to describe the scattering of visible light (532 nm) by spherical marine aerosols, (*e.g.* for a typical aerosol radius of 0.1 μm and for $\lambda = 532 \text{ nm}$, $x \approx 1.2$), and cloud droplets (*e.g.* for a typical droplet radius of 10 μm and for $\lambda = 532 \text{ nm}$, $x \approx 120$). Also, the Mie theory is used here to determine the amounts of scattering and absorption of terrestrial infrared (10 - 12 μm) radiation by cloud droplets, (*e.g.* for a typical droplet radius of 10 μm and for $\lambda = 10 - 12 \mu\text{m}$, $x \approx 6.3 - 7.5$).

Deirmendjian (1969) presented the Mie solution in a form readily transferrable to a computer algorithm, and improvements to the efficiency of computer calculations were made by Wiscombe (1980). Computer code based on the work of these authors was used to calculate the *in situ*

optical properties of the stratocumulus clouds, (section 4.2.1), and to calculate the optical properties of the marine aerosols as part of the calibration of the SOCEX1 lidar measurements (section 4.3.2).

An outline of the Mie scattering theory is given in section A2.7.2 of this appendix, and commonly used optical properties of clouds are given in section A2.7.3. Examples of Mie scattering cross sections are given for marine aerosols in section A2.7.4. Some basic microphysical properties of clouds are presented in section A2.7.5. A preview of the Mie properties of marine stratocumulus clouds is given in section A2.7.6, and a brief investigation into the infrared properties of water droplet clouds is given in section A2.7.7.

A2.7.2 The Mie Theory of Scattering of Electromagnetic Radiation by Spheres

There are three radiation fields to consider in the Mie solution: the incident planar wave, the radiation that penetrates the sphere, and the scattered radiation outside the sphere. A perfect boundary is assumed between the radiation inside and outside the sphere, and all the waves are expressed in terms of spherical co-ordinates with the origin at the centre of the sphere. The Mie solution describes the vector amplitude of the resultant field both inside and outside the sphere (*e.g.* Deirmendjian, 1969).

The major results of the Mie theory are the Mie coefficients: the Mie coefficients a_n and b_n are functions of the size parameter and refractive index only, and employ the Ricatti-Bessel functions and their derivatives. The angular coefficients π_n and τ_n are functions of scattering angle only and employ the Legendre polynomials and their derivatives (Note that the symbol τ_n used here should not be confused with the optical depth). Expressed in terms of the Mie coefficients the cross section for the backscatter coefficient is described by, (*e.g.* Deirmendjian, 1969),

$$\frac{dC(m, x, \pi)}{d\omega} = \frac{4}{x^2} \sum_{n=1}^{\infty} (-1)^n \frac{(2n+1)}{2} (a_n - b_n), \quad (\text{A2.49})$$

and the volume scattering coefficient,

$$C_{sc}(m, x) = \frac{2\pi a^2}{x^2} \sum_{n=1}^{\infty} (2n+1) (|a_n|^2 + |b_n|^2). \quad (\text{A2.50})$$

The extinction coefficient is described by,

$$C_{ex}(m, x) = \frac{2\pi a^2}{x^2} \operatorname{Re} \left\{ \frac{1}{2} \sum_{n=1}^{\infty} (2n+1) \operatorname{Re} \{ a_n + b_n \} \right\}. \quad (\text{A2.51})$$

A2.7.3 Mie Properties of Polydispersions

The Mie efficiency factors (Q) are commonly used for calculations of the optical properties of aerosols and cloud particles. The Mie backscatter efficiency (Q_β) is determined from the angular scattering cross section,

$$Q_\beta = \frac{dC(\pi)}{d\omega} \frac{1}{\pi a^2}, \quad (\text{A2.52})$$

and the extinction efficiency (Q_{ex}) is defined by,

$$Q_{ex} = \frac{C_{ex}}{\pi a^2}. \quad (\text{A2.53})$$

The scattering efficiency is defined similarly. The absorption efficiency is determined by,

$$Q_{ab} = Q_{ex} - Q_{sc}. \quad (\text{A2.54})$$

The volume scattering and extinction coefficients for polydispersions of spheres are then computed via the Mie efficiencies. The volume backscatter coefficient for a polydispersion of particles is,

$$\beta = \int_0^{\infty} Q_\beta(x, m, \pi) \pi a^2 N(a) da, \quad (\text{A2.55})$$

where $N(a)$ is the number density of the particles per unit particle radius, and describes the size distribution of the spherical particles of radii a . Similarly the volume extinction coefficient for a polydispersion of particles is,

$$\sigma_{ex} = \int_0^{\infty} Q_{ex}(x, m) \pi a^2 N(a) da. \quad (\text{A2.56})$$

The volume scattering and absorption coefficients are expressed likewise.

Three important parameters often used for studies of the optical properties of clouds (*e.g.* Slingo and Schrecker, 1982), and which may be obtained from the Mie theory are: (1) the (single scattering) extinction optical depth of the cloud,

$$\tau_{ex} = \int_{z_b}^{z_t} \sigma_{ex}(z) dz, \quad (\text{A2.57})$$

where z_b is the height of cloud base and z_t the height of cloud top, (2) the single scattering albedo (ω),

$$\omega = \frac{\sigma_{sc}}{\sigma_{ex}}, \quad (\text{A2.58})$$

and (3) the asymmetry parameter (g), which is calculated from the phase function by,

$$g = \frac{1}{2} \int_{-1}^1 \frac{p}{4\pi}(m, \cos \theta, \lambda) \cos \theta d \cos \theta, \quad (\text{A2.59})$$

(*e.g.* cf. equation (10) of Stephens, 1979). The asymmetry parameter describes the degree of forward scattering of a polydispersion of particles: for example, for scattering only in the forward direction $g = 1$, and for isotropic scattering $g = 0$. For water droplet clouds, in the visible region of the spectrum g lies between about 0.82 - 0.86 (Stephens, 1979). In the infrared (10 - 12 μm) region of the spectrum g lies between about 0.85 - 0.90 (Stephens, 1979).

A2.7.4 Mie Properties for Scattering of Visible (532 nm) Light by Stratocumulus Cloud Droplets

The radii of water droplets in marine cumuliform and stratiform clouds typically range up to 100 μm (*e.g.* Pruppacher and Klett, 1997). The *in situ* measurements of marine stratocumulus clouds by Boers *et al.* (1996) and Boers *et al.* (1998) showed that the majority of the droplets in these clouds had radii ranging from 1 - 20 μm with a typical mode radius of 10 μm . There were fewer numbers of larger droplets (drizzle), and typically their radii were confined to the range 20 - 400 μm .

For the wavelength of 532 nm, the Mie extinction and backscatter efficiencies for water droplets with radii ranging from 1 - 20 μm are shown in Figure A2.1. Mie efficiencies for water droplets with radii ranging from 1 - 100 μm are shown in Figure A2.2.

Mie Efficiencies for Water Droplets (532 nm)

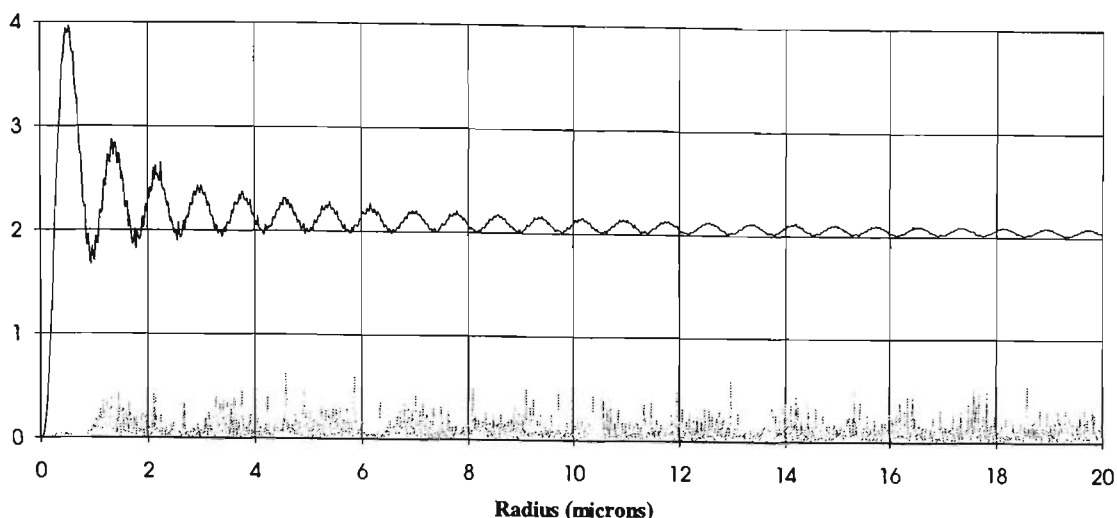


Figure A2.1. Mie extinction efficiencies over a range of radii that covers the majority of the droplets observed in stratocumulus clouds, for the Nd:YAG laser wavelength of 532 nm. The upper curve is the extinction efficiency (Q_{ex}), and the lower (and noisy) curve is the backscatter efficiency (Q_{β}).

To gain some insight into the optical properties of stratocumulus clouds, a rectangular droplet size distribution was modelled with $N' = 40 \text{ cm}^{-3}$, (typical of the marine stratocumulus clouds measured during SOCEX1). The droplet radii of the modelled distribution ranged from 8 - 12 μm to cover the typical mode radius of 10 μm . From the equations (A2.55) and (A2.56) the volume backscatter (β) and extinction (σ_{ex}) coefficients were calculated via the trapezoidal rule, using the 200 Q values obtained between the radii of 8 - 12 μm (shown in Figure A2.1). For this simple modelled cloud droplet size distribution $\sigma_{ex} = 2.65 \times 10^{-2} \text{ m}^{-1}$ and $\beta = 1.43 \times 10^{-3} \text{ m}^{-1} \text{ sr}^{-1}$. The values of σ_{ex} and β determined for the simple model give an extinction-to-backscatter ratio (S) of 18.5 sr. The larger drizzle droplets have only a small effect on the cloud visible optical properties because of their much smaller concentrations, so the visible optical properties of drizzle droplets were not investigated here.

Note that Q_{ex} approaches approximately 2 as the radii increase (Figures A2.1 and A2.2): using $Q_{ex} = 2$, the visible extinction of the simple modelled droplet distribution described above is $2.55 \times 10^{-2} \text{ m}^{-1}$, a figure near to that obtained using the exact Q values (see above). The approximation $Q_{ex} = 2$ is the basis of the following parameterisations commonly used in studies of the optical properties of clouds:

Mie Efficiencies for Water Droplets (532 nm)

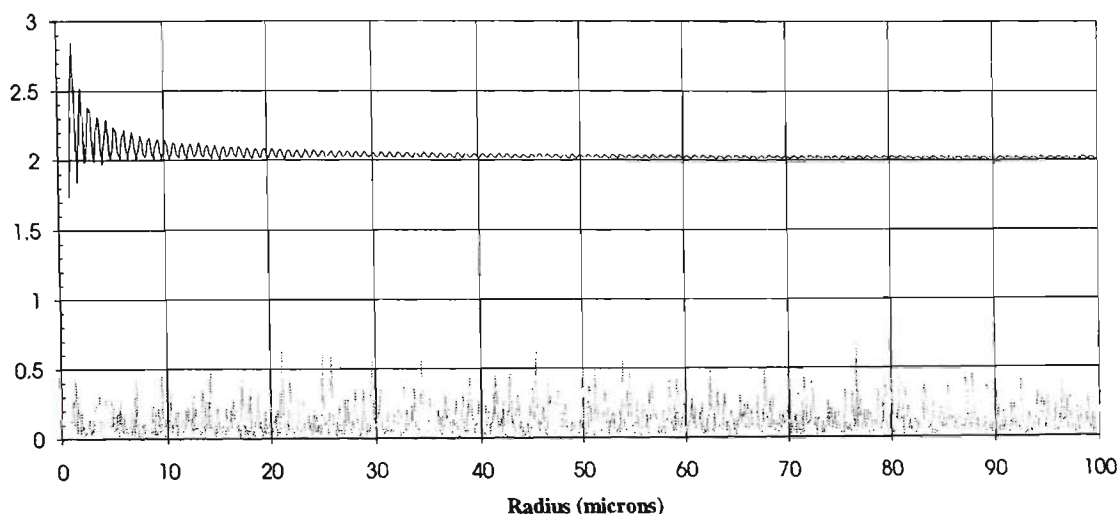


Figure A2.2. Mie extinction efficiencies over a range of radii that covers cloud and the smaller drizzle droplets, for the Nd:YAG laser wavelength of 532 nm. The upper curve is the extinction efficiency (Q_{ex}), and the lower (noisy) curve is the backscatter efficiency (Q_{β}).

$$\sigma_{ex} = \frac{3w}{2\rho a_{eff}}, \quad (\text{A2.60})$$

(e.g. Paltridge and Platt, 1976), and,

$$\tau = \frac{3W}{2\rho a_{eff}}, \quad (\text{A2.61})$$

(e.g. Slingo, 1990). These parameterisations are obtained by using the equations (A2.56), (A2.4), (A2.5) and (A2.6).

A2.7.5 Infrared (10 - 12 μm) Scattering in Water Droplet Clouds and Emittance

The ground-based infrared radiometers used during SOCEX measured downward radiances from stratocumulus clouds. The wavelength bands of the infrared radiometer measurements of the stratocumulus clouds during SOCEX1 and SOCEX2 were $10.84 \pm 1 \mu\text{m}$ and $10.86 \pm 0.50 \mu\text{m}$ respectively (see Chapter 3). The measured cloud infrared radiances contained strong signals due to the strong thermal emission by warm liquid water droplets in the low clouds. Using the Mie theory

and some basic radiative transfer, the effects of scattering on the derived cloud infrared properties is discussed in the following.

The Mie absorption and scattering efficiencies of water droplets in the 10 - 12 μm region of the spectrum are of comparable magnitudes {see Figure (A2.3)}, so the probability of the scattering of a photon by a droplet is about as equally likely as absorption. {This probability is given by the single scattering albedo, ω ; see (A2.58)}. Values of ω for a monodispersion (or a single droplet) in the infrared region of the spectrum are shown in Figure (A2.4), for the wavelengths 10 μm , 10.85 μm , 11 μm and 12 μm .

The effects of scattering on the downward measured infrared radiances, and therefore the calculated absorption optical depths, however, are small. The reason for this is that the phase function of a cloud droplet (typical radius 10 μm) is strongly peaked in the forward direction. This is illustrated in Figure A2.5, for Deirmendjian's (1969) modelled C1 and C2 water droplet clouds. As mentioned previously the forward-peaked phase functions of water droplet clouds result in asymmetry parameters of approximately 0.85 (*e.g.* Stephens, 1979; Stephens, 1984). Because of the high degree of forward scattering much of the scattered radiation remains in directions close to the original beam. The radiation scattered out of the beam is largely balanced by radiation scattered into the beam ('internal scattering'), so that it is sometimes assumed to be negligible (*e.g.* Platt, 1979). The small contribution of the resultant internal scattering to infrared cloud radiances, combined with the slight backscatter by clouds in the infrared (see the plot of $4\pi Q_B$ in Figure A2.3), is the basis of the absorption approximation (*e.g.* Paltridge and Platt, 1976; Platt, 1976). However the absorption approximation was not used in this thesis nor in previous LIRAD studies {Platt (1979) through to Platt *et al.* (1998)}. Instead, estimates of the infrared radiances due to scattering are calculated and subtracted from the total measured radiances. The remaining radiances are due to absorption only, from which the infrared absorption optical depths (τ_i) are calculated. The infrared absorption emittance (ϵ_i) is then defined by,

$$\epsilon_i = 1 - \exp(-\tau_i), \quad \{\text{cf. equation (A2.40)}\}$$

Here the subscript 'i' stands for infrared. It is noted that as,

$$\tau_i \rightarrow \infty, \quad \varepsilon_i \rightarrow 1.$$

(A2.62)

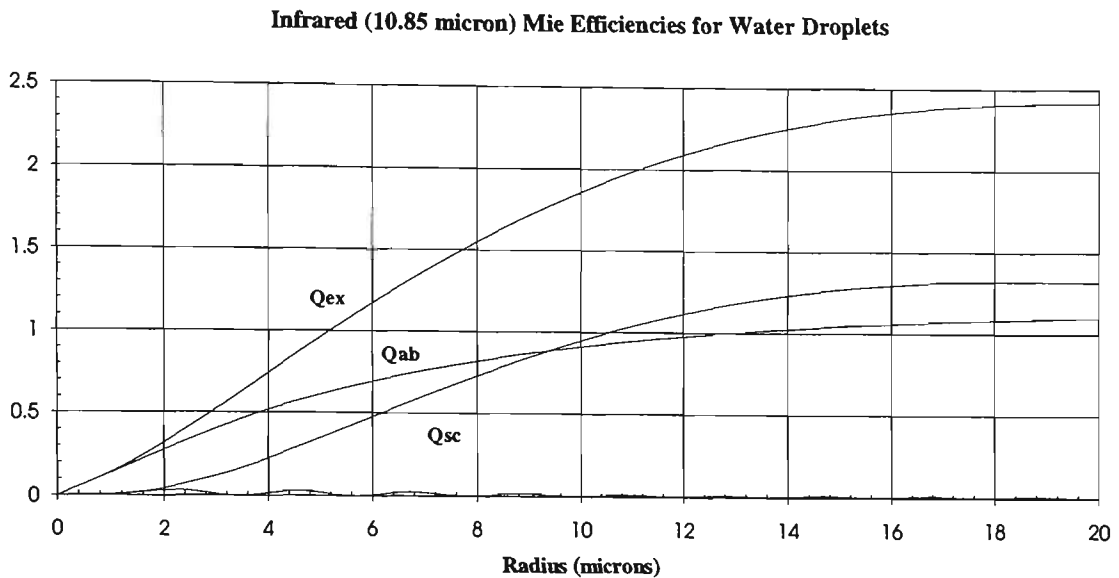


Figure A2.3. Mie efficiencies at $\lambda = 10.85 \mu\text{m}$ for water droplets of radius a . The top curve is the extinction efficiency (Q_{ex}). For $a < 1 \mu\text{m}$ nearly all the infrared extinction by water droplets is due to absorption, as here $Q_{\text{ab}} \approx Q_{\text{ex}}$. At $a \approx 2 \mu\text{m}$ the scattering efficiency (Q_{sc}) begins to increase until at $a \approx 10 \mu\text{m}$ about half of the extinction is due to scattering. The lower oscillating curve is $4\pi \text{ (sr)} \times Q_{\beta}$.

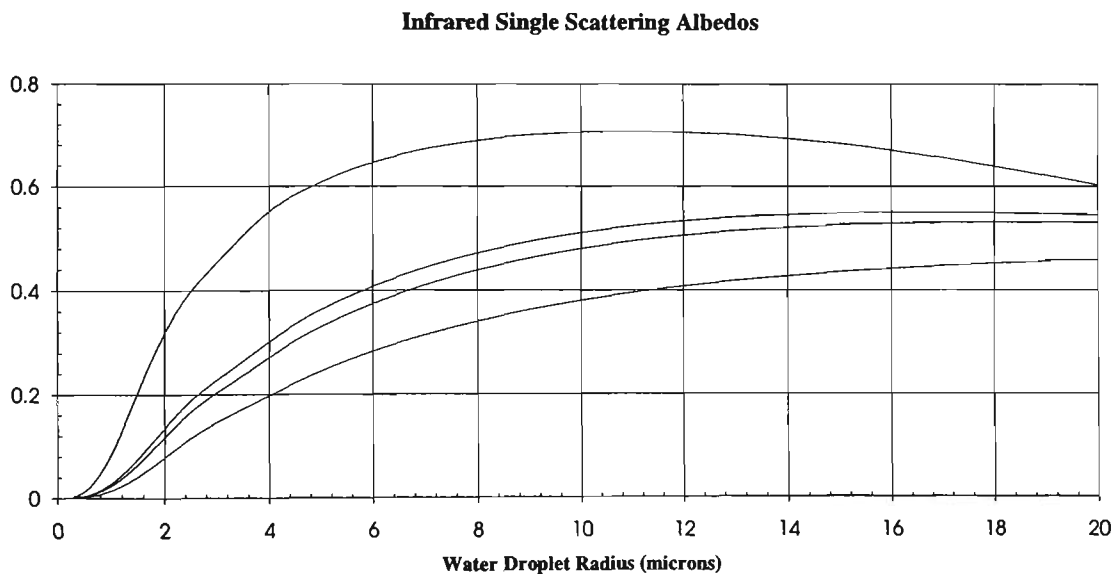


Figure A2.4. Single scattering albedos (ω) for monodispersions (or single droplets) of radii a . At $a = 10 \mu\text{m}$, from top to bottom, the 4 curves are for the 4 wavelengths: $\lambda = 10 \mu\text{m}$, $10.85 \mu\text{m}$, $11 \mu\text{m}$, and $12 \mu\text{m}$.

Infrared Scattering by Water Clouds

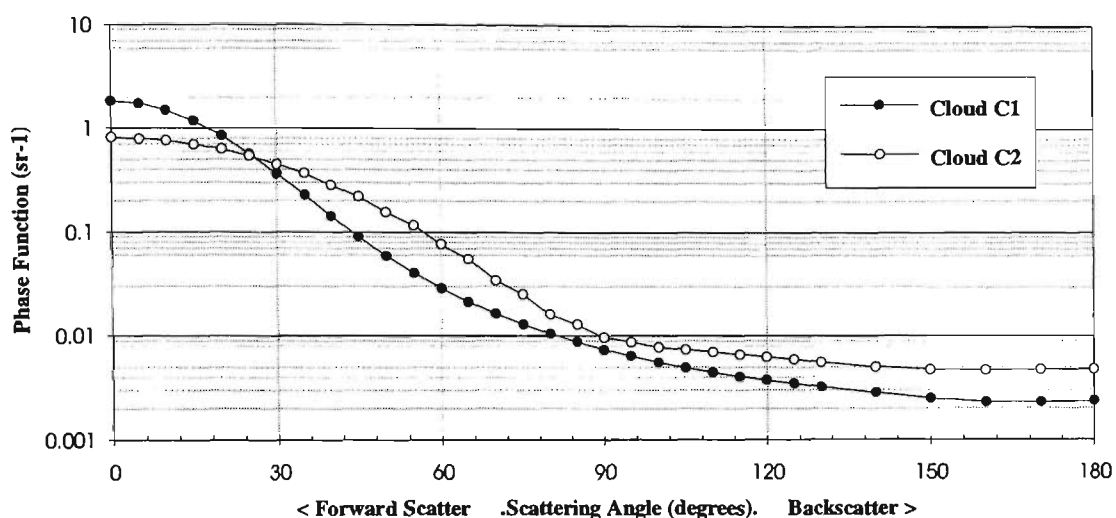


Figure A2.5. Phase functions for the wavelength $10\ \mu\text{m}$ calculated by Deirmendjian (1969) for the two modelled water droplet clouds *C1* and *C2*. Some of the results for scattering angles $< 90^\circ$ (in the backward hemisphere) for cloud *C2* have been linearly interpolated.

However the cloud infrared emittance, (symbol ε with subscript 'i' dropped), includes the effects of scattering and is defined as,

$$\varepsilon = 1 - \exp(-\tau_i) - (s + r), \quad (\text{A2.63})$$

where r is the quantity of radiant energy reflected downwards from the cloud, and s is the contribution to the downward beam due to internal scattering in the cloud. In a very thick cloud, where it may be expected that $s \approx 0$, as,

$$\tau_i \rightarrow \infty, \quad \varepsilon \rightarrow 1 - r. \quad (\text{A2.64})$$

Theoretical studies of the infrared radiative transfer in clouds shows that water clouds are only slightly reflective in the infrared. For example, theoretical studies show the reflectance of thick water clouds is approximately 5% (e.g. Yamamoto *et al.*, 1970). Thus by the definition (A2.63) the maximum emittance that may be expected from thick water droplet clouds is approximately 0.95.

A2.7.6 Cloud Infrared Optical Properties and Liquid Water Properties

Cloud liquid water paths (W), (units $\text{g}\cdot\text{m}^{-2}$), can be retrieved by microwave radiometer (*e.g.*, Hogg *et al.*, 1983; Boers, 1996a; Boers, 1996b; Boers and O'Brien 1996). This section investigates the relationship between cloud infrared (10 - 12 μm) optical depths (τ_i) and cloud liquid water paths (W).

Combining the expressions for the liquid water content, w , equation (A2.5), the infrared mass absorption coefficient (κ_i), {see equation (A2.18)}, and the infrared absorption coefficient for a polydispersion of droplets, {see equation (A2.56)}, κ_i (m^2g^{-1}) for a polydispersion of droplets is,

$$\kappa_i = \frac{3}{4\rho} \frac{\int_0^\infty a^2 Q_i(a) n(a) da}{\int_0^\infty a^3 n(a) da} \quad (\text{A2.65})$$

In this equation Q_i is the Mie efficiency for infrared absorption by water droplets (*e.g.*, see Figure A2.3). The value of Q_i increases approximately linearly with radius for droplet radii less than about 14 μm , so a gradient of $a_i = 0.105 \mu\text{m}^{-1}$ was determined by a fit by eye to the curve of Q_i vs. droplet radius. This value of a_i results in an error in Q_i (10.84 μm) of less than 25% for droplet radii between 2.5 μm and 10 μm , and the error is zero for a droplet radius of just over 7 μm . It is evident from equation (A2.62) that if the Mie absorption efficiency is approximated in this way, then, for small droplets, the following approximations could be used, (*e.g.* Platt, 1976):

$$\kappa_i = \frac{3a_1}{4\rho}, \quad (\text{A2.66})$$

and the infrared absorption coefficient is given by,

$$\sigma_i = \frac{3a_1 w}{4\rho}. \quad (\text{A2.67})$$

Note that in (A2.64) σ_i is calculated without any information about the cloud droplet size distribution.

Following from equation (A2.64), the infrared absorption optical depth (τ_i) may be related to W by,

$$\tau_i = \frac{3a_1 W}{4\rho}. \quad (\text{A2.68})$$

The value of Q_i is nearly constant for water droplets of radii greater than approximately 13 μm (e.g., for radii between 10 - 100 μm , $Q_i = 1.08$; see Figure A2.3). If Q_i is approximated by a constant a_2 then from equation (A2.62), (e.g. Chylek and Damiano, 1992),

$$\kappa_i = \frac{3a_2}{4\rho a_{\text{eff}}}, \quad (\text{A2.69})$$

thus,

$$\sigma_i = \frac{3a_2 w}{4\rho a_{\text{eff}}}, \quad (\text{A2.70})$$

and finally,

$$\tau_i = \frac{3a_2 W}{4\rho a_{\text{eff}}}. \quad (\text{A2.71})$$

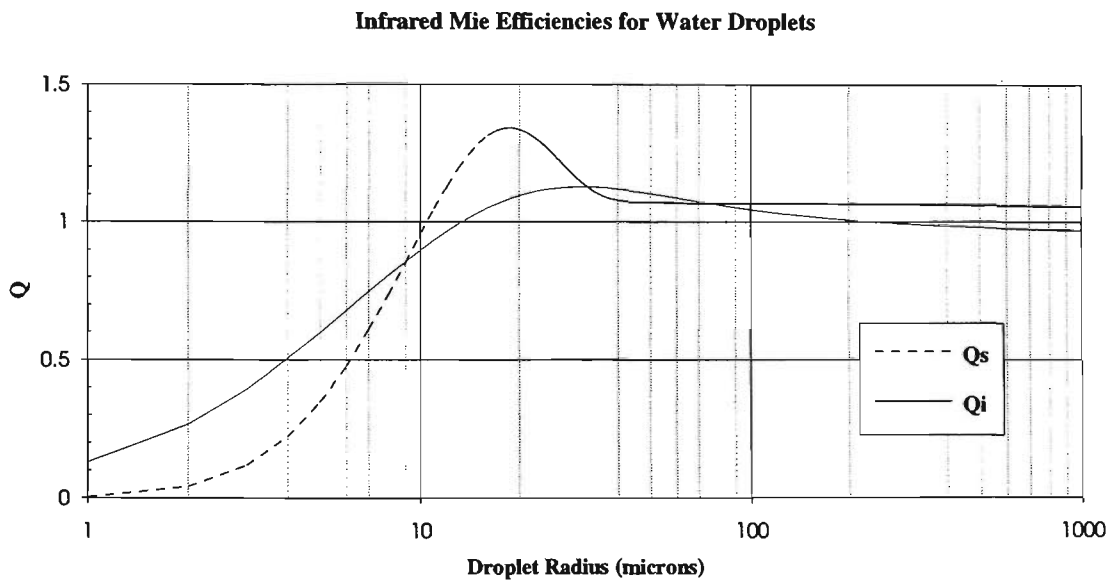


Figure A2.6. Infrared (10.84 μm) Mie efficiencies for large cloud droplets, for absorption (Q_i , solid line) and scattering (Q_s , dashed line) versus droplet radius (a). The Mie efficiencies are nearly constant for a $> 13 \mu\text{m}$.

Appendix A3. Derivations of Solutions to the Lidar Equation

A3.1. The Lidar Equation and Basic Quantities

The system-independent and range-corrected lidar equation used throughout this thesis is,

$$\chi(z) = \beta(z)T^2(0, z), \quad (\text{A3.1})$$

where β is the volume backscatter coefficient ($\text{m}^{-1} \text{sr}^{-1}$) and $T^2(0, z)$ is the two-way transmittance between the lidar and height z . Expanded, $T^2(0, z)$ may be written as,

$$T^2(0, z) = \exp(-2\eta\tau(0, z)), \quad (\text{A3.2})$$

where τ is the optical depth of the atmosphere between the lidar and the height z , and η is the multiple scatter factor. {For this definition of η see Platt (1981)}. The optical depth is expanded in terms of the volume extinction coefficient (σ) thus:

$$\tau(0, z) = \int_0^z \sigma(z') dz'. \quad (\text{A3.3})$$

A3.2. Solution for a Homogeneous Atmosphere (The Slope Technique)

Expanding (A3.1) and assuming a single scattering species, *e.g.* cloud particles only, a profile of χ between cloud base z_b and height z is described by,

$$\chi(z) = \beta(z) \exp\left(-2\eta \int_{z_b}^z \sigma(z') dz'\right). \quad (\text{A3.4})$$

The logarithmic variable is formed,

$$\zeta(z) \equiv \ln(\chi(z)), \quad (\text{A3.5})$$

so that,

$$\zeta(z) = \ln(\beta(z)) - 2\eta \int_{z_b}^z \sigma(z') dz'. \quad (\text{A3.6})$$

Differentiating with respect to z and rearranging gives,

$$\frac{d\beta(z)}{dz} - \beta(z) \left(\frac{d\zeta(z)}{dz} + 2\eta\sigma(z) \right) = 0. \quad (\text{A3.7})$$

In a homogeneous atmosphere where the backscatter coefficient is constant with range,

$$\sigma = -\frac{1}{2\eta} \frac{d\zeta(z)}{dz}. \quad (\text{A3.8})$$

A3.3. Solution for an Inhomogeneous Atmosphere (Logarithmic Variable)

If a power law relationship is assumed between σ and β ,

$$S = \frac{\sigma^g}{\beta}, \quad (\text{A3.9})$$

then equation (A3.9) combined with equation (A3.7) gives,

$$\frac{d\sigma(z)}{dz} - \frac{\sigma(z)}{g} \frac{d\zeta(z)}{dz} = \frac{2\eta}{g} \sigma^2(z). \quad (\text{A3.10})$$

This is a form of the Bernoulli equation with the solution,

$$\sigma(z) = \frac{\exp((\zeta(z) - \zeta_n)/g)}{\sigma_n^{-1} - \frac{2\eta}{g} \int_{z_n}^z \exp((\zeta(z') - \zeta_n)/g) dz'}, \quad (\text{A3.11})$$

(e.g. Klett, 1981). The boundary value σ_n is the extinction at a near-point range z_n ; i.e., $\sigma_n \equiv \sigma(z_n)$.

The more stable backward (or inward) solution, often referred to in the literature as the 'Klett solution', is formed by reversing the direction of integration:

$$\sigma(z) = \frac{\exp((\zeta(z) - \zeta_d)/g)}{\sigma_d^{-1} + \frac{2\eta}{g} \int_z^{z_d} \exp((\zeta(z') - \zeta_d)/g) dz'}. \quad (\text{A3.12})$$

Here the subscript 'd' refers to a distant calibration range z_d .

A3.4. Solutions for Inhomogeneous Atmospheres (Linear Variable)

If σ is assumed linearly proportional to β , *i.e.*, the exponent in equation (A3.9) is assumed equal to unity, a different approach can be used to derive expressions for β and σ from the lidar equation as done by, for example, Fernald *et al.* (1972) and Fernald (1984). The derivation for the simple case of a single scattering species is presented here first, followed by the more complicated derivation for an atmosphere with two scattering components.

The transmittance term of the lidar equation (A3.1) is separated into two parts at a near-point calibration range z_n ,

$$\chi(z) = \beta(z) T^2(0, z_n) T^2(z_n, z). \quad (\text{A3.13})$$

It is desired to invert the following form of the lidar equation for β :

$$\beta(z) = \frac{\chi(z)}{T^2(0, z_n) T^2(z_n, z)}. \quad (\text{A3.14})$$

The first transmittance term in the denominator of (A3.14) is a constant, and the remaining problem is the elimination of the second transmittance parameter. Expanded, the second transmittance term is,

$$T^2(z_n, z) = \exp\left(-2\eta \int_{z_n}^z \sigma(z') dz'\right), \quad (\text{A3.15})$$

and the derivative of this is,

$$\frac{d}{dz} \left(T^2(z_n, z) \right) = -2\eta \sigma(z) T^2(z_n, z). \quad (\text{A3.16})$$

Integrating from the near point (z_n) to z ,

$$T^2(z_n, z) - 1 = -2\eta \int_{z_n}^z \sigma(z') T^2(z_n, z') dz', \quad (\text{A3.17})$$

and eliminating the transmittance term from the integral using equation (A3.13),

$$T^2(z_n, z) = 1 - 2\eta \int_{z_n}^z \sigma(z') \frac{\chi(z')}{\beta(z') T^2(0, z_n)} dz'. \quad (\text{A3.18})$$

Now, the constant extinction-to-backscatter ratio S is,

$$S = \frac{\sigma}{\beta}, \quad (\text{A3.19})$$

so that from (A3.18),

$$T^2(z_n, z) = 1 - \frac{2\eta S}{T^2(0, z_n)} \int_{z_n}^z \chi(z') dz'. \quad (\text{A3.20})$$

An expression for β is obtained by substituting equation (A3.20) into (A3.14):

$$\beta(z) = \frac{\chi(z)}{T^2(0, z_n) - 2\eta S \int_{z_n}^z \chi(z') dz'}. \quad (\text{A3.21})$$

The first term in the denominator of (A3.21) is a boundary value of transmittance. If it is preferred to use a boundary value of backscatter the solution is simply,

$$\beta(z) = \frac{\chi(z)}{\frac{\chi(z_n)}{\beta(z_n)} - 2\eta S \int_{z_n}^z \chi(z') dz'}. \quad (\text{A3.22})$$

As S is a constant the solution for extinction is,

$$\sigma(z) = \frac{\chi(z)}{\frac{\chi(z_n)}{\sigma(z_n)} - 2\eta \int_{z_n}^z \chi(z') dz'}. \quad (\text{A3.23})$$

Note the absence of S in the denominator of (A3.23). Note also that this equation is equivalent to equation (A3.11) with the exponent in the latter equal to unity. The backward solution to the lidar equation is obtained by integrating from a distant calibration height z_d down to a height z ,

$$\beta(z) = \frac{\chi(z)}{\frac{\chi(z_d)}{\beta(z_d)} + 2\eta S \int_z^{z_d} \chi(z') dz'}. \quad (\text{A3.24})$$

The backward solution for extinction is,

$$\sigma(z) = \frac{\chi(z)}{\frac{\chi(z_d)}{\sigma(z_d)} + 2\eta \int_z^{z_d} \chi(z') dz'}. \quad (\text{A3.25})$$

The lidar equation for two classes of scatterers, for example, molecules (subscript 'm') and aerosols (subscript 'a') is,

$$\chi(z) = (\beta_m(z) + \beta_a(z)) T_m^{-2}(0, z) T_a^{-2}(0, z). \quad (\text{A3.26})$$

It is assumed that the molecular components are known. It is desired to solve the lidar equation (A3.26) for aerosol backscatter, and the first step is to rearrange that equation to give an expression for β_a :

$$\beta_a(z) = \frac{\chi(z)}{T_a^{-2}(0, z) T_m^{-2}(0, z)} - \beta_m(z). \quad (\text{A3.27})$$

A differential equation is required that will eliminate the aerosol transmittance term from the right hand side of equation (A3.27). The lidar equation (A3.26) is rewritten as,

$$\chi(z) T_m^{-2}(0, z) = \beta_a(z) T_a^{-2}(0, z) + \beta_m(z) T_a^{-2}(0, z). \quad (\text{A3.28})$$

Leaving out η for brevity, the aerosol transmittance term is expanded and differentiated with respect to z to obtain,

$$\frac{d}{dz}(T_a^2(0, z)) = -2\sigma_a(z)T_a^2(0, z), \quad (\text{A3.29})$$

and this combined with equation (A3.28) gives,

$$\chi(z)T_m^{-2}(0, z) = -\frac{1}{2S_a} \left(-2S_a\beta_m(z)T_a^2(0, z) + \frac{d}{dz}(T_a^2(0, z)) \right). \quad (\text{A3.30})$$

The term in brackets on the right-hand side of equation (A3.30) may be obtained from the following differential equation:

$$\begin{aligned} & \frac{d}{dz} \left(T_a^2(0, z) \exp \left[-2S_a \int_0^z \beta_m(z') dz' \right] \right) \\ &= -2S_a\beta_m(z)T_a^2(0, z) \exp \left(-2S_a \int_0^z \beta_m(z') dz' \right) + \frac{d}{dz} [T_a^2(0, z)] \exp \left(-2S_a \int_0^z \beta_m(z') dz' \right) \\ &= \exp \left(-2S_a \int_0^z \beta_m(z') dz' \right) \left(-2S_a\beta_m(z)T_a^2(0, z) + \frac{d}{dz} [T_a^2(0, z)] \right). \quad (\text{A3.31}) \end{aligned}$$

Combining equations (A3.30) and (A3.31),

$$\begin{aligned} & \chi(z)T_m^{-2}(0, z) \\ &= -\frac{1}{2S_a} \frac{d}{dz} \left(T_a^2(0, z) \exp \left[-2S_a \int_0^z \beta_m(z') dz' \right] \right) \exp \left(+2S_a \int_0^z \beta_m(z') dz' \right). \quad (\text{A3.32}) \end{aligned}$$

Rearranging (A3.32) gives,

$$\frac{d}{dz} \left(T_a^2(0, z) \exp \left[-2S_a \int_0^z \beta_m(z') dz' \right] \right)$$

$$= -2S_a \chi(z) T_m^{-2}(0, z) \exp\left(-2S_a \int_0^z \beta_m(z') dz'\right), \quad (\text{A3.33})$$

which may be solved to give,

$$\begin{aligned} & T_a^2(0, z) \exp\left(-2S_a \int_0^z \beta_m(z') dz'\right) \\ &= 1 - 2S_a \int_0^z \chi(z') T_m^{-2}(0, z') \exp\left(-2S_a \int_0^{z'} \beta_m(z'') dz''\right) dz'. \end{aligned} \quad (\text{A3.34})$$

This equation is equivalent to equation (11) of Fernald *et al.* (1972). If the following simplification is made,

$$\begin{aligned} & T_m^{-2}(0, z) \exp\left(-2S_a \int_0^z \beta_m(z') dz'\right) \\ &= \exp\left(+2S_m \int_0^z \beta_m(z') dz' - 2S_a \int_0^z \beta_m(z') dz'\right) \\ &= \exp\left(-2(S_a - S_m) \int_0^z \beta_m(z') dz'\right), \end{aligned} \quad (\text{A3.35})$$

and letting,

$$A_f(z) \equiv (S_a - S_m) \int_0^z \beta_m(z') dz', \quad (\text{A3.36})$$

(subscript 'f' for 'forward solution'), then we find,

$$T_a^2(0, z) \exp\left(-2S_a \int_0^z \beta_m(z') dz'\right) = 1 - 2S_a \int_0^z \chi(z') \exp(-2A_f(z')) dz'. \quad (\text{A3.27})$$

The solution for β_a is found after substitution of equation (A3.37) back into the lidar equation (A3.27);

$$\beta_a(z) = \frac{\chi(z) T_m^{-2}(0, z) \exp\left(-2S_a \int_0^z \beta_m(z') dz'\right)}{1 - 2S_a \int_0^z \chi(z') \exp(-2A_f(z')) dz'} - \beta_m(z), \quad (\text{A3.38})$$

which simplifies to,

$$\beta_a(z) = \frac{\chi(z) \exp(-2A_f(z))}{1 - 2S_a \int_0^z \chi(z') \exp(-2A_f(z')) dz'} - \beta_m(z). \quad (\text{A3.39})$$

This equation is equivalent to equation (14) of Fernald *et al.* (1972) and equation (2) of Fernald (1984). Fernald (1984) presents a summary of results of solutions to the lidar equation for two classes of scatterers for the purpose of numerical implementation. A summary of these results is presented in the following in mathematical form, but using the symbols chosen for this thesis. The simplification (A3.36) is rewritten as,

$$A_f(z) = (S_a - S_m) \int_{z_n}^z \beta_m(z') dz', \quad (\text{A3.40})$$

where z_n is a near-point calibration range. The forward solution for backscatter is,

$$\beta_a(z) + \beta_m(z) = \frac{\chi(z) \exp(-2A_f(z))}{\frac{\chi(z_n)}{\beta_m(z_n) + \beta_a(z_n)} - 2S_a \int_{z_n}^z \chi(z') \exp(-2A_f(z')) dz'}, \quad (\text{A3.41})$$

and the forward solution for extinction,

$$\sigma_a(z) + \frac{S_a}{S_m} \sigma_m(z) = \frac{\chi(z) \exp(-2A_f(z))}{\frac{S_a}{S_m} \frac{\chi(z_n)}{\sigma_m(z_n) + \sigma_a(z_n)} - 2 \int_{z_n}^z \chi(z') \exp(-2A_f(z')) dz'}. \quad (\text{A3.42})$$

For the backward solutions there is the simplification, (Fernald, 1984),

$$A_b(z) = (S_a - S_m) \int_z^{z_{df}} \beta_m(z') dz', \quad (\text{A3.43})$$

where the A subscript 'b' stands for 'backward', and z_d is a distant calibration range. The backward solution for backscatter is,

$$\beta_a(z) + \beta_m(z) = \frac{\chi(z) \exp(+2A_b(z))}{\frac{\chi(z_d)}{\beta_m(z_d) + \beta_a(z_d)} + 2S_a \int_z^{z_d} \chi(z') \exp(+2A_b(z')) dz'}, \quad (\text{A3.44})$$

and the backward solution for extinction is,

$$\sigma_a(z) + \frac{S_a}{S_m} \sigma_m(z) = \frac{\chi(z) \exp(+2A_b(z))}{\frac{\chi(z_d)}{\frac{S_a}{S_m} \sigma_m(z_d) + \sigma_a(z_d)} + 2 \int_z^{z_d} \chi(z') \exp(+2A_b(z')) dz'}. \quad (\text{A3.45})$$

Appendix A4. Lidar Data Acquisition Program.

A Lidar Data Acquisition Program (LDAP) was written by the author (January 1995) for the lidar used during the SOCEX2 experiment ('minilidar', see 3.2.2). The major aspects of the design of this program are described in the following.

The LDAP can be viewed by the lidar controller as being in either of three states: (1) waiting for a command, (2) adjusting lidar control parameters, (3) acquiring data. After the LDAP has attempted a task in the states (2) or (3) it returns to state (1). The lidar controller can be either a human user or a decision-making computer program.

The primary structure of the LDAP is a case statement nested in an interrupt-monitoring loop. The program starts by entering the main loop, presenting the lidar controller with various options. The controller chooses to change a lidar setting or begin data acquisition and, upon doing so, interrupts the main loop. Depending on the controller's choice, program control is diverted down one of the sub-programs of the main case statement. When one of these sub-programs is finished control passes back to the main loop where the program waits for another decision by the controller. The pseudocode for the entire program appears below:

Pseudocode:

```
begin Lidar Data Acquisition Program (LDAP)
  read digitiser configuration file and open a new output file
  if no error
    initialise program variables
    initialise digitiser parameters
    start main loop waiting
      present options to lidar controller
      check for interrupt
      case (interrupt) of
        "a" adjust control parameter "a"
        "b"      etc.
        "x" execute sub-program acquire
      end interrupt cases
    end main loop waiting
  end if no error
end LDAP
```

The pseudocode for the main sub-program 'acquire' appears below. Note that in each cycle of the loop 'acquiring' the digitiser is initialised at the beginning and disabled at the end. In this way, acquisition of each shot is started afresh, independently of any (electrical) interference with digitiser settings from the previous shot.

Pseudocode:

```
start sub-program acquire
  acquiring = true
  begin nested loop acquiring
    activate digitiser (start digitiser clock)
    enable computer access to digitiser memory
    initialise digitiser control settings (e.g. sampling rate, gain etc.)
    disable computer access to digitiser memory
    instruct digitiser to wait for a trigger event
    delay for required shot period (note: this delay should include a user
    interrupt)
    fire_lidar: i.e.,
      reset Energy Monitor (EM) and set preamp gain
      analog-to-digital conversion (zero value of EM)
      fire the laser
      analog-to-digital conversion (pulse value of the EM)
      store(EM zero value, EM pulse value)
    get time from computer clock
    increment the shot number
    wait until digitiser trigger received and digitiser memory is full
    read (digitiser status)
    case (digitiser status) of:
      trigger timeout - produce error message
      memory full timeout - produce error message
      - etc -
    default (assumed successful data acquisition)
      enable computer access to digitiser memory
      read a block of data from the digitiser memory
      display the shot
      save the data
    end (case statement)
    disable the digitiser
    if interrupt, acquiring = false
  end nested loop acquiring.
end sub-program acquire
```

Appendix A5. List of Publications and Reports by the Author

Platt, C. M. R., S. A. Young, R. T. Austin, and M. C. Pickett. Lidar and radiometer sounding of cloud properties. Proc. 19th Laser Radar Conference, NASA/CP-1998-207671/PT2. Annapolis, Md, pp. 77-78, July 1998.

M. C. Pickett, C. M. R. Platt, and S. A. Young. *Lidar and infrared radiometer remote sensing of the optical properties of Southern Ocean stratocumulus clouds*, abstract IM5kkkk in IAMAS/IAPSO Joint Assemblies. Ed. T. Beer and D. Jasper, Melbourne, July 1997.

M. C. Pickett, S. A. Young, R. Boers and C. M. R. Platt. *Lidar Observations of Boundary Layer Clouds during the Southern Ocean Cloud Experiment*, Baseline Atmospheric Program (Australia) 1994-95, pp. 10 - 21, October 1996.

M. C. Pickett, S. A. Young, and C. M. R. Platt. *Lidar and Infrared Radiometer Measurements of Clouds during SOCEX2*. Baseline Atmospheric Program (Australia) 1994-95. pp. 158-160, October 1996.

S. A. Young, M. C. Pickett, P. J. Manson and C. M. R. Platt. *Lidar and Infrared Radiometer Measurements of Clouds during SOCEX I*. Baseline Atmospheric Program (Australia) 1993, pp. 104 - 106, October 1996.

M. C. Pickett, S. A. Young, R. Boers and C. M. R. Platt. *Lidar Remote Sensing of Boundary Layer Clouds during SOCEX*, in Conference Proceedings of the 3rd National AMOS Conference (Incorporating the 4th Australasian Conference on the Physics of Remote Sensing of Atmosphere and Ocean), 5-7 February 1996, University of Tasmania, Hobart, p.84.

M. C. Pickett. *Lidar Studies of Boundary Layer Clouds*. BSc(Hons) thesis, Department of Applied Physics, Victoria University of Technology, 1993.

References

1. Ackerman, A.S., O.B. Toon and P.V. Hobbs. Numerical modeling of ship tracks produced by injections of cloud condensation nuclei into marine stratiform clouds. *J. Geophys. Res.*, 100, (D4), 7121-7133, 1995.
2. Albrecht, B.A., C.S. Bretherton, D. Johnson, W.H. Schubert, and A. S. Frisch. The Atlantic stratocumulus transition experiment - ASTEX. *Bull. Am. Meteorol. Soc.*, 76, 889-904, 1995.
3. Allen, J.R. Measurements of cloud emissivity in the 8-13 μ waveband. *J. Appl. Meteorol.*, 10, 260-265, 1970.
4. Allen, R.J. and Platt, C.M.R. Lidar for multiple backscattering and depolarization observations. *Appl. Opt.* 16, 3193-3199, 1977.
5. Ansmann, A., M. Riebesell, U. Wandinger, C. Weitkamp, E. Voss, W. Lahmann, and W. Michaelis. Combined Raman elastic-backscatter lidar for vertical profiling of moisture, aerosol extinction, backscatter, and lidar ratio. *Appl. Phys. B55*, 18-28, 1992.
6. Ayers, G.P. and J.L. Gras. Seasonal relationship between cloud condensation nuclei and aerosol methanesulphonate in marine air. *Nature* 353, 834-835, 1991.
7. Ayers, G.P., S.T. Bentley, J.P. Ivey, and B.W. Forgan. Dimethylsulfide in marine air at Cape Grim, 41°S. *J. Geophys. Res.* 100, No. D10, 21,013-21,021, 1995.
8. Barrett, E. W., and O. Ben-Dov. Application of the lidar to air pollution measurements. *J. Appl. Meteorol.*, 6, 500-515, 1967.
9. Baumgardner, D., W. Strapp, and J.E. Dye. Evaluation of the forward scattering spectrometer probe. Part II: corrections for coincidence and dead-time losses. *J. Atmos. Oceanic Technol.*, 2, 626-632, 1985.
10. Bigg, E.K. Comparison of aerosol at four baseline atmospheric monitoring stations. *J. Appl. Meteorol.*, 19, 521-533, 1980.
11. Bissonnette, L.R., and D.L. Hutt. Multiple scattering lidar. *Appl. Opt.*, 34, 5045 -5046, 1990.
12. Bissonnette, L.R. Sensitivity analysis of lidar inversion algorithms. *Appl. Opt.*, 25, 2122-2125, 1986.
13. Bissonnette, L.R., P. Bruscalioni, A. Ismaelli, G. Zaccanti, A. Cohen, Y. Benayahu, M. Kleiman, S. Egert, C. Flesia, P. Schwendimann, A.V. Starkov, M. Noormohammadian, U.G. Ooppel, D.M. Winker, E.P. Zege, I.L. Katsev, I.N. Polonsky. LIDAR multiple scattering from clouds. *Appl. Phys. B* 60, 355-362, 1995.
14. Boers, R. The Microwave Radiometer, in *Baseline Atmospheric Program (Australia) '93*, edited by R.J. Francey, A.L. Dick and N. Derek, pp. 103-104, Bureau of Meteorology and CSIRO Division of Atmospheric Research, Melbourne, Australia, 1996a.
15. Boers, R. Microwave Observations of Liquid Water Path and Water Vapour Path at Cape Grim, in *Baseline Atmospheric Program (Australia) 1994-95*, edited by R.J. Francey, A.L. Dick and N. Derek, pp. 22-29, Bureau of Meteorology and CSIRO Division of Atmospheric Research, Melbourne, Australia, 1996b.
16. Boers, R., and D. O'Brien. Microwave Observations at Cape Grim - 1994-1995, in *Baseline Atmospheric Program (Australia) 1994-95*, edited by R.J. Francey, A.L. Dick and N. Derek, p. 158, Bureau of Meteorology and CSIRO Division of Atmospheric Research, Melbourne, Australia, 1996.

17. Boers, R., G.P. Ayers, and J.L. Gras. Coherence between seasonal variation in satellite-derived cloud optical depth and boundary layer CCN concentrations at a mid-latitude Southern Hemisphere station. *Tellus* 46B, 123-131, 1994.
18. Boers, R., J.B. Jensen, and P.B. Krummel. Microphysical and short-wave radiative structure of stratocumulus clouds over the Southern Ocean: summer results and seasonal differences. *Quart. J. R. Meteorol. Soc.*, 124, 151-168, 1998.
19. Boers, R., J.B. Jensen, P.B. Krummel, and H. Gerber. Microphysical and short-wave radiative structure of wintertime stratocumulus clouds over the Southern Ocean. *Quart. J. R. Meteorol. Soc.*, 122, 1307-1339, 1996.
20. Boers, R., J.D. Spinhirne and W.D. Hart, Lidar observations of the fine-scale variability of marine stratocumulus clouds. *J. Appl. Meteorol.* 27, 797-810, 1988.
21. Boers, R.E. and R.H. Hill The Microwave Radiometer, in *Baseline Atmospheric Program (Australia) 1993*, edited by R.J. Francey, A.L. Dick and N. Derek, p. 103, Bureau of Meteorology and CSIRO Division of Atmospheric Research, Melbourne, Australia, 1996.
22. Caine, J. PhD Thesis, The Atmospheric Sulfur Cycle in the Remote Marine Environment, Monash University, Australia, 1998.
23. Carnuth, W. and R. Reiter, Cloud extinction profile measurements by lidar using Klett's inversion method. *Appl. Opt.* 25, No.17, 2899-2907, 1986.
24. Carrier, L.W., G.A. Cato and K.J. von Essen, The backscattering and extinction of visible and infrared radiation by selected major cloud models. *Appl. Opt.* 6, 1209-1216, 1967.
25. Cess, R.D., G.L. Potter, J.P. Blanchet, G.J. Boer, S.J. Ghan, J.T. Kiehl, H. Le Treut, Z.X. Li, X.Z. Liang, J.F.B. Mitchell, J.-J. Morcrette, D.A. Randall, M.R. Riches, E. Roeckner, U. Schlese, A. Slingo, K.E. Taylor, W.M. Washington, R.T. Wetherald, and I. Yagai. Interpretation of cloud climate feedback as produced by 14 atmospheric general circulation models. *Science*, 245, 513-516, 1989.
26. Chandrasekhar, S. *Radiative Transfer*, Dover, New York, 1960.
27. Charlson, R.J., J.E. Lovelock, M.O. Andreae, and S.G. Warren. Oceanic phytoplankton, atmospheric sulphur, cloud albedo, and climate. *Nature* 326, 655-661, 1987.
28. Chylek, P., and P. Damiano. Infrared Emittance of Water Clouds. *J. Atmos. Sci.*, 49, 1459 - 1472, 1992.
29. Collis, R.T.H. and P.B. Russell, Lidar measurement of particles and gases by elastic backscattering and differential absorption in *Topics in Applied Physics: Laser Monitoring of the Atmosphere*. Springer, New York, 1976.
30. Conover, J.H. Anomalous cloud lines, *J. Atmos. Sci.*, 23, 778-785, 1966.
31. *CRC Handbook of Chemistry and Physics, 63rd Edition 1982-1983*, Editors: R.C. Weast and M.J. Astle, CRC Press, Florida, USA, 1982-1983.
32. d'Almeida, G. A., P. Koepke, and E. P. Shettle. *Atmospheric Aerosols Global Climatology and Radiative Characteristics*. A. Deepak Publ., Hampton, Virginia USA, 1991.
33. Damiano, P. and P. Chylek, Shortwave radiative properties of clouds: numerical study. *J. Atmos. Sci.* 51, No.9, 1223-1233, 1994.
34. Davis, P.A. The analysis of lidar signatures of cirrus clouds. *Appl. Opt.* 8, No.10, 2099-2102, 1969.

35. Deirmendjian, D. *Electromagnetic Scattering on Spherical Polydispersions*. American Elsevier, New York, 1969.
36. Deirmendjian, D. Scattering and polarization properties of water clouds and hazes in the visible and infrared. *Appl. Opt.* 3, No.2, 187-196, 1964.
37. Derr, V.E. Estimation of the extinction coefficient of clouds from multiwavelength lidar backscatter measurements. *Appl. Opt.* 19, No.14, 2310-2314, 1980.
38. Eloranta, E. W.. Calculation of doubly scattered lidar returns. Ph.D. dissertation, University of Wisconsin, Madison, Wisconsin, 1972.
39. Elterman, L. Aerosol measurements in the troposphere and stratosphere. *Appl. Opt.*, 5, 1769-1776, 1966.
40. Elterman, L. Atmospheric attenuation model, 1964, in the ultraviolet, visible, and infrared regions for altitudes to 50 km. Environment Research Paper No. 46, Optical Physics Laboratory Project 7670, Air Force Cambridge Research Laboratories, U.S.A.F., 1964.
41. Fernald, F.G. Analysis of atmospheric lidar observations: some comments. *Appl. Opt.*, 23, 652-653, 1984.
42. Fernald, F.G., B.M. Herman and J.A. Reagan. Determination of aerosol height distributions by lidar. *J. Appl. Meteorol.* 11, 482-489, 1972.
43. Feynman, R., R.B. Leighton, and M. Sands. *The Feynman Lectures on Physics Mainly Mechanics, Radiation, and Heat*. Addison Wesley Publishing Company, California Institute of Technology, 1963.
44. Flamant, C., J. Pelon, P.H. Flamant, and P. Durand. Lidar determination of the entrainment zone thickness at the top of the unstable marine atmospheric boundary layer. *Boundary-Layer Meteorol.* 83, 247-284, 1997.
45. Fleagle, R.G., and J.A. Businger, *An Introduction to Atmospheric Physics. 2nd Edition*. Academic Press, New York, 1980.
46. Francey, R. J., A. L. Dick, and N. Derek. Preface to *Baseline Atmospheric Program (Australia) 1993*, edited by R. J. Francey, A. L. Dick and N. Derek, p. iv, Bureau of Meteorology and CSIRO Division of Atmospheric Research, Melbourne, Australia, 1996.
47. Gambling, D.J., and K. Bartusek. Discussions. Lidar observations of tropospheric aerosols. 6, 869-870, 1972b.
48. Gambling, D.J., and K. Bartusek. Lidar observations of tropospheric aerosols. *Atmos. Env.*, 6, 181-190, 1972a.
49. Garratt, J.R. *The Atmospheric Boundary Layer*. Cambridge University Press, Cambridge, 1992.
50. Garvey, D. M. and R. G. Pinnick. Response characteristics of the Particle Measuring Systems Active Scattering Aerosol Spectrometer Probe (ASASP-X). *J. Aerosol Sci. Technol.*, 2, 477 - 488, 1983.
51. Gebbie, H.A., Burroughs, W.J., Chamberlain, J., Harris, J.E. and Jones, R.G. Dimers of the water molecule in the earth's atmosphere. *Nature* 221, 143, 1969.
52. Goody, R. M. and Yung, Y.L. *Atmospheric Radiation*, 2nd Ed., Oxford University Press, New York, 1989.
53. Gras, J.L. and G.P. Ayers. Marine aerosol at southern mid-latitudes. *J. Geophys. Res.*, 88 (C15), 10661-10666, 1983.

54. Gras, J.L. Southern hemisphere tropospheric aerosol microphysics. *J. Geophys. Res.*, 96 (D3), 5345-5356, 1991.
55. Gras, J.L., C.M.R. Platt, W.D. Jones, R.M. Huffaker, S.A. Young, S.M. Banks, and D.J. Booth. Southern hemisphere tropospheric aerosol backscatter measurements - implications for a laser wind system. *J. Geophys. Res.*, 96 (D3), 5357-5367, 1991.
56. Grund, C.J. and, E.W. Eloranta. The 27-28 October 1986 FIRE cirrus case study: cloud optical properties determined by high spectral resolution lidar. *Mon. Wea. Rev.*, 118, 2344-2355, 1990.
57. Hale, G.M. and M.R. Querry. Optical constants of water in the 200 nm to 200 μ m wavelength region. *Appl. Opt.*, 12, 555-563, 1973.
58. Halldorsson, T. and J. Langerholc. Geometrical form factors for the lidar function. *Appl. Opt.* 17, No. 2, 240 - 244, 1978.
59. Hansen, J. E. and L. D. Travis. Light scattering in planetary atmospheres. *Space Sci. Rev.*, 16, 527 - 610, 1974.
60. Harms, J. Lidar return signals for coaxial and noncoaxial systems with central obstruction. *Appl. Opt.* 18, No. 10, 1559 - 1566, 1979.
61. Harms, J. W. Lahmann, and C. Weitkamp. Geometrical compression of lidar return signals. *Appl. Opt.* 17, No. 7, 1131 - 1135, 1978.
62. Herzberg, G. *Spectra of Diatomic Molecules, Vol. 1.* Van Nostrand, Princeton, 1950.
63. Hill, R.H. and A.B. Long, The CSIRO dual-frequency microwave radiometer. *CSIRO Division of Atmospheric Research Technical Paper*, No. 35, 1995.
64. Hitschfeld, W. and J. Bordan. Errors inherent in the radar measurement of rainfall at attenuating wavelengths. *J. Meteor.*, Vol. 11, pp. 58 - 67, 1954.
65. Hogg, D.C., F.O. Guiraud, J.B. Snider, M.T. Decker and E.R. Westwater. A steerable dual-channel microwave radiometer for measurements of water vapour and liquid in the troposphere. *J. Clim. Appl. Meteorol.*, 22, 789-806, 1983.
66. Houghton, J.T. *The Physics of Atmospheres.* Cambridge University Press, Great Britain, 1977.
67. Iribarne, J.V. and H.-R. Cho. *Atmospheric Physics.* (D. Reidel Publishing Company, Dordrecht, Holland, 1980).
68. Janssen, M.A. An introduction to the passive microwave remote sensing of atmospheres in *Atmospheric Remote Sensing by Microwave Radiometry*, Ed. M.A. Janssen, New York, Wiley, 1993.
69. Junge, C., *Tropospheric Aerosols in Radiation in the Atmosphere.* Science Press, Princeton, 1977.
70. Katsev, I. L., E. P. Zege, A. S. Prikhach, and I. N. Polonsky. Efficient technique to determine backscattered light power for various atmospheric and oceanic sounding imaging systems. *J. Opt. Soc. Am. A*, 14, 1338-1346, 1997.
71. Klett, J.D. Lidar inversion with variable back-scatter/extinction ratios. *Appl. Opt.* 20, 1638-1645, 1985.
72. Klett, J.D. Stable analytical inversion solution for processing lidar returns. *Appl. Opt.*, 20, 211-220, 1981.
73. Kolev, L.N., O.P. Parvanov, B.K. Kaprielov and S.I. Kolev. Lidar observation of time and spatial variations of backscattering coefficient near the stratiform cloud base. *Atmos. Res.* 24, 13-32, 1989.

74. Kovalev, V. A. Sensitivity of the lidar solution to errors of the aerosol backscatter-to-extinction ratio: influence of a monotonic change in the aerosol extinction coefficient. *Appl. Opt.*, 34, 3457-3462, 1995.
75. Krummel, P. The structure of the cloud topped marine boundary layer during the Southern Ocean Cloud Experiment (SOCEX). Masters Thesis, Monash University, Vic., Australia, to be submitted in 1998.
76. Kunkel, K.E. and J.A. Weinman. Monte Carlo analysis of multiply scattered lidar returns. *J. Atmos. Sci.*, 33, 1772-1781, 1976.
77. Kunz, G.J. and G. de Leeuw. Inversion of lidar signals with the slope method. *Appl. Opt.*, 32, 3249-3256, 1993.
78. Lindberg, J.D., W.J. Lentz, E.M. Measure and R. Rubio, Lidar determinations of extinction in stratus clouds. *Appl. Opt.* 23, No.13, 2172-2177, 1984.
79. McCartney, Earl J., *Optics of the Atmosphere*. John Wiley & Sons Inc. New York, 1976.
80. Measures, R. M. *Laser Remote Sensing: Fundamentals and Applications*. Wiley, New York, 1984.
81. Minnis, P., D.F. Young, K. Sassen, J.M. Alvarez and C.J. Grund. The 27-28 October 1986 FIRE IFO cirrus case study: cirrus parameter relationships derived from satellite and lidar data. *Mon. Wea. Rev.* 118, 2402-2425, 1990.
82. Nicolas, F., L. R. Bissonnette, and P. H. Flamant. Lidar effective multiple-scattering coefficients in cirrus clouds. *Appl. Opt.* 36, 3458-3468, 1997.
83. O'Brien, D.M., L.J. Rikus, A.C. Dille, and M. Edwards. Spectral analysis of infrared heating in clouds computed with two-stream radiation codes. *J. Quant. Spectrosc. Radiat. Transfer* Vol. 57, 725 - 737, 1997.
84. Pal, S.R. and A.I. Carswell. Multiple scattering in atmospheric clouds: lidar observations. *Appl. Opt.* 15, No.8, 1990-1995, 1976.
85. Pal, S.R. and A.I. Carswell. Polarization properties of lidar backscattering from clouds. *Appl. Opt.*, 12, 1530-1535, 1973.
86. Pal, S.R., A.I. Carswell, I. Gordon, and A. Fong. Lidar-derived cloud optical properties obtained during the ECLIPS program. *J. Appl. Meteorol.*, 34, pp. 2388 - 2399, 1995.
87. Palmer, K. F., and D. Williams. Optical constants of sulfuric acid: application to the clouds of Venus. *Appl. Opt.*, 14, 208-219, 1975.
88. Paltridge, G.W. Infrared emissivity, short-wave albedo, and the microphysics of stratiform water clouds. *J. Geophys. Res.*, 79, 4053-4058, 1974.
89. Paltridge, G.W. and C.M.R. Platt, *Radiative Processes in Meteorology and Climatology*. Elsevier, Amsterdam, 1976.
90. Pickett, M.C., S.A. Young, and C.M.R. Platt. Lidar and Infrared Radiometer measurements of clouds during SOCEXII, in *Baseline Atmospheric Program (Australia) 1994-1995*, edited by R.J. Francey, A.L. Dick and N. Derek, pp. 158-159, Bureau of Meteorology and CSIRO Division of Atmospheric Research, Melbourne, Australia, 1996b.
91. Pickett, M.C., S.A. Young, R. Boers, and C.M.R. Platt. Lidar observations of boundary layer clouds during the Southern Ocean Cloud Experiment, in *Baseline Atmospheric Program (Australia) 1994-1995*, edited by R.J. Francey, A.L. Dick and N. Derek, pp. 10-21, Bureau of Meteorology and CSIRO Division of Atmospheric Research, Melbourne, Australia, 1996a.

92. Pinnick, R.G., S.G. Jennings, P. Chylek, C. Ham and W.T. Grundy Jr., Backscatter and extinction in water clouds, *J. Geophys. Res.*, Vol. 88, No. C11, 6787-6796, August 20, 1983.
93. Plass, G.N. and G.W. Kattawar. Reflection of light pulses from clouds. *Appl. Opt.*, 10, 2304-2310, 1971.
94. Platt, C.M.R. Infrared absorption and liquid water content in stratocumulus clouds. *Quart. J. R. Meteorol. Soc.*, 102, 553-562, 1976.
95. Platt, C.M.R. The effect of cirrus varying optical depth on the extraterrestrial radiative flux. *Quart. J. R. Meteorol. Soc.*, 107, 671-678, 1981b.
96. Platt, C.M.R. A narrow-beam radiometer for atmospheric radiation studies. *J. Appl. Meteorol.*, 10, 1307-1313, 1971.
97. Platt, C.M.R. Airborne infrared radiance measurements (10- to 12-micron wavelength) off tropical east-coast Australia. *J. Geophys. Res.* 77, 1597-1609, 1972.
98. Platt, C.M.R. Lidar and Radiometric Observations of Cirrus Clouds. *J. Atmos. Sci.* 30, No. 6, 1191-1204, 1973.
99. Platt, C.M.R. Remote sounding of high clouds. Pt. I. Calculation of visible and infrared optical properties from lidar and radiometer measurements. *J. Appl. Meteorol.*, 18, 1130-1143, 1979.
100. Platt, C.M.R. Remote sounding of high clouds. III: Monte carlo calculations of multiple-scattered lidar returns. *J. Atmos. Sci.* 38, No.1, 156-167, 1981a.
101. Platt, C.M.R. The role of cloud microphysics in high-cloud feedback effects on climate change. *Nature*, 341, 428-429, 1989.
102. Platt, C.M.R. and Dilley, A.C. Remote sensing of high clouds. IV: Observed temperature variations in cirrus optical properties. *J. Atmos. Sci.* 38, 1069-1082, 1981.
103. Platt, C.M.R. and Dilley, A.C. Remote sounding of high clouds: II. Emissivity of cirrostratus. *J. Appl. Meteorol.* 18, 1144-1150, 1979.
104. Platt, C.M.R. and Gambling, D.J. Laser radar reflexions and downward infrared flux enhancement near small cumulus clouds. *Nature* 232, 182-185, 1971a.
105. Platt, C.M.R. and D.J. Gambling, Emissivity of high layer clouds by combined lidar and radiometric techniques. *Quart. J. R. Meteorol. Soc.*, 97, 322-325, 1971b.
106. Platt, C.M.R. and G.L. Stephens, The interpretation of remotely sensed high cloud emittances. *J. Atmos. Sci.* 37, No.10, 2314-2322, 1980.
107. Platt, C.M.R. and T. Takashima. Retrieval of water cloud properties from carbon dioxide lidar soundings. *Appl. Opt.* 26, 1257-1263, 1987.
108. Platt, C.M.R., D.W. Reynolds, and N.L. Abshire. Satellite and lidar observations of the albedo, emittance, and optical depth of cirrus compared to model calculations. *Mon. Wea. Rev.*, 108, 195-204, 1980.
109. Platt, C.M.R., J.C. Scott and A.C. Dilley. Remote sounding of high clouds. Part VI: optical properties of midlatitude and tropical cirrus. *J. Atmos. Sci.* 44, 729-747, 1987.
110. Platt, C.M.R., S.A. Young, R.T. Austin and M.C. Pickett. Lidar and radiometer sounding of cloud properties. *Proc. 19th Laser Radar Conference, NASA/CP-1998-207671/PT2.* pp. 77-78, Annapolis, Md, July 1998a.

111. Platt, C.M.R., A.C. Dilley, J.C. Scott, I.J. Barton and G.L. Stephens, Remote sounding of high clouds. V: Infrared properties and structures of tropical thunderstorm anvils. *J. Clim. App. Meteorol.* 23, 1296-1308, 1984.
112. Platt, C.M.R., S.A. Young, P.J. Manson, G.R. Patterson, S.C. Marsden, and R.T. Austin. The optical properties of equatorial cirrus from observations in the ARM pilot radiation observation experiment. Accepted by *J. Atmos. Sci.*, July 1998b.
113. Platt, C.M.R., J.W. Bennett, S.A. Young, M.D. Fenwick, P.J. Manson, G.R. Patterson, And B. Petraitis. Narrow-beam fast filter radiometry and the use of the lidar/radiometer method in the Atmospheric Radiation Measurement Program. *Proc. of the Third Atmospheric Radiation Measurement (ARM) Science Team Meeting*, March 1-4, Norman, Oklahoma, United States Department of Energy, 293-297, 1993.
114. Platt, C.M.R., S.A. Young, A.I. Carswell, S.R. Pal, M.P. McCormick, D.M. Winker, M. DelGuasta, L. Stefanutti, W.L. Eberhard, M. Hardesty, P.H. Flamant, R. Valentin, B. Forgan, G.G. Gimmetstad, H. Jager, S.S. Khmelevtsov, I. Kolev, B. Kaprieolev, Da-ren Lu, K. Sassen, V.S. Shamanaev, O. Uchino, Y. Mizuno, U. Wandinger, C. Weitkamp, A. Ansmann, and C. Wooldridge. The experimental cloud lidar pilot study (ECLIPS) for cloud-radiation research. *Bull. Am. Meteorol. Soc.*, 75, 1635-1654, 1994.
115. Pruppacher, H.R., and J.D. Klett. *Microphysics of Clouds and Precipitation*. 2nd Ed., Kluwar Academic Publishers, Dordrecht, 1997.
116. Qiu Jinhuan. Sensitivity of lidar equation solution to boundary values and determination of the values. *Adv. Atmos. Sci.*, 5, 229-241, 1988.
117. Randall, D. A., B. Albrecht, S. Cox, D. Johnson, P. Minnis, W. Rossow and D. O'C. Starr. On FIRE at ten, in *Advances in Geophysics Volume 38*, edited by R. Dmowska and B. Saltzman, pp 37-163, Academic Press, San Diego, 1996.
118. Randall, D.A., J.A. Coakley Jr. C.W. Fairall, R.A. Kropfli and D.H. Lenschow. Outlook for research on subtropical marine stratiform clouds. *Bull. Amer. Meteor. Soc.* 65, No.12, 1290-1301, 1984.
119. Reif, F. *Fundamentals of Statistical and Thermal Physics*. McGraw-Hill, 1965.
120. Rossow, W. B. and A. A. Lacis. Global seasonal cloud variations from satellite radiance measurements. Part II: Cloud properties and radiative effects. *J. Climate*, 3, 1204-1253, 1990.
121. Sasano, Y. and H. Nakane, H. Significance of the extinction/backscatter ratio and the boundary value term in the solution for the two-component lidar equation. *Appl. Opt.*, 23, 11-13, 1984.
122. Sassen, K. The polarization lidar technique for cloud research: a review and current assessment. *Bull. Am. Meteorol. Soc.*, 72, 1848-1866, 1991.
123. Sassen, K. and R.L. Petrilla, Lidar depolarization from multiple scattering in marine stratus clouds. *Appl. Opt.* 25, 1450-1459, 1986.
124. Sassen, K., H. Zhao and G.C. Dodd, Simulated polarization diversity lidar returns from water and precipitating mixed phase clouds. *Appl. Opt.* 31, No.15, 2914-2923, 1992.
125. Schiffer, R.A. and W.B. Rossow, The International Satellite Cloud Climatology Project (ISCCP): the first project of the World Climate Research Programme. *Bull. Amer. Meteor. Soc.* 64, 779-784, 1983.
126. Schotland, R.M. Errors in lidar measurement of atmospheric gases by differential absorption. *J. Appl. Meteor.* 13, 71-77, 1974.

127. Slingo, A. Sensitivity of the Earth's radiation budget to changes in low clouds. *Nature*, 343, 49-51, 1990.
128. Slingo, A. and H.M. Schrecker. On the shortwave radiative properties of stratiform water clouds. *Quart. J. R. Meteorol. Soc.*, 108, 407-426, 1982.
129. Slingo, A., R. Brown and C.L. Wrench. A field study of nocturnal stratocumulus; III. high resolution radiative and microphysical observations. *Quart. J. R. Meteorol. Soc.*, 108, 145-165, 1982.
130. Spinhirne, J.D., R. Boers and W.D. Hart, Cloud top liquid water from lidar observations of marine stratocumulus. *J. Appl. Meteor.* 28, 81-90, 1989.
131. Stamnes, K., and Collaborators. 'DISORT', A Discrete Ordinates Radiative Transfer Fortran 77 Program for a Multi-Layered Plane-Parallel Medium. Version 1.1, Jan. 1993. Knut Stamnes (knut@kaja.gi.alaska.edu), Geophysical Institute, University of Alaska, Fairbanks, Alaska 99701, 1993.
132. Stamnes, K., S-Chee Tsay, W. Wiscombe, and K. Jayaweera. Numerically stable algorithm for discrete-ordinate-method radiative transfer in multiple scattering and emitting layered media. *Appl. Opt.*, 27, 2502-2509, 1988.
133. Stephens, G.L. Optical properties of eight water cloud types. CSIRO Div. Atmos. Phys. Tech. Pap., No. 36, 1- 35, 1979.
134. Stephens, G.L. *Remote Sensing of the Lower Atmosphere*, Oxford University Press, New York, 1994.
135. Stephens, G.L., G.W. Paltridge and C.M.R. Platt. Radiation profiles in extended water clouds. III: observations. *J. Atmos. Sci.*, 35, 2133-2141, 1978.
136. Strapp, J. W., W. R. Leitch, and P. S. K. Liu. Hydrated and dried aerosol-size-distribution measurements from the Particle Measuring Systems FSSP-300 probe and the deiced PCASP-100X probe. *J. Atmos. Oceanic Technol.*, 9, 548 - 555, 1992.
137. Tampieri, F. and C. Tomasi, Size distribution models of fog and cloud droplets in terms of the modified gamma function. *Tellus* 28, 333-347, 1976.
138. Tang, I. N., and H. R. Munkelwitz. Ammonium bisulfate aerosols in a moist atmosphere. *J. Aerosol Sci.*, 8, 321 - 330, 1977.
139. Tang, I. N., Chemical and size effects of hygroscopic aerosols on light scattering coefficients. *J. Geophys. Res.*, 101 (D14), 19245 - 19250, 1996.
140. Tang, I. N., H. R. Munkelwitz and J. G. Davis. Aerosol growth studies II. Preparation and growth measurements of monodisperse salt aerosols. *J. Aerosol Sci.*, 8, 149 - 159, 1977.
141. Toon, O.B., J.B. Pollack, and B.N. Khare. The optical constants of several atmospheric species: ammonium sulfate, aluminum oxide, and sodium chloride. *J. Geophys. Res.*, 8, 5733-5748, 1976.
142. Twomey, S. *Atmospheric Aerosols*. Elsevier Scientific Publishing Company, Amsterdam, 1977.
143. Twomey, S. The influence of pollution on the shortwave albedo of clouds. *J. Atmos. Sci.*, 34, 1149-1152, 1977.
144. Twomey, S.A., M. Piepgrass, and T.L. Wolfe. An assessment of the impact of pollution on global cloud albedo. *Tellus* 36 B, 356-366, 1984.
145. Ulaby, F.T., Moore, R.K. and Fung, A.K., *Microwave Remote Sensing: Active and Passive Volume I: Microwave Remote Sensing Fundamentals and Radiometry*, Addison-Wesley 1981.

146. Ulaby, F.T., Moore, R.K. and Fung, A.K., *Microwave Remote Sensing: Active and Passive Volume III: From Theory to Applications*, Artech House 1986.
147. Valley, S.L. ed. *Handbook of Geophysics and Space Environments*. Air Force Cambridge Research Lab. Bedford, Mass. (1965).
148. van de Hulst, H.C. *Light Scattering by Small Particles* (Dover, New York, 1981).
149. Vaughan, J.M. *The Fabry-Perot Interferometer. History, Theory, Practice and Applications*. Adam Hilger, Bristol (UK) and Philadelphia (USA), IOP Publishing Ltd., 1989.
150. Vizee, W., E.E. Uthe, and R.T.H. Collis. Lidar observations of airfield approach conditions: an exploratory study. *J. Appl. Meteorol.*, 8, 274 - 283, 1969.
151. Westwater, E.R. Ground-based microwave remote sensing of meteorological variables in *Atmospheric Remote Sensing by Microwave Radiometry*, Ed. M.A. Janssen, New York, Wiley, 1993.
152. Wiscombe, W.J. Improved Mie scattering algorithms. *Appl. Opt.* 19, 1505-1509, 1980.
153. Yamamoto, G., N. Tanaka, and S. Asano. Radiative transfer in water clouds in the infra-red region. *J. Atmos. Sci.* 27, 282-292, 1970.
154. Young, S.A. Analysis of lidar backscatter profiles in optically thin clouds. *Appl. Opt.*, 34, 7019-7031, 1995.
155. Young, S.A. Lidar studies of atmospheric aerosols. PhD Thesis, University of Adelaide, 1980.
156. Young, S.A., M.C. Pickett, P.J. Manson, and C.M.R. Platt. Lidar and infrared radiometer measurements of clouds during SOCEX I, in *Baseline Atmospheric Program (Australia) 1993*, edited by R.J. Francey, A.L. Dick and N. Derek, pp. 104-106, Bureau of Meteorology and CSIRO Division of Atmospheric Research, Melbourne, Australia, 1996.
157. Zdunkowski, W.G. and W.K. Crandall. Radiative transfer of infrared radiation in model clouds. *Tellus* 23, 517 - 527, 1971.
158. Zege, E. P., I. L., Katsev, and I. N. Polonsky. Analytic solution to lidar return signals from clouds with regard to multiple scattering. *Appl. Phys. B*, 60, 345-353, 1995.
159. Zuev, V.E., in *Topics in Applied Physics: Laser Monitoring of the Atmosphere*, Springer, New York, 1976.